Head Office: Università degli Studi di Padova

Department of Geosciences

Ph.D. COURSE IN: Geosciences
38th SERIES

DIAGNOSTIC AND EXPERIMENTAL APPROACHES FOR THE CONSERVATION OF GYPSUM REPLICAS: FROM INDOOR CLIMATE ASSESSMENT TO AGEING-INDUCED MATERIAL TRANSFORMATION

Thesis written with the financial contribution of the European Union – Next Generation EU

Coordinator: Prof. Andrea D'Alpaos
Supervisor: Prof. Claudio Mazzoli
Co-Supervisors: Dr. Chiara Coletti
Dr. Eleonora Balliana

Ph.D. student: Federica Bubola

Abstract

In this PhD thesis, a diagnostic and experimental study was conducted to investigate the conservation behaviour of gypsum-based replicas used in 19th century heritage collections. These casts, widely adopted for educational and display purposes in museums, are often housed in indoor environments lacking environmental control, making them highly vulnerable to degradation. The first part of the study focuses on selected group of historical plaster replicas conserved at the Museum of Roman Civilisation, in Rome, combining microclimatic monitoring with non-invasive and micro-invasive analyses to assess their composition, state of conservation, and the relationship with the indoor microclimatic conditions to which they are exposed.

In the second phase, mock-up samples replicating historical formulations were prepared and subjected to artificial ageing to evaluate the material response and the effectiveness of protective treatments commonly applied in conservation practice, using a combination of analytical techniques including Fourier-Transform Infrared spectroscopy, optical profilometry, scanning electron microscopy, and colourimetric analysis.

The final part of the research investigates the pore structures and their relationship with environmental factors, using a multi-analytical and multi-scale approach. Techniques such as nitrogen physisorption, mercury intrusion porosimetry, imaging digital analysis and X-ray micro-tomography were employed to characterise porosity before and after artificial ageing. By combining the study of historical case studies with controlled laboratory experiments, this research provides new insight into the deterioration mechanisms of gypsum materials and supports the development of preventive conservation strategies that account for their physical properties and response to indoor environmental stresses.

Sommario

Il progetto di dottorato presenta uno studio diagnostico-sperimentale volto ad indagare l'evoluzione conservativa dei calchi in gesso realizzati nel XIX secolo, oggi parte integrante di numerose collezioni storico-artistiche. Questi manufatti, ampiamente impiegati a fini didattici ed espositivi, sono spesso conservati in ambienti interni privi di climatizzazione e controllo microclimatico, risultando quindi particolarmente vulnerabili al degrado. La prima parte della ricerca si concentra su un nucleo di calchi storici conservati al Museo della Civilità Romana a Roma, esaminati mediante monitoraggio microclimatico *in situ* e tecniche diagnostiche non invasive e micro-invasive, per valutarne la composizione, lo stato di conservazione e la relazione con le condizioni microclimatiche di esposizione.

La seconda fase riguarda campioni di laboratorio formulati come analoghi di miscele storiche, sottoposti a cicli di invecchiamento accelerato per valutare la risposta dei materiali e l'efficacia di trattamenti protettivi correntemente impiegati nella pratica conservativa, attraverso analisi quali spettroscopia infrarossa, profilometria ottica, microscopia elettronica a scansione e colorimetria.

L'ultima parte della tesi indaga l'evoluzione della porosità e il suo rapporto con i fattori ambientali mediante un approccio muli-analitico e multi-scala. Combinando casi studio in situ e prove controllate in laboratorio, la ricerca chiarisce i meccanismi di degrado dei materiali a base di gesso e sostiene la definizione di strategie di conservazione preventiva calibrate sulle loro proprietà fisiche e sulla risposta agli stress ambientali in interno.

Contents

Abstract i

Sommario ii

Contents iii

List of Abbreviations viii

1. Introduction 1

1.1 Properties and transformation of gypsum 2

1.2 Environmental conditions and conservation challenges 4

1.3 Research background and objectives 6

1.4 Structure of the thesis 8

· Part 1: Gypsum replicas in indoor environments: the case of Trajan's Column at the Museum of Roman Civilisation 8

· Part 2: Conservation strategies for plaster replicas: insight into gypsum mixtures and protective coatings 8

· Part 3: Inside porosity: effects of artificial ageing on the decay of heritage gypsum materials 9

References 11

2. Materials and methods 15

· Part 1: Gypsum replicas in indoor environments: the case of Trajan's Column at the Museum of Roman Civilisation 15

· Part 2: Conservation strategies for plaster replicas: insight into gypsum mixtures and protective coatings 16

· Part 3: Inside porosity: effects of artificial ageing on the decay of heritage gypsum materials 16

3. Part 1: Gypsum replicas in indoor environments: the case of Trajan's Column at the Museum of Roman Civilisation 18

3.1 Introduction 19

3.1.1 Indoor microclimate and the preservation of gypsum replicas 19
3.1.2 Representativeness of the Trajan's Column plaster replicas 20
3.1.3 Historical background of the plaster replicas of Trajan's Column 21
3.1.4 Room LI: Trajan's Column replicas at the Museum of Roman Civilisation 22
3.2 Materials 23
3.3 Methods 26
3.3.1 Microclimatic monitoring 26
3.3.2 In situ survey 27
3.3.3 Microchemical and mineralogical characterisation 28
3.3 Results 30
3.3.1 Microclimatic monitoring 30
3.3.1.1 First phase: November 2022-May 2024 30
3.2.1.2 Thermal survey and identification of critical areas 32
3.3.1.3 Second phase: May 2024-May 2025 33
3.3.1.4 Monthly mean indoor temperature 36
3.3.2 Case study: plaster replica MCR_3052 36
3.3.2.1 On-site survey and degradation mapping 36
3.3.2.2 Spectrophotometric analysis 40
3.3.2.3 Active infrared thermography 42
3.3.3 Microchemical and mineralogical characterisation 43
3.3.3.1 XRPD 43
3.3.3.2 FESEM-EDS 44
3.3.3.3 μ-Raman spectroscopy 46
3.3.3.4 ATR-FTIR 48
3.3.3.5 TGA-DSC 50
3.3.3.6 HIS 51
3.4 Discussion 55
3.4.1 Microclimatic monitoring 55

3.4.2 On-site survey 57
3.4.3 Microchemical and mineralogical characterisation 58
3.5 Conclusion 60
References 62
Annex – Part 1 68
4. Part 2: Conservation strategies for plaster replicas: insight into gypsum mixtures and protective coatings 86
4.1 Introduction 87
4.2 Materials 90
4.2.1 Technical specifications of raw materials 95
4.3 Methods 97
4.3.1 Analytical techniques 97
4.3.2 Accelerated ageing 99
4.4 Results 102
4.4.1 Chemical and mineralogical characterisation 102
4.4.2 Hygrothermal ageing 104
4.4.2.1 Macroscopic evaluation after ageing 104
4.4.2.2 FTIR spectroscopy 105
4.4.2.3 Optical light profilometry 107
4.4.2.4 Colourimetry 110
4.4.3 Light ageing 112
4.4.3.1 FTIR spectroscopy 112
4.4.3.2 Optical light profilometry 112
4.4.3.3 Colourimetry 114
4.5 Discussion 115
4.5.1 Chemical and mineralogical characterisation 115
4.5.2 Hygrothermal ageing 118
4.5.2.1 Macroscopic evaluation after ageing 118

4.5.2.1 FTIR spectroscopy 119
4.5.2.2 Optical light profilometry 121
4.5.2.3 Colourimetry 125
4.5.3 Light ageing 128
4.5.3.1 FTIR spectroscopy 128
4.5.3.2 Optical light profilometry 129
4.5.3.3 Colourimetry 131
4.5.4 Summary of the outcomes 133
4.6 Conclusion 135
References 136
5. Part 3: Inside porosity: effects of artificial ageing on the decay of heritage gypsum materials 141
5.1 Introduction 142
5.2 Materials 145
5.3 Methods 147
5.3.1 Analytical procedure 147
5.3.1.1 Porosity 148
5.3.1.2 Accelerated ageing 152
5.3.1.3 Hygroscopic water adsorption 152
5.4 Results 153
5.4.1 Nitrogen physisorption (NP) 153
5.4.2 MIP 154
5.2.3 2D Image Processing 155
5.2.3 3D Micro-CT 158
5.4.5 Hygroscopic sorption behaviour 162
5.5 Discussion 163
5.5.1 Nitrogen physisorption (NP) 163
5.5.2 MIP 166

5.5.3 2D Image processing 169
5.5.4 3D Micro-CT 172
5.5.5 Correlation between porosity and hygroscopic sorption behaviour 176
5.6 Conclusion 177
References 178
6. Overall conclusions 183
6.1 Future developments 185
Reference 186
Supplementary materials 187
Acknowledgements 206

List of Abbreviations

ATR	Attenuated Total Reflectance
BET	Brunauer-Emmett-Teller
BJH	Barrett-Joyner-Halenda
BSE	Backscatter Electron
CPR	Critical Pore Radius
DIA	Digital Image Analysis
DSC	Differential Scanning Calorimetry
EDS	Energy-Dispersive X-ray Spectroscopy
ER	External Reflection (FTIR mode)
FESEM	Field Emission Scanning Electron Microscopy
FTIR	Fourier Transform Infrared Spectroscopy
HIS	Hyperspectral Imaging
MCR	Museum of Roman Civilasion
micro-CT	X-ray Microtomography
MIP	Mercury Intrusion Porosimetry
NIR	Near-Infrared
PCA	Principal Component Analysis
PVA	Polyvinyl Alcohol
RH	Relative Humidity
Sa	Arithmetical Mean Height (surface parameter)
SAM	Spectral Angle Mapper
SEM	Scanning Electron Microscopy
Sq	Root Mean Square Height (surface parameter)
SWIR	Short-Wave Infrared
T	Temperature
Tb.Th	Trabecular Thickness
TGA	Thermogravimetric Analysis
TPR	Threshold Pore Radius
XRPD	X-ray Powder Diffraction
XRF	X-ray Fluorescence

1. Introduction

Gypsum has a long tradition of use in the arts, owing to its low cost, wide availability, and suitability for moulding. Since antiquity, calcium sulphate-based materials have been employed in a variety of context, from Egyptian funerary architecture to Roman stucco and the plaster decorations of Islamic and Renaissance buildings [1-3].

Between the 18th and 19th centuries, plaster became increasingly important for the reproduction of ancient sculpture. The development of public museums and the growing interest in antiquity encouraged the production of casts as teaching and documentary tools, widely disseminated across European academies and institutions [4].

Due to its workability, rapid setting, and ability to retain fine details, gypsum was particularly suited to the large-scale production. At the same time, historical recipe books document a wide range of additives, both organic and inorganic, introduced to adjust workability, setting time, cohesion, or appearance [4-7]. This resulted in mixtures with notably different porosity, strength, and long-term durability.

Despite their historical and educational significance, 19th century plaster casts are often among the most fragile and challenging objects to conserve in museum collections. Their softness, high porosity, and sensitivity to moisture make them particularly vulnerable to fluctuating indoor climates. Repeated cycles of water absorption, drying, and temperature variation may induce swelling, cracking, salt migration, and surface powdering, effects that can be exacerbated by incompatible past conservation materials [8].

Although research on the conservation of gypsum materials has expanded in recent years, several critical aspects remain insufficiently investigated. In particular, the long-term behaviour of historical formulations under fluctuating indoor conditions is still poorly documented, as is the stability of protective treatments over extended periods.

This research originates from the study of the 19th century plaster replicas of Trajan's Column, currently housed in Room LI of the Museum of Roman Civilisation in Rome. This case provided a representative example of gypsum artefacts exposed to unsuitable indoor environments. From this context, the investigation expanded to explore the properties and conservation behaviour of gypsum-based materials through analytical characterisation and artificial ageing experiments.

1.1 Properties and transformation of gypsum

Gypsum, or calcium sulphate dihydrate ($CaSO_4 \cdot 2H_2O$), is a widely available mineral that has been employed since antiquity in a broad range of applications, appreciated for its ease of extraction, affordability and ability to capture fine details through moulding and casting processes [4,9].

Upon heating, gypsum undergoes a thermal dehydration process. Between approximately 100 and 200 °C, it releases part of its structural water and transforms into calcium sulphate hemihydrate ($CaSO_4 \cdot ½H_2O$), commonly known as Paris gypsum. This transformation, known as calcination, forms the basis of traditional plaster production and can be summarised by the following reaction [10]:

- Calcination (dehydration):
  $CaSO_4 \cdot 2H_2O\ (s) \rightarrow CaSO_4 \cdot ½H_2O\ (s) + 1.5H_2O\ (g)$

When combined with water, the hemihydrate rapidly rehydrates and recrystallises into gypsum [11]. This exothermic reaction leads to the formation of an intergrown network of crystals, whose morphology depends on the type of hemihydrate, additives, and setting conditions [12,13]. Once hardened, it forms a cohesive and rigid structure, whose mechanical behaviour depends on the formulation and setting process:

- Setting (hydration):
  $CaSO_4 \cdot ½H_2O\ (s) + 1.5H_2O\ (l) \rightarrow CaSO_4 \cdot 2H_2O\ (s) + \sim 137\ kJ$

Two main forms of hemihydrate can be produced depending on the calcination environment:

- β-hemihydrate, obtained through dry calcination in open vessels and commonly referred to as Paris gypsum;
- α-hemihydrate, produced under pressure in a saturated steam atmosphere, often associated with alabaster gypsum.

Although they share the same chemical composition, these two forms differ in morphology and behaviour. The β-form typically results in a more porous, less cohesive material, while the α-form leads to denser, more homogeneous network, characterised by improved mechanical properties and lower water absorption [14,15].

In traditional production settings, particularly in pre-industrial kilns, temperature control during calcination was limited, and some areas could locally rise to 600-800 °C. As a result, historical gypsum-based materials often consist of a mixture of calcium sulphate phases: unreacted dihydrate, hemihydrate, and various forms of anhydrite ($CaSO_4$), including anhydrite II [13]. This multiphase composition has a direct impact on the setting behaviour and mechanical properties of the final product. For instance, the presence of anhydrite II may improve mechanical resistance, but also slow down the hydration process. Residual dihydrate, on the other hand, can act as a filler, conversely, compromise material's cohesion [12].

Moreover, recent researches on thermodynamics and phase diagrams have shown that gypsum dehydrates to anhydrite at temperature above approximately 42 °C under equilibrium conditions. However, the transformation is kinetically slow, and metastable intermediates such as bassanite and soluble anhydrite are typically formed [11]. These metastable phases are particularly relevant in heritage materials, where they can persist over time and affect both moisture interaction and reactivity [11].

Historical gypsum formulations were often modified through the addition of organic and inorganic additives, aimed at enhancing specific characteristics such as plasticity, setting time, surface finish, or durability. Animal glue, for instance, was frequently employed to improve workability and internal cohesion, although its hygroscopicity and biodegradable nature increased the material's vulnerability to biological activity and water retention [9]. Additionally, high concentration of organic additives has also been found to stabilise metastable phases such as bassanite [16].

Inorganic components such as marble powder, kaolin, or lime were frequently added to improve surface appearance or reduce shrinkage. Marble powder, which is fine and chemically inert, functions as a pore-filling agent that enhances density and whiteness. Meanwhile, kaolin can improve plasticity and minimise drying cracks, although it may also increase the material's sensitivity to moisture [17].

From a conservation perspective, porosity represents a critical parameter, as it controls moisture transport, mechanical stability, and the material's response to environmental fluctuations. The rapid setting of hemihydrate-based formulations results in a heterogeneous pore network, whose morphology depends on both the intrinsic characteristics of the raw material and the processing conditions. Capillary water uptake, dissolution-recrystallisation cycles, and dehydration phenomena are all directly related to the geometry, size, and distribution of these pores.

Compared to other heritage materials, such as lime-based mortars, gypsum exhibits significantly higher solubility and water sensitivity, which makes it particularly susceptible to damage in unstable indoor environments. Understanding its physical and chemical transformations, as well as its textural properties, is therefore essential not only to assess degradation mechanisms, but also to develop conservation strategies that are both effective and sustainable.

1.2 Environmental conditions and conservation challenges

Although gypsum has historically been employed in indoor settings, where direct exposure to weathering agents is reduced, it remains highly vulnerable to fluctuations in temperature and relative humidity. Its porous and hygroscopic nature makes it particularly sensitive to variations in temperature (T) and relative humidity (RH). In the absence of adequate environmental control systems, which are often lacking in historic buildings and museum contexts, fluctuations of T and RH can lead to progressive and cumulative damage over time [18,19].

Microclimatic variations may occur on different spatial and temporal scales, with variable intensity depending on material properties, architectural layout, and the specific location within the room. Even within the indoor environment, factors such as solar exposure, air circulation, and the proximity of objects to external walls or windows can generate significant hygrothermal gradients. In gypsum-based artefacts, these fluctuations can promote the absorption and desorption of water vapour, phase transitions, and facilitate the mobilisation and crystallisation of soluble salts, resulting in cracking, surface powdering, delamination, and loss of cohesion [4].

Water can accumulate within the pore network through vapour adsorption or capillary condensation when RH exceeds critical thresholds. If these humid conditions are followed by rapid drying, crystallisation and shrinkage processes may occur, generating internal stress and promoting micro-fracturing of the matrix. When repeated over time, wet-dry cycles gradually weaken the internal cohesion of the material and accelerate surface degradation [20]. Under particularly dry conditions, characterised by low RH and elevated temperatures, partial dehydration may induce the transformation of gypsum into bassanite, resulting in a loss of mechanical integrity and cohesion. Although this phase change is theoretically reversible, extended dehydration can lead to structural instability and irreversible damage [19].

At the same time, prolonged exposure to high RH, typically above 80 %, can promote salt solubilisation and recrystallisation cycles, as well as microbial proliferation, particularly in areas affected by condensation or water infiltration. Moisture also acts as a catalyst for redox and hydrolytic reactions, further contributing to chemical degradation [18]. In such conditions, gypsum itself may partially dissolve, leading to the formation of secondary mineral phases and significant alterations in surface texture and porosity [21,22].

In this context, long-term microclimatic monitoring is essential for preventive conservation. According to European standard UNI EN 15757 (2010), environmental monitoring in indoor heritage settings should be carried out for a minimum duration of one year to reliably assess seasonal variations and confirm the stability of temperature and humidity conditions over time [23]. It enables for the identification of seasonal and daily cycles, spatial variability, and critical risk thresholds, thus supporting the development of site-specific conservation strategies. Although international standards such as UNI 10829:1999 [24] suggest optimal conservation parameters for gypsum artefacts (typically 45-60 % RH and 15-25 °C), recent researches have questioned the validity of fixed thresholds, highlighting the importance of assessing the so-called *historic climate*, i.e., the environmental conditions to which artefacts have gradually adapted over time [25].

The long-term stability of gypsum replicas depends on a complex interaction between material composition, microclimatic variability, and architectural features. Material heterogeneities, such as metal reinforcements, coatings, or restoration compounds, can create localised weathering phenomena with formation of secondary products of alteration or mechanical discontinuities, causing internal cracks or detachments, e.g., due to moisture transport or thermal stress, which may exacerbate localised decay phenomena [4,19].

Although less common in indoor settings, freeze-thaw mechanisms may still be relevant in unheated buildings during winter months, especially when temperature fluctuations fall below 0 °C. In these cases, the formation of ice crystals within the pore network can promote microcracking and material detachment over time [26].

Overall, the environmental response of gypsum-based materials is governed by the equilibrium between thermal and hygroscopic processes. Ensuring their long-term preservation requires a clear understanding of both their intrinsic fragility and the complexity of the surrounding microclimate. In this context, integrated monitoring strategies campaigns and material-specific risk assessments represent essential tools for site-specific conservation strategies [21,27]. Given the environmental vulnerabilities, a more in-depth investigation into the behaviour of historical gypsum materials was needed.

1.3 Research background and objectives

While many studies have addressed the properties of historic plasters and mortars [19,28-31], with a focus on aspects such as mechanical properties [9,20,32,33] and mineralogical composition [13,34,35], specific studies addressing the conservation of plaster replicas are still relatively scarce.

One of the main challenges in preserving historical casts is the lack of sufficient documentation regarding the variability in their composition and microstructure. As discussed in several historical manuals [6,7], these materials were not standardised; formulations were often modified by incorporating organic and inorganic components such as animal glue, marble powder, and kaolin, aimed at improving cohesion, workability, or surface finish [9]. These modifications, combined with the lack of strict control over traditional calcination processes, meant that the physical, mechanical and microstructural properties of the final product could not be guaranteed, leading to wide variability. As a result, plaster casts not only differ from modern industrial gypsum materials, but also significantly from one another, with their degradation patterns strongly linked to this heterogeneity. Nonetheless, many conservation studies are still based on simplified formulations. Tests are often carried out on pure forms of gypsum, failing to reproduce the more complex and heterogenous mixtures typically found in historical casts. These variables influence setting behaviour, porosity, and long-term durability, and should be carefully considered when evaluating conservation options.

Another aspect that is still not well understood is how gypsum replicas respond to changes in indoor climate. Due to its partial solubility and high hygroscopicity, gypsum is very sensitive to variations in temperature and humidity. These conditions can lead to processes such as surface erosion, pulverisation, cracking and dissolution of the material. This is further complicated by the presence of metastable phases, such as bassanite, which can rehydrate over time and weaken the structure.

Previous conservation treatments could also add complexity to their preservation process. Traditional coatings such as wax, shellac (a natural resinous varnish), and kaolin were often applied to reduce porosity and protect the surface [4,5]. In more recent years, synthetic materials like acrylic resins or polyvinyl alcohol have been tested as consolidants or reversible protective layers. However, their long-term stability under fluctuating environmental conditions is still not fully understood. Some coatings may block moisture exchange or promote salt crystallisation behind the treated layer, while others can change the surface appearance or react incompatibly with the underlying material.

Understanding how historical gypsum materials behave under environmental stress required a comprehensive analytical approach. This study combined *in situ* observations, laboratory analysis, and artificial ageing to investigate the conservation behaviour of 19th century plaster casts, with a particular focus on how composition, porosity, and environmental conditions influenced their stability over time. A wide range of complementary techniques was employed to characterise the materials and monitor their changes, including X-Ray Powder Diffraction (XRPD) for phase identification, Field Emission Scanning Electron Microscopy coupled with Energy Dispersive Spectroscopy (FESEM-EDS) for microstructural and elemental analysis, Attenuated Total Reflectance Fourier Transform Infrared Spectroscopy (ATR-FTIR) and μ-Raman spectroscopy for detecting organic and inorganic components, and Thermogravimetric Analysis coupled with Differential Scanning Calorimetry (TGA-DSC) for investigating dehydration behaviour. Porosity was assessed using Nitrogen Physisorption (NP), Mercury Intrusion Porosimetry (MIP), and Digital Image Analysis (DIA), while X-ray Microtomography (micro-CT) provided insights into the internal structure before and after ageing.

To reproduce the variability observed in historical casts, mock-up samples were prepared based on traditional recipes using both alabaster and Paris gypsum, mixed with traditional additives such as marble powder, kaolin, animal glue, and wood powder. Selected samples were coated with protective coatings, including PVA, acrylic resin and kaolin suspensions, and then subjected to artificial ageing cycles simulating temperature, humidity and UV fluctuations.

This multidisciplinary approach was developed to reach the following research objectives:

- Assess conservation state of original casts through in situ measurements;
- Characterise the composition, and microstructure of historical samples;
- Replicate historical formulations and monitor their response under controlled hygrothermal and photo-induced ageing, focusing on both surface and bulk porosity changes;
- Evaluate the stability and long-term behaviour of protective coatings;
- Better understand the main degradation mechanisms and identify conservation strategies that consider the specific features of the materials and the environments.

By improving the understanding of how material composition, porosity, and environmental exposure interact, this research provides a solid foundation of the development of more effective and tailored conservation strategies.

1.4 Structure of the thesis

The structure of the thesis reflects the interdisciplinary approach adopted in this research, combining on-site surveys, laboratory experiments, and multi-analytical investigations. The thesis is divided into three parts, each addressing a different aspect of the research while contributing to a cohesive investigation of gypsum-based replicas.

The overall structure of the thesis and the contribution of each part to the research is presented in Figure 1. Below is a brief presentation of the main goals for each part.

- **Part 1: Gypsum replicas in indoor environments: the case of Trajan's Column at the Museum of Roman Civilisation**

This part focuses on the 19th century plaster replicas of Trajan's Column preserved in Room LI of the Museum of Roman Civilisation in Rome, currently housed in an environment without climate control. A two-year microclimatic monitoring campaign was conducted to analyse temperature, relative humidity, and dew point trends. These data were integrated with a diagnostic survey of 35 casts and a multi-analytical investigation of selected samples using colourimetry, infrared thermography, FESEM, XRPD, ATR-FTIR, μ-Raman spectroscopy, hyperspectral imaging, and TGA-DSC. The results provide insight into the relationship between environmental conditions and material degradation, supporting preventive conservation strategies. This work further develops the findings presented in Bubola et al., (2024) [36].

- **Part 2: Conservation strategies for plaster replicas: insight into gypsum mixtures and protective coatings**

The second part investigates the formulation of historical gypsum mixtures and the effectiveness of protective coatings under fluctuating environmental conditions. Mock-up samples, prepared using traditional additives and gypsum types, were treated with historical and modern coatings and subjected to artificial ageing through controlled hygrothermal cycles and light exposure. Analytical methods, including optical profilometry, ER-FTIR, and colourimetry, were used to monitor surface and chemical changes over time. The results

contribute to understand the interaction between materials, coatings, and environmental stress, providing a basis for selecting compatible conservation treatments.

- **Part 3: Inside porosity: effects of artificial ageing on the decay of heritage gypsum materials**

Porosity plays a central role in the deterioration of gypsum-based artefacts, influencing moisture transport and mechanical stability. This part presents the results of an ageing experiment on mock-up samples made from different gypsum types and additives, analysed before and after cyclic hygrothermal ageing. A multi-analytical approach was applied, including nitrogen physisorption, MIP, FESEM with image analysis, micro-CT, and hygroscopic tests. The comparative analysis of pore characteristics highlights how formulation influences porosity and its evolution, offering insight into degradation mechanisms and material vulnerability.

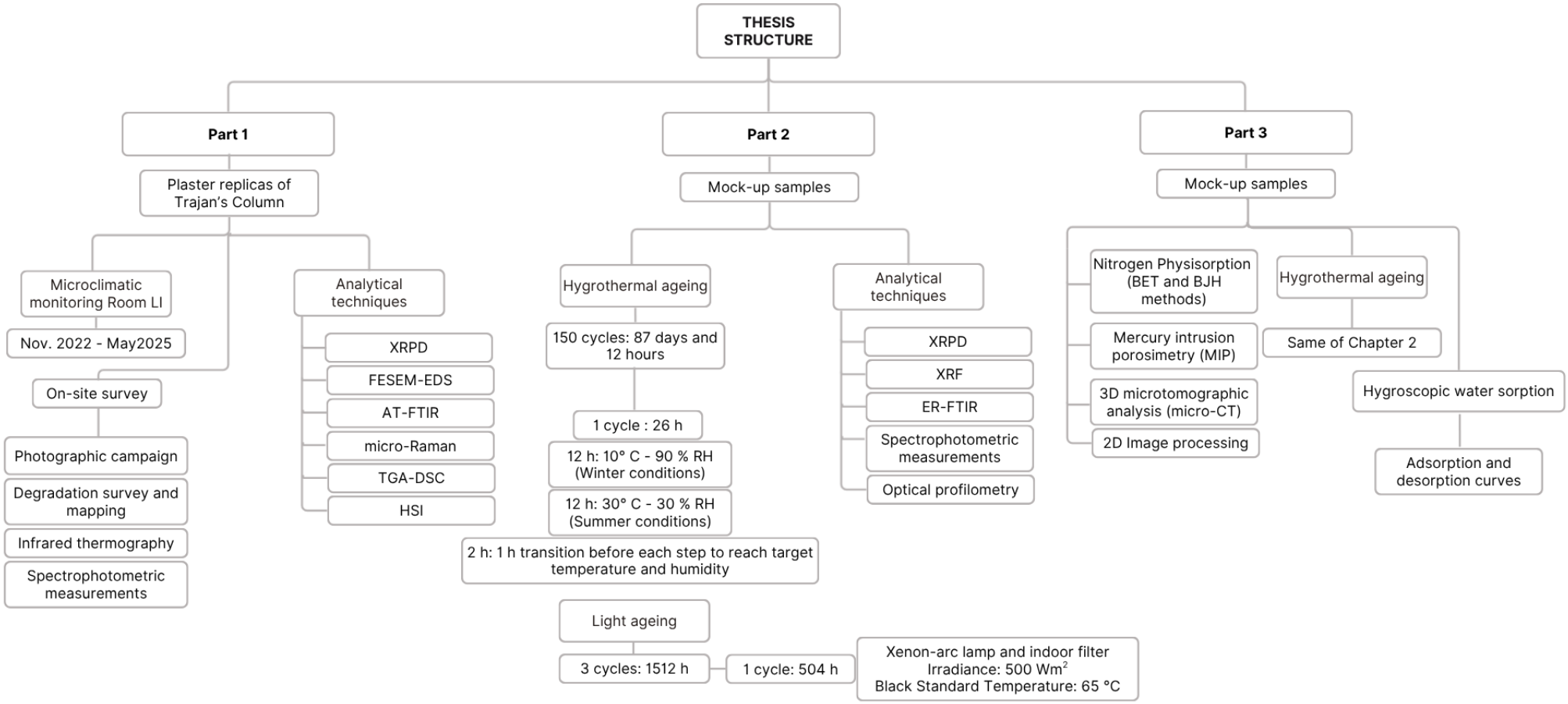

Figure 1. Overview of the thesis structure and methodology. The diagram illustrated the methodological workflow and analytical procedure of each part.

References

[1] V. Risdonne, C. Hubbard, J. Puisto, C. Theodorakopoulos, A multi-analytical study of historical coated plaster surfaces: the examination of a nineteenth-century V&A cast of a tombstone, Herit. Sci., vol.9 (2021), pp. 70-89.

[2] M. T Freie, A. Santos Silva, M. do Rosário Veiga, C. Barrocas Dias, A. Manhita, Stucco marble in the Portuguese architecture: multi-analytical characterisation, Int. J. Archit. Herit., vol. 14 (2020), pp. 977-993.

[3] G. Gariani, P. Lehuédé, L. Leroux, G. Wallez, F. Goubard, A. Bouquillon, M. Bormand, First insight on the mineral composition of "stucco" devotional reliefs from Italian Renaissance Masters: investigating technological practices and raw material sourcing, J. Cult. Herit., vol. 34 (2018), pp. 23-32.

[4] E. M. Payne, The conservation of plaster casts in the nineteenth century, Stud. Conserv., vol. 65 (2020), pp. 37-58.

[5] V. Risdonne, C. Hubbard, V. H. López Borges, C. Theodorakopoulos, Materials and Techniques for the Coating of Nineteenth-century Plaster Casts: A Review of Historical Sources, Stud. Conserv., vol. 67 (2022), pp. 186-208.

[6] C. Arcolao, Le ricette del Restauro: Malte, intonaci, stucchi dal XV al XIX secolo, Saggi Marsilio, Venezia, 1998. [In Italian]

[7] Turco, Il gesso lavorazione – trasformazione – impieghi, Ulrico Hoepli, Milano, 1861. [In Italian]

[8] V. Brunello, D. Bersano, L. Rampazzi, A. Sansonetti, C. Tedeschi, Gypsum based mixes for conservation purposes: evaluation of microstructural and mechanical features, Mat. Const., vol 70 (2020), e207, pp. 1-14.

[9] E. Salavessa, S. Jalali, L. M. O. Sousa, L. Fernandes, A. M. Duarte, Historical plasterwork techniques inspire new formulations, Constr. Build. Mater., vol. 48 (2013), pp. 858-867.

[10] A. Vimmorová, J. Krejsová, L. Scheinherrová, M. Doleželová, M. Keppert, Changes in structure and composition of gypsum paste at elevated temperature, J. Therm. Anal. Calorim., vol. 142 (2020), pp. 19-28.

[11] A. E. Charola, J. Pühringer, M. Steiger, Gypsum: a review of its role in the deterioration of building materials, Environ. Geol., vol. 52 (2007), pp. 339-352.

[12] N. B. Singh, B. Middendorf, Calcium sulphate hemihydrate hydration leading to gypsum crystallization, Prog. Cryst. Growth Charact. Mater., vol 53 (2007), pp. 57-77.

[13] K. Elert, P. Bel-Anzué, M. Burgos-Ruiz, Influence of calcination temperature on hydration behaviour, strength, and weathering resistance of traditional gypsum plaster, Constr. Build. Mater., vol. 367 (2023), pp. 130361-130371.

[14] Z. Wei, Q. Zhang, X. Li, Crystallization Kinetics of α-Hemihydrate Gypsum Prepared by Hydrothermal Method in Atmospheric Salt Solution Medium, Crystals, vol. 11 (2021), 843.

[15] B. Lee, G. Kim, J. Nam, K. Lee, G. Kim, S. Lee, K. Shin, T. Koyama, Influence of α-Calcium Sulfate Hemihydrate on Setting, Compressive Strength, and Shrinkage Strain of Cement Mortar, Mat., vol. 12 (2019), 163.

[16] K. Elert, C. Benavldes-Reyes, C. Cardell, Effect of animal glue on mineralogy, strength and weathering resistance of calcium sulphate-based composite materials, Cem. Concr. Compos., vol. 96 (2019), pp. 274-283.

[17] M. Murat, A. Attari, Modification of some physical properties of gypsum plaster by addition of clay minerals, Cem. Concr. Res., vol.21 (1991), pp. 378-387.

[18] A. Spagnulo, C. Vetromile, A. Masiello, M. F. Alberghina, S. Schiavone, C. Lubritto, Climate and Cultural Heritage: The Case Study of "Real Sito of Carditello", Heritage, vol. 2 (2019), pp. 2053-2066.

[19] M. Caroselli, G. Cavallo, A. Felici, S. Luppichini, G. Nicoli, L. Aliverti, G. Jean, 2019. Gypsum in Ticinese stucco artworks of the 16–17th century: Use, characterization, provenance and induced decay phenomena. J. Archaeol. Sci. Rep. 24, 208–219.

[20] M. T. Freie, M. do Rosário Veiga, A. Santos Silva, J. de Brito, Restoration of ancient gypsum-based plasters: design of compatible materials, Cem. Concr. Compos., vol. 120 (2021), pp. 104014-104027.

[21] M. Torres-Gonzàlez, C. Rubio-Bellido, D. Bienvenido-Huertas, J. M. Alducin-Ochoa, V. Flores-Alés, Long-Term environmental monitoring for preventive conservation of external historical plasterworks, J. Build. Eng., vol. 47 (2022), 103896-103910.

[22] S. Ramírez, M. Zarzo, A. Perles, F. J. García-Diego, A methodology for discriminant time series analysis applied to microclimate monitoring of fresco paintings, Sensors, vol. 21 (2019), pp. 1-29.

[23] UNI EN 15757:2010, Beni Culturali – Specifiche per la temperatura e l'umidità per limitare i danni meccanici indotti dal clima nei materiali organici igroscopici. Ente Nazionale Italiano di Unificazione (UNI), Milano, 2010. [In Italian]

[24] UNI 10829:1999, Beni Culturali – Condizioni ambientali in ambienti confinati per la conservazione – Misurazione ed analisi. Ente Nazionale Italiano di Unificazione (UNI), Milano, 1999. [In Italian]

[25] K. Fabbri, Historic Climate in Heritage Building and Standard 15757: Proposal for a Common Nomenclature, Climate, vol. 10 (2022), pp. 4-12.

[26] S. Salvini, C. Coletti, L. Maritan, M. Massironi, A. Pieropan, R. Spiess, C. Mazzoli, Petrographic characterization and durability of carbonate stones used in UNESCO World Heritage Sites in northeastern Italy, Environ. Earth Sci., vol. 82 (2023), pp. 49-72.

[27] X. Li, M. Ran, Gypsum-based humidity-control material: preparation, performance and its impact on building energy consumption, Mater., vol. 16 (2023), pp. 5211-5226.

[28] M. Uccelli, M. Caroselli, J. Válek, J. Zapletalová, A. Felici, G. Nicoli, G. Jean, Characterization of the stucco decoration by Baldassarre Fontana in the Gallery of the Angels at Uherče Castle (Cz), J. Archaeol. Sci. Rep., vol. 44 (2022), pp. 103493-103505.

[29] L. Rampazzi, B. Rizzo, C. Colombo, C. Conti, M. Realini, U. Bartolucci, M. P. Colombini, A. Spiriti, L. Facchin, The stucco decorations from St. Lorenzo in Laino (Como, Italy): The materials and the techniques employed by the "Magistri Comacini", Anal. Chem. Acta., vol. 630 (2008), pp. 91-100.

[30] M. Caroselli, G. Cavallo, A. Felici, L. Aliverti, S. Luppichini, G. Jean, G. Nicoli, Characterisation of the stucco decorations at the "Sacro Monte di Ossuccio" (16^{th}-17^{th} century, Como, Italy, Int. J. Conserv. Sci., vol. 7 (2016), pp. 857-870.

[31] M. Caroselli, S. A. Ruffolo, F. Piqué, Mortars and plasters – how to manage mortars and plasters conservation, Archaeol. Anthropol. Sci., vol. 13 (2021), pp. 188-208.

[32] M. T. Freie, M. do Rosário Veiga, A. Santos Silva, J. De Brito, Studies in ancient gypsum based plasters toward their repair: Physical and mechanical properties, Constr. Build. Mater., vol. 202 (2019), pp. 319-331.

[33] A. Magalhães, R. Veiga, Physical and mechanical characterisation of historic mortars. Application to the evaluation of the state of conservation, Mater. Constr., vol. 59 (2009), pp. 61-77.

[34] G. Gariani, P. Lehuéde, L. Leroux, G. Wallez, F. Goubard, Anne Bouquillon, Marc Bormand, First insights on the mineral composition of "Stucco" devotional reliefs from Italian Rennaissance Masters: investigating technological practices and raw material sourcing, J. Cult. Herit., vol. 34 (2018), pp. 23-32.

[35] M. T. Freie, A. Santos Silva, M. do Rosário Veiga, J. De Brito, Studies in ancient gypsum based plasters towards their repair: Mineralogy and microstructure, Constr. Build. Mater., vol. 196 (2019), pp. 512-529.

[36] F. Bubola, C. Coletti, E. Balliana, C. Cecamore, C. Parisi Presicce, C. Mazzoli, The diagnostic study of the plaster replicas of the Trajan's Column conserved at the Museum of Roman Civilisation (Rome), ACTA IMEKO, vol. 13 (2024), pp. 1-8.

2. Materials and methods

Understanding how gypsum-based materials interact with environmental variables and conservation treatments requires a multi-analytical and multidisciplinary approach. Due to the compositional heterogeneity, structural complexity, and environmental sensitivity of historical plaster replicas, a single technique cannot fully capture their behaviour over time. For this reason, this research combines diagnostic surveys, laboratory characterisation, and accelerated ageing tests, integrating complementary methods across different analytical scales.

The selection of analytical techniques was defined by the specific objectives of each phase of the research. Non-invasive and on-site surveys, such as photographic documentation, infrared thermography, colourimetry, were employed to assess the state of conservation and surface alteration in the Museum context.

Laboratory-based analysis, including optical profilometry, XRPD, FESEM-EDS, ATR-FTIR, ER-FTIR, μ-Raman spectroscopy, Hyperspectral Imaging, and TGA-DSC, were used to investigate the composition and microstructure of historical samples and mock-ups. A particular focus was placed on the study of porosity, investigated through nitrogen physisorption, MIP, FESEM with image analysis, and micro-CT, in order to evaluate how different formulations, respond to environmental stress.

This combination of techniques was selected to gather complementary information, allowing for a more complete understanding of material composition, surface alterations, and internal structure.

Further methodological details, including sampling procedures, analytical settings, and processing protocols, are discussed in the corresponding part.

- **Part 1: Gypsum replicas in indoor environments: the case of Trajan's Column at the Museum of Roman Civilisation**

The materials examined in Part 1 consist of a selection of 35 plaster replicas conserved in Room LI of the Museum of Roman Civilisation in Rome, reproducing the reliefs of Trajan's Column. Their selection was based on degradation class (as defined in a 2012 Museum survey), spatial distribution within the gallery, and conservation priorities. A detailed description of the collection, the criteria adopted for sample selection, and the cast layout is provided in Section 3.2 of the chapter.

The methods adopted in this study include:

- Microclimatic monitoring, based on the use of dataloggers and infrared thermography to characterise thermal and humidity fluctuations within the gallery space (section 3.3.1, Part 1);
- In situ diagnostic survey, including photographic documentation, infrared thermography, and colourimetric analysis to assess chromatic alterations and surface changes across the casts (section 3.3.2, Part 1);
- Microchemical and mineralogical characterisation of two micro-samples from cast MCR_3045, using a combination of XRPD, ATR-FTIR, μ-Raman, FESEM-EDS, TGA-DSC, and Hyperspectral Imaging (section 3.3.3, Part 1).

- **Part 2: Conservation strategies for plaster replicas: insight into gypsum mixtures and protective coatings**

The experimental activities described in Part 2 were designed to explore the behaviour of historical gypsum formulations and the effectiveness of selected protective coatings under artificial ageing conditions. The mock-ups were prepared using alabaster and Paris gypsum, in combination with additives historically documented in recipe books, and then treated with different coatings. The preparation process is described in section 4.2 of Part 2.

These specimens were subjected to two distinct artificial ageing protocols: cyclic hygrothermal ageing in a climatic chamber, and light ageing in a Solarbox system. The design of the environmental cycles is presented in section 4.3.2 of Part 2.

To assess the impact of ageing on chemical composition and surface morphology, a multi-analytical approach was adopted. The analytical techniques included XRPD, FESEM, XRF, FTIR in external reflection mode (ER-FTIR), optical profilometry, and spectrophotometric colour measurements. The methodological details of these techniques are provided in section 4.3.1 of Part 2.

- **Part 3: Inside porosity: effects of artificial ageing on the decay of heritage gypsum materials**

The methodologies employed in Part 3 focus on the role of porosity in gypsum-based formulations subjected to environmental stress. Six mock-ups were prepared using the same materials described in Part 2, and the full composition of the mixtures are reported in section 5.2 of Part 3.

A multi-analytical approach was adopted to assess porosity before and after artificial ageing. This included nitrogen physisorption, MIP, 2D digital image analysis of SEM-BSE

images, and 3D micro-CT. These complementary techniques allowed for the characterisation of pore size distribution, connectivity, sphericity, and surface area across different scales. Details on sample preparation and analytical procedures are provided in section 5.3.1.1 of Part 3.

The samples were subjected to the same accelerated hygrothermal ageing cycles described in Part 2. The ageing protocol is summarised in section 5.3.1.2 of Part 3.

To complement the porosity analysis, sorption tests were conducted to evaluate the moisture uptake and release behaviour of each formulation. Adsorption and desorption isotherms were obtained under controlled RH conditions and are discussed in section 5.3.1.3 of Part 3.

3. Part 1: Gypsum replicas in indoor environments: the case of Trajan's Column at the Museum of Roman Civilisation

This manuscript is currently in preparation for publication. FB, EB, CC and CM designed the study and developed the methodology. The in-situ survey campaign was conducted by FB, CC, and EB. XRPD analyses were performed by Marco Favero, and FESEM analysis and Jacopo Nava (non-author contributors); in both cases the data were processed and interpreted by FB. ATR-FTIR measurements were carried out by EB, while μ-Raman analyses were conducted by FB and CM. TGA-DSC measurements were performed by EB, and Hyperspectral Imaging by FB and Bruno Casarotto. All datasets were processed and interpreted by FB. All authors discussed the results and agreed on their interpretation. FB wrote the manuscript, with all co-authors contributing to the final revision. This chapter expands on the results previously published in Bubola et al., (2024) [1].

Federica Bubola[1*], Eleonora Balliana[2], Chiara Coletti[1], Claudio Parisi Presicce[3], Claudia Cecamore[3], Claudio Mazzoli[1]

[1] Department of Geosciences, University of Padova, via Giovanni Gradenigo 6, 35131 Padova, Italy

[2] Department of Environmental Sciences, Informatic and Statistics, Ca' Foscari University, Via Torino 155, 30172 Mestre, Italy

[3] Sovrintendenza Capitolina ai Beni Culturali, Piazza Lovatelli 35, Rome, Italy

---

Abstract

The conservation of gypsum-based materials is highly dependent on environmental conditions, due to their hygroscopic nature and limited mechanical strength. This study focuses on the 19th century plaster replicas of Trajan's Column preserved in Room LI of the Museum of Roman Civilisation in Rome, a large-scale collection currently housed in an uncontrolled indoor environment. In preparation for the museum's reopening, a microclimatic monitoring campaign was conducted over a two-year period to evaluate trends in temperature, relative humidity, and dew point. To assess the relationship between environmental conditions and material degradation, the monitoring was combined with a diagnostic survey of 35 casts and a multi-analytical investigation of representative samples. Analytical methods included colourimetric measurements, thermographic analysis, Scanning Electron Microscopy (SEM), X-ray Powder Diffraction (XRPD), Attenuated Total Reflectance-Fourier Transform Infrared Spectroscopy (ATR-FTIR), μ-Raman spectroscopy, Hyperspectral Imaging and Thermogravimetric-Differential Scanning Calorimetry (TGA-DCS). The correlation between environmental parameters and material properties provided

insights into the impact of indoor microclimatic conditions on the casts and supported conservation planning. This chapter further develops the findings presented in Bubola et al., (2024) [1].

3.1 Introduction

3.1.1 Indoor microclimate and the preservation of gypsum replicas

The stability of indoor environmental conditions strongly influences the conservation of cultural heritage. Variations in temperature (T) and relative humidity (RH) are key factors affecting the behaviour of porous and hygroscopic materials [2]. These conditions are common in historical buildings and museums, where climate control systems are often absent or inadequate. Seasonal cycles, restricted ventilation, and thermal exchange with the outdoor environment can cause significant hygrothermal fluctuations, accelerating degradation and compromising long-term preservation [2].

Among the materials commonly found in heritage contexts, those based on gypsum are particularly prone to alteration when exposed to environmental variations. Their porous microstructure, developed during the setting and drying phases, promotes moisture exchange with the surrounding atmosphere. An increase in RH can lead to water absorption within the pore system, resulting in swelling, mineral dissolution, and reduced cohesion. Conversely, when RH decreases, the rapid evaporation of moisture can induce shrinkage and connected internal stress, cracking, and surface powdering [3]. Repeated wetting-drying cycles exacerbate these phenomena, potentially resulting in structural damage. In parallel, condensation events or prolonged exposure to high RH levels may promote salt migration and crystallisation, and favour biological colonisation [4].

19th century plaster replicas, typically composed of gypsum and a range of additives such as clays, marble powder, gums, or resins, in order to improve mechanical behaviour or modify setting times are particularly susceptible to the above-mentioned forms of degradation [3-6]. In addition, structural reinforcements in wood or iron were frequently incorporated during casting, or added in later restoration campaigns [3,6]. These components respond differently to environmental changes: gypsum is highly hygroscopic, wood may swell or shrink, and metal elements can corrode. The resulting internal stresses and incompatibilities, may lead to localised deformation, mechanical detachment, and loss of structural cohesion.

Although these replicas are historically significant, they have not always received sufficient attention in conservation [7]. Often seen as simple copies with limited artistic or

material worth, they have actually played a vital role as educational tools and as recreations of lost or damaged artworks. Many of these casts now serve as valuable records of sculptures that have since decayed or become inaccessible [3,6]. Effective conservation strategies must therefore assess not only their physical state but also the historical and cultural contexts in which they were made, used, and displayed.

In terms of environmental management, the traditional approach has often involved applying standard thresholds for temperature and humidity, typically defined by international guidelines. However, this method may not fully consider the specific environmental history of each object. In recent years, the concept of the *historic climate* has gained increasing relevance. As proposed by Fabbri (2022), conservation strategies should account for the conditions to which an object has adapted over time, rather than applying predefined climate parameters [8]. Understanding this equilibrium is particularly important in contexts where environmental regulation is not possible, such as in many archaeological museums and historic buildings. In these cases, analysing long-term trends, seasonal fluctuations and extreme values becomes essential for defining realistic conservation parameters and for developing sustainable strategies.

While many studies have addressed the properties of historic plasters and mortars [4,9-12], focusing on aspects such as mechanical behaviour [13-16] or mineralogical composition [17-19], research specifically focused on the conservation of plaster replicas remains limited. Few works have examined the environmental impact on gypsum casts, particularly those with complex formulations, internal reinforcements, and surface coatings [3].

This chapter addresses the conservation of the Trajan's Column plaster replicas conserved at the Museum of Roman Civilisation (Rome), with a focus on the impact of environmental conditions on the stability of gypsum-based materials. The results support further investigation and contribute to the planning of the conservation strategies in preparation for the Museum's reopening. This chapter presents an analysis of the conservation conditions of the casts in Room LI, combining environmental monitoring and material characterisation to support preventive interventions.

3.1.2 Representativeness of the Trajan's Column plaster replicas

The plaster replicas of the Trajan's Column constitute a particularly meaningful case study within the broader context of gypsum-based heritage objects preserved in historic indoor environments. Form a technical standpoint, they are fully aligned with 19th century casting practices, which commonly relied on alabaster gypsum and clay- or carbonate-based

additives to reproduce sculptural reliefs with high fidelity. Typologically, they exemplified a widespread tradition of large-scale didactic and museum replicas, and thus provide insights that extend beyond the specific monument. From a conservation perspective, their long-term exposure to an indoor environment characterised by limited ventilation, marked thermal gradients and persisted RH fluctuations mirrors the conditions found in many historic museums and monumental building lacking climate control. For these reasons, the casts may be considered representative not only of their own production context, but also of the environmental challenges affecting numerous gypsum artefacts preserved in similarly unstable settings.

3.1.3 Historical background of the plaster replicas of Trajan's Column

Casts of Trajan's Columns were first produced in 1540 at the request of King Francis I of France, who commissioned the painter Francesco Primaticcio to mould the reliefs of the lower section of the monument. A second phase followed between 1640 and 1642, when Fréart brothers created approximately seventy additional casts intended for the decoration of the Grande Galerie of the Palais du Louvre, at that time still a royal residence rather than a museum. Over the following decades, the collection expanded to nearly 450 pieces, although only very few have survived to the present day [20].

A second campaign was carried out during the 17th century under Louis XIV, to reproduce the full sequence of reliefs. However, only a few fragments from this series have survived.

The Exposition Universelle held in Paris in 1867 marked a turning point in the use of plaster casts, confirming their transition from educational tools used in art academies to central exhibits in major European museums. The casts of Trajan's Column exemplify this transformation and role, given the size and complexity of the project. Between 1861 and 1862, Napoleon III promoted a large-scale casting campaign in Rome, which resulted in a complete set of moulds of the monument. From these moulds, three full series of casts were later produced.

The first set was donated to the Lateran Museum in Rome and remained there until 1953, when it was transferred by Pope Pius XII to the Museum of Roman Civilisation which was founded in 1939. The second set was used as a model for producing a metal version of the Column, created using the galvanoplastic process. This metal reproduction was first displayed in July 1864 in a ground-floor gallery of the Louvre Museum. Subsequently, the

original casts from Rome were divided between the École des Beaux-Arts and the rooms of the Château de Saint-Germain-en-Laye in Paris.

Due to their monumental scale, the galvanoplastic casts were eventually removed from the Louvre's storage spaces and transferred to Saint-Germain, where they reappeared, at least partially, in 1887, displayed in the castle's moat. The first five sections of the spiral relief, assembled in their original sequence, are still visible today in the moat of the Château.

The third series of the plaster casts, derived from the French moulds, was produced for the South Kensington Museum in London (now the Victoria and Albert Museum), where the casts are displayed as two separate cylindrical structures [21].

Although the historical accounts describe the chronology of the casting phases, the available archival sources provide only limited insight into the technical aspects of production, and the specific formulations used for the plaster replicas are not documented. 19th century casting manuals indicate that alabaster gypsum was widely employed for high-quality sculptural and architectural replicas, and the analytical results obtained in this study align well with these historical practices. Considered together, these elements suggest that the original casts were likely produced using mixtures consistent with those commonly adopted at that time.

3.1.4 Room LI: Trajan's Column replicas at the Museum of Roman Civilisation

The Museum of Roman Civilisation (Figure 2), founded in 1939 and housing the first set of casts made between 1861 and 1862, commissioned by Napoleon III, has been closed since 2014, and has remained inaccessible to the public for over ten years. This prolonged closure provided an opportunity to study the casts in a stable, though uncontrolled environment, free from the unpredictable environmental variations caused by visitor flow. It also highlights the importance of continuous environmental monitoring in the absence of visitors, particularly in light of the museum's planned reopening. This gallery houses the complete series of 125 plaster casts of the reliefs, except for four panels, located in another room.

Originally conceived as a permanent display, the gallery was arranged to reproduce the narrative sequence of the relief along four rows, two along the walls and two in the central lines, allowing visitors to follow the unfolding of the campaigns in chronological order. Although currently not accessible to the public, the casts remain in place, mounted on metal structures designed to support them.

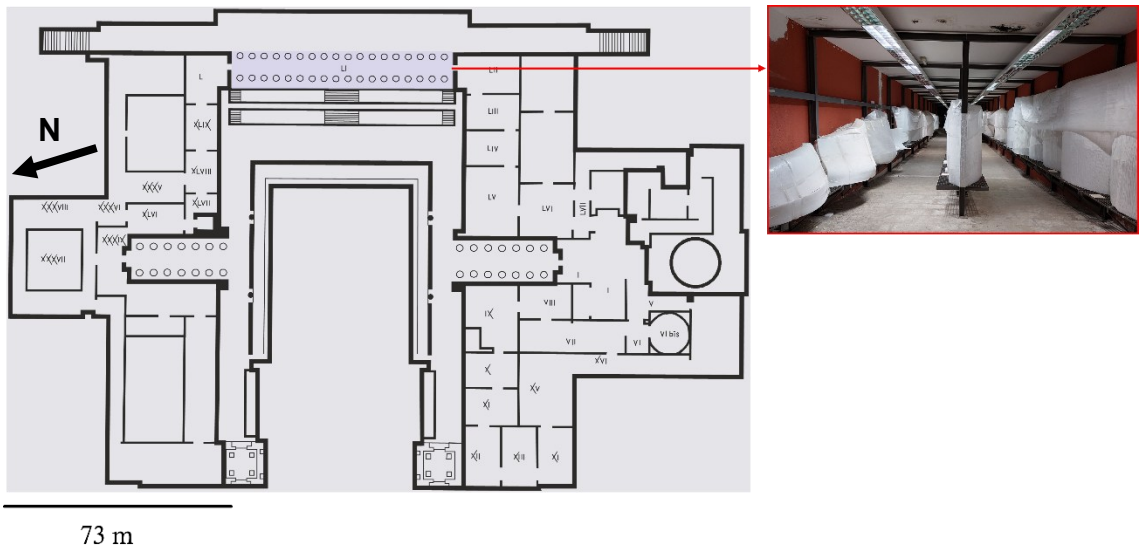

Figure 2. Plan of the Museum of Roman Civilisation showing the location of Room LI, where the plaster replicas of Trajan's Column are preserved (highlighted in purple). The arrow and the letter "N" indicate the north. The image on the right shows an interior view of the gallery, with the casts aligned along both sides of the room. Room LI measures 73.55 m in length, 5.12 m in width, and 3.35 m in height. Scale bar: 73 m.

3.2 Materials

The complete set of plaster replicas reproducing the reliefs of Trajan's Column has been housed in Room LI of the museum since the mid-20th century. The collection comprises 125 panels made primarily of alabaster gypsum, and placed on metallic frames. The casts are arranged in chronological order along the two lateral walls and the central corridor of the gallery. Despite their historical and documentary value, the casts have been exposed for an extended period to uncontrolled environmental conditions, and limited documentation is available regarding past conservation treatments.

In 2012, the museum conducted a large-scale conservation survey to assess the overall condition of the entire collection (*unpublished internal report*). Based on visual inspection and photographic documentation, each cast was assigned to one of four degradation categories, *mediocre*, *discreet*, *poor*, or *bad* depending on the type, extent, and severity of the observed alterations. This classification has served as an essential reference point for subsequent conservation planning and to this study, providing insight into the current conservation state and deterioration rate of the casts by comparison with the 2012 survey. In particular, the comparison revealed a general worsening of their conditions, with more widespread powdering and increased loss of cohesion, leading several replicas to shift to more severe conservation categories and to display more extensive degradation features.

For this study, 35 plaster casts were selected to allow for a representative and comparative analysis. The selection criteria included:

- The inclusion of nearly equal number of casts per class, as defined in the 2012 survey;
- The addition of four unclassified casts exhibiting distinctive or complex patterns of decay;
- The spatial distribution of the casts within Room LI, covering both the lateral walls and central structures;
- The presence of different surface alterations, such as chromatic changes, pulverisation, erosion, and cracking;
- And finally, the museum's internal priorities, favouring casts either planned for imminent restoration or already subjected to recent conservation treatments.

Table 1 presents the plaster replicas under study, grouped according to the conservation categories defined, alongside with the corresponding inventory number.

Table 1. Plaster replicas under study, grouped by conservation condition as defined in the 2012 visual survey. The classification includes four main categories: mediocre, discreet, poor, and bad, alongside a small number of unclassified or recently restored casts.

Plaster replicas under study					
Mediocre	**Discreet**	**Poor**	**Bad**	**Not classified**	**Restored**
MCR_3023	MCR_3024	MCR_3026	MCR_3051	MCR_3028	MCR_3135
MCR_3029	MCR_3025	MCR_3038		MCR_3033	
MCR_3031	MCR_3027	MCR_3039		MCR_3724	
MCR_3042	MCR_3030	MCR_3045			
MCR_3053	MCR_3032	MCR_3050			
MCR_3059	MCR_3034	MCR_3052			
MCR_3064	MCR_3035	MCR_3058			
MCR_3083	MCR_3043	MCR_3072			
MCR_3102	MCR_3097	MCR_3125			
MCR_3105	MCR_3113				
MCR_3110					

The spatial distribution of the selected casts within Room LI is shown in Figure 3. The image illustrates the layout of the gallery and highlights the position of each analysed cast, colour-coded according to the 2012 conservation classification. This visual overview confirms that the selection includes casts from both lateral walls and different sectors of the gallery, ensuring an adequate representation of diverse microenvironmental conditions and exposure contexts.

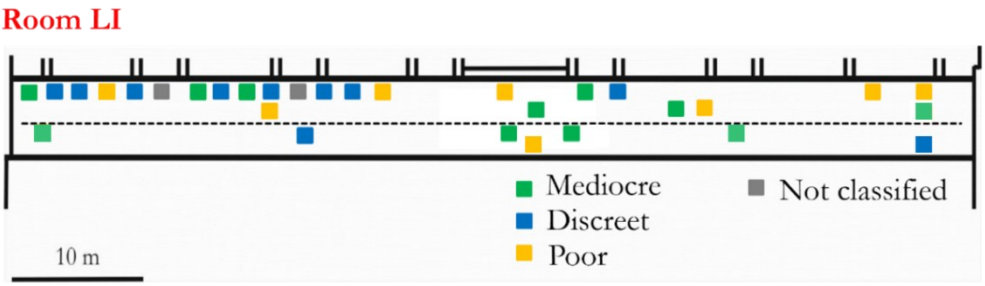

Figure 3. Location of the analysed replicas in Room LI at the Museum of Roman Civilisation. Colours indicate the 2012 conservation class: green = *mediocre*; blue = *discreet*; yellow = *poor*; grey = *not classified*. The *bad* category is not represented here, as the only cast classified as *bad* (MCR_3051) is located in another room. Scale bar = 10 m.

As shown in Figure 3, 31 of the selected casts are located within Room LI, while four additional casts (MCR_ 3045, MCR_3051, MCR_3135, and MCR_3724) are positioned in other rooms of the museum. These replicas were included upon the museum's request: MCR_3045, MCR_3051, MCR_3724 are scheduled for imminent restoration, whereas MCR_3135 was chosen as an example of a cast that has already undergone conservation treatment (Figure 4).

Figure 4. Plaster cast MCR_3135, recently restored and without evident alterations at the time of the survey.

To support material characterisation, two micro-samples (1-2 cm in size), referred to as sample A and sample B (Figure 5), were collected from the back side of the cast MCR_3045, selected as a representative case due to the presence of multiple degradation patterns. The samples were extracted from an area with missing fragments, thus avoiding any further

damage. Sample A was taken from the inner bulk, while sample B was collected from the surface layer. Both samples were analysed to investigate the material composition and assess the stratigraphic differences between the bulk and the surface of the cast.

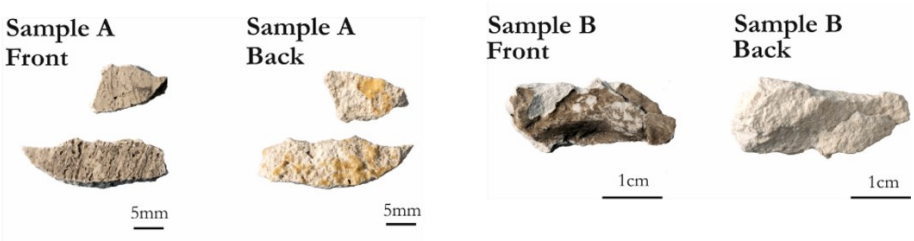

Figure 5. Front and back view of the micro-samples collected from plaster cast MCR_3045. Sample A was taken from the inner bulk, while sample B corresponds to the surface layer. The image was previously published in *Bubola et al., 2024* [1].

Among the casts investigated, MCR_3052 was selected as a representative case study for an in-depth presentation of the degradation phenomena observed during the on-site survey. This cast was previously classified in the *poor* conservation category, and it exemplifies a wide range of decay forms, such as fractures, erosion, and pulverisation, which were also observed, to varying degrees, in several other casts. The results presented here should therefore be considered as illustrative of broader trends affecting the entire set of replicas conserved in Room LI.

3.3 Methods

3.3.1 Microclimatic monitoring

The present microclimatic investigation aimed to compare the current environmental conditions of Room LI at the Museum of Roman Civilisation with those recorded during a previous conservation assessment conducted in 2012 by the Museum. This comparison provides insight into the evolution of the indoor climate and its potential impact on the preservation state of the plaster casts.

Microclimate environmental data were collected using an OM-EL-USB-2-LCD datalogger (OMEGA®), initially placed at the centre of the gallery. The first monitoring phase, conducted from 23 November 2022 to 14 May 2024, involved a single sensor recording temperature and relative humidity every 30 minutes. At that stage, only one datalogger was available for installation, and although this configuration did not capture the full spatial variability of the environment, it provided a preliminary overview of the room's microclimatic behaviour and seasonal trends, forming the basis for planning a more extensive monitoring campaign.

To complement and guide the second phase of the monitoring campaign, infrared thermography was employed to analyse the thermal behaviour of the architectural envelope surrounding the gallery. The aim was to identify critical areas where environmental sensors could be strategically placed. A single thermographic campaign was conducted approximately one month before installing the additional dataloggers. This survey provided an overview of thermal anomalies and moisture-prone areas, which guided the positioning of the additional dataloggers. Infrared analyses were carried out inside Room LI, with particular attention to the upper sections of the two vertical walls and the ceiling. Thermal distribution and anomalies were assessed using a FLIR infrared camera, with thermal images processed via FLIR ResearchIR 4 Max + HSDR® software. The thermograms were saved as false-colour images using the GF White Hot palette, within a thermal range of 25-33 °C, and enhanced through the Digital Detail Enhancement (DDE) algorithm to highlight fine temperature gradients.

A second monitoring campaign started on 14 May 2024 and continued until 28 May 2025, involving a network of 8 dataloggers distributed at different points within Room LI to obtain a more detailed overview of the environmental conditions in different areas of the gallery.

To monitor critical environmental changes more effectively, the sensors were configured with an active alarm system based on predefined thresholds. Alarm triggers were set at 50 °C for the maximum temperature and -1 °C for the minimum. For relative humidity, threshold values were defined at 80 % RH (maximum) and 19.5 % RH (minimum), allowing for the detection of significant fluctuations.

According to European guidelines UNI EN 15757 (2010), the environmental monitoring programme in an indoor environment must be conducted over a period of at least one year in order to identify seasonal variations in temperature and relative humidity and to evaluate the impact of short-term fluctuations on the indoor environment [22].

3.3.2 In situ survey

High-resolution visible photographs were taken using a Canon EOS 2000D digital camera under controlled lighting conditions provided by 230 V, 750 W halogen lamps. The white balance was set directly on-site using the camera settings to ensure accurate colour rendering.

Colourimetric analysis was performed on the plaster replicas to detect and quantify potential chromatic alterations. Measurements were acquired using a Konica Minolta CM-

700d spectrophotometer, operating in the CIELab colour space. This system defines colour using three coordinates: lightness (L^*: from 0 = black to +100 = white), red-green (a^*), and yellow-blue (b^*) [23]. Measurements were conducted under standard CIE D65 illumination (simulating daylight at 6504 K), using SCI/SCE acquisition modes in the 400-700 nm wavelength range.

Active infrared thermography was employed to investigate both surface and subsurface characteristics of the plaster casts and to assess their thermal behaviour. The technique involved irradiating the surface with halogen lamps (via a heating plate) for 20 minutes, followed by the acquisition of infrared images using a FLIR camera placed at a distance of 1 m. Thermographic images were recorded in time-lapse mode every 30 seconds (41 frames in total). Thermal diffusion patterns were analysed using FLIR ResearchIR 4 Max + HSDR® software. Images were saved in false colour (GF White Hot palette), within a thermal range of 11-35 °C, and enhanced using the Digital Detail Enhancement (DDE) algorithm to improve contrast and highlight thermal gradients.

3.3.3 Microchemical and mineralogical characterisation

X-ray powder diffraction (XRPD) analysis was performed to identify the mineralogical composition of the samples. Data were collected with a PANalytical X'Pert PRO diffractometer, operating in Bragg-Brentano reflection geometry with CoKα radiation (40 kV, 40 mA) and an X'Celerator detector. Phase identification was carried out using X'Pert HighScore Plus® software and the PDF-2 database.

μ-Raman spectroscopy was applied to investigate both the bulk composition and surface features of the samples, including targeted analysis of specific inclusions. Measurements were performed using a Thermo Scientific DXR Raman Microscope with a 532 nm laser source, a 50x long-working distance objective, ~2.5 cm^{-1} spectral resolution, and ~1 μm pinhole, operating at 3 mW. Each spectrum was recorded 30 times with a 1 s exposure. Data were collected in the 100-3500 cm^{-1} range and processed using Thermo Scientific OMNIC Spectra software.

Attenuated Total Reflectance-Fourier Transform Infrared (ATR-FTIR) was employed to identify both inorganic and organic compounds. Spectra were acquired using a Bruker ALPHA II FTIR spectrometer equipped with a synthetic diamond ATR crystal. Each sample and background were scanned 48 times with a resolution of 4 cm^{-1} in the 4000-400 cm^{-1} range. Spectra were processed using OMNIC Spectra Software (v9) and further analysed with OriginPRO 2018b. A Nicolet iS20 FT-IR spectrometer coupled with a Nicolet iN5

microscope, equipped with a cooled MCT/A detector and a germanium μATR crystal was also used to confirm and identify the organic matter possibly present. Spectra were collected in the 4000-650 cm^{-1} range, with a resolution of 4 cm^{-1} and 32 background scans.

Morphological and microchemical characterisation was conducted using a Tescan Solaris Field Emission Scanning Electron Microscopy (FESEM). Mineralogical phases were analysed via EDS with an Oxford Instruments Ultim Max 65 Silicon Drift Detector, operating at 15 kV, 3 nA, and a 5 mm working distance. High-resolution BSE images were acquired at 5 kV and 300 pA, with a working distance of 4 mm, to enhance image clarity.

Thermogravimetric Analysis - Differential Scanning Calorimetry (TGA-DSC) was performed to investigate the thermal behaviour and compositional characteristics of the samples. A Netzsch 409/C system was used, with a heating rate of 10 °C/min from 25 °C to 1000 °C. Analyses were conducted under a mixed flow of air and nitrogen (40 mL/min), with alumina as the calibration standard.

Hyperspectral imaging (HIS) was conducted on the bulk and surface areas of samples A and B from MCR_3045, using two acquisition modules covering the Visible-Near Infrared (VNIR 400-1000 nm), and the Short-Wave Infrared (SWIR, 1000-2500 nm) spectral ranges using two different setups:

- Nano-Hyperspec (VNIR, 400-1000 nm): 270 spectral bands, 640 spatial pixels, spatial resolution ~0.15 mm.
- Micro-Hyperspec (SWIR, 900-2500 nm): 166 spectral bands, 384 spatial pixels, spatial resolution ~0.35 mm.

The objective was to investigate the spectral variability, map potential material differences, and identify specific hydrated phases or surface treatments. Data processing was carried out using the Principal Component Analysis (PCA) and Spectral Angle Mapping (SAM), implemented in the ENVI® software environment, to generate distribution maps of the detected materials across the samples. For each acquisition, regions of interest (ROIs) were selected to extract representative spectra. These spectra were used to generate distribution maps, allowing for visual correlation between spectral classes and macroscopic features on the sample surface.

3.3 Results

3.3.1 Microclimatic monitoring

3.3.1.1 First phase: November 2022-May 2024

The first phase of the microclimatic monitoring was conducted in Room LI of the museum between 23 November 2022 and 14 May 2024, using a single datalogger positioned at the centre of the gallery. The device recorded temperature and relative humidity, calculating the relative dew point at regular intervals.

Temperature values followed a seasonal pattern, with lower values during the winter months and a gradual increase towards the summer. The lowest temperature (8.0 °C) was recorded on 10 February 2023, while the highest (34.0 °C) occurred in July of the same year. The overall average value calculated over the entire period was approximately 18.8 °C (Figure 6A).

Relative humidity exhibited wide and persistent fluctuations, frequently exceeding the 80 % upper threshold defined during sensor configuration. Peaks above this value were particularly frequent in the colder season. The recorded RH ranged from a minimum of 34.5 % to a maximum of 86 %, with an average value of 64.7 % (Figure 6B).

The dew point followed the temperature trend, with values ranging from -3.0 °C in February 2023, to 25.2 °C in August 2023 (Figure 6 C).

These values are summarised in Table 2, which reported the minimum, maximum and average parameters recorded during this first monitoring phase.

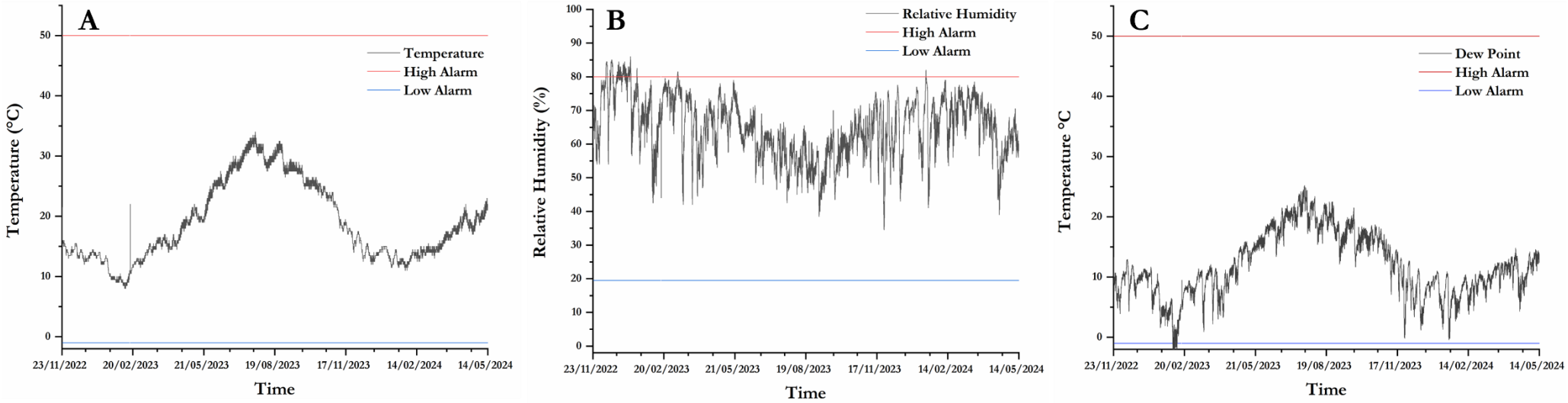

Figure 6. Trends of microclimatic parameters recorded in Room LI from November 23rd, 2022, to May 14th, 2024: (A) temperature (°C), (B) relative humidity (%), and (C) dew point (°C). High and low alarm thresholds are shown in red and blue, respectively. Data were acquired using a single datalogger positioned at the centre of the gallery.

Table 2. Summary of microclimatic parameters recorded in Room LI during the first phase of the campaign (November 2022-May 2024), including minimum, maximum and average values, with corresponding time periods.

Parameter	Minimum	Maximum	Average
Temperature (°C)	8.0 (Feb 2023)	34.0 (Jul 2023)	18.8
Relative humidity (%)	34.5 (Nov 2023)	86.0 (Jan 2023)	64.7
Dew point (°C)	-3.0 (Feb 2023)	25.2 (Jul 2023)	-

3.2.1.2 Thermal survey and identification of critical areas

In parallel with the ongoing microclimatic monitoring, a thermographic survey was conducted inside Room LI, to identify zones affected by thermal anomalies and residual moisture.

The gallery was subdivided into two sectors: Sector A on the eastern side and Sector B on the western side. Six critical areas were identified (Figure 7) based on visible moisture stains, evidence of water infiltration, and surface temperature differentials (Figure 8A-D). These include ceiling sections showing traces of previous infiltration, as well as upper wall portions affected by moisture accumulation. The observations were used to define the most appropriate positions for the additional dataloggers installed during the second phase of the monitoring campaign.

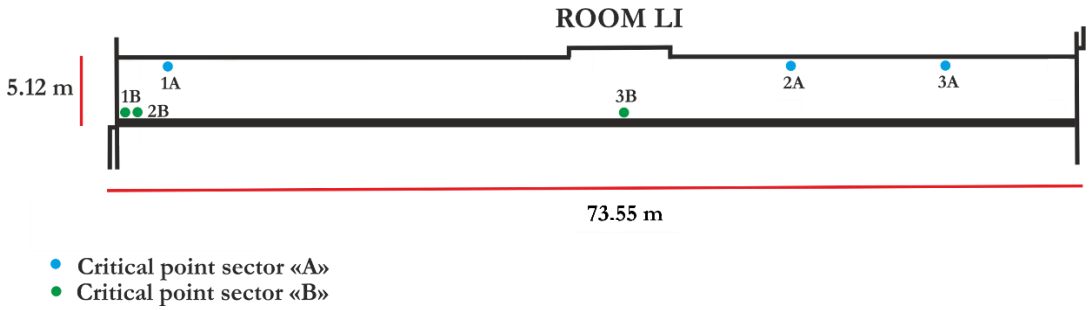

Figure 7. Schematic plan of Room LI showing the position of the six critical points identified through infrared thermographic survey. Points in blue refer to critical zones in Sector A (eastern side of the gallery), while points in green correspond to Sector B (western side of the gallery).

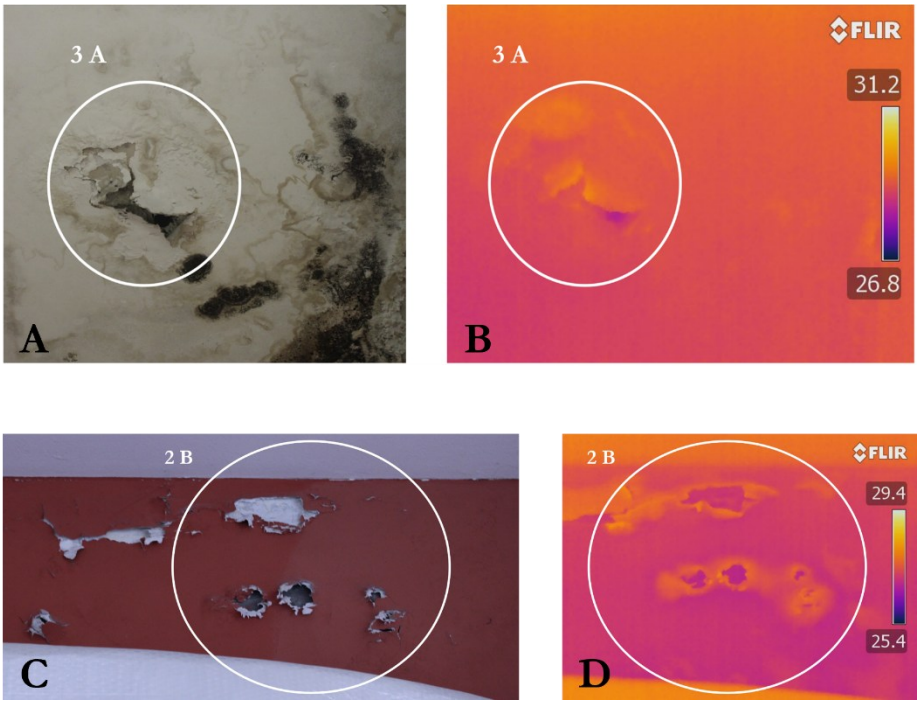

Figure 8. Visible and infrared thermographic documentation of two critical points identified in Room LI. A-B: detail of critical point 3A (sector A) on the ceiling, showing material degradation and bio-colonisation (A) and corresponding thermal image (B). C-D: critical point 2B (sector B) on the upper wall, showing surface detachment (A), with thermal evidence of moisture retention.

3.3.1.3 Second phase: May 2024-May 2025

During the second phase of microclimatic monitoring, conducted between 14 May 2024, and 28 May 2025, eight dataloggers were installed at selected locations corresponding to some of the critical points previously identified. This configuration was designed to provide a more comprehensive understanding of the microclimatic variations within Room LI. The positions of the eight dataloggers (labelled A-H) are shown in Figure 9.

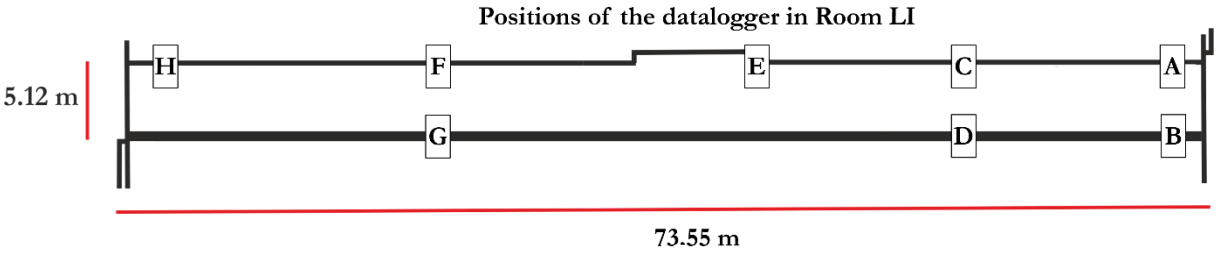

Figure 9. Plan view of Room LI showing the positions of the eight dataloggers (A-H) installed for the second phase of the microclimatic monitoring campaign (May 2024-May 2025).

The temperature curves recorded by the eight sensors show a clear seasonal pattern, with the lowest values observed during winter months and the highest during the summer (Figure 10). Daily fluctuations were evident throughout the monitoring period, with more pronounced variations occurring between late spring and early autumn. Across all devices, temperature values range approximately between 8.5 °C and 34.5 °C.

Relative humidity also showed seasonal trends, with higher values recorded during colder months and lower values during the warmer season. Measured RH values ranged from approximately 34.0 % to 86.0 %, with short-term variations and daily oscillations observed in all locations.

The dew point followed the general trend of temperature, but remained consistently about 7-8 °C lower, both in terms of minimum and maximum values. In some periods, particularly during the winter, the dew point approached the air temperature curve across all logger positions.

This distributed dataset provided a more detailed representation of the environmental conditions inside Room LI over the one-year monitoring period.

A summary of the minimum, maximum, and average values recorded by each datalogger is presented in Table 3.

Table 3. Minimum, maximum and average values of temperature (°C), relative humidity (%), and dew point (°C) recorded by each datalogger during the second monitoring phase (May, 2024-May, 2025).

Datalogger	Parameter	Minimum	Maximum	Average
A	Temperature (°C)	10.0 (Jan 2025)	34.0 (Jul 2024)	20.6
	Relative humidity (%)	35.0 (Sep 2024)	82.5 (Jan 2025	61.4
	Dew point (°C)	-2.1 (Dec 2024)	23.1 (Mar 2025)	-
B	Temperature (°C)	10.0 (Jan 2025)	34.5 (Jul 2024)	20.9
	Relative humidity (%)	34.0 (Sep 2024)	82.0 (Jan 2025	59.0
	Dew point (°C)	-2.1 (Dec 2024)	23.4 (Mar 2025)	-
C	Temperature (°C)	9.5 (Jan 2025)	34.5 (Jul 2024)	20.6
	Relative humidity (%)	38.0 (Sep 2024)	83.5 (Jan 2025	61.2
	Dew point (°C)	-1.7 (Dec 2024)	23.7 (Mar 2025)	-
D	Temperature (°C)	9.5 (Jan 2025)	34.0 (Jul 2024)	20.5
	Relative humidity (%)	36.0 (Sep 2024)	83.5 (Jan 2025	61.1
	Dew point (°C)	-1.9 (Dec 2024)	23.7 (Mar 2025)	-
E	Temperature (°C)	9.0 (Jan 2025)	34.0 (Jul 2024)	20.4
	Relative humidity (%)	37.0 (Sep 2024)	83.0 (Jan 2025	61.0
	Dew point (°C)	-1.8 (Dec 2024)	23.6 (Mar 2025)	-
F	Temperature (°C)	9.0 (Jan 2025)	33.5 (Jul 2024)	20.2
	Relative humidity (%)	36.5 (Sep 2024)	85.0 (Jan 2025	61.5
	Dew point (°C)	-2.3 (Dec 2024)	23.7 (Mar 2025)	-
G	Temperature (°C)	9.0 (Jan 2025)	33.0 (Jul 2024)	20.2
	Relative humidity (%)	36.5 (Sep 2024)	85.5 (Jan 2025	62.8
	Dew point (°C)	-1.9 (Dec 2024)	23.9 (Mar 2025)	-
H	Temperature (°C)	8.5 (Jan 2025)	33.0 (Jul 2024)	20.0
	Relative humidity (%)	35.5 (Sep 2024)	86.0 (Jan 2025)	62.8
	Dew point (°C)	-2.3 (Dec 2024)	25.3 (Mar 2025)	-

Temperature values across the eight monitoring points ranged from 8.5 °C (H, January 2025) to 34.5 °C (B and C, July 2024), with average values between 20.0 and 20.9 °C. Relative humidity showed greater variability, ranging from 34.0 % (B, September 2024) to 86.0 % (H, January 2025), with average RH values between 59.0 % (B) and 62.8 % (G and H). Dew point values followed a similar seasonal trend, ranging from -2.3 °C (F and H, December 2024), to 25.3 °C (H, March 2025).

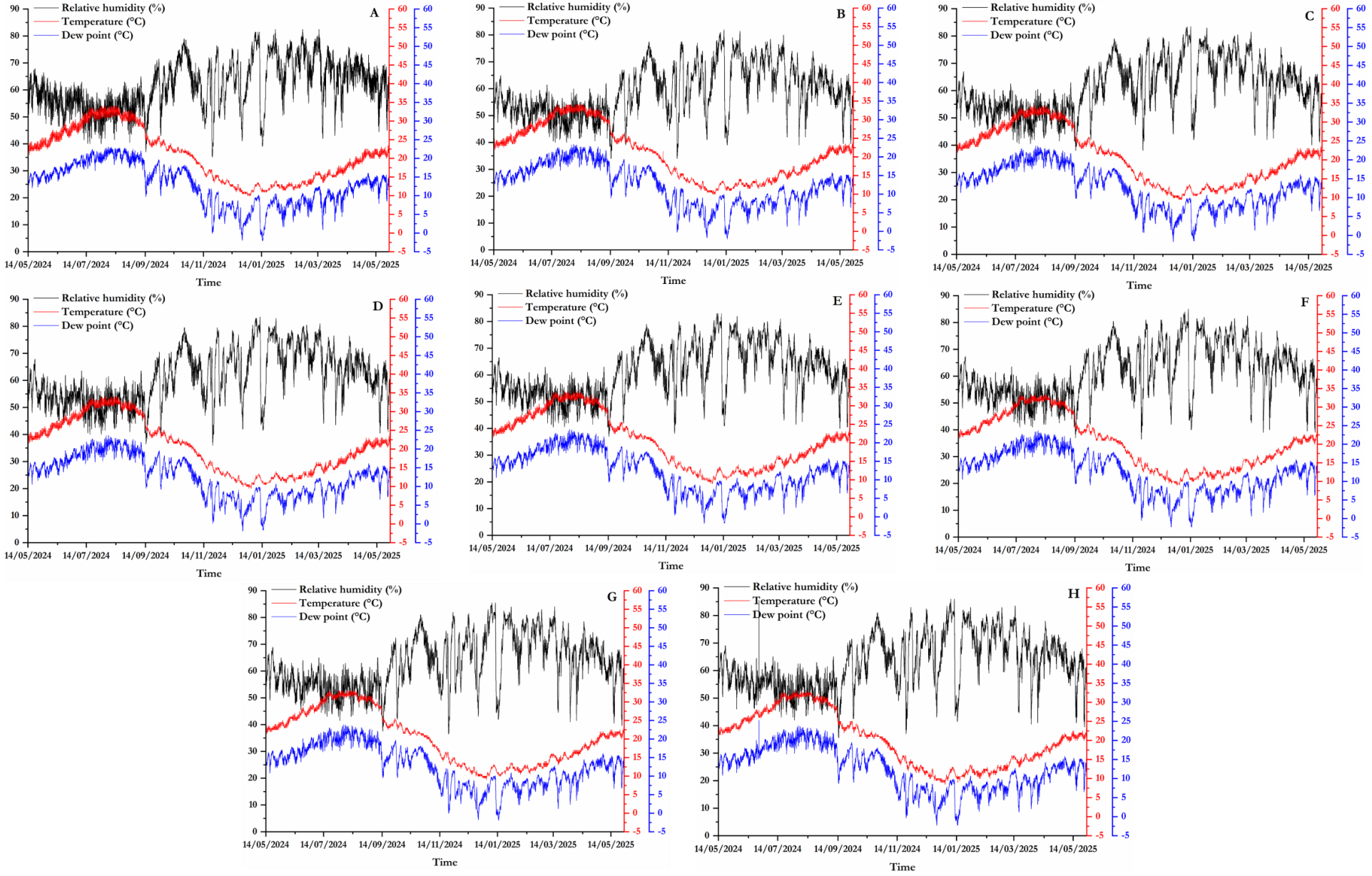

Figure 10. Temperature (°C, red curves), relative humidity (%, black curves), and dew point (°C, blue curves) trends recorded by the eight data loggers (A-H) placed in Room LI during the second phase of the microclimatic monitoring campaign (May 14th, 2024-May 28th, 2025).

3.3.1.4 Monthly mean indoor temperature

Table 4 shows the monthly means indoor temperature (°C) from Room LI from November 2022 to May 2025. During the second monitoring phase (May 2024-May 2025), monthly mean indoor temperatures were obtained by first computing, for each datalogger (A-H), the monthly mean and then using the arithmetic mean across the eight loggers for each month. The table is organised by month and year; blank cells indicate months not covered by the monitoring.

Over the reported period, monthly means range between 11.19 °C (February 2023) and 31.93 °C (August 2024). Within the first phase (November 2022-May 2024), values range from 11.19 °C (February 2023) to 30.66 °C (July 2023); within the second phase, from 11.54 °C (January 2025) to 31.93 °C (August 2024).

Table 4. Monthly mean indoor temperature (°C) for Room LI (November 2022-May 2025).

Month	Mean T indoor 2022	Mean T indoor 2023	Mean T indoor 2024	Mean T indoor 2025
January		11.91	13.20	11.54
February		11.19	13.49	12.16
March		14.40	15.42	14.61
April		16.43	18.58	17.75
May		20.55	22.90	21.44
June		25.88	24.15	
July		30.66	30.82	
August		29.90	31.93	
September		27.20	26.49	
October		24.40	21.87	
November	14.97	18.53	16.38	
December	13.73	14.25	11.58	

3.3.2 Case study: plaster replica MCR_3052

3.3.2.1 On-site survey and degradation mapping

The plaster cast MCR_3052 (Figure 11), part of the complete series reproducing the reliefs of Trajan's Column, was selected for a detailed description and subjected to a comprehensive visual and instrumental diagnostic survey. Additional casts representing each conservation class were included in the annex, with three examples per category. The cast, measuring approximately 1.15 m in height and 1.50 m in length, reproduces Scene 37, portraying Trajan receiving a group of Dacian prisoners and, on the right, a Roman military hospital [24]. Although access to the back of the cast was limited due to its position near the wall, the visible portion of the rear structure was consistent and did not show significant irregularities.

Figure 11. Plaster replica MCR_3052, reproducing scene 37 of Trajan's Column, conserved in Room LI of the Museum of Roman Civilisation (Rome). The relief shows Emperor Trajan receiving a group of Dacian prisoners, with a Roman military hospital depicted on the right. This cast was selected as a representative case study for on-site diagnostic investigations due to its complex degradation condition and classification in the *poor* conservation category.

The artefact is composed of two sections, supported by a wooden and metal structure on the back, which was partially visible during the survey. Rust stains were detected in the lower-left area of the rear side (Figure 12A). The wooden structure, consisting of two curved, horizontal ribs, is covered with an irregular layer of gypsum. On the front of the cast, a small metal plate located in the bottom right-hand corner, bears the museum's inventory number: MCR_3052 (Figure 12B).

A

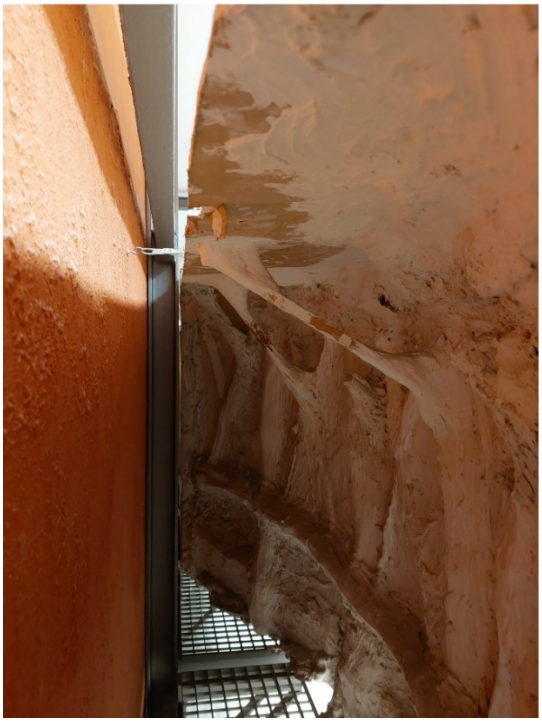

B

Figure 12. Photographic documentation of plaster cast MCR_3052. A: partial view of the reverse side of the cast, showing the supporting structure and traces of gypsum application; access to the back was limited due to the cast's position near the wall. B: detail of the lower right edge of the cast, displaying the identification label "MCR 3052" embedded in the surface.

A detailed degradation map was produced (Figure 13) based on visual inspection, photographic documentation, and contact microscopy. Several forms of deterioration were identified and are listed below, with corresponding photographic evidence in Figure 14:

- A major vertical fracture extends nearly the full height of the cast on the left side. A restoration mortar fill is clearly visible within the fracture (Figure 14D-E);
- Several micro-cracks are visible, especially near the bottom and lateral margins, associated with surface fillings of variable thickness (Figure 14D-E);
- Coherent surface deposits are present, particularly in the more exposed areas (Figure 14B);
- Tonal alterations in yellow and pink hues are visible across the surface (Figure 14F);
- Pencil marks and engraved lines can be observed in multiple areas (Figure 14F);
- Surface scratches are widespread (Figure 14F);
- The left side of the cast shows areas of erosion and pulverisation (Figure 14B-C);
- Possible biological colonisation is present at the lower edge, where greenish surface patterns were observed;

· Multiple dark and reddish stains are visible on the right side, along with visible residues of *maltina* (plaster mixture) (Figure 14F).

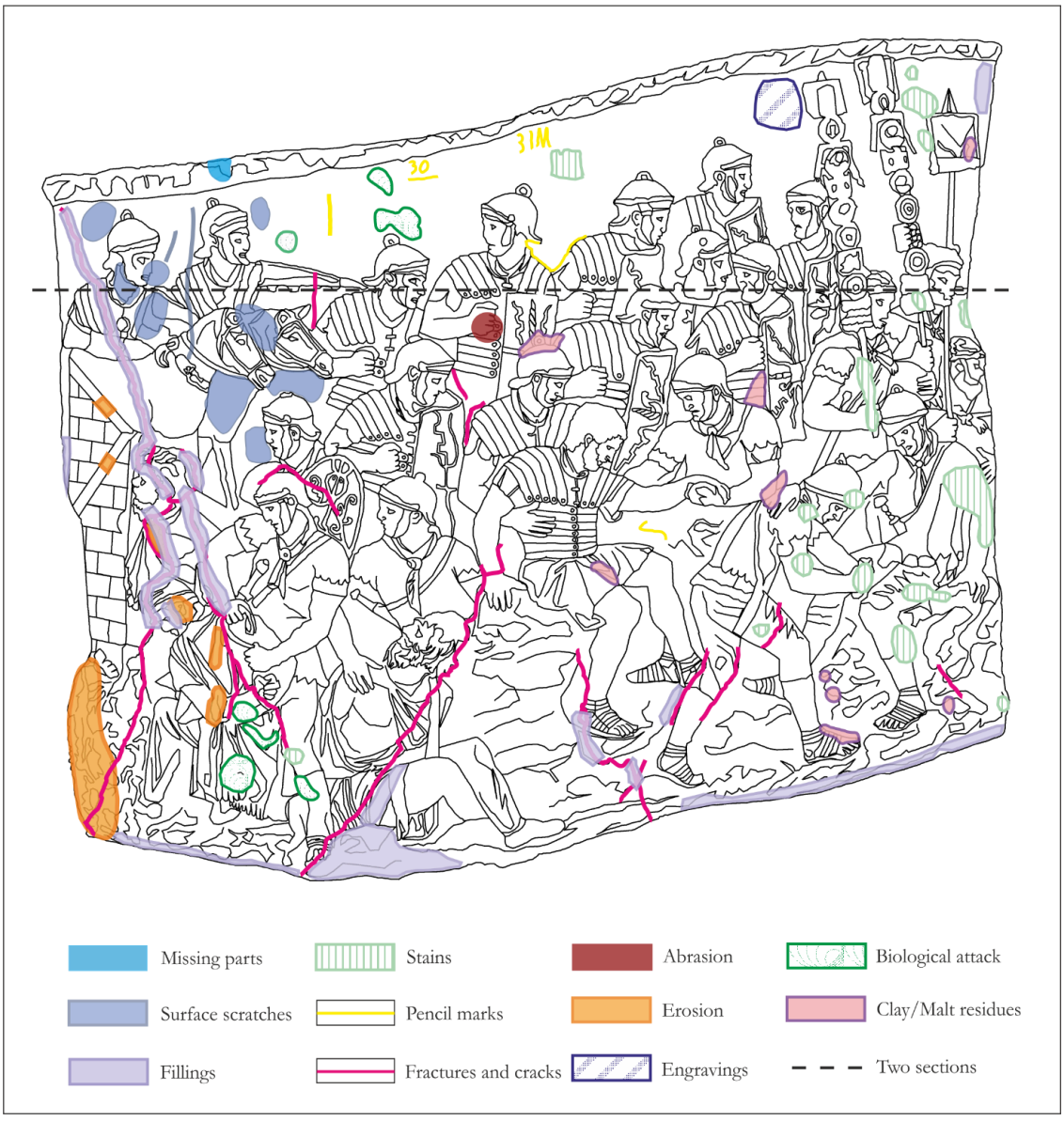

Figure 13. Outline of the MCR_3052 plaster cast drawn in CorelDRAW with: missing parts (light blue), surface scratches (blue), fillings (light purple), stains (light green stripes), pencil marks (yellow), fractures and cracks (fuchsia), abrasion (red), erosion (orange), engravings (blue stripes), biological attack (green dots), clay/malt residues (pink). The cast is divided into two sections (dashed black line).

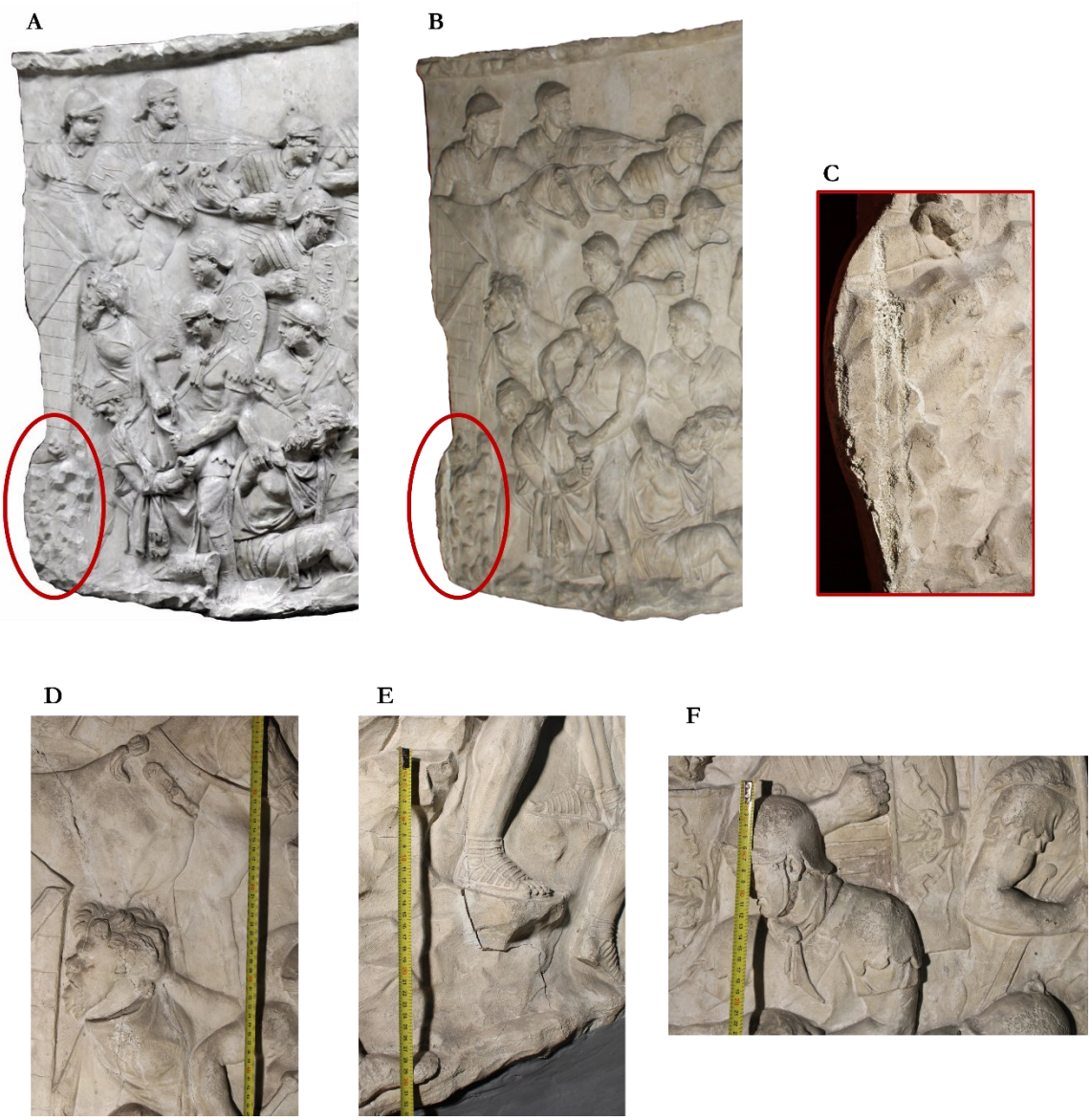

Figure 14. Comparative documentation of the plaster replica MCR_3052, reproducing Scene 37 of Trajan's column. A: archival photograph from the 2012 survey, showing the left portion of the cast in a relatively preserved condition; B: current photograph taken during the 2023 on-site diagnostic campaign, where visible surface erosion is now evident in the same area (circled in red); C: detail of the eroded edge, showing granular loss and deterioration of the surface profile (also published in *Bubola et al., 2024*); D-E: details of structural fractures and areas filled during previous restorations, measuring tape included for scale; F: area displaying surface alterations, including tonal variations, dark stains, and pencil marks.

3.3.2.2 Spectrophotometric analysis

Colourimetric measurements were carried out using a portable spectrophotometer operating in the CIELab* colour space. A total of 20 points was acquired on representative areas of the surface to evaluate chromatic alterations (Figure 15). The a* and b* values, describing the red-green and yellow-blue chromatic components, ranged from 0.489 to 1.999, and from 8.526 to 14.612, respectively. Chroma (C*) values ranged from 8.540 (T_041)

to 14.71 (T_051). The highest chroma values were recorded at points T_051 (14.710), T_050 (14.310), and T_044 (13.950), and the lowest at T_041 (8.540), T_060 (9.489), and T053 (10.680). These results are consistent with the variations in L*, indicating differences in surface reflectance and chromatic saturation.

Figure 15. Colourimetric measurement points (T_041 to T_060) on the surface of plaster replica MCR_3052, acquired in the CIELab* colour space. The distribution of points was designed to sample areas with varying surface conditions to assess chromatic alterations.

Table 5. Colourimetric measurements acquired on plaster replicas MCR_3052 in the CIELab* colour space. The table reports values of lightness (L*), red-green (a*) and yellow-blue (b*) components, chroma (C*), and hue angle (h°) for each of the 20 analysis points (T_041 to T_060). Values in bold correspond to the darkest areas of the surface (lower L*), which were visually associated with greater accumulation of surface deposits.

Colourimetric measurements MCR_3052					
Analysis point	**L***	**a***	**b***	**C***	**h°**
T_041	84.592	0.489	8.526	8.540	86.715
T_042	78.176	1.376	11.498	11.580	83.177
T_043	81.513	1.245	13.342	13.400	84.667
T_044	82.592	0.846	13.924	13.950	86.521
T_045	78.676	0.836	11.076	11.108	85.684
T_046	**69.218**	1.209	10.078	10.151	83.157
T_047	83.142	0.743	12.182	12.204	86.511
T_048	75.608	0.756	11.767	11.791	86.325
T_049	79.394	1.229	12.459	12.519	84.368
T_050	73.922	1.616	14.221	14.312	83.516
T_051	76.707	1.691	14.612	14.710	83.400
T_052	77.441	1.212	13.505	13.559	84.871
T_053	**60.918**	1.730	10.538	10.679	80.679
T_054	**63.448**	1.999	10.669	10.854	79.387
T_055	**68.579**	1.483	10.512	10.616	81.969
T_056	84.702	0.707	10.413	10.437	86.116
T_057	76.394	1.147	11.817	11.873	84.455
T_058	81.996	0.759	12.281	12.305	86.464
T_059	82.238	0.908	10.381	10.421	84.999
T_060	**65.921**	1.424	9.382	9.489	81.370

3.3.2.3 Active infrared thermography

Active infrared thermography was performed to assess the presence of subsurface features, including fractures, detachments, and areas with varying thermal responses. The surface of the cast was uniformly irradiated using halogen lamps as a controlled heat source. Thermograms were acquired in time-laps mode, recording the cast's cooling behaviour. One significant result is shown in Figure 16, where a vertical fracture on the left side is clearly visible as a yellow band with higher thermal response. Other areas exhibited delayed cooling or greater thermal retention, associated with past restoration interventions.

Figure 16. Overlay of the plaster replica MCR_3052 with the active infrared thermographic acquisition. The thermogram, obtained during a time-lapse cooling phase, reveals thermal patterns in the central area of the cast. The vertical zone with higher thermal response (yellow-orange tones) corresponds to a known fracture, as indicated by the white arrow, while other variations in thermal behaviour may indicate material inconsistencies or prior restorations not visible in standard imagery.

3.3.3 Microchemical and mineralogical characterisation

3.3.3.1 XRPD

XRPD analyses were carried out on sample A (bulk) and sample B (surface) to investigate the mineralogical composition of the replica MCR_3045. As shown in Figure 17, both diffractograms are dominated by intense gypsum (*Gp*, $CaSO_4 \cdot 2H_2O$) peaks, consistent with its characteristic diffraction pattern, marked by the most intense peak at 2θ = 13.50 ° [25,26].

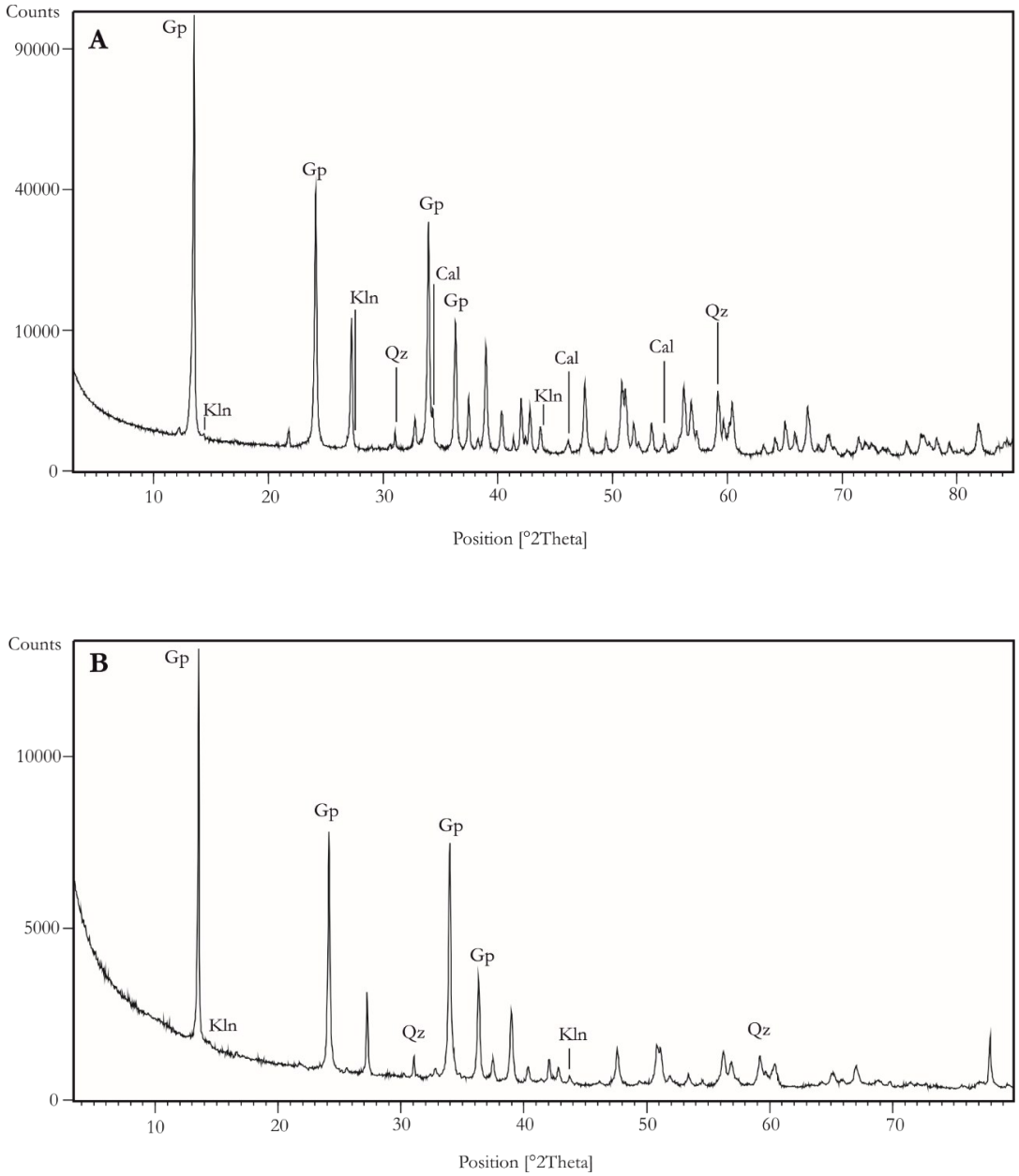

Figure 17. XRPD patterns of sample A (bulk) and sample B (surface) collected from plaster replica MCR_3045. Gypsum (*Gp*) is the main mineral phase in both samples. Additional reflections of calcite (*Cal*), quartz (*Qz*), and kaolinite (*Kln*) are visible in the bulk (sample A), while the surface (sample B) shows mainly gypsum, and quartz with traces of kaolinite. Patterns correspond to improved data representations of those previously published in *Bubola et al., 2024* [1]. Mineral abbreviation from Warr (2021) [26].

In sample A, taken from the inner portion of the cast, additional reflections of calcite (*Cal*) [27], quartz (*Qz*) and kaolinite (*Kln*) were detected alongside gypsum. In contrast, the diffractogram of sample B, corresponding to the surface layer, exhibited only gypsum and quartz peaks, with calcite and kaolinite barely detectable.

3.3.3.2 FESEM-EDS

High-resolution FESEM analysis was used to investigate the texture and microstructure of both the bulk and surface layers, as well as their chemical composition. The matrix of sample A, taken from the inner portion of the cast, was characterised by high porosity, with large tubular and needle-like gypsum crystals.

In contrast, the surface of sample B exhibited a different texture, composed of smaller mineral grains and a denser, more compact arrangement, forming a continuous outer layer with an estimated thickness of approximately 150-200 μm. Point EDS analysis performed in this outer (Figure 18) revealed a composition dominated by *Ca*, *S*, *O* and *Si*, consistent with a gypsum-based matrix. Minor peaks of *Al*, *K*, *Mg* and *Fe* were also detected, along with distinct *Ti* signals, which are absent in the bulk.

Elemental distribution maps further confirm this elemental composition. The EDS maps (Figure 19) show a *Ca*- and *S*-rich matrix, while the outer layer is enriched in *Al*, *Si*, and *K*, in agreement with the presence of a kaolinite-based coating. Oxygen is homogeneously distributed across the section, and *Fe* occurs only in trace amounts.

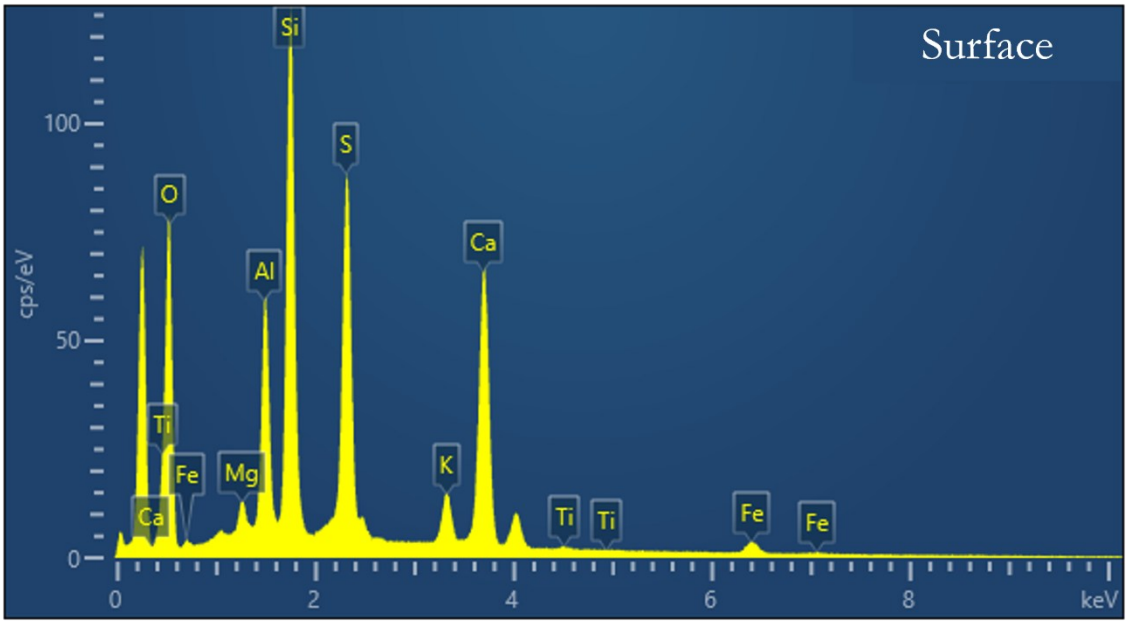

Figure 18. EDS spectrum acquired on sample B (surface) from plaster cast MCR_3045. The main elements detected are *Ca*, *S*, *O*, and *Si*, consistent with a gypsum-based matrix. Minor peaks of *Al*, *K*, *Mg* and *Fe* are present, along with detectable *Ti* signals.

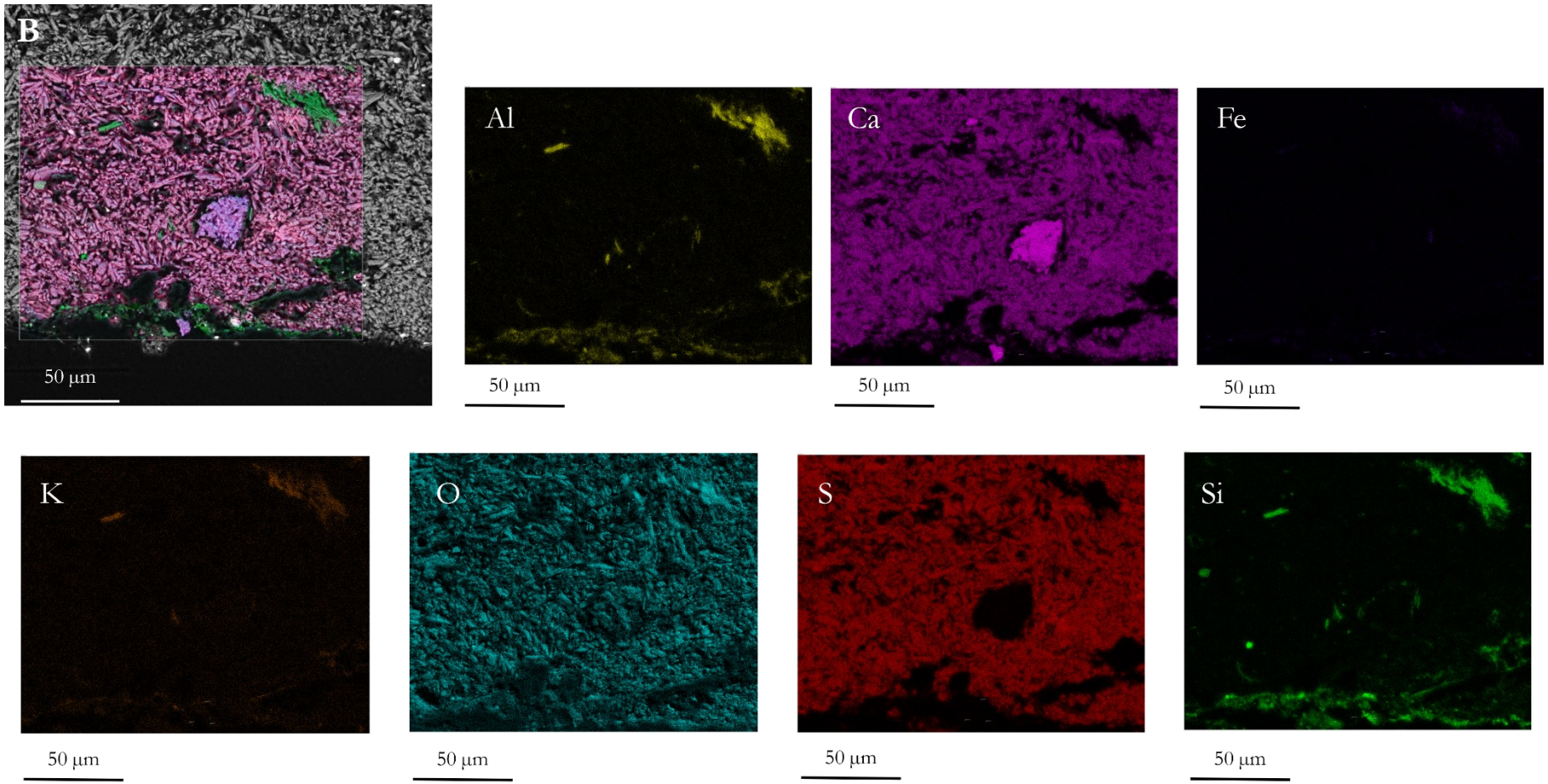

Figure 19. FESEM-BSE image (top left) and EDS elemental maps of sample B (surface layer from plaster cast MCR_3045). *Al*: aluminium; *Ca*: calcium; *Fe*: iron; *K*: potassium; *O*: oxygen; *S*: sulphur; *Si*: silicon. Scale bar: 50 µm.

3.3.3.3 μ-Raman spectroscopy

The μ-Raman spectra were acquired from different areas of the samples: the bulk, the surface, and a black inclusion visible on sample A (Figure 20C). All spectra displayed the characteristic bands of gypsum ($CaSO_4 \cdot 2H_2O$) at approximately 1140, 1008, 673, 492, and 414 cm^{-1}, corresponding to the vibrational modes of the sulphate group (SO_4^{2-}) [28-35]. In addition, O-H stretching bands of water molecules were observed around 3490 and 3450 cm^{-1} in all three spectra [31,33]. The spectrum acquired on the black inclusion presented additional features:

- Peaks at 1170, 1026, 675, 630 and 606 cm^{-1}, attributed to anhydrite ($CaSO_4$) [31,33,35];
- Broad bands between 1600-1300 cm^{-1}, associated to amorphous carbon [32,36];
- CH stretching vibrations at 3054, 2897, and 2734 cm^{-1}, indicative of the presence of organic compounds.

The main Raman bands identified in the spectra of the bulk, surface and black inclusion are summarised in Table 6, along with their vibrational assignments and corresponding compounds.

Table 6. Raman shift values (cm^{-1}), vibrational mode assignments, and corresponding compounds detected in the spectra acquired on the bulk, surface, and black inclusion of samples from plaster replica MCR_3045.

Raman shift (cm^{-1})			**Vibrational assignment**	**Compound**
Black inclusion in the Bulk	**Bulk**	**Surface**		
3495	3491	3495	ν OH	H_2O
3407	3405	3407	ν OH	H_2O
3054			ν CH	Organic matter
2897			ν CH	Organic matter
2734			ν CH	Organic matter
1568			Wide bands	Amorphous carbon
1333			Wide bands	Amorphous carbon
1170			ν SO_4	Anhydrite $CaSO_4$
1142	1137	1139	ν SO_4	Gypsum $CaSO_4 \cdot 2H_2O$
1026			ν SO_4	Anhydrite $CaSO_4$
1008	1008	1008	ν SO_4	Gypsum $CaSO_4 \cdot 2H_2O$
	675		ν SO_4	Anhydrite $CaSO_4$
673		674	ν SO_4	Gypsum $CaSO_4 \cdot 2H_2O$
630			ν SO_4	Anhydrite $CaSO_4$
	623	624	ν SO_4	Gypsum $CaSO_4 \cdot 2H_2O$
		606	ν SO_4	Anhydrite $CaSO_4$
493	498	498	ν SO_4	Gypsum $CaSO_4 \cdot 2H_2O$
414	418	414	ν SO_4	Gypsum $CaSO_4 \cdot 2H_2O$

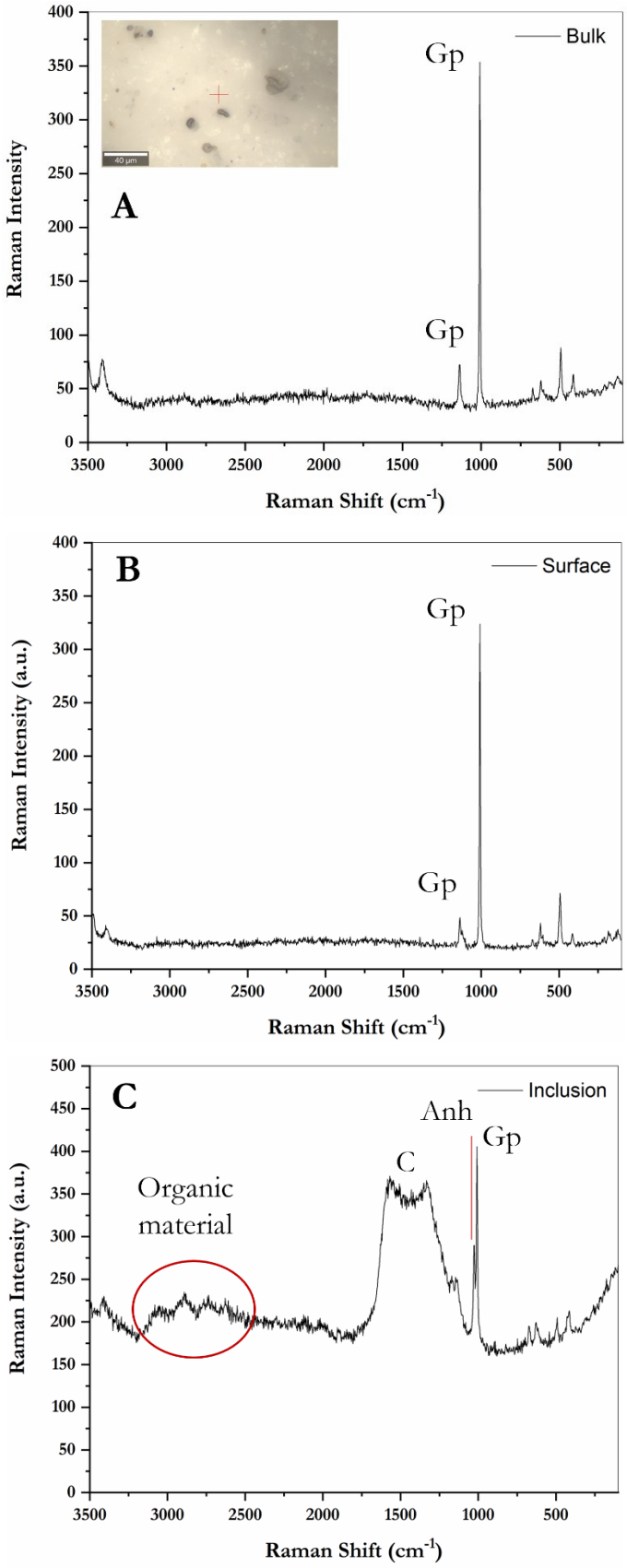

Figure 20. μ-Raman spectra acquired on samples A and B from plaster cast MCR_3045. The spectra show the characteristic bands of gypsum (*Gp*) in all measurements. The signal from the black inclusion (C), shows additional peaks corresponding to anhydrite (*Anh*), amorphous carbon (*C*), and an organic component. The inset in (A) shows the optical image of the analysed spot.

3.3.3.4 ATR-FTIR

ATR-FTIR analysis was performed on both samples collected from plaster cast MCR_3045. An additional spectrum was acquired directly on the organic matter observed on the surface of sample B. The spectra are shown in Figure 21A (bulk and surface) and Figure 21B (organic surface material).

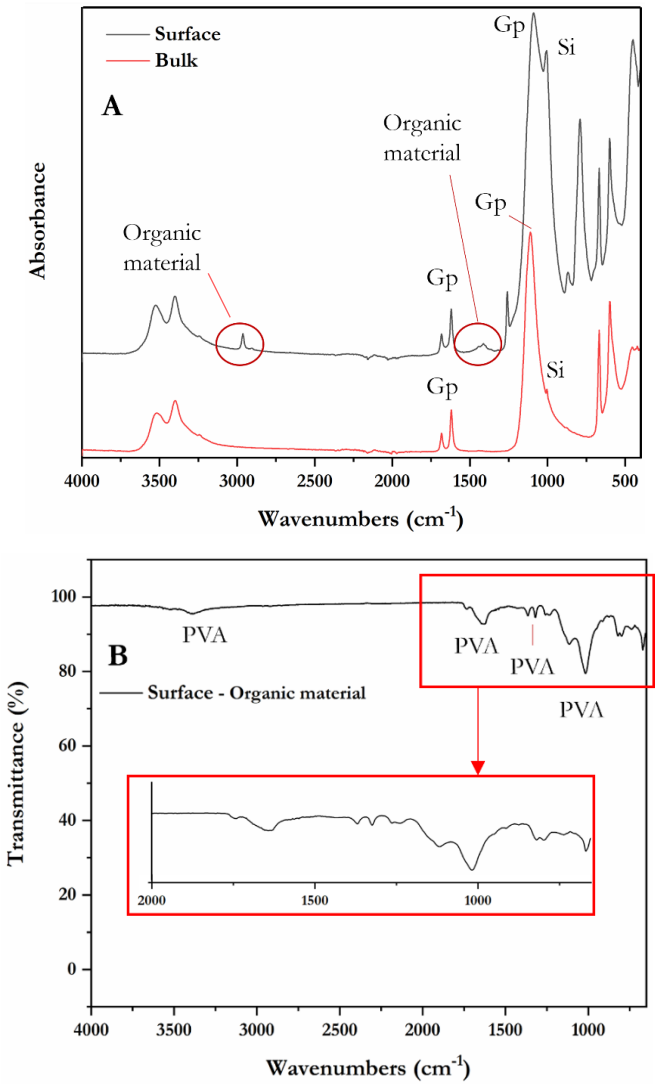

Figure 21. A: ATR-FTIR spectra of the bulk (red) and surface (black) samples from plaster cast MCR_3045. Characteristic bands of gypsum (*Gp*), calcite (*Cal*) and silicates (*Si*) are observed in both spectra. The surface spectrum additionally showed bands associated with an organic component (highlighted in red circles). B: ATR-FTIR spectrum acquired from the organic layer on the surface of sample B. The spectrum showed absorption bands consistent with those of polyvinyl alcohol (PVA). The inset in red provides an enlarged view of the diagnostic region, allowing clearer visualisation of the characteristic PVA absorptions.

The spectra of both bulk and surface samples displayed a broad absorption band in the range of 3517-3240 cm^{-1}, assigned to O-H stretching vibrations of water molecules associated with gypsum ($CaSO_4 \cdot 2H_2O$). Bending vibrations of O-H are present at 1683 cm^{-1} and 1621 cm^{-1} in both spectra. The most intense bands related to sulphate groups (SO_4^{2-}) were detected at 1261, 1114, 868, 672, 604, and 451 cm^{-1} [37-40]. The surface spectrum exhibited additional

absorption bands, including 2965 cm^{-1} and 2912 cm^{-1} (C-H stretching), 1320 cm^{-1}, (C-H bending), and a group of bands in the 1447-1420 cm^{-1} and 1230-1260 cm^{-1} ranges. These bands are absent in the bulk spectrum. Calcite-related absorptions are observed at 1443, 1093, and 870 cm^{-1} in the bulk sample, and at 1447, 1420, and 1093 cm^{-1} in the surface sample [9,39-43]. Weak bands associated with silicate components are detected at 1005 cm^{-1} (bulk) and 792 cm^{-1} (surface).

The ATR-FTIR spectrum acquired from the surface organic layer (Figure 21B) showed a broad O-H stretching band at 3300 cm^{-1}, C-H stretching bands between 2960 and 2916 cm^{-1}, a prominent carbonyl (C=O) absorption at ~1730 cm^{-1}, and multiple features in the 1460-1230 cm^{-1} range [44,45]. Additional peaks between 1100 and 900 cm^{-1} are associated with C-O and C-C vibrations. The main absorption bands identified in the spectra of the bulk, surface, and organic matter, along with their vibrational assignments and associated compounds, are summarised in Table 7.

Table 7. Main ATR-FTIR absorption bands detected in the spectra of the bulk, surface, and organic matter of plaster cast MCR_3045, with respective vibrational assignment and associated compounds.

Peak wavenumber (cm^{-1})			Vibrational assignment	Compound
Bulk	**Surface**	**Organic matter**		
3517	3525		ν OH	Gypsum $CaSO_4 \cdot 2H_2O$
3398	3398	3390	ν OH	Gypsum $CaSO_4 \cdot 2H_2O$
3240	3244		ν OH	H_2O
	2965	2960	ν CH	PVA
	2912	2916	ν CH	PVA
		1731	Residual acetate group	PVA
1683	1683		δ OH	Gypsum $CaSO_4 \cdot 2H_2O$
1621	1621		δ OH	Gypsum $CaSO_4 \cdot 2H_2O$
1443	1447		ν CO	Calcite
		1425	δ CH	PVA
	1420		ν CO	Calcite
		1364	δ CH	PVA
	1320	1319	δ CH	PVA
	1261	1260	ν SO_4^{2-}	Gypsum $CaSO_4 \cdot 2H_2O$
		1230	ν CO	PVA
1114		1116	ν SO_4^{2-}	Gypsum $CaSO_4 \cdot 2H_2O$
	1093		ν CO	Calcite
1005	1007	1010	ν SiO	Silicates
		914	ν C=C	PVA
874			ν CO	Calcite
	868		ν SO_4^{2-}	Gypsum $CaSO_4 \cdot 2H_2O$
		845	ν C=C	PVA
	792		ν SiO	Silicates
		737		PVA
670	672	673	ν SO_4^{2-}	Gypsum $CaSO_4 \cdot 2H_2O$
600	604		ν SO_4^{2-}	Gypsum $CaSO_4 \cdot 2H_2O$
453	451		ν SO_4^{2-}	Gypsum $CaSO_4 \cdot 2H_2O$

3.3.3.5 TGA-DSC

The TGA curve (Figure 22) showed a major weight loss of 19.03 % occurring between approximately 100 °C and 180 °C, with a corresponding endothermic peak in the DSC curve centred at 149.3 °C. This thermal event is attributed to the dehydration of gypsum ($CaSO_4 \cdot 2H_2O$), resulting in the formation of bassanite ($CaSO_4 \cdot ½H_2O$). A second endothermic peak is visible around 354.3 °C, without an associated significant mass loss. Finally, a minor mass loss of 2.61 % is observed above 650 °C, with an inflection point near 665.3 °C, which can be attributed to organic components and minor carbonate phases.

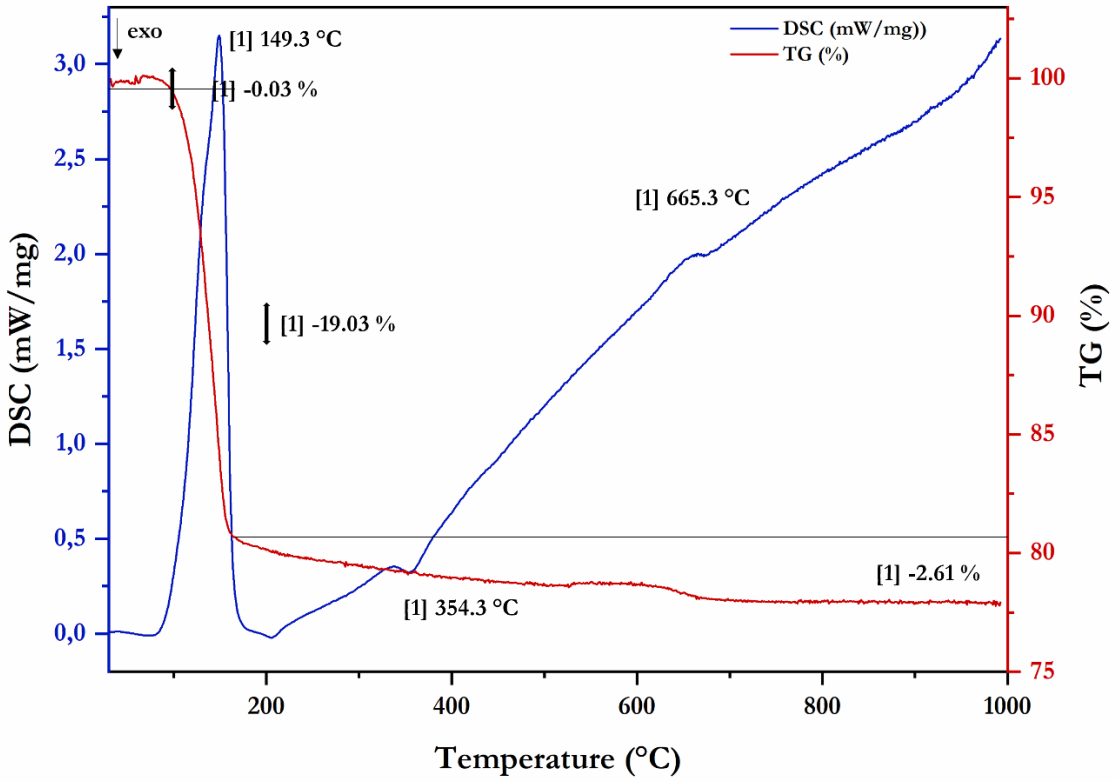

Figure 22. TGA (red) and DSC (blue) curves of the plaster sample from cast MCR_3045. The analysis was carried out from 25 °C to 1000 °C at 10 °C/min under a mixed air/nitrogen atmosphere. Major thermal events include the dehydration of gypsum at ca. 149 °C and a minor mass loss above 650 °C.

3.3.3.6 HIS

Hyperspectral imaging was conducted on the bulk and surface areas of both sample A and sample B, using two spectral acquisition modules, one covering the VNIR (400-1000 nm) and the other the SWIR (1000-2500 nm).

In the VNIR range, all samples showed variations in spectral reflectance, though without clearly defined absorption features. Nevertheless, the analysis allowed for the identification of surface heterogeneities based on differences in overall reflectance and spectral slope. Higher reflectance was generally observed in lighter areas (*white* and *grey* classes). At the same time darker zones (*brown* and *dark brown*) showed lower reflectance values and reduced intensity in the red-NIR region. These differences were particularly evident in the surface of sample A, where VNIR classification maps revealed subtle surface differences that were not clearly visible in standard photographs.

In the SWIR range, additional chemically informative spectral features were detected (Table 8). Across all samples, the spectra exhibited absorption bands typical of minerals containing structural water, particularly gypsum ($CaSO_4 \cdot 2H_2O$) [46,47].

Notable bands included:

- A weak band near 1000 nm, corresponding to the first overtone of O-H stretching and H-O-H bending;
- A distinct absorption at ~1200 nm, assigned to the combination of H-O-H bending and the overtone of O-H stretching;
- A broad absorption between 1400 and 1600 nm, with shoulders at 1450, 1490, and 1545 nm, associated with O-H stretching of bound water;
- Bands at ~1750, 1945, 2210, and 2270 nm, attributed to a combination of O-H, H-O-H, and sulphate (S-O) vibrational modes, respectively.

For sample A (surface), five spectral classes were identified in SWIR: *white*, *brown*, *brown_2*, *dark brown* and *grey*. These classes were defined based on variations in the depth and position of the main absorption features (Figure 23).

In sample B, both bulk and surface areas showed similar spectral trends, though with generally lower contrast and less pronounced absorptions.

The extracted spectra were processed using continuum removal to allow comparison. False colour classification maps were generated for each acquisition to visualise the spatial distribution of the identified spectral classes (Figure 24).

Table 8. Main absorption bands identified in the SWIR spectra (1000-2500 nm) of both samples. The table includes the corresponding vibrational assignments and associated compounds, primarily related to hydrated sulphate phases.

SWIR		
Wavelength (nm)	**Assignment**	**Compound**
1200	Combination of 1st overtone of ν O-H and δ H-O-H	$H_2O/CaSO_4{\cdot}2H_2O$
1450	ν O-H bound water	$H_2O/CaSO_4{\cdot}2H_2O$
1490	ν O-H variation of 1450	$H_2O/CaSO_4{\cdot}2H_2O$
1545	ν O-H overlapping hydration band	$H_2O/CaSO_4{\cdot}2H_2O$
1750	Combination band of δ O-H and δ H-O-H	H_2O
1945	δ H-O-H	Water of crystallisation
2210	SO_4^{2-} combination (δ S-O and OH)	$CaSO_4{\cdot}2H_2O$
2270	δ O-H, δ S-O	$CaSO_4{\cdot}2H_2O$

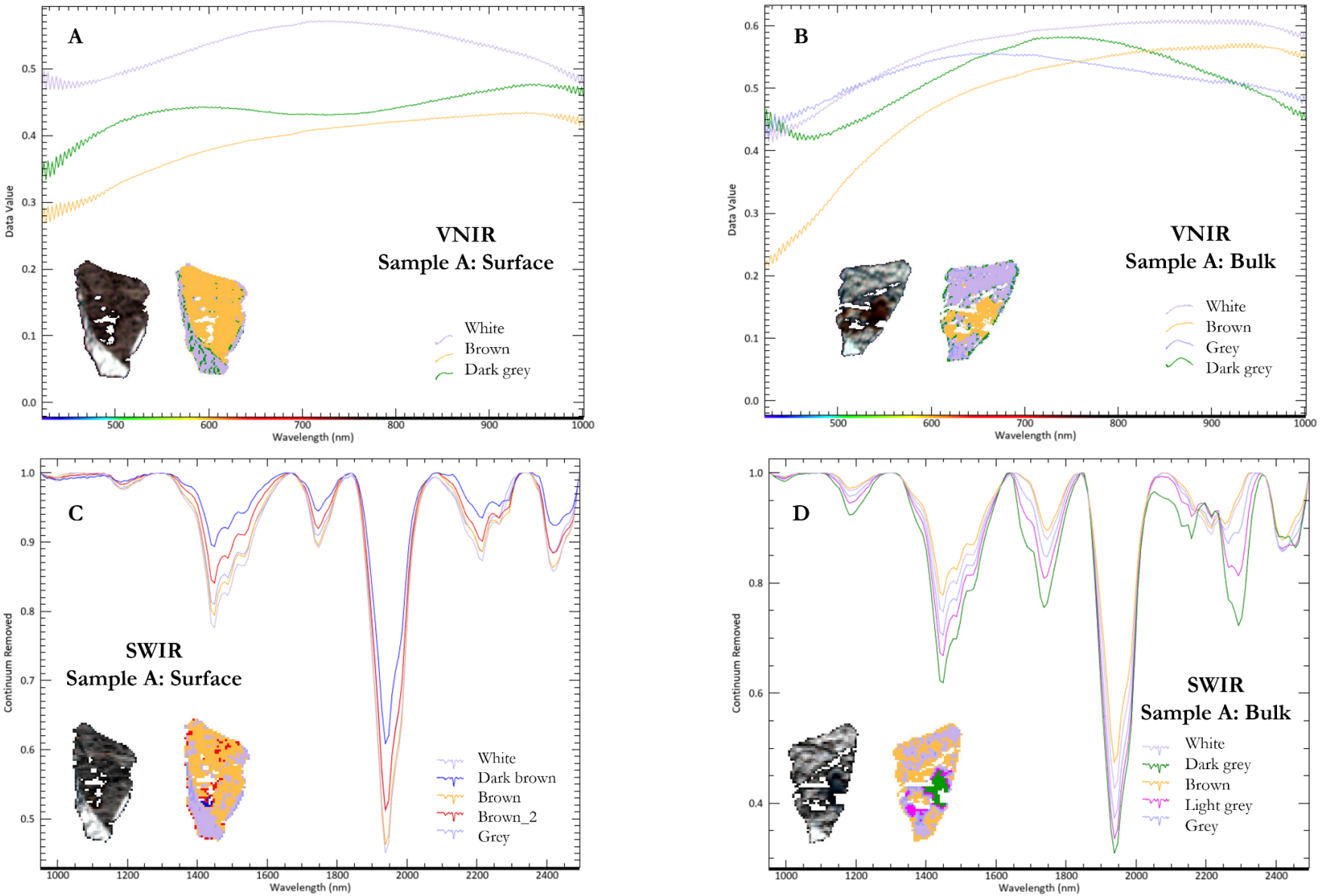

Figure 23. Hyperspectral imaging results for sample A, showing representative spectra and classification maps derived from VNIR (A, B) and SWIR (C, D) acquisition. A, B: VNIR reflectance spectra and classification map of the surface and bulk, respectively; C, D: SWIR continuum-removed reflectance spectra and classification map of the surface and bulk, respectively. Spectral classes were defined using SAM.

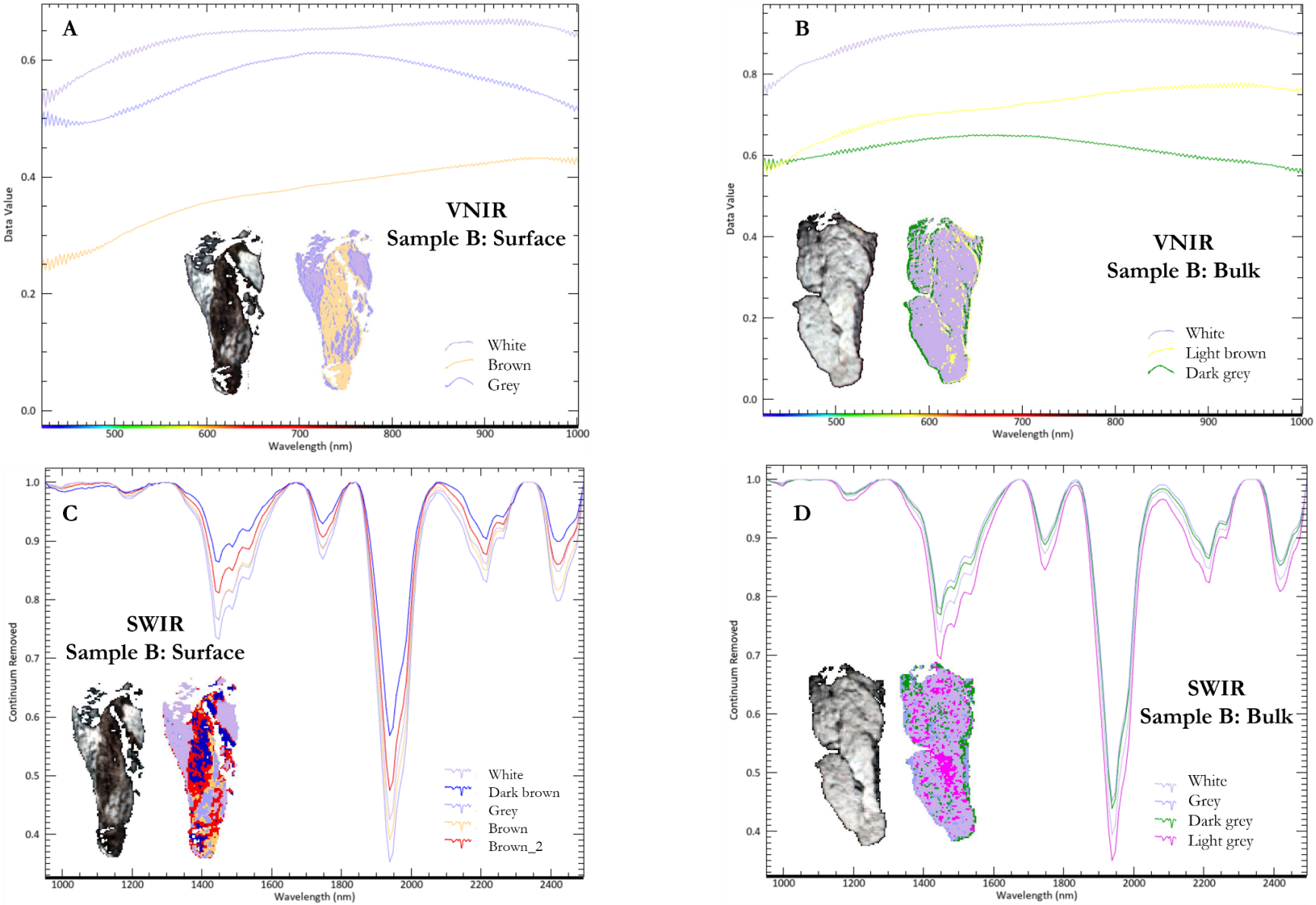

Figure 24. Hyperspectral imaging results for sample A, showing representative spectra and classification maps derived from VNIR (A, B) and SWIR (C, D) acquisition. A, B: VNIR reflectance spectra and classification map of the surface and bulk, respectively; C, D: SWIR continuum-removed reflectance spectra and classification map of the surface and bulk, respectively. Spectral classes were defined using SAM.

3.4 Discussion

3.4.1 Microclimatic monitoring

The long-term microclimatic monitoring campaign conducted in Room LI of the Museum of Roman Civilisation highlighted the unstable and highly variable indoor climate, particularly in terms of RH, confirming the lack of environmental stability in the absence of any control system. These findings are consistent with the condition of many historic museum buildings, which often lack controlled environmental systems and require site-specific evaluations based on the so-called *historic climate* to which artefacts have gradually adapted over time [8].

During the first phase of monitoring (November 2022-May 2024), a single datalogger positioned at the centre of the gallery recorded a distinct seasonal trend in temperature and persistent fluctuations in RH. The temperature ranged between 8.0 °C and 34.0 °C, with an average of 18.8 °C, while RH values ranged between 34.5 % and 86.0 %, with an average of 64.7 % (Table 2). In particular, RH values frequently exceeded the critical 80 % threshold, especially during winter months, falling outside the ideal conservation range of 45-60 % RH and 15-25 °C suggested by UNI 10829:1999 and other standards for gypsum-based artefacts [2,48]. These conditions are known to promote dissolution and recrystallisation of salts, which can result in surface deformations, cracking, and mechanical detachment, thus accelerating existing decay phenomena or initiating new damage patterns [4,7]. In addition to absolute values, the short-term variability of the indoor environment is equally relevant for conservation. According to UNI 10829:1999, the daily excursions of temperature and RH represent a critical indicator for assessing the suitability of museum climates, as rapid changes can influence the moisture content and internal stress conditions of hygroscopic materials [48]. Although the standard is primarily intended as a methodological guideline rather than a strict prescriptive threshold, the microclimatic data collected in Room LI showed that pronounced daily variations are frequent throughout the year. These short-term fluctuations can modify the moisture content of gypsum-based materials and promote repeated wetting-drying conditions at the microstructural level, which are known to favour microcracking, powdering, and the mobilisation of soluble salts. Over time, these processes may contribute to the progressive deterioration of plaster casts in unstable environments. Although the presence of moisture and high RH was frequently recorded, the observed temperature fluctuations are not compatible with freeze-thaw cycles, which typically require repeated transitions below 0 °C. Therefore, deterioration mechanisms in the studied casts

are unlikely to be attributed to freezing effects, which may affect open pore systems in colder conditions [4,7,49].

The thermographic survey conducted in 2023 was fundamental in defining the second monitoring campaign (May 2024-May 2025). The thermographic results highlighted specific critical points, such as the upper wall junctions, ceiling corners, and areas previously effected by infiltration and condensation, which were selected for the installation of eight dataloggers (A-H). Positioning the sensors in these moisture-prone and thermally unstable areas ensured that the monitoring network provided a more targeted and spatially comprehensive assessment of the indoor climate.

The second monitoring phase confirmed a coherent seasonal pattern across all the 8 logger positions. Temperature values ranged from 8.5 °C to 34.5 °C, with average temperatures spanning from 20.0 °C to 20.9 °C. RH values fluctuated between 34.0 % and 86.0 %, with mean values from 59.0 % to 62.8 %. Dew point values followed a consistent seasonal curve (-2.3 °C to 25.3 °C) (Table 3).

While some minor spatial differences were observed, such as marginally higher thermal amplitude in loggers A, B, and F or increased RH variability in logger A during winter, the overall indoor environment remained spatially homogeneous. This may be partially attributed to prior waterproofing and structural repairs conducted in the most affected zones. Systematic differences between critical and non-critical zones in terms of RH behaviour, dew point proximity, or temperature trends were not observed.

Although dew point curves remained consistently below air temperature values, occasional convergence during colder months suggests that sporadic condensation events may have occurred on colder surfaces (Figure 10). However, these were not frequent or widespread in the monitored sections.

The monthly mean indoor temperatures (Table 4) confirm a regular seasonal cycle, with winter levels around 11-12 °C and late-summer peaks above 30 °C (minimum 11.19 °C in February 2023; maximum 31.93 °C in August 2024). Monthly differences between years are evident, but a consistent warming signal is not apparent in this record. For conservation, the data highlighted two recurring risk periods: cold months with elevated RH, when threshold exceedances are more frequent and moisture-driven processes are favoured; and late summer, when higher temperatures can intensify drying stresses. These observations support targeted preventive measures and confirm the need for continued monitoring.

In summary, the integration long-term monitoring and spatially distributed sensors provided detailed information of the environmental dynamics in Room LI. The current

microclimatic conditions are not suitable for the long-term conservation of gypsum-based materials, which are highly sensitive to RH and temperature fluctuations [50]. The findings emphasise the need for a preventive conservation strategy, based on environmental stabilisation through the introduction of an active system and continuous monitoring. These actions are essential to preserve the plaster replicas in view of the museum's imminent reopening.

3.4.2 On-site survey

The visual and instrumental survey of plaster cast MCR_3052 provided valuable insights into the complex degradation phenomena affecting the replicas conserved in Room LI. The artefact (Figure 11), reproducing Scene 37 of Trajan's Column, was selected as a representative case due to its advanced state of deterioration and its location within the gallery, close to datalogger A. As such, it offers a meaningful contribution to the understanding of the degradation dynamics affecting the wider collection.

The internal support system, composed of a wooden and metal structure partially embedded within the gypsum matrix, not only reflects historical casting techniques, but also represents a critical point of structural vulnerability. Rust stains visible on the rear side of the cast (Figure 12A), confirm the onset of corrosion in the metallic framework, likely caused by the high and fluctuating relative humidity recorded during environmental monitoring. These conditions are known to promote oxidation and volumetric expansion of iron-based elements, exacerbating surface deformation, and detachment in gypsum-based artefacts [4,7].

The degradation map (Figure 13) produced during the survey revealed a wide range of alteration features, highlighted significant structural instability with a large vertical fracture extending nearly the full height of the cast. The presence of restoration binders within the fracture indicates prior interventions, and the current propagation of cracks suggests ongoing mechanical stress. Micro-cracks, uneven fillings, and areas of erosion or pulverisation were primarily concentrated along the lower and lateral zones, which are more exposed to external factors such as humidity accumulation, dust deposition, and mechanical stress.

Surface observations also revealed coherent deposits, chromatic alterations, and residual casting materials. Dust accumulation, particularly evident in the more exposed sections, is consistent with the porous and hygroscopic nature of gypsum, which favours retention of particles, especially in the presence of high humidity [51-54]. Although the museum has remained closed to the public for several years, external factors such as urban pollution or road traffic are still likely to contribute to the internal dust load. Diffuse yellow and pink

tonal variations were observed on the surface, which may correspond to historical patinas or aged coatings historically applied to enhance legibility [4,7]. Pencil marks and engraved lines were also documented, alongside widespread scratches and abrasions that may have resulted from handling, transportation, or cleaning. Additionally dark reddish stains and residual traces of *maltina* (plaster mixture) are visible in several areas, especially on the right portion of the cast, and may be linked to the original moulding and assembly process.

Colourimetric analysis supported the visual observations, confirming variations in lightness and chromatic saturation across the surface. Lower L^* values were associated with areas showing greater surface degradation (e.g., T_046, T_053 and T_069) (Table 5), while higher chroma (C^*) values were found in better preserved or possibly retouched areas, indicating heterogeneity in surface conditions. These results reflect the combined impact of ageing, environmental stress, and restoration history.

The application of active infrared thermography (Figure 16) further reinforced these findings. The large vertical fracture was clearly identified as an area of increased thermal response, confirming the sensitivity of this method in detecting subsurface discontinuities. Areas with delayed cooling or greater thermal retention were also highlighted, potentially corresponding to dense mortar fillings, voids, or areas with higher moisture content. These thermographic responses provide important diagnostic data, always visible under standard illumination conditions, and confirm the technique's value in non-invasive structural assessment [55].

These observations highlighted the complexity of the degradation phenomena affecting the gypsum replicas, which result from the interaction between material vulnerabilities, such as porosity, hygroscopic behaviour, and heterogeneous internal structures, and environmental stress factors, including RH fluctuations, temperature variations, and dust deposition. The combined use of visual inspection, spectrophotometry, and infrared thermography provided a comprehensive understanding of both surface and subsurface alterations, offering insight into ongoing deterioration processes as well as traces of previous restoration. This diagnostic approach proved particularly effective in identifying degradation patterns and supporting future conservation planning.

3.4.3 Microchemical and mineralogical characterisation

The combined application of XRPD, FESEM-EDS, μ-Raman, ATR-FTIR, TGA-DSC and Hyperspectral Imaging allowed for a comprehensive characterisation of the materials composing the plaster cast MCR_3045. This multi-analytical strategy enabled the

identification of both inorganic and organic components, as well as the observation of stratigraphic heterogeneities between the bulk and the surface of the artefact.

XRPD analysis revealed that gypsum is the main mineral phase in both bulk (sample A) and the surface (sample B) (Figure 17), as indicated by the strong diffraction peaks, especially the one associated with the (020) crystal plane [25]. In addition to gypsum, the bulk sample revealed minor peaks of calcite, quartz and kaolinite [27], suggesting the presence of either natural impurities or additives, in line with historical plaster formulations consistent with historical gypsum-based casting practices [56]. The absence of calcite and only weak traces of kaolinite in the surface sample support the hypothesis of a finishing layer with a different composition, possibly applied to enhance aesthetic qualities by giving the surface a more marble-like appearance.

High-resolution FESEM analysis confirmed the distinction between the porous bulk matrix and the denser surface layer. The bulk sample displayed large tabular and needle-like gypsum crystals, while the surface is characterised by a fine-grained, compact texture forming a continuous layer approximately 150-200 μm thick. EDS elemental maps (Figure 19) showed that the matrix is rich in *Ca*, *S*, and *O*, consistent with gypsum ($CaSO_4 \cdot 2H_2O$), while the surface layer is enriched in *Al*, *Si*, and *K*, indicating the presence of a clay-based finish. The presence of titanium and magnesium in the surface layer may be due to natural impurities in the clay or to the addition of small amounts of other materials during production or restoration treatments.

μ-Raman spectroscopy further confirmed the material composition. Spectra collected from the bulk and surface (Figure 20) showed characteristic bands of gypsum at ~1140, 1008, 673, 492, and 414 cm^{-1} [28-35], as well as O-H stretching vibrations around 3405 and 3490 cm^{-1} [31,33]. A black inclusion observed in the bulk sample revealed additional spectral features, including peaks attributed to anhydrite (1170, 1026, 675 cm^{-1}) [29,31,35], broad bands between 1600 and 1300 cm^{-1} associated with amorphous carbon [32,36], and C-H stretching bands between 3054 and 2734 cm^{-1}. These results suggest the presence of an organic matter used either during production or a previous conservation campaign [45,46].

ATR-FTIR spectra (Figure 21) supported the Raman results, confirming the main presence of gypsum through strong absorption bands related to O-H and SO_4^{2-} vibrations, with additional signals for calcite at ~1447-1420 and 870 cm^{-1} [9,39,41-43]. A notable peak at 3340 cm^{-1} suggests the presence of bound water molecules. The surface spectrum also revealed bands associated with organic functional groups including C-H stretching, C=O

and C-C, along with CH bending bands [44,45] related to the presence of PVA, probably added as a finishing treatment during restoration interventions.

TGA-DSC analysis provided thermal evidence supporting the mineralogical and chemical data. The major mass loss of 19.03 % between 100 °C and 180 °C, with an endothermic peak at 149.3 °C, corresponds to the dehydration of gypsum to hemihydrate [9,57,58]. A minor mass loss at 354.3 °C and additional weak losses above 650 °C may be attributed to the decomposition of organic components and minor carbonate phases (Figure 22).

Hyperspectral imaging added spatial information about the surface composition and state of preservation. In the VNIR range, variations in reflectance correlated with chromatic differences, while in the SWIR range, characteristic absorption bands related to bound water and sulphates were consistent with gypsum (Table 8) [39]. Classification maps revealed subtle heterogeneities on the surface of sample A that were not visible through traditional imaging, reinforcing the hypothesis of different surface treatments or localised degradation.

Overall, the results confirm the heterogeneous nature of the replica, reflecting both its original manufacture and subsequent alteration processes. The presence of a distinct surface layer composed of clay materials, differing from the bulk, suggests that a finishing layer was applied during production to modify the surface texture and appearance. Additionally, the identification of polyvinyl alcohol provides valuable evidence of the materials used in past conservation treatments. This information is particularly valuable in absence of written reports, and is essential for planning appropriate cleaning methods and ensuring compatibility and reversibility of future conservation interventions.

3.5 Conclusion

The diagnostic investigation conducted on the plaster replicas of Trajan's Column, conserved in Room LI of the Museum of Roman Civilisation, has demonstrated the relevance of an integrated, multi-analytical approach for the assessment and long-term conservation of complex gypsum-based artefacts. Through the combination of environmental monitoring, *in-situ* visual and thermographic surveys, and laboratory-based characterisation, it was possible to reconstruct not only the material composition of the casts, but also the main deterioration processes and the impact of long-term environmental exposure.

Microclimatic monitoring revealed the absence of a controlled indoor environment and recorded significant thermo-hygrometric fluctuations, with relative humidity levels

frequently exceeding 80 %, especially during the winter months. Although substantial spatial variability was not observed, the values consistently fell outside the recommended conservation range for gypsum-based materials. The current environmental data revealed a trend of increasing temperatures and persistent humidity fluctuations, suggesting a progressive alteration of the indoor climate. These conditions have likely contributed to the development and acceleration of deterioration phenomena such as cracking, erosion, pulverisation, and chromatic alterations.

The *in-situ* analysis of selected casts, particularly the representative example MCR_3052, confirmed the presence of both surface and structural damage. Fractures, micro-cracks, coherent deposits, tonal variations, and signs of previous restorations were documented, along with possible traces of biological colonisation. The application of active infrared thermography proved especially valuable in identifying subsurface anomalies such as hidden detachments, previous interventions, or areas with altered thermal behaviour that are not visible through standard inspection.

Laboratory analyses on samples from cast MCR_3045 provided a detailed characterisation of the materials. XRPD, FESEM-EDS, μ-Raman, and ATR-FTIR confirmed that gypsum ($CaSO_4 \cdot 2H_2O$) is the main constituent of both bulk and surface layers, but with clear stratigraphic differentiation. The surface displayed a compact microstructure enriched in kaolinite and magnesium, associated with the original formulation of the casts. Conversely, the detection of titanium, probably in the form of TiO_2, a pigment not used in the mid-19th-century, may indicate the presence of later restoration products or protective surface treatments. The identification of organic compounds, such as polyvinyl alcohol, further supports the hypothesis of recent interventions. These findings highlight the importance of characterising the surface layers before planning cleaning or consolidation procedures.

Thermal and spectroscopic analyses supported the mineralogical findings, while hyperspectral imaging provided a non-invasive visualisation of subtle surface heterogeneities and material differences. Colourimetric measurements further captured tonal variations across the surface, supporting and complementing the visual assessment. Overall, the results confirmed the complex and stratified nature of the casts, reflecting a combination of original features and later modifications, both structural and superficial.

This study highlighted how the condition of the casts is influenced by their material properties, an unstable environment, and previous restoration treatments. Combining visual,

analytical and environmental data has been important for understanding their current state and planning conservation measures that address their specific needs.

In view of the planned reopening of the museum, it will be essential to stabilise environmental conditions within Room LI, and to improve environmental monitoring. Future studies should focus on developing suitable restoration methods, choosing cleaning techniques based on surface characteristics, and ensuring the long-term preservation of these valuable plaster casts.

References

[1] F. Bubola, C. Coletti, E. Balliana, C. Cecamore, C. Parisi Presicce, C. Mazzoli, The diagnostic study of the plaster replicas of the Trajan's Column conserved at the Museum of Roman Civilisation (Rome), ACTA IMEKO, vol. 13 (2024), pp. 1-8.

[2] A. Spagnulo, C. Vetromile, A. Masiello, M. F. Alberghina, S. Schiavone, C. Lubritto, Climate and Cultural Heritage: The Case Study of "Real Sito of Carditello", Heritage, vol. 2 (2019), pp. 2053-2066.

[3] V. Risdonne, C. Hubbard, J. Puisto, C. Theodorakopoulos, A multi-analytical study of historical coated plaster surfaces: the examination of a nineteenth-century V&A cast of a tombstone, Herit. Sci., vol.9 (2021), pp. 70-89.

[4] Caroselli, M., Cavallo, G., Felici, A., Luppichini, S., Nicoli, G., Aliverti, L., Jean, G., 2019. Gypsum in Ticinese stucco artworks of the 16–17th century: Use, characterization, provenance and induced decay phenomena. J. Archaeol. Sci. Rep. 24, 208–219.

[5] V. Risdonne, C. Hubbard, V. H. López Borges, C. Theodorakopoulos, Nineteenth-century Plaster Casts: a Review of Historical Sources, Stud. Conserv., vol. 67 (2022), pp. 186-208.

[6] V. Risdonne, A. Francescutto Miró, S. Morio, C. Theodorakopoulos, The Victoria and Albert Museum Plaster Casts by the Nineteenth-Century Workshop of the Notre-Dame Cathedral: Scientific Analysis and Conservation, Herit., vol. 5 (2022), pp. 3427-3445.

[7] Payne, E.M., 2020. The Conservation of Plaster Casts in the Nineteenth Century. Stud. Conserv. 65, 37–58.

[8] K. Fabbri, Historic Climate in Heritage Building and Standard 15757: Proposal for a Common Nomenclature. Climate, vol. 10 (2022), pp. 4-12.

[9] M. Uccelli, M. Caroselli, J. Válek, J. Zapletalová, A. Felici, G. Nicoli, G. Jean, Characterization of the stucco decoration by Baldassarre Fontana in the Gallery of the Angels at Uherče Castle (Cz), J. Archaeol. Sci. Rep., vol. 44 (2022), pp. 103493-103505.

[10] L. Rampazzi, B. Rizzo, C. Colombo, C. Conti, M. Realini, U. Bartolucci, M. P. Colombini, A. Spiriti, L. Facchin, The stucco decorations from St. Lorenzo in Laino (Como, Italy): The materials and the techniques employed by the "Magistri Comacini", Anal. Chem. Acta., vol. 630 (2008), pp. 91-100.

[11] M. Caroselli, G. Cavallo, A. Felici, L. Aliverti, S. Luppichini, G. Jean, G. Nicoli, Characterisation of the stucco decorations at the "Sacro Monte di Ossuccio" (16th-17th century, Como, Italy, Int. J. Conserv. Sci., vol. 7 (2016), pp. 857-870.

[12] M. Caroselli, S. A. Ruffolo, F. Piqué, Mortars and plasters – how to manage mortars and plasters conservation, Archaeol. Anthropol. Sci., vol. 13 (2021), pp. 188-208.

[13] M. T. Freie, M. do Rosário Veiga, A. Santos Silva, J. De Brito, Restoration of ancient gypsum-based plasters: Design of compatible materials, Cem. Concr. Compos., vol. 120 (2021), pp. 104014-104027.

[14] M. T. Freie, M. do Rosário Veiga, A. Santos Silva, J. De Brito, Studies in ancient gypsum based plasters toward their repair: Physical and mechanical properties, Constr. Build. Mater., col. 202 (2019), pp. 319-331.

[15] E. Salavessa, S. Jalali, L. M. O. Sousa, L. Fernandes, A. M. Duarte, Historical plasterwork techniques inspire new formulation, Constr. Build. Mater., vol. 48 (2013), pp. 858-867.

[16] A. Magalhães, R. Veiga, Physical and mechanical characterisation of historic mortars. Application to the evaluation of the state of conservation, Mater. Constr., vol. 59 (2009), pp. 61-77.

[17] G. Gariani, P. Lehuéde, L. Leroux, G. Wallez, F. Goubard, Anne Bouquillon, Marc Bormand, First insights on the mineral composition of "Stucco" devotional reliefs from Italian Rennaissance Masters: investigating technological practices and raw material sourcing, J. Cult. Herit., vol. 34 (2018), pp. 23-32.

[18] K. Elert, P. Bel-Anzué, M. Burgos-Ruiz, Influence of calcination temperature on hydration behaviour, strength, and weathering resistance of traditional gypsum plaster, Constr. Build. Mater., vol. 367 (2023), pp. 130361-130371.

[19] M. T. Freie, A. Santos Silva, M. do Rosário Veiga, J. De Brito, Studies in ancient gypsum based plasters towards their repair: Mineralogy and microstructure, Constr. Build. Mater., vol. 196 (2019), pp. 512-529.

[20] V. Di Giuseppe Di Paolo, Il valore della copia nell'Accademia di Francia (1666-1699): funzioni, modelli, destinazioni e pratiche, Fondazione 1563 per l'arte e la cultura della Compagnia di San Paolo, Torino, 2017. [In Italian]

[21] G. Agosti, V. Farinella, Il fregio della colonna traiana. Avvio ad un registro della fortuna visive, Annali della Scuola Normale Superiore di Pisa. Classe di Lettere e Filosofia, vol. 15 (1985), pp. 1103-1150. [In Italian]

[22] UNI EN 15757:2010, Beni Culturali – Specifiche per la temperatura e l'umidità per limitare i danni meccanici indotti dal clima nei materiali organici igroscopici. Ente Nazionale Italiano di Unificazione (UNI), Milano, 2010. [In Italian]

[23] M. Mattone, S. Rescic, F. Fratini, R. Mangalli Del Fà, Experimentation of Earth-Gypsum Plasters for the Conservation of Earthen Constructions, Int. J. Archit. Herit., vol. 11 (2017), pp. 763-772.

[24] G. Deperiot, Iconographie, monnaie et propagande sous Trajan. I. La colonne Trajane, Collection Moneta, Moneta, Wetteren. ed, 2007. [In French]

[25] C. A. Boevens, V. V. H. Ichharam, Redetermination of the crystal structure of calcium sulphate dihydrate, $CaSO_4 \cdot 2H_2O$, Z. Kristallogr., vol. 217 (2002), pp. 9-10.

[26] L. N. Warr, IMA-CNMNC approved mineral symbols, Mineral. Mag., vol. 85 (2021), pp. 291-320.

[27] S. S. Pawelkowicz, P. Svora, Z. Prosek, M. Keppert, E. Vejmelková, N. Murafa, T. Sawoszczuk, J. Sygula-Cholewńiska H. Bíbová, Laboratory assessment of photoactive Gypsum-based repair plaster, constr. Build. Mater., vol. 346 (2022), pp. 128426-124852.

[28] V. Antunes, A. Candeias, M. J. Oliveira, S. Longelin, V. Serrão, A. I. Seruya, J. Coroado, L. Dias, J. Mirão, M. L. Carvalho, Characterizaion of gypsum and snhydrite ground layers in 15th and 16th centuries Portuguese paintings by Raman Spectroscopy and other techniques, J. Raman Spectrosc., vol. 45 (2014), pp. 1026-1033.

[29] N. Prieto-Taboada, O. Gómez-Laserna, I. Martínez-Arkarazo, M. A. Olazabal, J. M. Madariaga, Raman Spectra of the Different Phases in the $CaSO_4 \cdot H_2O$ System, Anal. Chem., vol. 86 (2014), pp. 10131-10137.

[30] H. G. M. Edwards, M. T. Doménech-Carbó, M. D. Hargreaves, A. Doménech-Carbó, A Raman spectroscopic and combined analytical approach to the restoration of severely damaged frescoes: the Palomino project, J. Raman Spectrosc., vol. 39 (2008), pp. 444-452.

[31] T. Schmid, P. Dariz, Chemical imaging of historical mortars by Raman microscopy, Constr Build Mater., vol. 114 (2016), pp. 506-516.

[32] I. Martínez-Arkarazo, D. C. Smith, O. Zuloaga, M. A. Olazabal, J. M. Madariaga, Evaluation of three different mobile Raman microscopes employed to study deteriorated civil building stones, J. Raman Spectrosc., vol. 39 (2008), pp. 1018-1029.

[33] P. S. R. Prasad, A. Pradhan, T. N. Gowd, In situ micro-Raman investigation of dehydration mechanism in natural gypsum, Curr. Sci., vol. 80 (2001), pp. 1203-1207.

[34] H. G. M. Edwards, S. E. J. Villar, J. Parnell, C. S. Cockell, P. Lee, Raman spectroscopic analysis of cyanobacterial gypsum halotrophs and relevance for sulfate deposits on Mars, R. Soc. Chem., vol. 130 (2005), pp. 917-923.

[35] A. Sarmiento, M. maguregui, I. Martinez-Arkazo, M. Angulo, K. Castro, M. A. Olazábal, L. A. Fernández, M. D. Rodríguez-Laso, A. M. Mujika, J. Gómez, J. M. Madariaga, Raman spectroscopy as a tool to diagnose the impacts of combustion and greenhouse acid gases on properties of Built Heritage, J. Raman Spectrosc. Vol. 39 (2008), pp. 1042-1049.

[36] S. E. Spoto, G. Paladini, F. Caridi, V. Crupi, S. D'Amico, D. Majolino, V. Venuti, Multi-Technique Diagnostic Analysis of Plaster Mortars from the Church of the Annunciation (Tortorici, Sicily), Mater., vol. 15 (2022), pp. 958-972.

[37] D. Gramtorp, K. Botfeldt, J. Glastrup, K. P. Simonsen, Investigation of Anne Marie Carl-Nielsen's wax models, Stud. Conserv., vol. 60 (2015), pp. 97-106.

[38] G. Vasco, A. Serra, D. Manno, G. Buccolieri, L. Calcagnile, L. Miotto, L. Valli, A. Buccolieri, Diagnostic investigation to support the restoration of the polychrome terracotta relief "Madonna and Child" in Piove di Sacco (Padova, Italy), J. Cult. Herit., vol. 53 (2021), pp. 80-87.

[39] G-L. Liu, S. G. Kazarian, Recent advances and applications to cultural heritage using ATR-FTIR spectroscopy and ATR-FTIR spectroscopic imaging, R. Soc. Chem., vol. 147 (2022), pp. 1777-1797.

[40] L. Bishop, M. D. Dyar, S. J. King, A. J. Brown, G. A. Swayze, What Lurks in the Martian Rocks and Soil? Investigation of Sulfates, Phosphates, and Perchlorates. Spectral properties of Ca-sulfates: Gypsum, bassanite and anhydrite, Am. Mineral., vol. 99 (2014), pp. 2105-2115.

[41] F. A. Andersen, L. Brečevic, Infrared Spectra of Amorphous and Crystalline Calcium Carbonate, Acta Chem. Scand., vol. 45 (1991), pp. 1018-1024.

[42] T. Lamhasni, H. El-Marjaoui, A. El Bakkali, S. Ait Lyazidi, M. Haddad, A. Be-Ncer, F. Benyaich, A. Bonazza, M. Tahri, Air pollution impact on architectural heritage of Morocco: Combination of synchronous fluorescence and ATR-FTIR spectroscopies for the analyses of black crusts deposits, Chemosphere, vol. 225 (2019), pp. 517-523.

[43] M. M. Jordán, J. Jordá, F. Pardo, M. A. Montero, Mineralogical Analysis of Historical Mortars by FTIR, Mater., vol. 12 (2018), pp. 55-59.

[44] F. Pozzi, E. Basso, S. Alderson, J. Levinson, M. Neimar, S. Alcalá, Aiding the cleaning of four 19th century Tsimshian house posts: investigation of museum-applied surface coatings and original polychromy, Herit. Sci., vol. 9 (2021), pp. 42-59.

[45] V. Guglielmi, C. A. Lombardi, G. Fiocco, V. Comite, A. Bergomi, M. Borelli, M. Azzarone, M. Malagodi, M. Colella, P. Fermo, Multi-Analytical Investigation on Rennaissance Polychrome Earthenware Attributed to Giovanni Antonio Amedeo, Appl. Sci., vol. 13 (2023), pp. 3924-3944.

[46] J. K. Crowley, Visible and Near-Infrared (0.4-2.5 μm) Reflectance Spectra of Playa Evaporite Minerals, J. Geophys. Res., vol. 96 (1991), pp. 16231-16240.

[47] N. Mangold, A. Gendrin, B. Gondet, S. LeMouelic, C. Quantin, V. Ansan, J. P. Bibring, Y. Langevin, P. Masson, G. Neukum, Spectral and geological study of the sulphate-rich region of West Candor Chasma, Mars, Icarus, vol. 194 (2008), pp. 519-543.

[48] UNI 10829:1999, Beni Culturali – Condizioni ambientali in ambienti confinati per la conservazione – Misurazione ed analisi. Ente Nazionale Italiano di Unificazione (UNI), Milano, 1999. [In Italian]

[49] S. Salvini, C. Coletti, L. Maritan, M. Massironi, A. Pieropan, R. Spiess, C. Mazzoli, Petrographic characterization and durability of carbonate stones used in UNESCO World Heritage Sites in northeastern Italy, Environ. Earth Sci., vol. 82 (2023), pp. 49-72.

[50] M. T. Doménech-Carbó, A. Doménech-Carbó, L. Osete-Cortina, M. C. Saurí-Peris, Characterization of organic materials in art conservation and archaeometry, Technologia Artis, vol. 1 (2006), pp. 39-58.

[51] G. Battista, R. de Lieto Vollaro, Correlation between air pollution and weather data in urban areas: Assessment of the city of Rome (Italy) as spatially and temporally independent regarding pollutants, Atmos. Environ., vol. 165 (2017), pp. 240-277.

[52] A. Winkler, T. Contardo, V. Lapenta, A. Sgamellotti, S. Loppi, Assessing the impact of vehicular particulate matter on cultural heritage by magnetic biomonitoring at Villa Farnesina in Rome, Italy, Sci. Total Environ., vol. 823 (2022), pp. 153729-153742.

[53] A. Proietti, M. Panella, F. Leccese, E. Svezia, Dust detection and analysis in museum environment based on pattern recognition, Meas., vol. 66 (2015), pp. 62-72.

[54] A. Proietti, L. Liparulo, F. Leccese, M. Panella, Shapes classification of dust deposition using fuzzy kernel-based approaches, Meas., vol. 77 (2016), pp. 344-350.

[55] F. Mercuri, U. Zammit, N. Orazi, S. Paoloni, M. Marinelli, F. Scudieri, Active infrared thermography applied to the investigation of art and historic artefacts, J. Therm. Anal. Calorim., vol. 104 (2011), pp. 475-485.

[56] Turco, Il gesso lavorazione – trasformazione – impieghi, Ulrico Hoepli, Milano, 1861. [In Italian]

[57] V. Brunello, D. Bersano, L. Rampazzi, A. Sansonetti, C. Tedeschi, Gypsum based mixes for conservation purposes: evaluation of microstructural and mechanical features, Mat. Const., vol 70 (2020), e207, pp. 1-14.

[58] J. Pires, A. J. Cruz, Techniques of thermal analysis applied to the study of cultural heritage, J. Therm. Anal. Calorim., vol. 87 (2007), pp. 411-415.

Annex – Part 1

Photographs and degradation maps – conservation class: *mediocre* MCR_3029

Annex – Figure 1: Photographic documentation of plaster cast MCR_3029, classified as *mediocre* in the 2012 survey.

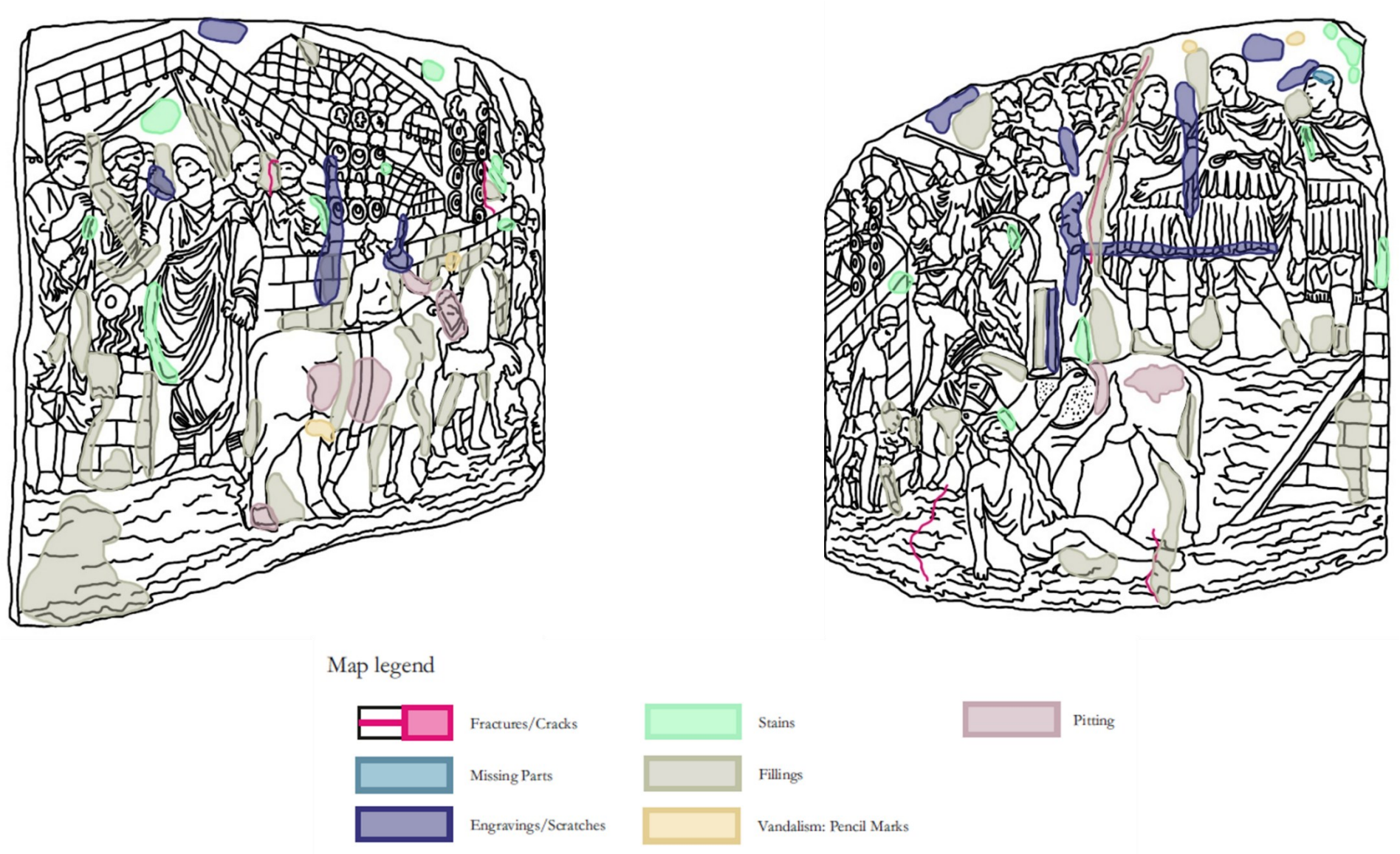

Annex – Figure 2: Degradation map of plaster cast MCR_3029, classified as *mediocre* in the 2012 survey. The map legend indicates the colours used to identify each degradation pattern.

Photographs and degradation maps – conservation class: *mediocre* MCR_3031

Annex – Figure 3: Photographic documentation of plaster cast MCR_3031, classified as *mediocre* in the 2012 survey.

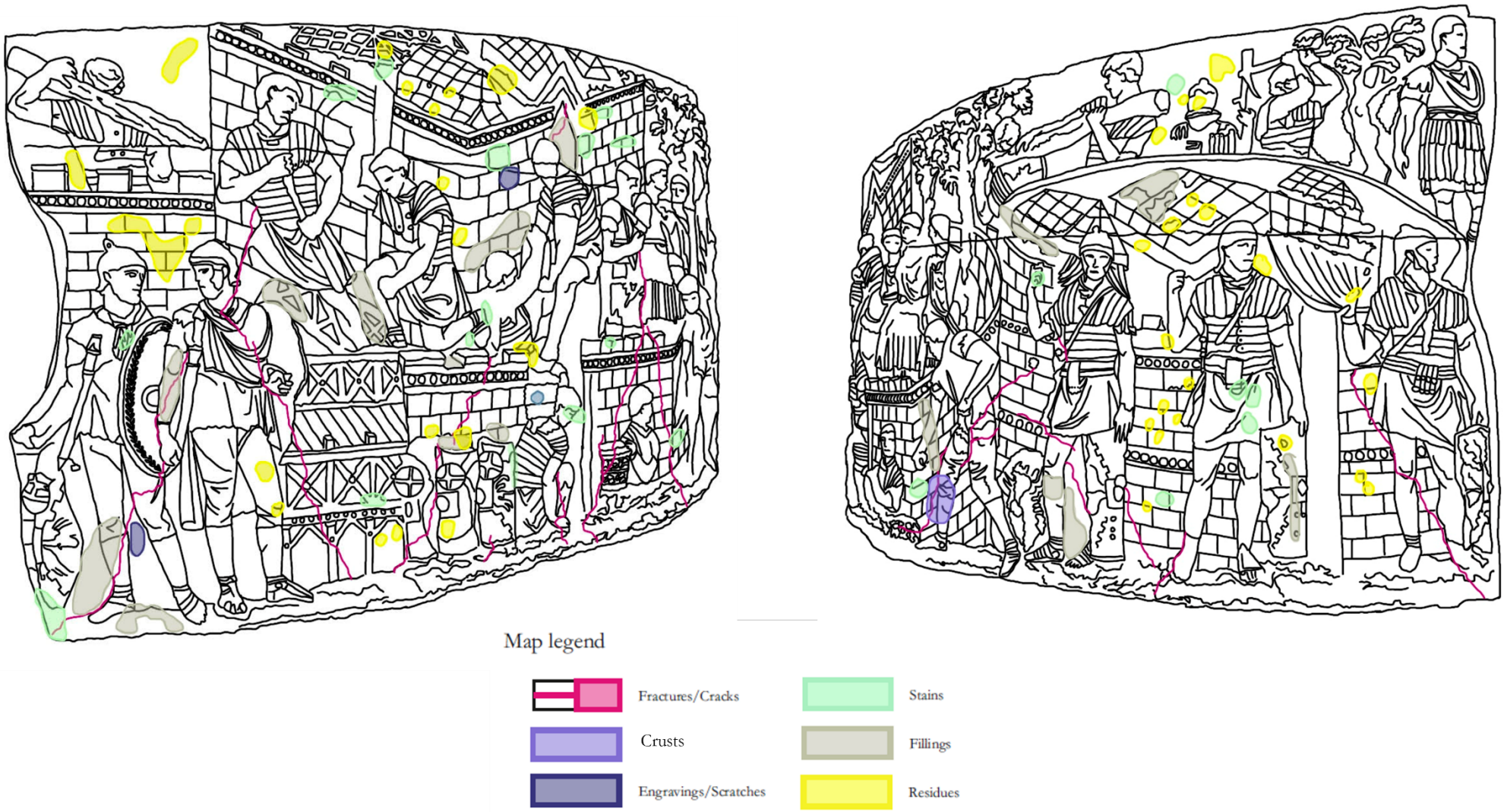

Annex – Figure 4: Degradation map of plaster cast MCR_3031, classified as *mediocre* in the 2012 survey. The map legend indicates the colours used to identify each degradation pattern.

Annex – Figure 5: Photographic documentation of plaster cast MCR_3064, classified as *mediocre* in the 2012 survey.

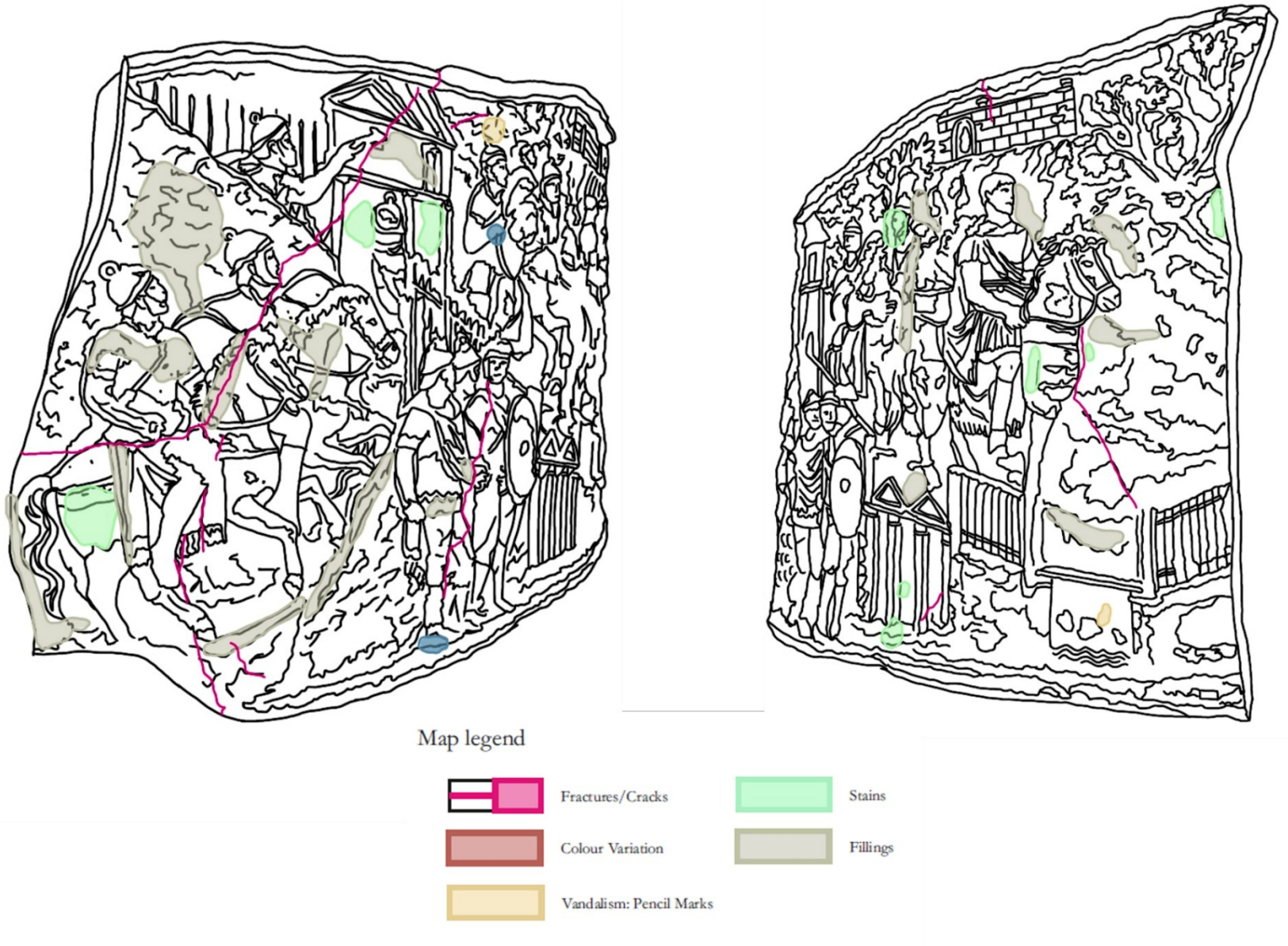

Annex – Figure 6: Degradation map of plaster cast MCR_3064, classified as *mediocre* in the 2012 survey. The map legend indicates the colours used to identify each degradation pattern.

Photographs and degradation maps – conservation class: *discreet* MCR_3027

Annex – Figure 7: Photographic documentation of plaster cast MCR_3027, classified as *discreet* in the 2012 survey.

Annex – Figure 8: Degradation map of plaster cast MCR_3027, classified as *discreet* in the 2012 survey. The map legend indicates the colours used to identify each degradation pattern.

Photographs and degradation maps – conservation class: *discreet* MCR_3030

Annex – Figure 9: Photographic documentation of plaster cast MCR_3030, classified as *discreet* in the 2012 survey.

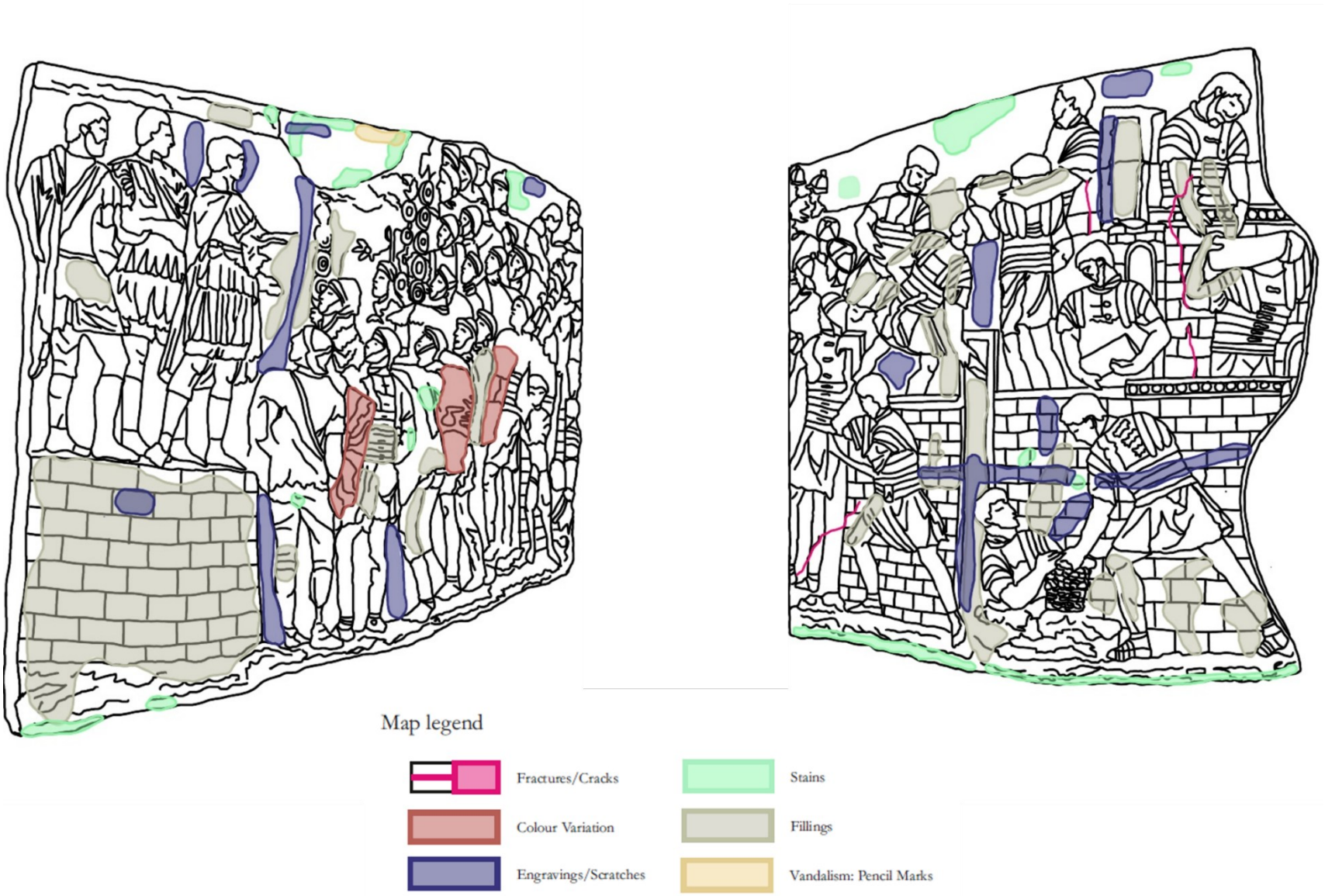

Annex – Figure 10: Degradation map of plaster cast MCR_3030, classified as *discreet* in the 2012 survey. The map legend indicates the colours used to identify each degradation pattern.

Photographs and degradation maps – conservation class: *discreet* MCR_3050

Annex – Figure 11: Photographic documentation of plaster cast MCR_3050, classified as *discreet* in the 2012 survey.

Annex – Figure 12: Degradation map of plaster cast MCR_3050, classified as *discreet* in the 2012 survey. The map legend indicates the colours used to identify each degradation pattern.

Photographs and degradation maps – conservation class: *poor* MCR_3045

Annex – Figure 13: Photographic documentation of plaster cast MCR_3045, classified as *poor* in the 2012 survey.

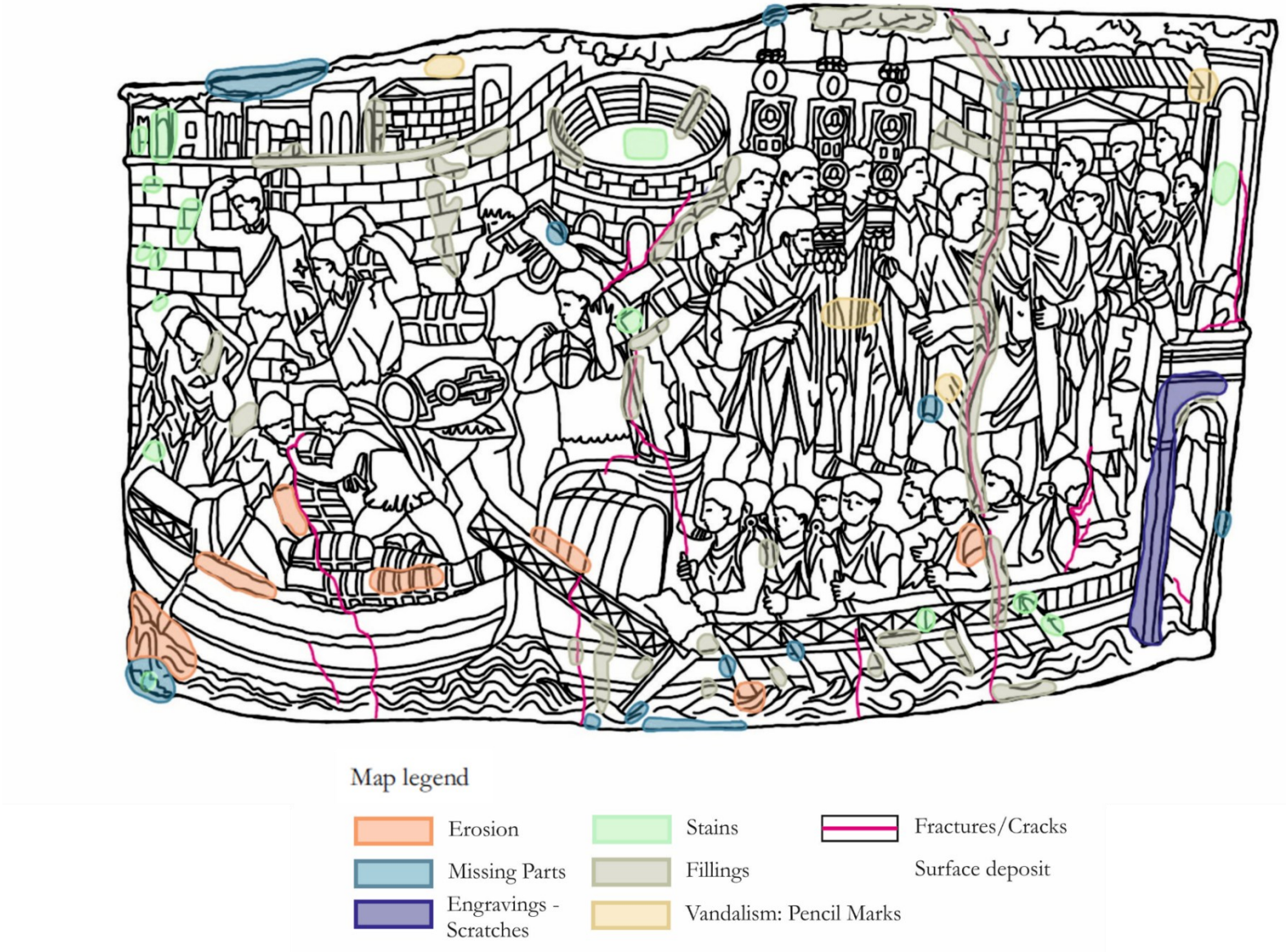

Annex – Figure 14: Degradation map of plaster cast MCR_3045, classified as *poor* in the 2012 survey. The map legend indicates the colours used to identify each degradation pattern.

Photographs and degradation maps – conservation class: *poor* MCR_3058

Annex – Figure 15: Photographic documentation of plaster cast MCR_3058, classified as *poor* in the 2012 survey.

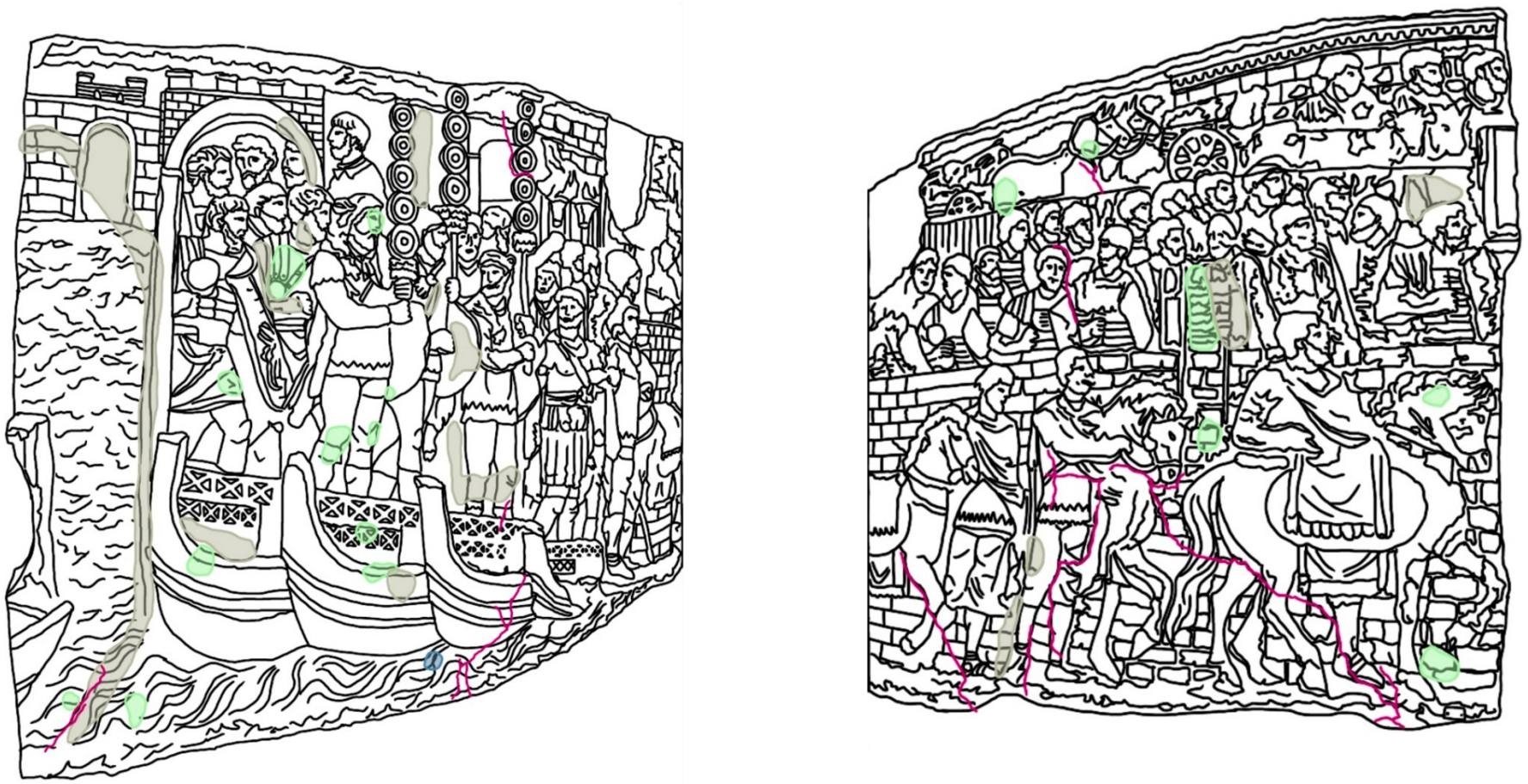

Annex – Figure 16: Degradation map of plaster cast MCR_3058, classified as *poor* in the 2012 survey. The map legend indicates the colours used to identify each degradation pattern.

Photographs and degradation maps – conservation class: *poor* MCR_3125

Annex – Figure 15: Photographic documentation of plaster cast MCR_3125, classified as *poor* in the 2012 survey.

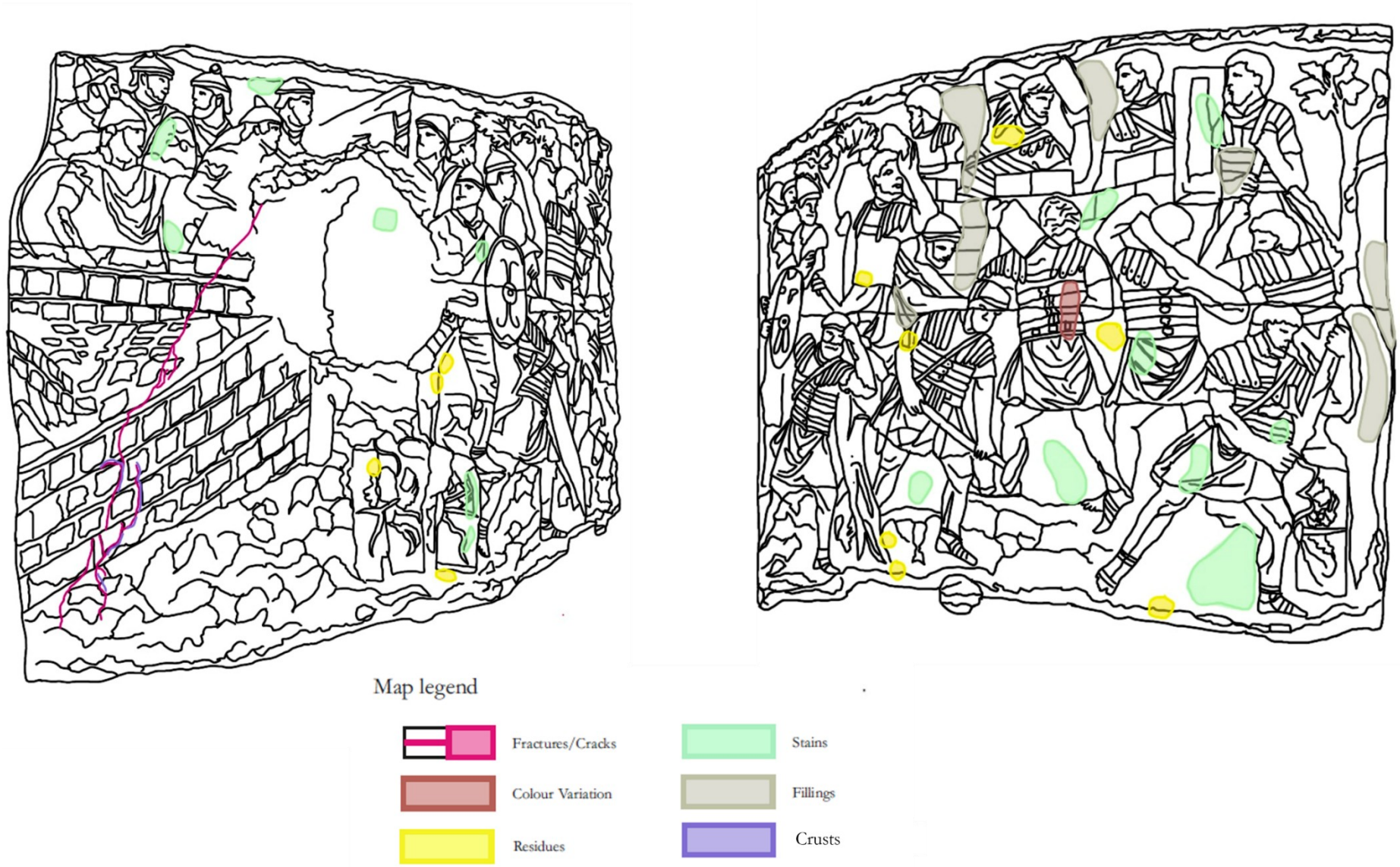

Supplementary materials – Figure 16: Degradation map of plaster cast MCR_3125, classified as *poor* in the 2012 survey. The map legend indicates the colours used to identify each degradation pattern.

4. Part 2: Conservation strategies for plaster replicas: insight into gypsum mixtures and protective coatings

This manuscript is currently in preparation for publication. FB, EB, CC and CM designed the study and developed the methodology. Hygrothermal ageing was carried out by FB, while light ageing was performed by FB and TDK at the University of Antwerp. XRF analyses were performed by EB in collaboration with Ca' Foscari University of Venice; XRPD analyses were conducted by FB in collaboration with Marco Favero; and FESEM analyses were carried out by FB in collaboration with Jacopo Nava. All these data were interpreted by FB. ER-FTIR analyses were conducted by FB and EB. Optical light profilometry and colourimetric measurements were performed by FB. All data from the above analyses were processed by FB. All authors discussed the results and agreed on their interpretation. FB wrote the manuscript, and all co-authors contributed to the final revision.

Federica Bubola[1*], Eleonora Balliana[2], Chiara Coletti[1], Tim De Kock[3], Claudio Mazzoli[1]

[1] Department of Geosciences, University of Padova, 1via Giovanni Gradenigo 6, 35131 Padova, Italy

[2] Department of Environmental Sciences, Informatic and Statistics, Ca' Foscari University, Via Torino 155, 30172 Mestre, Italy

[3] Department of Design Sciences, University of Antwerp, Mutsaardstraat 31, 2000 Antwerp, Belgium

---

Abstract

Plaster replicas of ancient sculptures, widely produced and collected in the 19th century for educational and documentary purposes, are particularly vulnerable to deterioration. The porous and hygroscopic nature of gypsum makes them highly sensitive to fluctuations in temperature and humidity, conditions commonly found in historical buildings lacking climate control systems. Protective coatings are therefore essential for mitigating degradation processes and ensuring the long-term stability of these artefacts. This research investigates historical gypsum mixtures and their interaction with environmental conditions, identifying key constituent materials and testing protective coatings. Mock-up samples were coated with finishes used in 19th century moulding processes and later restoration treatments to assess their protective effectiveness. The samples underwent accelerated ageing through sun-box exposure and controlled temperature and humidity cycles, simulating museum environments. Periodic monitoring included surface colour changes, roughness analysis via profilometry, and ER-FTIR for chemical characterization. This study aims to improve understanding of

material deterioration and to evaluate conservation methods for the long-term preservation of plaster casts.

4.1 Introduction

In the second half of the 19th century, plaster casts became widely used by museums and academic institutions to support the study and dissemination of artworks from different cultures and periods. As highlighted by Payne (2020) [1], they offered a practical and affordable solution for reproducing sculptures that were difficult to transport or preserve. Their ability to capture fine details made them ideal for educational and artistic purposes, while their wide availability enabled large-scale cast production [1]. This use responded to a growing interest in archaeology and antiquity, as well as the ambition to make ancient sculpture accessible to a wider audience.

However, the porous and hygroscopic nature of gypsum makes it particularly vulnerable to fluctuations in humidity and temperature, often resulting in both structural and aesthetic degradation [1,2]. Because of their educational value and the delicate nature of gypsum, protective coatings were introduced to prevent damage and help preserve the casts over time.

Gypsum ($CaSO_4 \cdot 2H_2O$) is a widely available and versatile material that has been employed since antiquity, and over time, various types of gypsum mixtures and processing techniques have been developed for specific functional and aesthetic requirements [1,3,4].

From a chemical and physical perspective, the mineralogical composition, microstructure, and behaviour of gypsum-based materials are strongly influenced by the calcination process and the temperature applied during production [5]. When heated, gypsum undergoes dehydration and recrystallisation, resulting in hemihydrate forms [6]. Two main types of hemihydrates are commonly obtained: β-hemihydrate, or Paris gypsum, produced by dry calcination, and α-hemihydrate, or alabaster gypsum, typically produced in humid conditions under pressure [7-9].

These two forms differ significantly in terms of porosity, mechanical properties, and suitability for specific uses. Paris gypsum, being more porous and less dense, is generally employed in building applications, temporary moulds, and low-detail casting. In contrast, alabaster gypsum exhibits lower porosity, better cohesion, and smoother workability, making it more suitable for artistic and detailed moulding processes, such as those used in the production of finer plaster casts [10,11].

When mixed with water, hemihydrate gypsum reacts exothermically to form calcium sulphate dihydrate, leading to a stable crystalline structure under controlled conditions [7]:

$$CaSO_4 \cdot ½H_2O + 1.5\ H_2O \rightarrow CaSO_4 \cdot 2H_2O + \sim 137\ kJ$$

Upon rehydration, both hemihydrate forms develop a crystalline network ensuring a stable structure under suitable and controlled conditions.

Over time, and especially in the 19th century, different plaster recipes were developed by adding materials like fibres, binders, or fillers (such as animal glue, marble powder, or kaolin) to enhance specific characteristics of the final product, such as setting time and texture [2,12-15]. These formulations were used to improve strength, surface quality, or workability, and played a crucial role in the production of cast collections. Many of these mixtures remain relevant today for conservation practices [3,4].

Marble powder, for instance, was widely added to give the mixture a more compact structure and achieve a bright white finish. Being chemically inert and extremely fine, it filled micro-voids within the plaster matrix, increasing density and long-term stability. Studies confirm that adding limestone or marble powder improves compressive strength by filling voids and enhancing cohesion [2]. Arabic gum, a natural resin mainly derived from *Acacia Senegal* and *Acacia Seyal*, was commonly employed as a plasticiser and binder. It improved the workability of the mixture and slowed down the setting time, ensuring better control during the reproduction of large or finely detailed elements [12]. However, its organic nature makes it susceptible to biological growth and degradation in humid environments. Similarly, animal glue was added to enhance cohesion and regulate the setting process [15], although it remains particularly vulnerable to high temperatures and moisture. Kaolin, a fine clay, was often incorporated to reduce shrinkage and enhance surface finish, although its water-absorption capacity could increase the mixture's sensitivity to moisture [16]. Finally, wood powder, sometimes used for textural purposes or as a lightweight filler, introduced additional organic content that could compromise long-term stability [17]. Due to the wide variability in historical mixtures and the lack of systematic documentation, the behaviour of 19th-century plaster casts under environmental stress is difficult to predict. Each object presents a unique combination of materials and physical conditions, which may react differently to the same conservation treatments or storage environments. This complexity underscores the importance of studying historical formulations under controlled conditions in order to assess their long-term behaviour and support the development of more effective conservation methods.

Most historical buildings, where these casts are collected, lack the environmental conditions necessary for proper conservation and require specific climate control systems based on the historic climates [18]. Environmental control is often limited or absent, and plaster objects remain exposed to significant microclimatic variations. Under these

conditions, degradation phenomena such as cracking, chromatic alterations, erosion, material pulverisation, and even fragmentation are frequently observed. In addition, previous restoration interventions and the use of different surface coatings have often introduced further variables, adding complexity to the conservation process [1].

In recent years, the conservation of gypsum-based artefacts has gained increasing attention within the field of heritage science. New approaches combine historical research with experimental analysis under controlled conditions to better understand degradation mechanisms and evaluate the effectiveness of protective coatings [19]. Artificial ageing procedures are used to accelerate natural ageing and observe material behaviour within a limited testing period.

The research presented in this thesis investigates the behaviour of historical gypsum mixtures and surface coatings through a multi-analytical study conducted on artificially aged mock-up samples. These mock-ups were prepared according to historical recipes using two types of gypsum (alabaster and Paris gypsum), combined with three additives: marble powder, Arabic gum, and a kaolin–wood powder mix. Each mixture was tested in its uncoated state and in combination with three surface treatments: polyvinyl alcohol (PVA), a modern acrylic resin (Acryl-EM 33), and kaolin.

Samples were subjected to two distinct artificial ageing processes. The first involved thermo-hygrometric cycles in a climate chamber designed to replicate the environmental conditions observed at the Museum of Roman Civilisation (Part 1), where a significant collection of plaster casts, such as the replicas of Trajan's Column, is preserved. The second process involved light ageing using a Solarbox equipped with a xenon lamp to simulate solar radiation indoors. These conditions were selected to reflect real exposure scenarios typically encountered by plaster casts in historical buildings. By subjecting mock-up samples to specific temperature, humidity and light conditions, it is possible to assess how different materials change over time [20]. This approach is particularly valuable for identifying which combinations of additives and coatings offer the best protection against environmental stressors.

To monitor the effects of ageing, External Reflection FTIR spectroscopy (ER-FTIR) was used to investigate chemical changes in the matrix and coatings. Surface roughness was analysed with 3D optical profilometry. Colour variations were recorded through spectrophotometric analysis in the CIELab* colour space, following standardised protocols. Mineralogical and microstructural characteristics were further evaluated through X-ray Powder Diffraction (XRPD) and Scanning Electron Microscopy (SEM) before ageing. This

research aims to provide new insight into the interaction between gypsum-based materials and environmental factors, and to identify which material combinations and treatments offer greater stability over time. The results can support more effective conservation strategies, especially for gypsum-based casts with complex composition.

4.2 Materials

To assess the response of the material to its surrounding environment, six types of gypsum mixtures were prepared based on materials and technologies mentioned in recipe books [3,4]. These mixtures included alabaster gypsum (A) and Paris gypsum (P), both combined with various additives, such as marble powder (M, Bianco Zandobbio, a fine dolomitic marble powder originating from the quarries of Zandobbio in the Val Cavallina district, northern Italy), Arabic gum (AG), and a mixture of kaolin and wood powder (KW) (Table 9). The preparation of the mock-ups was guided by the observations and analytical data obtained from the casts of Trajan's Column presented in Part 1. Although historical accounts describe different phases of the 19th century campaigns, the available archival sources provide only limited information on the technical aspects of the mixture used. For this reason, the formulations adopted in this study were developed by combining historical casting manuals with the mineralogical evidence obtained through XRPD on the casts. These analyses consistently revealed the presence of alabaster gypsum together with minor components, in line with mixtures commonly described in the recipes. The mock-ups were therefore prepared using alabaster and Paris gypsum, together with additives that reflect the materials either identified on the casts or documented for similar historical moulding practices, with the aim not only of reflecting as closely as possible the materials identified in the casts of Trajan's Column, but also of extending the investigation to a broader range of gypsum formulations commonly found in 19th century cast collections.

Alabaster gypsum is a calcined form obtained by firing ground gypsum dihydrate ($CaSO_4 \cdot 2H_2O$). Due to its fine texture and workability, it is widely used for making moulds, plastering and ceramic restoration. The preparation involves gradual mixing of plaster with water until a homogeneous, aggregate-free mixture is obtained. Paris gypsum, a hemihydrate of calcium sulphate ($CaSO_4 \cdot \frac{1}{2}H_2O$), is known for its high purity and fine grinding, making it suitable for artistic moulding and casting applications [4].

The workability of the gypsum was optimised by gradually adding it to water to prevent the formation of aggregates. The mixture was left to stand to ensure uniform wetting and air

release, and was then stirred until a uniform consistent texture was achieved. The optimal water temperature for mixing ranged from 16 °C to 22 °C [4].

In addition to gypsum, specific additives were incorporated. Traditional recipes suggest the use of liquid animal glue, which remains in a liquid state at room temperature without requiring continuous heating [2]. For this reason, a diluted solution of animal glue was added to each mixture to ensure a slow-setting composition and facilitate better manipulation before complete hardening.

Table 9. Materials used in the preparation of the samples.

Gypsum	Glue	Additives	Coatings
Alabaster gypsum	Animal glue	Marble powder (Bianco Zandobbio)	Kaolin
Paris gypsum		Arabic gum	PVA
		Kaolin	Acryl-EM 33
		Wood powder	

The preparation of the samples required multiple preliminary tests to refine the formulations and adapt them to the specific characteristics of the materials used. One of the main challenges was determining the correct water-to-gypsum ratio. Excessive water led to cracking and structural weaknesses, while insufficient water compromised workability and uniformity. The compositions were adjusted based on the appropriate quantity of water, which allowed for proper handling (Table 10) and will be described in detail below.

Table 10. Proportions of components (in parts) used for creating the mixtures.

Mixture	Gypsum (parts)	Demineralised Water (parts)	Animal glue (parts)	Marble powder (parts)	Kaolin (parts)	Wood powder (parts)	Arabic gum (parts)
1	50	28	15	-	25	1	-
2	100	30	30	25	-	-	-
3	1000	500	20	-	-	-	20

Variations in the absorption properties of the additives, particularly Arabic gum and kaolin, influenced the setting process, requiring adjustments to the based proportions. The initial formulations resulted in inconsistent textures, requiring repeated adjustments to stabilise the mixtures and improve their mechanical performance. Through successive trials, the water content was carefully regulated to strike a balance between workability and structural integrity. The final formulations ensured that the samples remained free of cracks while maintaining the necessary cohesion for subsequent analyses. These refinements were essential to guarantee reproducibility and comparability across all test specimens.

The animal glue was prepared at a 1:15 ratio (10 g of glue in 150 g of water), allowing it to swell before being heated to a maximum temperature of 90° C.

The specific formulations varied depending on the type of gypsum and additives used. Three different formulations were prepared, each tested using both Paris gypsum (P) and alabaster gypsum (A) as the base binder. These mixtures, referred to as M1, M2, and M3, differ in the type of additive incorporated, while the binder-additive rations were maintained across both gypsum types.

- **Mixture M1:** gypsum + animal glue+ kaolin + wood powder
    - **P_M1:** 365 g Paris gypsum, 190 g animal glue, 270 g kaolin, 4.5 g wood powder, 385 g water;
    - **A_M1:** same dry components, with 360 g water;
    - Each mixture yielded 7 moulds.
- **Mixture M2:** gypsum + animal glue+ marble powder
    - **P_M2:** 720 g Paris gypsum, 240 g animal glue, 270 g kaolin, 340 g marble powder, 170 g water;
    - **A_M2:** same dry components, with 125 g water;
    - Each mixture yielded 6 moulds.
- **Mixture M3:** gypsum + animal glue+ Arabic gum
    - **P_M3:** 1140 g Paris gypsum, 32 g animal glue, 32 g Arabic gum, 730 g water;
    - **A_M3:** same dry components, with 700 g water;
    - Each mixture yielded 10 moulds.

Arabic gum was dissolved prior to addition using a 1:3 ratio (e.g., 10 g gum in 30 g water).

These precise measurements were essential to achieve consistent and reproducible results across all experimental samples.

The selected coatings included materials that have historically been used as protective layers and modern conservation products. The coatings consisted of:

- a 5% kaolin-water solution (K)
- a 5% polyvinyl alcohol (PVA) solution, prepared by dissolving PVA powder in water with constant stirring
- a 10% Acryl-EM 33 (Ac) solution

The selection of these coatings was guided by both historical evidence and the analytical results from Part 1. Kaolin-based finishes were chosen because thin clay films were identified

on the casts in Room LI, consistent with 19th century moulding practices. PVA was included because traces were detected on the casts, suggesting its use during past restoration campaign. Acryl-EM 33, although more recent, represents a widely employed conservation product and was selected to provide a comparative reference between traditional and modern surface treatments.

A total of 24 distinct sample types were prepared, each measuring 5×5×5 cm, resulting in 72 specimens. Four replicas were created for each sample, with one left untreated and the others coated with different treatments. Of these, 48 specimens (two replicas per type) were subjected to hygrothermal ageing in a climate chamber, while the remaining 24 (one replica per type) underwent artificial light ageing. Periodic analyses were conducted to monitor and assess the chemical and morphological variations induced by environmental stressors.

The prepared gypsum samples were categorised based on the type of gypsum used (alabaster gypsum or Paris gypsum), the additives incorporated (marble powder, Arabic gum, or a kaolin-wood powder mix), and the surface coatings applied (kaolin, Acryl-EM 33, or PVA). Table 11 presents the acronyms assigned to each sample, along with the corresponding materials used in their preparation.

Table 11. Acronyms and composition of the samples.

Sample (acronym)	Gypsum	Additives	Coatings
A_M	Alabaster	Marble powder	-
A_M_K	Alabaster	Marble powder	Kaolin (K)
A_M_Ac	Alabaster	Marble powder	Acryl-EM 33
A_M_PVA	Alabaster	Marble powder	PVA
P_M	Paris	Marble powder	-
P_M_K	Paris	Marble powder	Kaolin
P_M_Ac	Paris	Marble powder	Acryl-EM 33
P_M_PVA	Paris	Marble powder	PVA
A_AG	Alabaster	Arabic Gum	-
A_AG_K	Alabaster	Arabic Gum	Kaolin
A_AG_Ac	Alabaster	Arabic Gum	Acryl-EM 33
A_AG_PVA	Alabaster	Arabic Gum	PVA
P_AG	Paris	Arabic Gum	-
P_AG_K	Paris	Arabic Gum	Kaolin
P_AG_Ac	Paris	Arabic Gum	Acryl-EM 33
P_AG_PVA	Paris	Arabic Gum	PVA
A_KW	Alabaster	Kaolin / Wood powder	-
A_KW_K	Alabaster	Kaolin / Wood powder	Kaolin
A_KW_Ac	Alabaster	Kaolin / Wood powder	Acryl-EM 33
A_KW_PVA	Alabaster	Kaolin / Wood powder	PVA
P_KW	Paris	Kaolin / Wood powder	-
P_KW_K	Paris	Kaolin / Wood powder	Kaolin
P_KW_Ac	Paris	Kaolin / Wood powder	Acryl-EM 33
P_KW_PVA	Paris	Kaolin / Wood powder	PVA

Legend:

A: Alabaster gypsum
P: Paris gypsum
M: Marble powder
AG: Arabic gum
KW: Kaolin and wood powder
K: Kaolin
Ac: Acryl-EM 33
PVA: Polyvinyl alcohol

This classification ensures clarity in analysing the effects of different additives and coatings on the material properties.

4.2.1 Technical specifications of raw materials

To better characterise the commercial materials employed in the preparation of the mock-ups, the specifications provided by the manufacturers were examined. The data offered useful reference information when interpreting the XRF results and identifying the origin of minor elemental components (Table 12).

Table 12. Commercial raw materials employed in the preparation of the gypsum mixtures, with indication of brand and specifications derived from manufacturer technical sheets.

Product	Brand	Specifications
Alabaster gypsum	Axton®	Calcinated calcium sulphate dihydrate with high whiteness and fine granulometry. Although detailed chemical composition is not provided by the manufacturer, the product is intended for decorative moulting and includes naturally occurring mineral impurities typically associated with gypsum deposits.
Paris gypsum	Weber® - Saint Gobain	The *plâtre fin de Paris* consists mainly of calcium sulphate hemihydrate obtained through calcination. As reported for similar commercial products, minor silicate impurities may be present due to the geological provenance of the raw material.
Marble powder (Bianco Zandobbio)	Valli Granulati®	The material is predominantly composed of calcite ($CaCO_3$ 55.61 %) and dolomite ($MgCO_3$ 44.20 %), with very low levels of silica (SiO_2 0.12 %) and iron oxides (Fe_2O_3 0.0016 %).
Kaolin	ANTA.RES®	The white micronised kaolin is characterised by a high content of aluminosilicates, with $SiO_2 \approx 49$ %, $Al_2O_3 \approx$ 36.5 %, and minor quantities of Fe_2O_3 /0.5 %), TiO_2 (0.15 %) and CaO (0.1 %).
Wood powder	Hendi®	The beech smoking dust consists of fine lignocellulosic particles derived from natural beech wood.
Animal glue	ANTA.RES®	Rabbit-skin glue consists of proteinaceous collagen extracts, essentially inorganic-free apart from traces of mineral salts.
Polyvinyl alcohol (PVA)	ANTA.RES®	The PVA is supplied as a partially hydrolysed polymer without any relevant inorganic content.
Acryl-EM 33	ANTA.RES®	The acrylic dispersion contains 45-47 % of acrylic copolymer and does not include inorganic fillers according to the technical specifications.

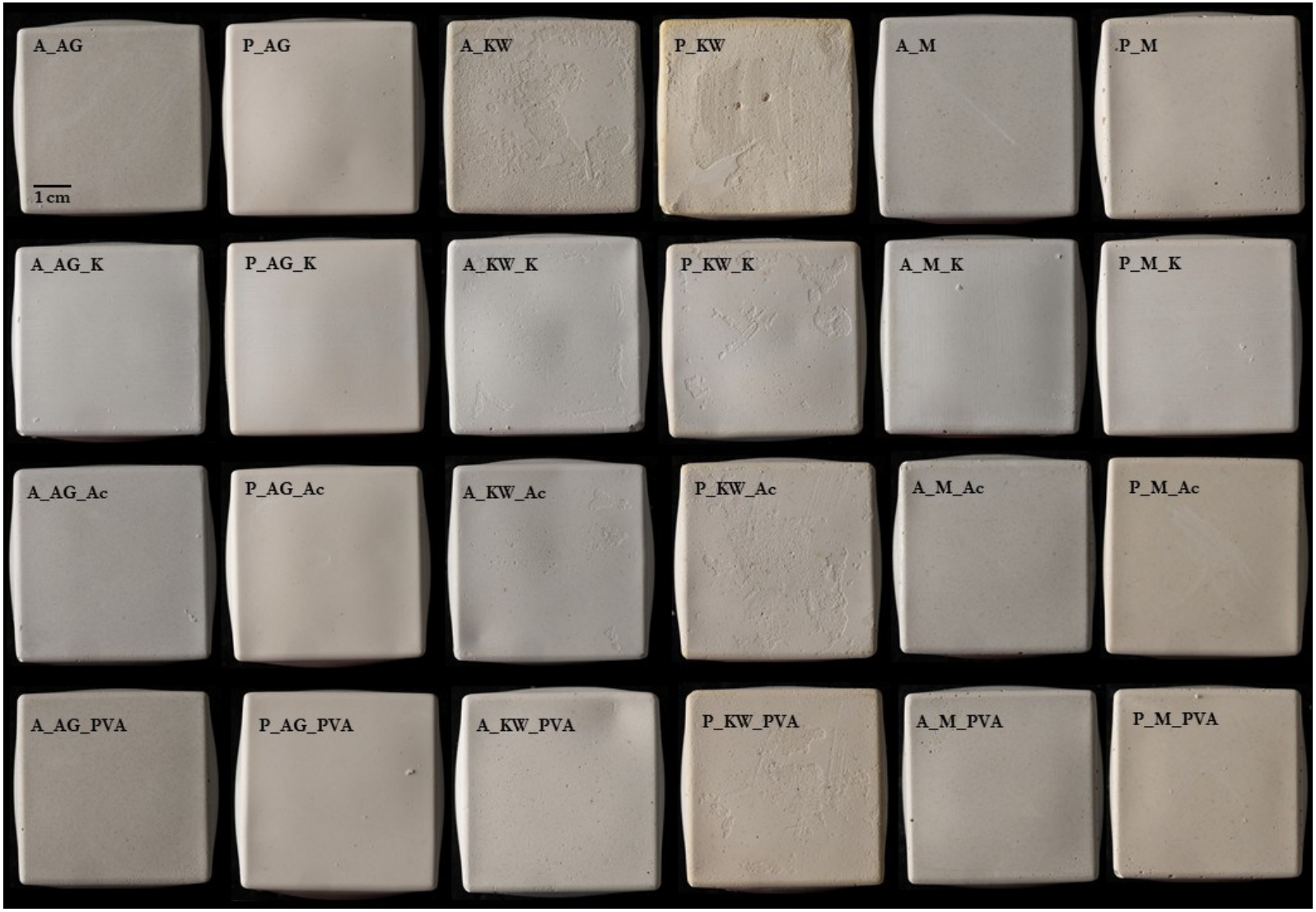

Figure 25. Visual comparison of gypsum-based samples before ageing. The samples are arranged by additive type and coating treatment. Each column represents a different formulation: A (alabaster gypsum) or P (Paris gypsum) combined with AG (Arabic gum), KW (kaolin + wood powder), or M (marble powder); while each row shows untreated, kaolin-treated, acrylic treated and PVA-treated specimens. All samples measure 5x5x5 cm. Scale: 1 cm.

4.3 Methods

4.3.1 Analytical techniques

The selected gypsum samples were analysed through a comprehensive characterisation, including X-Ray Powder Diffraction (XRPD), Field Emission Scanning Electron Microscopy (FESEM), and X-Ray Fluorescence (XRF). Additionally, optical light profilometry, colourimetric measurements, and External Reflection FTIR (ER-FTIR) spectroscopy were performed at different ageing intervals, starting from t_0 and periodically after each ageing cycle, to monitor any chemical and morphological changes over time. Each sample underwent three ageing cycles under a single ageing protocol, either in the climatic chamber or under light exposure. The two protocols were applied to separate sets of samples.

Table 13 presents the analytical techniques employed to characterise the materials at different stages. In this study, t_0 always indicates the condition of the samples before any artificial ageing. For cyclic ageing the timepoints t_1, t_2, an t_3 in optical profilometry and ER-FTIR refer to the end of each individual ageing cycle, while colourimetric measurements were only taken at t_0 and t_3, corresponding respectively to the initial condition and the end of the last cycle. In the case of light ageing, colourimetric data were collected at t_0, t_1, t_2 and t_3, reflecting the end of each phase. However, for both profilometry and ER-FTIR under light ageing, only two timepoints were considered: t_0, before the beginning of the exposure, and t_3, at the end of the complete ageing process.

Table 13. Overview of the ageing protocols, analytical techniques and acquisition times used in the study.

Ageing protocol	Analytical technique	Acquisition time
Cycle ageing	Optical light profilometry	t_0, t_1, t_2, t_3
	ER-FTIR	t_0, t_1, t_2, t_3
	Colourimetric measurements	t_0, t_3
Light ageing	Optical light profilometry	t_0, t_3
	ER-FTIR	t_0, t_3
	Colourimetric measurements	t_0, t_1, t_2, t_3

The following description outlines the applied methods and specifies the number of specimens tested for each gypsum formulation in the technical analyses.

Mineralogical analyses by XRPD were conducted using a PANalytical X'Pert PRO diffractometer operating in Bragg-Brentano reflection geometry with CoKα radiation, 40 kV voltage, and 40 mA filament current, and equipped with an X'Celerator detector. Qualitative diffraction data analysis was performed using X'Pert HighScore Plus® software (PANalytical) in combination with the PDF-2 database.

The mineralogy and morphology of the samples were further examined using a FESEM Tescan Solaris. Microchemical analysis of the mineral phases, as observed under FESEM

was performed with an Oxford Instrument Ultim Max 65 Silicon drift detector (EDS) operating at 15 keV, 3 nA, and a working distance of 5 mm. Backscattered electron (BSE) imaging was carried out at enhanced resolution, using a lower voltage and current setting (5 keV, 300 pA) at a working distance of 4 mm.

Elemental analyses by XRF were performed using a Minipal PW4025/00 spectrometer (Philips Analytical, Almelo, Netherlands) at 20 kV and 70 μA. Analyses were carried out in open air, with a Kapton filter employed. XRF analyses were performed in semiquantitative mode, which allows the detections of elements with atomic number > 11 (Na). The technique is particularly suitable for identifying minor and trace inorganic components within commercial gypsum preparations and additives, complementing the information provided by the manufacturer's technical sheets.

A Bruker Alpha FTIR spectrometer, equipped with an external reflection module (20°/20° geometry) and a coaxial visual camera, was used for chemical analysis. The instrument was calibrated weekly with a polystyrene film at room temperature. Prior to each scan, a 3-minute background recording was performed using a gold coated mirror to correct each spectrum for atmospheric absorption during the scan. ER-FTIR spectra were recorded over a range from 7500 to 400 cm^{-1}, with a resolution of 4 cm^{-1} and an acquisition time of 3 min. The acquisition and processing of the spectra were managed using a Bruker OPUS 6.0 software package, and then further processed with OriginPRO 2018b.

For surface topography analysis, a NANOVEA Jr-25 non-contact 3D profilometer was used. This equipment enables the study of surface topography with submicrometric precision, graphically represented using False Colour Height maps, 3D profiles, and surface changes according to the standard normative ISO 25178 (Geometrical Product Specifications – Surface Texture). The arithmetical mean height (Sa) and root mean square height (Sq) were considered for the evaluation of surface texture.

A Konica-Minolta CM-700d spectrophotometer equipped with a pulsed xenon lamps and diffuse reflectance geometry was used to record reflectance spectra, collected in the wavelength range from 360 to 740 nm with s resolution of 20 nm. The measurements were taken using a D65 standard illuminant, 10° observer, and SCI mode with an 8 mm measurement area. Five measurements were performed per sample, and the colour difference (ΔE^*) was calculated according to the CIELab 1976 system, and the L^* (lightness, from 0 to 100), a^*, related to the red – green component, and b^*, related to the yellow – blue component, (chromatism, from -60 to +60) parameters were calculated, following the UNI-EN 15886 (2010) standard [21,22]:

$$\Delta E^* = \sqrt{(L_1^* - L_2^*)^2 + (a_1^* - a_2^*)^2 + (b_1^* - b_2^*)^2}$$

where L^*_1, a^*_1 and b^*_1 are the parameters at t_0, while L^*_2, a^*_2 and b^*_2 are the parameters after each ageing cycle. For each sample, 5 measurements were carried out.

4.3.2 Accelerated ageing

The accelerated ageing protocols were developed based on of empirical observations collected from gypsum casts displayed in uncontrolled museum conditions (see Part 1). The degradation phenomena identified, such as abrasion, pulverisation, and material leaching, were attributed to prolonged exposure to unsuitable hygrothermal conditions and served as reference for simulating comparable deterioration in the laboratory. The environmental cycles applied to the mock-ups aimed to reproduce the microclimatic fluctuations recorded at the Museum of Roman Civilisation, using controlled temperature-humidity changes and light exposure to test the long-term stability of different formulations.

An FDM Series C Environmental chamber, capable of controlling temperature and relative humidity, was employed to subject 48 samples to controlled ageing. The environmental chamber operates within a temperature range of -25 °C to +70 °C, and a humidity range of 10 % to 98 %. The ageing process comprised 150 cycles of 12 hours each, simulating the extreme environmental fluctuations corresponding to roughly 150 years of natural exposure. Each cycle consisted of 6 hours at a temperature (T) of 30 °C and relative humidity (RH %) of 30 %, representing summer conditions, followed by 6 hours at T of 10 °C and a RH of 90 %, representing winter conditions (see Part 1) Additionally, an extra hour was allocated for each parameter transition to allow the system to reach the designed temperature and humidity levels gradually. As a result, each cycle lasted 14 hours instead of 12, leading to a total ageing duration of approximately 87 days and 12 hours (Figure 26). Samples were analysed at different stages: before the ageing process began (t_0) and subsequently after every 50 (t_1), 100 (t_2), and 150 (t_3) cycles.

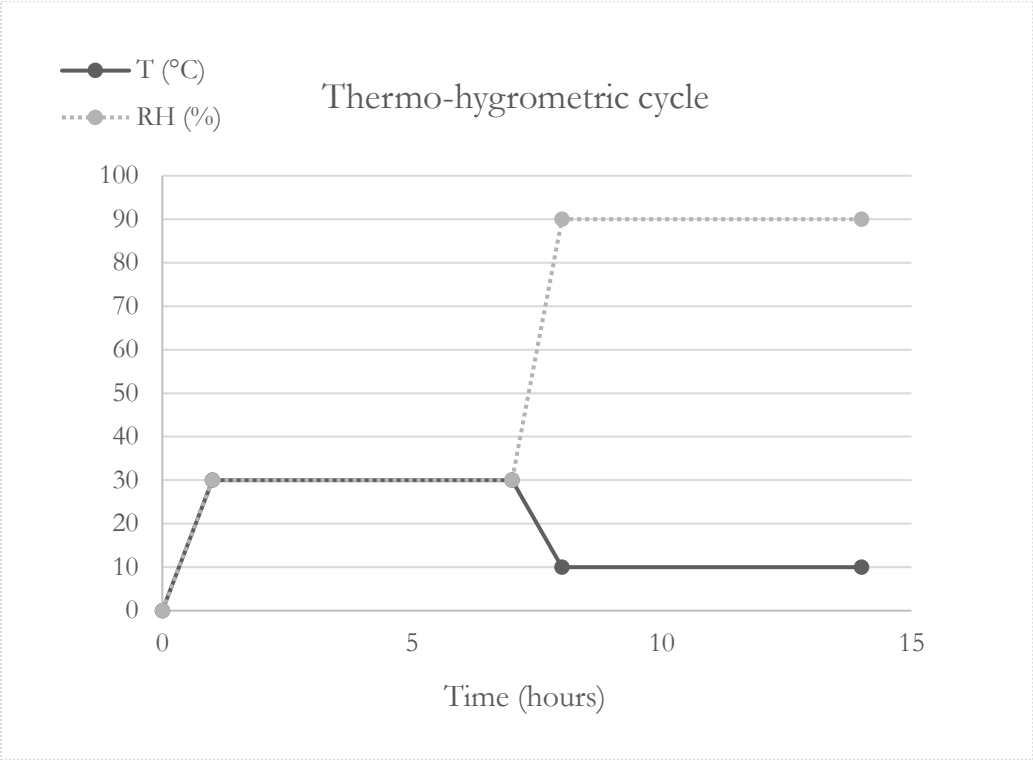

Figure 26. Thermo-hygrometric cycle used for artificial ageing in the climate chamber. The cycle simulates alternating seasonal conditions, consisting of 6 hours at 30 °C and 30 % RH (summer), followed by 6 hours at 10 °C and 90 % RH (winter). An additional 2 hours were included for the gradual transition between the two phases, resulting in a total cycle duration of 14 hours.

One set of 24 samples, each corresponding to a distinct material formulation, was exposed to artificial solar radiation using a Solarbox 1500, equipped with a 1500-W xenon-arc lamp to simulate the solar spectrum, leaving out wet cycles to simulate an indoor environment. Ageing was carried out for a total of 1512 hours (three cycles of 504 hours each), under an irradiance of 550 W/m² and a Black Standard Temperature (BST) of 65 °C. The samples were monitored at the end of each cycle.

The following table summarizes the conditions for both the cycle ageing and light ageing processes applied to the gypsum samples (Table 14). These processes were designed to simulate long-term degradation caused by environmental factors including humidity, temperature variations, and solar radiation exposure.

Table 14. Comparison of cycle ageing and light ageing conditions, outlining the specific environmental parameters and total duration of each process.

Condition	Ageing process	Total duration
Cycle ageing	150 thermo-hygrometric cycles, each lasting 14 hours, simulating 150 years of natural ageing: · 6 hours at 30 °C and 30 % RH (summer conditions; · 6 hours at 10 °C and 90 % RH (winter conditions); · 2 hours for parameter transition, to allow the system to reach the designated T and RH levels gradually.	87 days and 12 hours, including an extra hour per cycle for transition between temperature and humidity parameters.
Light ageing	Exposure to artificial solar radiation using a Solarbox 1500 with a 1500 W xenon-arc lamp and indoor filter, leaving out wet cycle to simulate the indoor environment. Irradiance of 550 W/m² with a Black Standard Temperature (BST) of 65 °C.	1512 hours, divided into three cycles of 504 hours each.

All samples were analysed to assess potential chemical, morphological, and colourimetric variations induced by the ageing processes. Chemical composition was evaluated using FTIR spectroscopy, while surface morphology was characterized with a 3D non-contact profilometer. Colourimetric variations were measured according to standardised protocols [21]. These complementary analytical techniques provided a comprehensive evaluation of the samples' responses to the simulated ageing conditions.

4.4 Results

4.4.1 Chemical and mineralogical characterisation

The chemical composition of the mock-up formulations was determined by X-ray fluorescence (XRF). The results, summarised in Table 15, show the presence of calcium- and sulphate-based compounds in all specimens, consistent with the gypsum-based nature of the matrix. The most abundant oxides detected in each sample are CaO, SO_3 and SiO_2.

Table 15. Chemical composition of major elements expressed in wt % of oxides for the mock-up formulations.

Compound	A_AG	A_M	A_KW	P_AG	P_M	P_KW
Al_2O_3	2.04	5.79	2.17	2.14	5.36	2.04
SiO_2	21.68	28.49	22.56	22.08	32.01	21.99
Fe_2O_3	0.10	0.43	0.09	0.08	0.34	0.04
MgO	0.51	0.26	0.59	0.63	0.61	0.65
K_2O	0.11	0.09	0.07	0.05	0.04	0.01
CaO	53.08	52.49	55.69	53.08	51.08	54.98
SO_3	22.48	12.45	18.83	21.94	10.57	20.29

The mineralogical composition of the mock-up samples was investigated by X-ray powder diffraction (XRPD), to identify crystalline phases and assess potential variations associated with the type of gypsum and the presence of additives. The results are summarised in Table 16.

Table 16. Mineralogical characterisation of all the formulations according to XRPD data. Mineral abbreviation from Warr (2021) [23]: *Gp* = gypsum; *Bss* = bassanite; *Anh* = anhydrite; *Dol* = dolomite; *Cal* = calcite; *Kln* = kaolinite; *Qz* = quartz; *Clt* = celestine. * = present; - = absent.

Sample	Gp	Bss	Anh	Dol	Cal	Kln	Qz	Clt
A_AG	*	*	*	*	*	-	-	*
A_M	*	*	*	*	-	-	-	*
A_KW	*	*	*	*	*	*	*	*
P_AG	*	*	-	-	-	-	-	-
P_M	*	*	-	*	-	-	*	-
P_KW	*	*	*	-	*	*	*	-

All samples showed gypsum as the main crystalline phase. Bassanite is also present in every sample, and anhydrite was detected in most cases. Additional phases varied depending on the formulation. Dolomite was observed in A_AG, A_M, A_KW and P_M, consistent with the dolomitic nature of the marble powder and with minor impurities in the alabaster gypsum. Calcite was identified in A_AG, A_KW and P_KW, indicating its occurrence in both alabaster gypsum and in kaolin-containing formulations, but it was not detected in the marble powder samples. Quartz was observed in kaolin-wood samples (A_KW, P_KW), reflecting the siliceous fraction of the additive. Celestine was consistently detected in alabaster gypsum formulations, but was absent in those made with Paris gypsum. Since the

analyses were carried out before artificial ageing, the occurrence of these additional phases should be interpreted as mineral impurities naturally present in the commercial gypsum and additives employed. In particular, the relatively high silica content is accounted for by quartz and kaolinite, reflecting the composition of the raw materials.

The microstructural characteristics of the samples were examined by Scanning Electron Microscopy (SEM) in backscattered electron mode (BSE).

Figure 27 shows the microstructure of sample P_M (Paris gypsum with marble powder) at 327 x magnification. The matrix resulted porous and heterogeneous, with visible carbonate inclusions surrounded by voids. Two distinct inclusions are enlarged in Figure 27 B, where dimensional measurements are provided: the upper inclusion measures approximately 764.00 µm in height (segment 1–2) and 548.20 µm in width (segment 3–4), while the lower one is 433.70 µm in height (segment 5–6) and 450.00 µm in width (segment 7–8). The gypsum matrix surrounding these inclusions displays irregular boundaries with gaps at the interface.

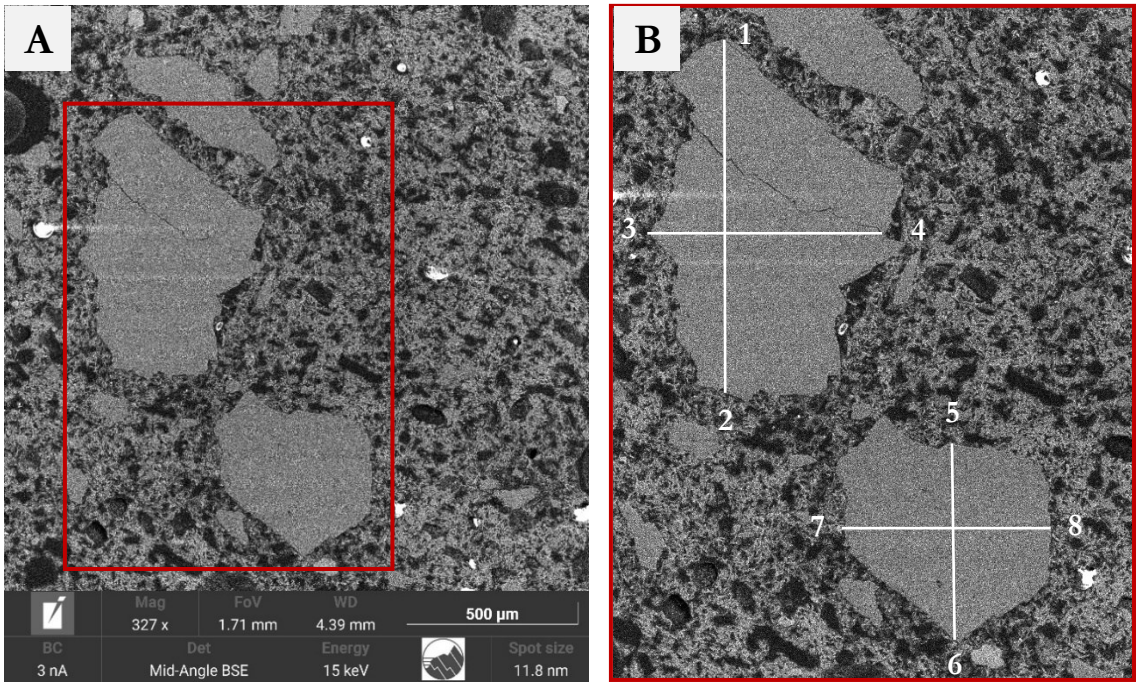

Figure 27. FESEM-BSE images: (A) Sample P_M at 327 x magnification. The overview shows two carbonates' inclusions within a porous gypsum matrix. The red rectangle indicates the area enlarged in (B); (B) Sample P_M, detail of image with dimensional measurements of the calcite grains. White lines represent maximum height and width: (1-2) and (3-4) for the upper inclusion, (5-6) and (7-8) for the lower one.

In sample A_KW (alabaster gypsum with kaolin and wood powder), the matrix resulted denser. Figure 28 A shows wood fibres and kaolin particles dispersed within the gypsum matrix. The wood inclusions are fibrous and elongated, ranging in height from approximately 20 to 70 µm in height and up to 500 µm. Kaolin particles appear as flat, plate-like structures

measuring about 2–5 µm. Figure 28 B provides a detailed view of the wood fibres, which exhibit a porous internal morphology with longitudinal channels. Small gaps are present at the interface between the inclusions and the surrounding matrix.

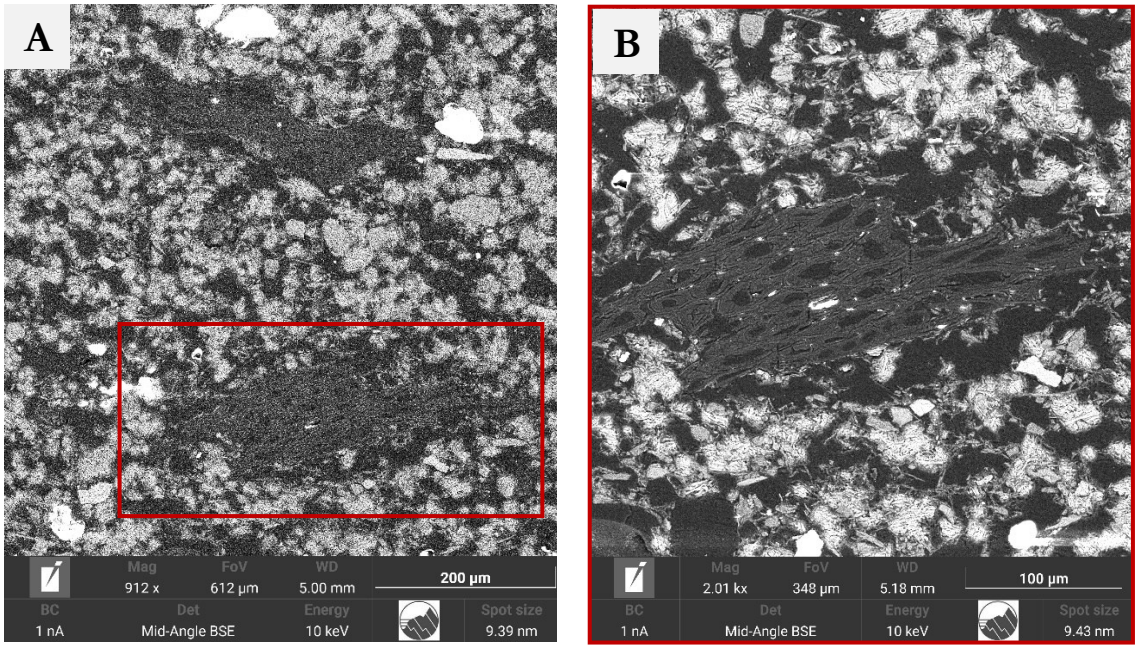

Figure 28. FESEM-BSE images: (A) Sample A_KW at 912 x magnification. The overview highlights the composite structure of the matrix, showing dispersed wood fibres within the gypsum framework. The red rectangle indicates the region enlarged in (B), where the internal structure of the wood inclusion is further detailed. (B) Higher magnification of the selected area (2.01 kx). The elongated fibre exhibits a porous internal morphology.

4.4.2 Hygrothermal ageing

4.4.2.1 Macroscopic evaluation after ageing

After artificial ageing, the surface condition of the mock-up samples was assessed through visual inspection. Representative photographs were taken under consistent lighting conditions, using a fixed camera setup and a 2 cm scale reference for comparison (Figure 29). The samples in Figure 29 are examples selected to illustrate the most recurring types of surface alterations observed across the different formulations.

The samples exhibited a range of macroscopic changes, including rounding edges, pulverisation, detachment of outer layers, and general loss of cohesion. Several recurring patterns were identified:

- Samples based on alabaster gypsum frequently exhibited mechanical damage at the edges and corners, especially in the absence of surface coatings or when treated with kaolin. In these cases, visible fractures and material losses were concentrated along the margins;

- Paris gypsum-based samples showed more evident surface-level degradation, such as powdering, while edge deterioration was less frequently observed;
- Formulations containing kaolin and wood powder, particularly without coatings, showed an irregular surface and pulverisation;
- Several uncoated samples showed more severe surface erosion, including superficial material loss;
- Samples treated with PVA or acrylic resin generally preserved smoother and more cohesive surface. However, some differences were observed depending on the formulation. In particular, the PVA-coated samples containing kaolin and wood powder (KW) showed more advanced surface alteration than the PVA-coated samples containing Arabic gum (AG).

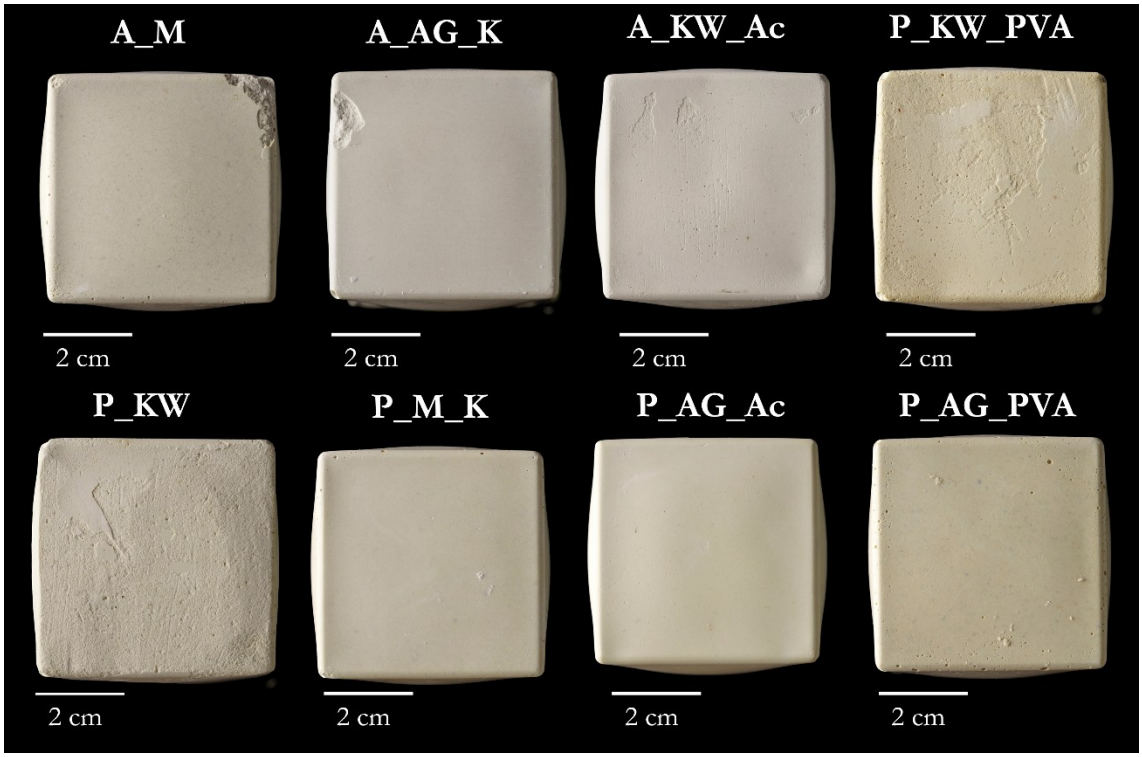

Figure 29. Visual comparison of some gypsum-based samples after ageing. The image shows differences in surface condition across various formulations, highlighting the combined effects of gypsum type, additives, and protective coatings.

4.4.2.2 FTIR spectroscopy

FTIR spectroscopy was employed to investigate the chemical evolution of mock-up samples before and after hygrothermal ageing, conducted under controlled conditions of temperature and relative humidity. The analysis aimed to assess the chemical stability of the

materials and their interaction with the environmental conditions simulated during the ageing cycles.

In all spectra, the characteristic bands of gypsum were clearly identified, confirming its presence as the main constituent across all samples. These included the O-H stretching vibrations of non-bonding water at 3548 and 3407 cm^{-1}, the sulphate stretching bands at 1110 and 670 cm^{-1}, and the SO_4^{2-} bending vibrations at 605 and 470 cm^{-1} [24-32]. These signals remained detectable after ageing.

A summary of the main characteristic peaks associated with each material, whether used as an additive or as a surface coating, is provided below to support the interpretation of the FTIR spectra (Table 17).

Table 17. Characteristic wavenumbers (cm^{-1}) and associated vibrational assignments identified in the ER-FTIR spectra of the materials used as additives and coatings in the mock-up samples. The table reports the main functional groups or lattice vibrations observed for Arabic gum, kaolin, PVA, Acrylic resin, and marble powder.

Material	Wavenumber (cm^{-1}) and Vibration Assignment
Animal glue	1632 (ν C=O Amide I)
Arabic Gum	1660 (ν C=C), 1621 (δ OH)
Kaolin as additive/coating	3690, 3670, 3645 (ν OH), 1065, 1010 (ν Si-O-Si), 940, 912 (δ Al-OH), 796, 793 (Si-O-Al and Al-O), 570, 470, 430 (lattice vibrations involving Al-O and Si-O-Al bonds)
PVA	2980, 2976, 2940, 2860, 2850 (ν CH), 1780, 1700 (residual acetate groups), 950-850 (ν C-O combined with skeletal vibrations of the polymer backbone)
Acrylic resin	3000, 2965, 2870, 2850 (ν CH aliphatic chains), 1716, 1710 (ν C=O carbonyl group of acrylic esters), 1450, 1430, 1380 (δ CH), 1150, 1050 (ν CO of ester groups)
Marble powder	3534, 3407 (ν OH), 1790 (ν CO_3^{2-} overtone), 1450, 1400 (ν CO_3^{2-})

Samples containing Arabic gum (AG) showed distinct organic signals at 1660 cm^{-1} (C=C stretching) and 1621 cm^{-1} (O-H bending), which remained visible after ageing [33].

Samples with marble powder exhibited the characteristic carbonate signals at 1790, 1450, 1400 cm^{-1}, together with broad bands at 3534, 3407 cm^{-1}. The latter are attributable to O-H stretching vibrations, likely related to adsorbed water or moisture associated with the carbonate filler. These features remained stable after ageing.

Before ageing, the spectra of samples containing kaolin and wood powder displayed clear kaolin signals, including intense O-H stretching at 3690, 3670, and 3645 cm^{-1}, Si-O-Si bands at 1065 and 1010 cm^{-1}, and Al-O and OH bending modes between 940 and 430 cm^{-1} [34]. After ageing, many of these bands were either significantly reduced or completely absent.

The PVA-coated samples (PVA) showed the characteristic C-H stretching bands (2980 – 2850 cm^{-1}) and signals attributed to residual acetate groups (1780 and 1700 cm^{-1}) both before and after ageing, as visible in the spectra reported in the discussion (Section 4.5.2.1). Similarly, samples coated with acrylic resin displayed the typical markers of acrylate-based polymers, including aliphatic C-H stretches (3000-2850 cm^{-1}), strong carbonyl absorptions of the ester groups at 1716 and 1710 cm^{-1}, CH bending modes at 1450, 1430, and 1380 cm^{-1}, and C-O stretching vibrations at 1150 and 1050 cm^{-1}.

Regarding the samples coated with kaolin, the characteristic peaks detectable before ageing, had almost entirely disappeared after ageing.

4.4.2.3 Optical light profilometry

The surface roughness analysis was assessed on all samples using Sq (root mean square height) and Sa (arithmetical mean height) parameters. The measurements were collected at four ageing stages (t_0-t_3) to monitor surface evolution under controlled environmental conditions.

Across the dataset, samples based on plaster of Paris generally showed higher Sq and Sa values with respect to alabaster gypsum samples. For example, the uncoated sample P_M recorded Sq values ranging from 9.11 μm at t_0 to 36.13 μm at t_3, and Sa values from 7.08 μm to 29.38 μm (Table 18). In contrast, A_KW exhibited Sq values between 14.09 μm at t_0 and 15.48 μm at t_3 and Sa values between 11.70 μm at t_0 and 10.88 μm at t_3.

Samples treated with PVA displayed lower roughness values. A_AG_PVA showed Sq values from 25.59 μm at t_0 to 9.85 μm at t_3, and Sa values from 21.63 μm to 7.91 μm. A similar trend was observed in P_M_PVA, with Sq ranging from 14.06 μm to 6.94 μm, and Sa from 11.03 μm to 4.48 μm. Regarding samples coated with acrylic resin, P_AG_Ac registered Sq values from 23.50 μm at t_0 to 8.14 μm at t_3, and Sa values from 19.13 μm to 6.21 μm. In A_KW_Ac, Sq values ranged from 17.66 μm to 33.94 μm and Sa from 14.13 μm to 28.13 μm over the same interval. A_M_Ac showed Sq from 6.21 μm to 8.28 μm and Sa from 4.82 μm to 6.45 μm. Samples treated with kaolin coatings showed differing results depending on the gypsum type. In the Paris gypsum-based sample P_KW_K, Sq values ranged from 7.33 μm to 34.90 μm, and Sa from 5.58 μm to 28.12 μm. In contrast, A_AG_K showed Sq values between 5.38 μm and 3.91 μm, and Sa between 4.17 μm and 3.12 μm across the ageing cycle. Through the uncoated samples, A_M showed Sq values ranging from 11.71 μm to 9.16 μm and Sa values from 9.68 μm to 7.19 μm, while P_AG ranged from Sq

values of 19.41 μm to 21.77 μm and Sa values from 15.38 μm to 17.98 μm. The full dataset is summarised in Table 18.

Table 18. Surface roughness parameters (Sq and Sa, in μm) measured for all mock-up samples at four ageing stages (t_0-t_3), as determined by optical light profilometry. Each sample is identified by its gypsum type and formulation (additive and/or coating).

Sample	Time	Sq (μm)	Sa (μm)	Sample	Time	Sq (μm)	Sa (μm)
A_AG	t_0	8.53	6.67	**P_AG**	t_0	19.41	15.38
	t_1	10.58	7.97		t_1	23.57	19.60
	t_2	15.93	12.29		t_2	22.13	18.31
	t_3	10.26	7.83		t_3	21.77	17.98
A_AG_Ac	t_0	8,83	7.12	**P_AG_Ac**	t_0	23.50	19.13
	t_1	5.12	3.94		t_1	8.08	6.03
	t_2	4.16	3.20		t_2	7.85	5.92
	t_3	4.92	3.72		t_3	8.14	6.21
A_AG_K	t_0	5.38	4.17	**P_AG_K**	t_0	7.38	5.55
	t_1	5.82	4.79		t_1	16.25	13.57
	t_2	6.17	5.09		t_2	16.40	13.79
	t_3	3.91	3.12		t_3	15.86	13.20
A_AG_PVA	t_0	25.59	21.63	**P_AG_PVA**	t_0	15.72	12.58
	t_1	11.42	8.95		t_1	10.62	8.93
	t_2	9.79	7.77		t_2	11.29	9.50
	t_3	9.85	7.91		t_3	21.32	10.42
A_KW	t_0	14.09	11.70	**P_KW**	t_0	12.46	8.82
	t_1	21.80	15.86		t_1	23.36	18.50
	t_2	14.41	10.03		t_2	24.73	19.37
	t_3	15.48	10.88		t_3	24.60	19.30
A_KW_Ac	t_0	17.66	14.13	**P_KW_Ac**	t_0	19.67	15.62
	t_1	32.36	27.20		t_1	19.60	15.38
	t_2	34.06	27.85		t_2	19.56	15.30
	t_3	33.94	28.13		t_3	19.75	15.38
A_KW_K	t_0	14.52	11.36	**P_KW_K**	t_0	7.33	5.58
	t_1	15.79	13.00		t_1	20.72	16.14
	t_2	13.54	10.78		t_2	34.83	28.44
	t_3	16.11	12.88		t_3	34.90	28.12
A_KW_PVA	t_0	14.70	11.38	**P_KW_PVA**	t_0	23.94	17.19
	t_1	8.61	6.55		t_1	21.70	17.17
	t_2	9.17	7.08		t_2	20.86	16.27
	t_3	9.27	7.16		t_3	19.78	15.43
A_M	t_0	11.71	9.68	**P_M**	t_0	9.11	7.08
	t_1	8.08	6.19		t_1	33.53	27.82
	t_2	9.50	7.51		t_2	32.88	27.22
	t_3	9.16	7.19		t_3	36.13	29.38
A_M_Ac	t_0	6.21	4.82	**P_M_Ac**	t_0	23.43	18.98
	t_1	12.07	10.07		t_1	54.69	45.75
	t_2	12.38	10.30		t_2	8.74	6.29
	t_3	8.28	6.45		t_3	8.58	6.36
A_M_K	t_0	7.01	5.32	**P_M_K**	t_0	14.30	11.40
	t_1	3.42	2.76		t_1	10.30	8.02
	t_2	2.82	2.22		t_2	10.53	8.21
	t_3	2.34	1.85		t_3	10.83	6.66
A_M_PVA	t_0	6.63	4.93	**P_M_PVA**	t_0	14.06	11.03
	t_1	5.24	4.03		t_1	6.14	4.22
	t_2	5.22	4.01		t_2	5.94	4.08
	t_3	5.77	4.50		t_3	6.94	4.48

4.4.2.4 Colourimetry

Colourimetric values were recorded for each mock-up sample before (t_0) and after (t_3) all the ageing cycles using the CIELab* system. Measurements were taken under SCI mode (specular component included) and expressed in terms of L* (lightness), a* (green-red), and b* (blue-yellow) coordinates. The colour difference ΔE* was calculated according to the CIELab* formula defined in UNI EN 15886:2011 [35-37].

Table 19 presents the mean values of L*, a*, and b* before and after ageing, along with the corresponding ΔE*. ΔE* values ranged between 0.12 and 2.32 across all formulations.

Table 19. Mean L*, a*, and b* values of the samples before (t_0) and after (t_3) ageing cycle (SCI measurements), with corresponding colour differences ΔE* calculated according to the CIELab formula (UNI EN 15886:2011).

Sample	L* t_0	a* t_0	b* t_0	L* t_3	a* t_3	b* t_3	ΔE*
A_AG	86.18	0.53	5.38	86.53	0.61	5.18	0.40
A_AG_Ac	86.33	0.49	5.55	86.16	0.62	5.51	0.21
A_AG_K	88.13	0.38	4.73	89.02	0.39	3.69	1.36
A_AG_PVA	80.54	0.95	7.39	80.56	1.06	7.45	0.12
A_KW	85.67	0.85	8.12	86.92	0.82	7.86	1.27
A_KW_Ac	89.05	0.60	5.69	89.00	0.82	5.60	0.24
A_KW_K	89.89	0.46	5.10	90.73	0.55	4.20	1.34
A_KW_PVA	86.86	1.02	7.57	86.90	1.17	7.35	0.27
A_M	83.91	0.80	7.25	84.27	0.87	6.76	0.60
A_M_Ac	84.92	0.66	6.61	84.85	0.78	6.63	0.14
A_M_K	87.49	0.43	4.94	88.26	0.49	3.96	1.23
A_M_PVA	83.51	0.85	7.50	83.48	0.98	7.54	0.14
P_AG	89.48	1.23	10.25	90.16	1.22	8.67	1.71
P_AG_Ac	89.86	0.98	9.75	89.82	1.23	9.53	0.33
P_AG_K	90.80	0.99	8.36	91.42	1.11	6.13	2.32
P_AG_PVA	89.00	1.29	9.64	88.95	1.40	9.65	0.12
P_KW	89.66	1.19	8.43	88.79	1.37	10.15	1.92
P_KW_Ac	89.37	1.19	8.54	89.24	1.33	8.34	0.27
P_KW_K	91.08	0.87	6.12	90.97	1.04	5.65	0.51
P_KW_PVA	86.31	1.87	11.68	86.69	1.99	11.67	0.39
P_M	88.49	0.95	8.28	87.88	1.36	8.93	0.99
P_M_Ac	84.74	1.67	12.28	84.45	1.90	12.25	0.37
P_M_K	87.92	1.25	8.36	87.46	1.41	7.62	0.88
P_M_PVA	85.64	1.61	11.02	85.37	1.78	11.43	0.52

Among the alabaster gypsum-based samples, L* values ranged between 80.54 and 89.89 at t_0, and between 80.56 and 90.73 at t_3. The corresponding a* values spanned 0.38-1.02 at t_0 and 0.39-1.17 at t_3, while b* values ranged 4.73-8.12 at t_0 and 3.69-7.86 at t_3. The calculated ΔE* values for this group were all below 1.36.

For Paris gypsum-based samples, L* values were in the range 84.74-91.08 at t_0 and 84.45-91.42 at t_3. a* values varied from 0.87-1.87 at t_0 to 1.04-1.99 at t_3, and b* values from 6.12-12.28 at t_0 to 5.65-12.25 at t_3. The ΔE* values for these samples extended up to 2.32.

The lowest colour variation was observed in samples A_AG_PVA and P_AG_PVA ($\Delta E^* = 0.12$). Other samples with similarly low ΔE^* values (≤ 0.30) were A_M_PVA, A_M_Ac, A_AG_Ac, and A_KW_Ac. In contrast, the highest ΔE^* values occurred in P_AG_K (2.32), P_KW (1.92), and P_AG (1.71).

All ΔE^* values remained below the commonly referenced perceptibility threshold ($\Delta E^* \geq 3$).

In addition to the overall colour difference (ΔE^*), the individual CIELab* coordinates were examined to identify which component contributed most to the observed variations (Table 20).

Table 20. Variations of the individual CIELab* coordinates (ΔL*, Δa*, Δb*).

Sample	ΔL*	Δa*	Δb*
A_AG	+0.35	+0.08	-0.20
A_AG_Ac	-0.17	+0.13	-0.04
A_AG_K	+0.89	+0.01	-1.04
A_AG_PVA	+0.02	+0.11	+0.06
A_KW	+1.25	-0.03	-0.26
A_KW_Ac	-0.05	+0.22	-0.09
A_KW_K	+0.84	+0.09	-0.90
A_KW_PVA	+0.04	+0.15	-0.22
A_M	+0.36	+0.07	-0.49
A_M_Ac	-0.07	+0.12	+0.02
A_M_K	+0.77	+0.06	-0.98
A_M_PVA	-0.03	+0.13	+0.04
P_AG	+0.68	-0.01	-1.58
P_AG_Ac	-0.04	+0.25	-0.22
P_AG_K	+0.62	+0.12	-2.23
P_AG_PVA	-0.05	+0.11	+0.01
P_KW	-0.87	+0.18	+1.72
P_KW_Ac	-0.13	+0.14	-0.20
P_KW_K	-0.11	+0.17	-0.47
P_KW_PVA	+0.38	+0.12	-0.01
P_M	-0.61	+0.41	+0.65
P_M_Ac	-0.29	+0.23	-0.03
P_M_K	-0.46	+0.16	-0.74
P_M_PVA	-0.27	+0.17	+0.41

4.4.3 Light ageing

4.4.3.1 FTIR spectroscopy

The chemical response of the mock-up samples to light exposure was evaluated using FTIR spectroscopy. Spectra collected before (t_0) and after (t_3) ageing were compared to identify possible changes in functional groups or matrix components.

In all samples, the characteristic vibrational bands of gypsum remained visible after ageing, including O–H stretching (3548, 3407 cm^{-1}), SO_4^{2-} stretching (1110, 670 cm^{-1}), and bending modes (605, 470 cm^{-1}) [24-32].

In samples containing kaolin as an additive, such as A_KW, the spectra collected after ageing showed a reduction in intensity of the main kaolinite bands, particularly at 1065, 1010, and 910 cm^{-1}. Only minor absorptions near 790 and 500-400 cm^{-1} were still detectable. In samples where kaolin was applied as a surface coating, such as A_KW_K, the characteristic bands of kaolinite observed before ageing at 3690, 3670, and 3645 cm^{-1} (O-H stretching) and at 1065 and 1010 cm^{-1} (Si-O-Si stretching), remained detectable after exposure, with only slight variations in intensity [34]. These differences are clearly visible when comparing the spectra reported in Section 4.5.3.1 of the Discussion.

Samples coated with PVA and acrylic resin did not show noticeable shifts or intensity changes in their characteristic spectral features after light exposure.

4.4.3.2 Optical light profilometry

The surface roughness parameters (Sq and Sa) measured before and after light ageing for each sample are reported in Table 21.

In alabaster gypsum samples, Sq values before ageing ranged from 5.38 μm (A_AG_K) to 25.59 μm (A_AG_PVA), and after ageing from 5.70 μm (A_AG_K) to 19.46 μm (A_KW_PVA). Sa values ranged from 4.17 μm (A_AG_K) to 21.63 μm (A_AG_PVA) at t_0 and from 4.39 μm (A_AG_K) to 15.51 μm (A_KW_PVA) at t_3.

In Paris gypsum samples, Sq values ranged from 7.33 μm in P_KW_K to 23.50 μm in P_AG_Ac before ageing, and from 6.39 μm in P_AG_K to 23.42 μm in P_M_Ac after ageing. The corresponding Sa values ranged from 5.55 μm to 19.13 μm at t_0, and from 5.15 μm to 19.33 μm at t_3.

Among samples treated with PVA, Sq values after ageing spanned from 6.60 μm (A_M_PVA) and 19.46 μm (A_KW_PVA), and Sa values from 5.26 μm and 15.51 μm. For samples treated with acrylic resin, Sq at t_3 ranged between 9.17 μm (A_M_Ac) and 17.34 μm (P_KW_Ac), and Sa between 7.29 μm and 13.95 μm.

Samples treated with kaolin showed Sq values at t_3 between 5.70 μm (A_AG_K) and 11.97 μm (A_KW_K), and corresponding Sa values between 4.39 μm and 9.50 μm.

The untreated samples A_AG and P_AG presented Sq values of 10.06 μm and 13.72 μm at t_3, and Sa corresponding values of 8.10 μm and 10.64 μm, respectively.

Table 21. Surface roughness values (Sq and Sa, in μm) for mock-ups before (t_0) and after three cycles of light ageing (t_3). The table highlights the changes in roughness associated with each formulation.

Sample	Measurement	Sq (μm)	Sa (μm)	Sample	Measurement	Sq (μm)	Sa (μm)
A_AG	t_0	8.53	6.67	**P_AG**	t_0	19.41	15.38
	t_3	10.06	8.10		t_3	13.72	10.64
A_AG_Ac	t_0	8.83	7.12	**P_AG_Ac**	t_0	23.50	19.13
	t_3	13.39	11.13		t_3	11.03	8.93
A_AG_K	t_0	5.38	4.17	**P_AG_K**	t_0	7.38	5.55
	t_3	5.70	4.39		t_3	6.39	5.19
A_AG_PVA	t_0	25.59	21.63	**P_AG_PVA**	t_0	15.72	12.58
	t_3	14.73	12.24		t_3	9.65	7.53
A_KW	t_0	14.09	11.70	**P_KW**	t_0	12.46	8.82
	t_3	15.81	13.21		t_3	18.76	14.07
A_KW_Ac	t_0	17.66	14.13	**P_KW_Ac**	t_0	19.67	15.62
	t_3	19.27	15.40		t_3	17.34	13.95
A_KW_K	t_0	14.52	11.36	**P_KW_K**	t_0	7.33	5.58
	t_3	11.97	9.50		t_3	7.87	6.16
A_KW_PVA	t_0	14.70	11.38	**P_KW_PVA**	t_0	23.94	17.19
	t_3	19.46	15.51		t_3	14.82	11.49
A_M	t_0	11.71	9.68	**P_M**	t_0	9.11	7.08
	t_3	8.07	6.20		t_3	6.49	5.15
A_M_Ac	t_0	6.21	4.82	**P_M_Ac**	t_0	23.43	18.98
	t_3	9.17	7.29		t_3	23.42	19.33
A_M_K	t_0	7.01	5.32	**P_M_K**	t_0	14.30	11.40
	t_3	7.61	6.18		t_3	9.56	7.70
A_M_PVA	t_0	6.63	4.93	**P_M_PVA**	t_0	14.06	11.03
	t_3	6.60	5.26		t_3	7.51	5.97

4.4.3.3 Colourimetry

Colourimetric measurements were collected before and after each of the three light ageing cycles. The corresponding ΔE^* values were calculated according to the CIELab* colour space (UNI EN 15886:2011) [35-37] and are reported in Table 22.

Table 22. ΔE^* values calculated for each sample after the three light ageing cycles. ΔE^*_1, ΔE^*_2, and ΔE^*_3 correspond respectively to the colour differences measured between t_0-t_1, t_0-t_2, t_0-t_3 in the CIELab* colour space (UNI EN 15886:2011 [35-37]). Values above 3 units (in bold) indicate colour changes perceptible to the human eye.

Sample	ΔE^*_1	ΔE^*_2	ΔE^*_3	Sample	ΔE^*_1	ΔE^*_2	ΔE^*_3
A_M	0.58	0.58	0.58	**P_M**	**3.38**	**3.62**	**3.9**
A_M_K	0.48	1.17	1.22	**P_M_K**	2.00	2.05	2.05
A_M_Ac	0.77	1.26	1.35	**P_M_Ac**	**3.64**	**4.40**	**4.41**
A_M_PVA	1.11	1.12	1.18	**P_M_PVA**	**3.25**	**3.54**	**3.82**
A_KW	0.88	0.94	0.95	**P_KW**	**5.39**	**6.93**	**7.16**
A_KW_K	0.50	0.53	0.54	**P_KW_K**	1.33	0.92	1.41
A_KW_Ac	1.13	1.43	1.44	**P_KW_Ac**	2.52	2.50	2.92
A_KW_PVA	0.70	0.46	0.77	**P_KW_PVA**	1.78	2.50	2.55
A_AG	0.57	2.25	2.28	**P_AG**	**3.00**	**3.56**	**3.60**
A_AG_K	0.30	0.31	0.31	**P_AG_K**	1.16	1.20	1.2
A_AG_Ac	0.22	0.31	0.31	**P_AG_Ac**	**3.00**	**3.00**	**3.43**
A_AG_PVA	0.27	0.27	2.45	**P_AG_PVA**	2.46	2.57	**3.52**

Most samples exhibited ΔE^* values below the commonly accepted threshold of 3, beyond which colour differences are considered perceptible to the human eye. This trend was particularly evident in mixtures prepared with alabaster gypsum, where all ΔE^* values remained consistently low. Similarly, stable results were recorded in PVA-treated samples such as A_KW_PVA and A_M_PVA, which showed limited variations across the three measurement cycles.

In contrast, Paris gypsum-based samples displayed a broader range of ΔE^* values. Several of these samples exceeded the threshold of 3, particularly in formulations containing Arabic gum or marble powder. The highest colour variations were recorded in the untreated P_KW sample, with ΔE^* values of 5.39, 6.93, and 7.16 after the first, second, and third cycles, respectively.

Mock-ups treated with PVA or acrylic resin generally presented lower ΔE^* values compared with their untreated corresponding samples. For instance, P_KW_Ac and P_KW_PVA showed final ΔE^* values of 2.92 and 2.55, respectively. Similarly, alabaster gypsum samples treated with the same coatings, such as A_AG_PVA and A_M_PVA, remained below the perceptibility threshold throughout all three cycles.

4.5 Discussion

4.5.1 Chemical and mineralogical characterisation

The XRF data confirm the dominant presence of CaO and SO_3 across all formulations, reflecting the gypsum-based composition of the matrix. SiO_2 is also consistently detected, with values ranging from 21.68 wt % to 32.01 wt % (Table 15). The consistent presence of silica suggests that part of the siliceous content is inherent to the gypsum itself or originates from common mineral impurities found in both alabaster and Paris gypsum types [23]. It is important to note that XRF was not employed to determine the main constituents of the mixtures, which were already known from the preparation protocol, but rather to verify the presence of minor inorganic components and natural impurities within the commercial raw materials. As XRF operates in semiquantitative mode and detects elements with atomic number greater than 11 (Na), the technique is suitable for identifying minor constituents or natural inorganic impurities associated with gypsum-, kaolin- and marble-powders. The compositional data provided in the manufacturers' technical sheets for these materials, which report the presence of silicates, alumina, magnesium and iron traces, are fully consistent with the results observed in the XRF analysis.

The slightly higher SiO_2 content observed in samples with marble powder may result from minor siliceous impurities naturally present in the filler. In contrast, kaolin-containing samples (A_KW and P_KW) do not show a notable increase in silica concentration, despite the high SiO_2 content of the additive (approximately 49 wt % according to the supplier). This may indicate that the quantity of kaolin incorporated was relatively low compared to the total mass of gypsum.

A moderate increase in Al_2O_3 is observed in samples containing kaolin, in agreement with its alumina-rich composition [38]. The presence of MgO in the formulations with marble powder (A_M and P_M) is consistent with the technical specifications (55.61 wt % $CaCO_3$ and 44.20 wt % $MgCO_3$), indicating that the material corresponds to a dolomitic marble. Interestingly, Fe_2O_3 values in the same samples are slightly higher than the declared content in the marble (0.016 wt %). This discrepancy may be attributed to minor impurities in the gypsum matrix itself, which is known to contain variable traces of iron oxides depending on the geological origin [39].

Potassium oxide (K_2O) was detected in trace amounts in all samples, with slightly higher values in the alabaster-based formulations. This may reflect the presence of K-bearing accessory minerals in the raw gypsum or minor contributions from kaolin, which typically contains low levels of potassium [38].

XRPD analysis confirmed gypsum as the predominant crystalline phase across all mock-up formulations, indicating that the hardening reaction occurred as expected in each case (Figure 30). The co-presence of bassanite and, in several samples, traces of anhydrite may reflect either incomplete hydration or minor thermal alteration of the raw material [7].

Calcite was identified in the alabaster-based samples A_AG and A_KW, reflecting the mineralogical composition of the raw gypsum, as well as in the Paris gypsum formulation P_KW, where its occurrence is linked to the kaolin-based additives. In contrast, calcite was not detected in the marble powder formulations. Instead, these samples (A_M and P_M) showed dolomite, consistent with the dolomitic composition of the filler. Dolomite was also detected in A_AG and A_KW, suggesting its occurrence as a minor impurity in the alabaster gypsum. The detection of small amounts of quartz in A_KW and P_KW samples may be related to common siliceous impurities found in kaolin clays. The presence of kaolinite in these same samples reflects the addition of the kaolin-based additive [38].

Several minor phases, including anhydrite, dolomite, calcite, and quartz, were identified across multiple samples and are typically associated with either mineral impurities in the raw materials or transformations during the drying process [39]. The detection of anhydrite, for instance, may be attributed to high-temperature exposure during calcination [40] or to its natural occurrence in evaporitic gypsum deposits [39]. Dolomite, which is frequently found in association with gypsum and calcite, may provide insights into the geological origin of the raw materials.

Notably, a consistent diffraction peak at approximately 35° 2θ (Co-Kα) was observed exclusively in samples made with alabaster gypsum. This signal, which does not correspond to any major sulphate or carbonate phase, is attributed to celestine ($SrSO_4$). Although its identification is based on a single peak, the reproducibility of this peak across multiple samples with the same gypsum source supports the hypothesis [41,42]. Celestine is a common minor mineral in evaporitic environments and is often used as an indicator of gypsum provenance [43].

While standard XRPD identification requires multiple diffraction peaks for phase assignment, in complex multi-phase matrices like those studied here, minor signals may be masked by dominant reflections or fall below the detection threshold. In such cases, single but consistent peaks can still provide valuable information, particularly when observed across independent samples with a shared raw material origin. Overall, XRPD results demonstrate that while the primary phase remains gypsum, the presence of other phases depends on both the type of gypsum and the additive used.

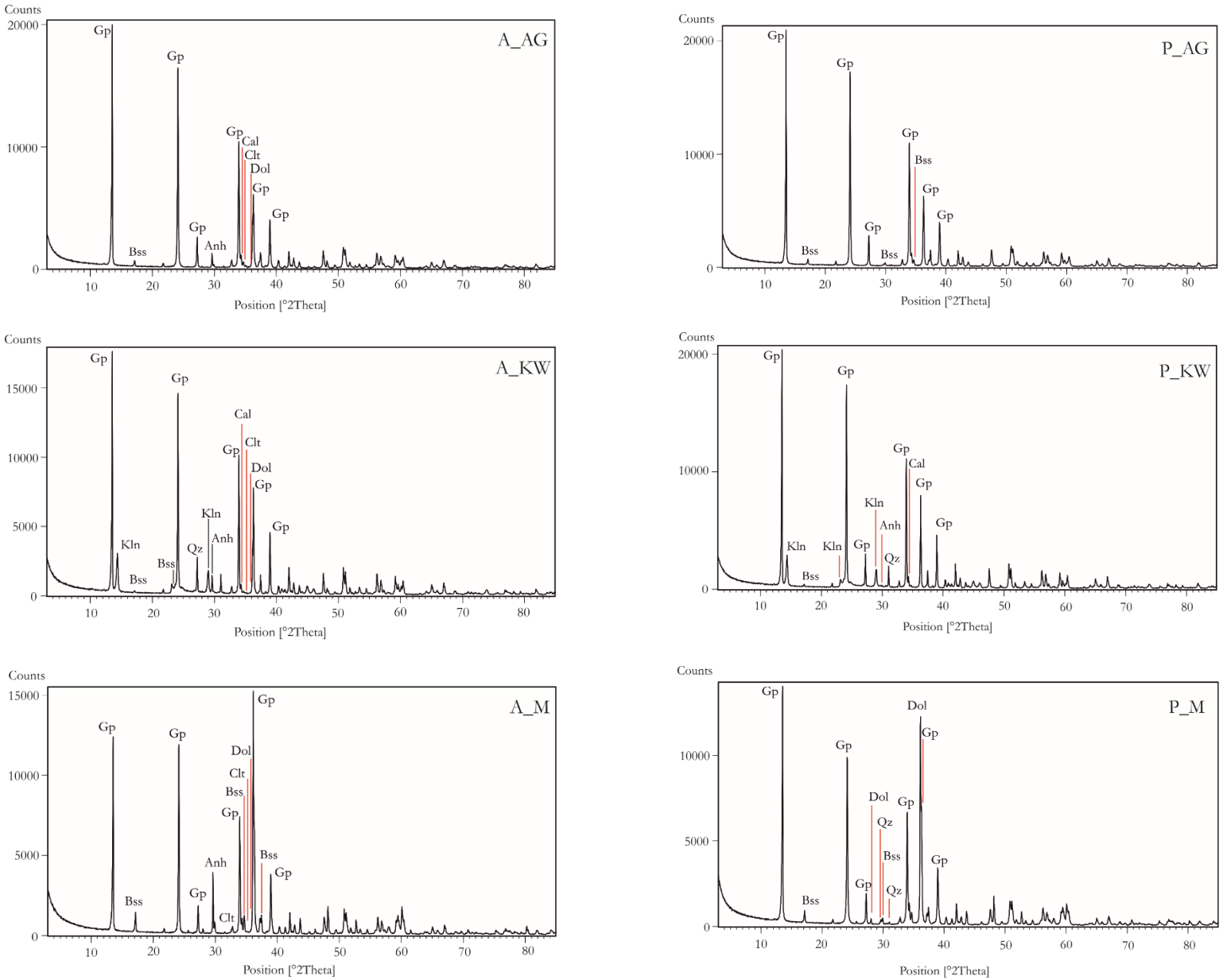

Figure 30. XRPD patterns of mixtures composed by alabaster gypsum and Paris gypsum. Mineral abbreviation from Warr (2021) [23]: *Gp* = gypsum; *Bss* = bassanite; *Anh* = anhydrite; *Dol* = dolomite; *Cal* = calcite; *Kln* = kaolinite; *Qz* = quartz; *Clt* = celestine.

The SEM analysis of sample P_M highlighted a heterogeneous microstructure, with irregular pores dispersed within the matrix. Large inclusions of carbonate fragments are embedded in the material, likely calcite or dolomite fragments from the filler, while the surrounding matrix show crystals of variable size and orientation. This results in a porous and discontinuous structure, indicative of limited compactness and low cohesion at the microscale. While β-hemihydrate gypsum (commonly referred to as Paris gypsum) is described in the literature as forming prismatic or elongated crystals under ideal conditions [7], the morphology observed here deviates from that standard description. The presence of interfacial gaps and the lack of cohesion around the marble powder inclusions suggest incomplete integration during setting, possibly influenced by production parameters such as drying rate, water-to-gypsum ratio, or insufficient mechanical compaction [44,45].

In contrast, a more compact microstructure is observed in A_KW, although the inclusion of wood fibres and kaolin introduces heterogeneity (Figure 28). The wood inclusions are not fully embedded within the matrix and generate localised voids and microcracks, compromising the overall uniformity of the material [46]. The kaolin particles, although smaller and more dispersed, contribute to irregularity in the microstructure due to their lamellar shape and uneven distribution.

Taken together, these observations confirm that both the type of gypsum and the specific additives used strongly influence the internal morphology of the hardened material. While Paris gypsum in formulation P_M resulted in a fragmented and discontinuous microstructure, the alabaster-based A_KW sample displayed greater structural compactness, with heterogeneities mainly associated with the organic filler.

4.5.2 Hygrothermal ageing

4.5.2.1 Macroscopic evaluation after ageing

The macroscopic evaluation of the samples after artificial ageing revealed that surface degradation patterns are influenced not only by the presence of a protective coating, but also by the specific combination of gypsum type and additives used in the formulation (Figure 29).

Samples based on alabaster gypsum were particularly prone to mechanical damage at edges and corners. This was especially evident in uncoated specimens or those treated with kaolin-based coatings, which frequently showed fractures and material loss along the margins. These findings suggest that the α-hemihydrate matrix is more susceptible to

mechanical degradation under environmental stress, especially in the absence of effective surface protection.

The performance of coatings was also strongly conditioned by the internal composition of the mixtures. Among the PVA-treated samples, for example, notable differences were observed depending on the additive: the PVA-coated sample containing Arabic gum (P_AG_PVA) retained a compact and stable surface, whereas the formulation with kaolin and wood powder (P_KW_PVA) exhibited visible degradation and surface irregularities. This indicates that the effectiveness of protective treatments depends on their compatibility with the entire formulation. In heterogeneous systems, particularly those containing fibrous organic fillers, coatings may be less effective in maintaining surface integrity.

Overall, these results highlighted the importance of accounting for material interactions when selecting protective treatments. The combined influence of gypsum type, additive content, and coating material determines the durability of plaster formulations under environmental ageing. Consequently, a uniform protection strategy cannot be applied across all historical mixtures.

4.5.2.1 FTIR spectroscopy

The FTIR results revealed clear differences in the ageing behaviour of the mock-up materials, depending on the nature of the additive or coating applied.

Samples containing Arabic gum showed distinct organic signals at 2660, 1632, and 1621 cm^{-1}, attributable to unsaturated bonds, carbonyl groups (possibly from associated animal glue), and hydroxyl groups [33]. These bands remained visible after ageing, though with slight reduced intensity, likely reflecting partial interaction between Arabic gum and the gypsum matrix.

Samples with marble powder were the most stable. Comparison of spectra before and after ageing revealed only minimal changes: the characteristic carbonate signals (1790, 1450, 1400 cm^{-1}) and O-H stretching bands (3534, 3407 cm^{-1}) remained essentially unchanged, suggesting that the carbonate-based additive was chemically stable throughout the ageing process. Conversely, samples containing kaolin and wood powder were the most affected by ageing. Before ageing, their spectra displayed well-defined kaolin bands, including O–H stretching bands at 3690, 3670, and 3645 cm^{-1}, Si–O–Si vibrations at 1065 and 1010 cm^{-1}, and Al–OH and bending modes between 940 and 430 cm^{-1} [34]. After ageing, many of these signals were significantly reduced or absent. These changes likely reflect the partial loss of kaolin from the surface, a process possibly amplified by the hygroscopic wood fibres, which

enhance moisture retention and may have facilitated degradation or detachment during thermal and hygrometric cycles [47].

The PVA-coated samples exhibited excellent chemical stability, as demonstrated by the persistence of their characteristic bands after ageing (Figure 31). The C-H stretching bands (2980 – 2850 cm^{-1}) and absorptions from residual acetate groups (1780 and 1700 cm^{-1}) remained clearly detectable, suggesting that the polymer film was not significantly affected by thermal or hygrometric stress. Similarly, acrylic resin coatings maintained their structural integrity throughout the ageing cycles. The spectra consistently showed the typical markers of acrylate-based materials, including aliphatic C-H stretching, ester carbonyl absorptions about 1726 cm^{-1}, and sharp bands at 1200, 1160, and 1020 cm^{-1} corresponding to C-O stretching vibrations, with only minor intensity variations [48].

In contrast, kaolin-coated samples proved to be the least effective among the tested treatments. The characteristic kaolinite bands present before ageing had almost entirely disappeared after ageing, leaving only the signals of gypsum. This indicates partial removal of the kaolin layer during exposure, likely caused by mechanical stress from temperature and humidity fluctuations. The powdery surface appearance supports the hypothesis of pulverisation or detachment, confirming the limited long-term effectiveness of kaolin coatings under such environmental conditions.

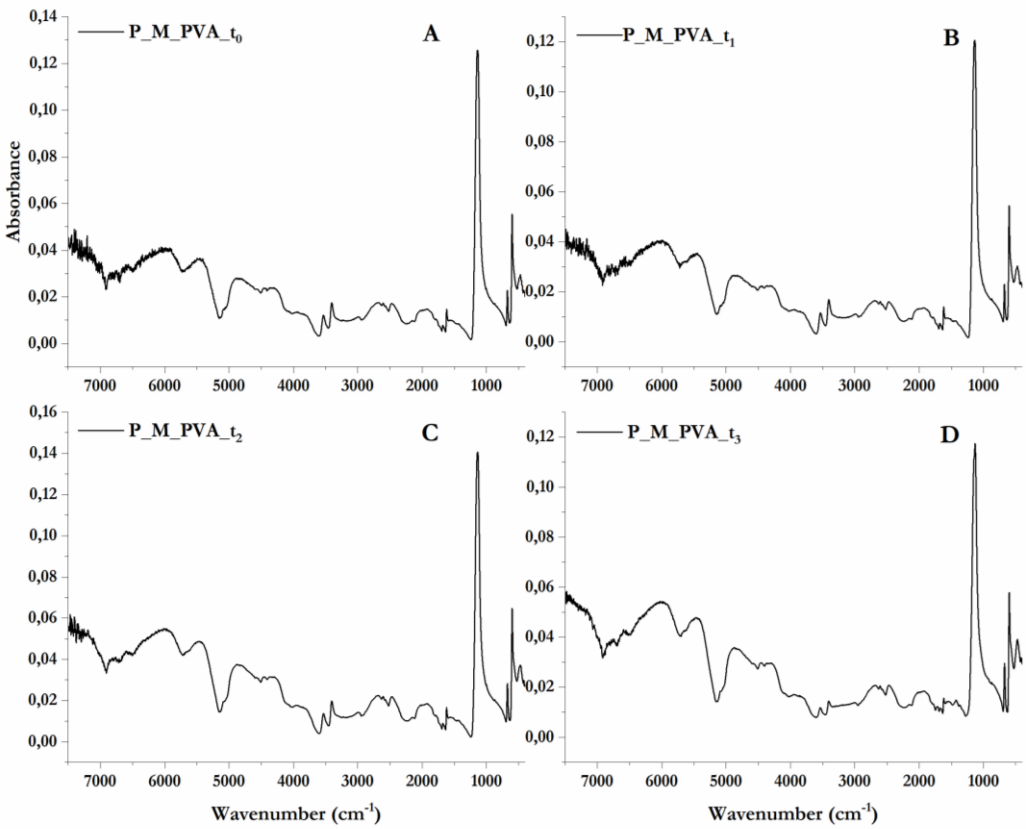

Figure 31. ER-FTIR spectra of sample P_M_PVA at four different ageing stages: (A) t_0, (B) t_1, (C) t_2, and (D) t_3. The main spectral features of the PVA coating, including the C-H stretching bands (2980-2850 cm^{-1}) and the peaks attributed to residual acetate groups (ca. 1780-1700 cm^{-1}), are visible across all the analysis, indicating good chemical stability of the protective layer during ageing.

In conclusion, FTIR analysis highlighted distinct differences in the ageing behaviour of the mock-ups. Arabic gum and marble powder showed good chemical stability, with marble powder remaining unchanged. Kaolin, whether used in combination with wood powder or as a coating, exhibited poor stability and was affected by hygrothermal fluctuations. By contrast, PVA and acrylic resin coatings demonstrated excellent chemical stability and remained effective throughout the ageing cycles.

4.5.2.2 Optical light profilometry

The surface roughness analysis across all samples revealed variable responses to ageing tests depending on material composition and applied treatments. A distinction was observed between the two gypsum types. In most cases, Paris gypsum (P_AG, P_AG_Ac, P_AG_K, P_KW_Ac, P_KW_PVA, P_M_Ac, P_M_K, P_M_PVA) exhibited higher Sq (root mean square height) and Sa (arithmetical mean height) values [49], along with greater fluctuations over the ageing period. In particular, untreated samples containing Paris gypsum mixed with either Arabic gum or kaolin and wood powder showed an increase in roughness parameters.

Similar trends were observed when these formulations were treated with kaolin. For example, in P_KW_K, Sq increased from 7.33 μm to 34.90 μm and Sa from 5.58 μm to 28.12 μm, suggesting that the combination of this matrix with specific additives, even when coated, does not effectively prevent surface degradation. A similar trend was recorded in the uncoated sample P_M, where Sq increased from 9.11 μm at t_0 to 36.13 μm at t_3, and Sa from 7.08 μm to 29.38 μm. In contrast, alabaster gypsum demonstrated overall greater surface stability. In most cases, Sq and Sa values remained stable or decreased throughout the ageing cycle. For instance, A_M_K showed a reduction in surface roughness, with Sq decreasing from 7.01 μm to 2.34 μm and Sa from 5.32 μm to 1.85 μm. A similar trend was observed in A_KW, where roughness values remained relatively stable: Sq varied from 14.09 μm at t_0 to 15.48 μm at t_3, and Sa from 11.70 μm to 10.88 μm.

Among the treatments tested, PVA was the most effective in limiting surface roughness evolution. Several PVA-treated samples exhibited either stable or decreasing Sq and Sa values over time, indicating a more protective effect under ageing conditions. This trend was particularly evident in sample A_AG_PVA, which showed a marked reduction in Sq from 25.59 μm to 9.85 μm and in Sa from 21.63 μm to 7.91 μm, and in sample P_M_PVA (Figure 32A, B, C, D), with Sq decreasing from 14.06 μm to 6.94 μm and Sa from 11.03 μm to 4.48 μm. Samples treated with acrylic resin exhibited variable behaviour depending on both the gypsum type and the additive formulation. In several cases, a sharp decrease in surface roughness was observed between t_0 and t_1, followed by relative stability over time. This trend was particularly evident in P_AG_Ac and A_AG_Ac, where Sq and Sa values decreased markedly from t_0 to t_1 and then remained constant throughout the ageing cycle, suggesting an initial surface consolidation effect. However, this behaviour was not consistent across all samples. A_M_Ac showed an initial increase in roughness from t_0 to t_2 (Sq: 6.21 μm to 12.38 μm; Sa: 4.82 μm to 10.30 μm), followed by a decrease at t_3, suggesting that surface stabilisation occurred only in the final phase of the ageing cycle. In contrast, A_KW_Ac showed a continuous increase in both Sq and Sa across all the measurements, reaching the highest roughness values among the acrylic resin-treated samples (Sq: 17.66 μm to 33.94 μm; Sa: 14.13 μm to 28.13 μm). Paris gypsum samples such as P_KW_Ac remained stable over time, with minimal variation in Sq and Sa, although roughness values remained consistently higher than those observed in other formulations. These findings indicate that the effectiveness of the acrylic resin is highly dependent on the nature of the substrate and the additive content, with some samples exhibiting improved surface stability following treatment, and others showing minimal effectiveness. Samples treated with kaolin as a surface

coating exhibited distinct behaviours depending on the gypsum type and formulation. In Paris gypsum, surface roughness generally increased during ageing. For instance, P_AG_K showed an increase in Sq from 7.38 μm at t_0 to 15.86 μm at t_3, and in Sa from 5.55 μm to 13.20 μm. A more pronounced rise was observed in P_KW_K, where Sq increased from 7.33 μm to 34.90 μm and Sa from 5.58 μm to 28.12 μm over the same period. By contrast, alabaster samples treated with kaolin displayed more stable behaviour. In A_AG_K, Sq decreased slightly from 5.38 μm to 3.91 μm and Sa from 4.17 μm to 3.12 μm by the end of the ageing cycle. A_KW_K also showed limited variation across all measurements, without significant increase in either parameter. These results indicate that kaolin contributes to surface stability when applied to alabaster gypsum, but shows reduced effectiveness with Paris gypsum, which proved more sensitive to ageing. The analysis further identified a subset of formulations with inferior surface stability, predominantly those based on Paris gypsum. P_M and P_KW_K (Figure 32E, F, G, H) exhibited the most pronounced increases in Sq and Sa throughout the ageing cycle. Among the less stable samples, several involved kaolin, either as an additive or as a surface treatment, a trend most evident in the Paris gypsum group.

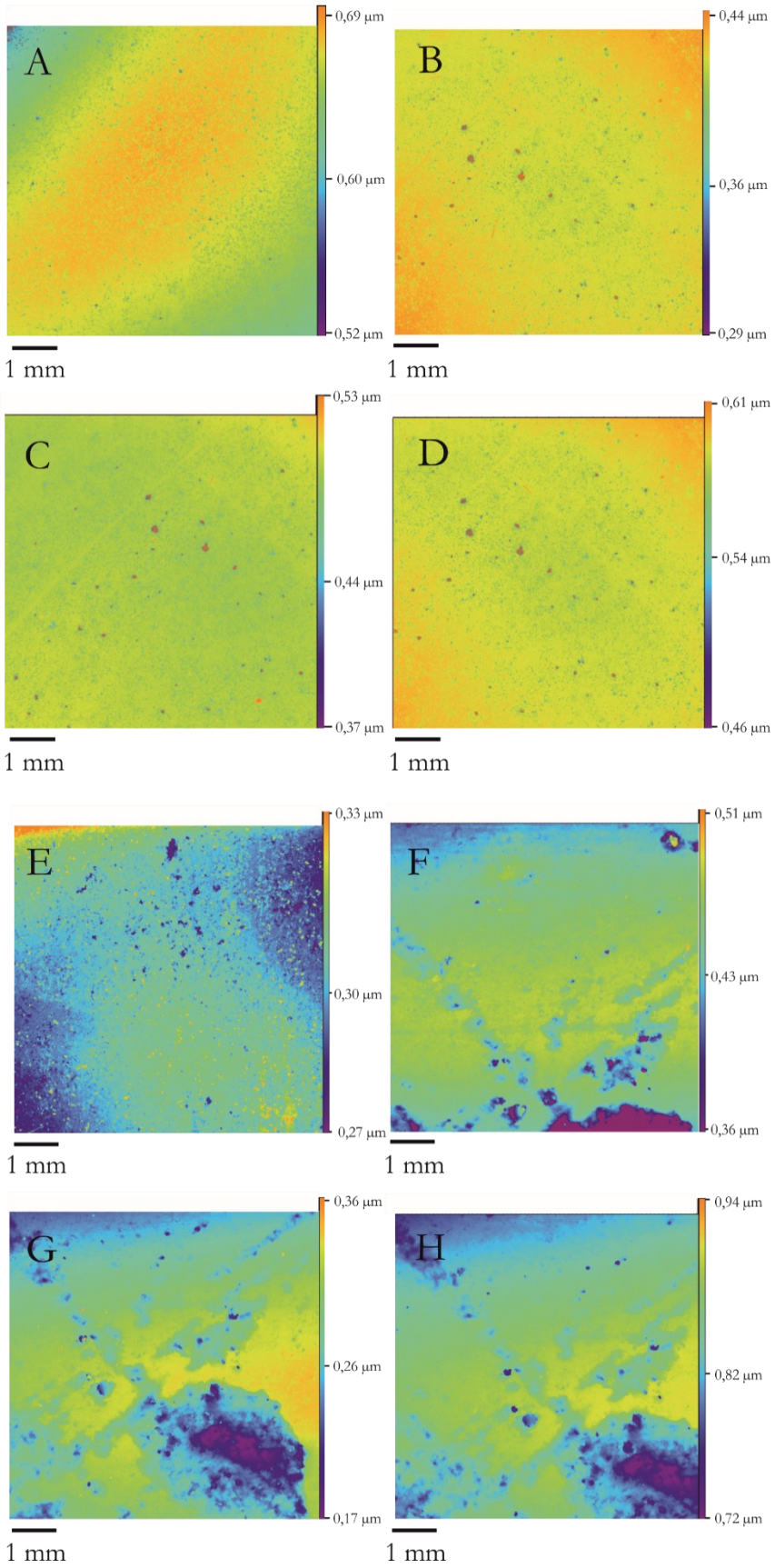

Figure 32. 3D surface comparison of sample P_M_PVA at different ageing stages: (A) t_0, (B) t_1, (C) t_2, and (D) t_3. 3D surface comparison of sample P_KW_K at different ageing stages: (E) t_0, (F) t_1, (G) t_2, and (H) t_3. Area of analysis = 49 mm^2.

4.5.2.3 Colourimetry

After the ageing cycles, all samples exhibited variations in their L^*, a^*, and b^* values. However, these changes were generally minor and often imperceptible to the human eye. The calculated ΔE^* values ranged from 0.12 to a maximum of 2.32, without samples exceeding the commonly accepted perceptibility threshold of $\Delta E^* \approx 3$ [35-37]. This suggests an overall good chromatic stability under the applied ageing conditions.

Among the most stable samples were A_AG_PVA and P_AG_PVA, both with $\Delta E^* = 0.12$, and A_M_PVA and A_M_Ac, both with $\Delta E^* = 0.14$ (Table 19). These results suggested a potential protective role of coatings such as PVA and Acryl-EM 33, particularly when applied to alabaster gypsum substrates. Similarly, samples such as A_AG_Ac and A_KW_Ac exhibited minimal variation ($\Delta E^* \leq 0.30$), confirming the relative effectiveness of the treatments. Alabaster gypsum-based samples generally showed good resistance to chromatic change, even when coated with kaolin. For instance, A_AG_K and A_KW_K showed moderate ΔE^* values of 1.36 and 1.34, respectively, mainly due to decrease in b^* values. Notably, even the uncoated samples such as A_AG and A_M exhibited only limited colour variation. These findings suggested that the base material plays a fundamental role in colour stability, while surface treatments can further enhance resistance to ageing effects.

Slightly higher variations were observed in some uncoated or differently treated samples, particularly those based on Paris gypsum. The highest ΔE^* value was recorded for P_AG_K ($\Delta E^* = 2.32$), followed by P_KW ($\Delta E^* = 1.92$) and P_AG ($\Delta E^* = 1.71$). Although these values remain below the perceptibility threshold, they represent the most notable colour differences within the dataset. In these cases, changes in the b^* were particularly significant, often combined with a slight increase in a^* and decrease in L^*, resulting in an overall darkening effect, as observed in samples P_M and P_KW [37].

From the analysis of the differences in the individual CIELab* coordinates (Table 20), most samples showed minor changes in lightness (ΔL^* ranging approximately from -0.90 to +1.30), indicating limited darkening or lightening after hygrothermal ageing. More relevant trends were observed in the b^* coordinate, particularly in formulations containing the kaolin-wood mixture and in the Paris gypsum specimens with Arabic gum. Several samples exhibited negative Δb^* values (up to -2.23 in P_AG_K), indicating a shift towards a less yellow appearance under the applied hygrothermal cycles. Conversely, positive Δb^* values were recorded in some KW-based formulations such as P_KW ($\Delta b^* = +1.72$), suggesting a yellowing tendency attributable to the lignocellulosic component. Variations in the a^*

coordinate were generally small ($\Delta a^* < 0.50$) and did not contribute significantly to the overall chromatic change.

The 3D scatterplots in Figure 33 (L^*, a^*, b^*) provide a visual representation of the chromatic shift before (t_0) and after ageing (t_3) for each group of samples. The displacements in the colour space illustrate how ageing influenced the chromatic parameters. In general, samples remained clustered or shifted only slightly, confirming the limited variation observed numerically. However, some samples, such as P_KW, P_AG_K, A_KW_K, and A_AG_K, showed more noticeable displacements, correlating with their relatively higher ΔE^* values. Interestingly, samples treated with kaolin, especially those based on Paris gypsum, but also in some alabaster mixtures. exhibited greater shifts in colour space. This suggested that kaolin does not always ensure optimal protection and, in some formulations, may even contribute to increased colour variability.

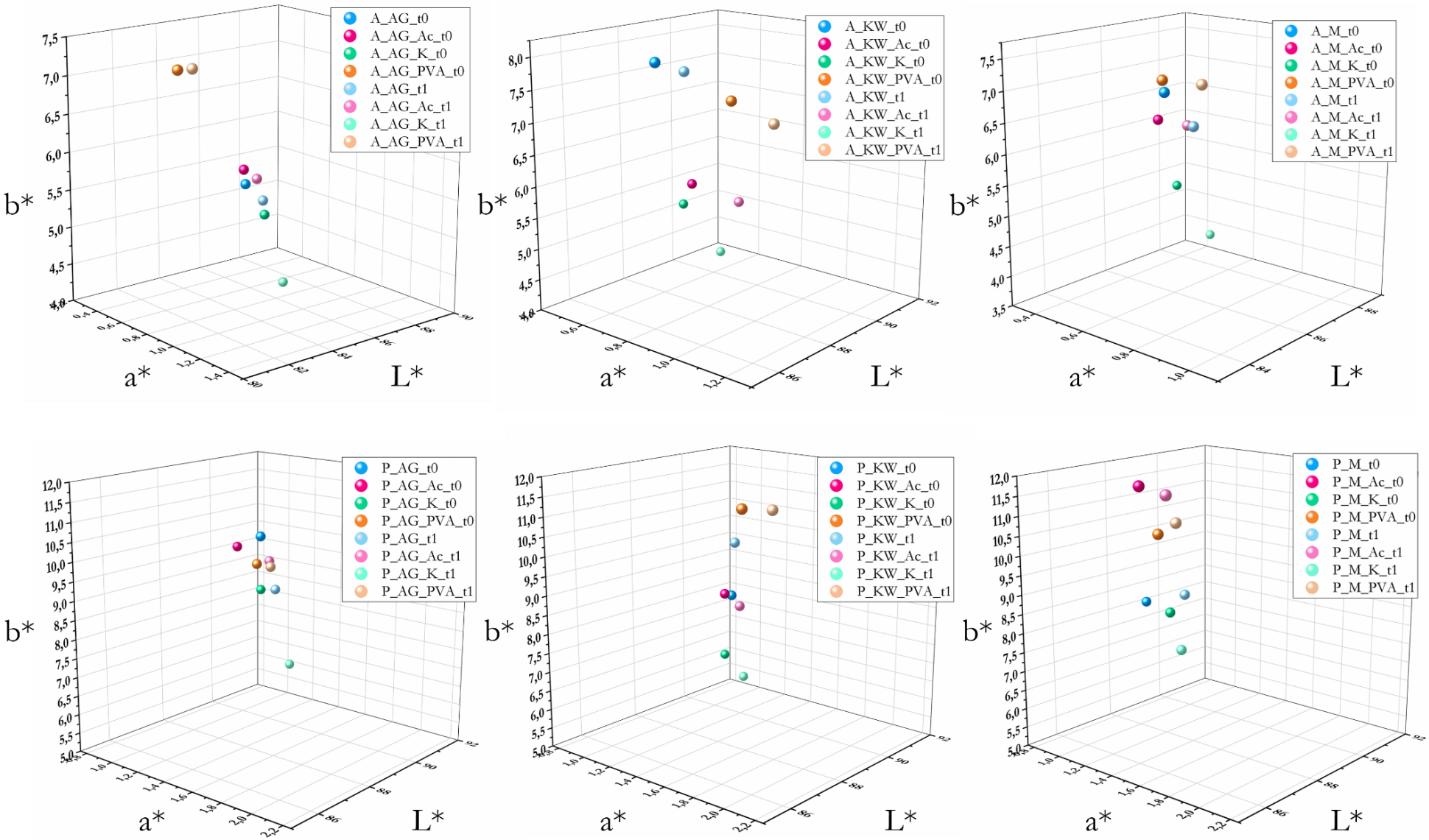

Figure 33. Colour measurements before and after all the cycle ageing (t_0 and t_3): mock-ups in L^*, a^*, b^* = colour coordinates.

4.5.3 Light ageing

4.5.3.1 FTIR spectroscopy

The chemical stability of the mock-up samples after light ageing was assessed through FTIR spectroscopy. The comparison of the spectra before and after ageing allowed the evaluation of possible changes in the materials and coatings exposed to light under controlled conditions. FTIR spectra indicated overall good chemical stability across most materials. In contrast to the results observed after ageing cycles, the kaolin coatings proved to be more stable. In samples A_KW_K and P_KW_K, the characteristic kaolinite bands, including the O-H stretching vibrations at 3690, 3670, and 3645 cm^{-1} and the Si-O-Si stretching bands, remained detectable after light exposure (Figure 34C, D) [34]. Similarly, the samples coated with PVA exhibited excellent chemical stability, with their main spectral features remaining unchanged after ageing, confirming the stability of the polymeric films to light exposure. The acrylic coating also showed good chemical stability under the applied light-ageing conditions, despite the well-documented sensitivity of acrylic polymers to UV radiation [50,51]. This behaviour is likely related to the relatively short exposure time, which limited the extent of photodegradation typically observed under prolonged irradiation. Conversely, samples incorporating kaolin as an additive exhibited a different behaviour. In particular, after ageing, the spectra of samples containing kaolin within the matrix, such as A_KW and P_KW, showed a marked loss of the kaolinite bands at 1065, 1010 and 910 cm^{-1}. Only minor absorptions around 790 cm^{-1} and 500-400 cm^{-1} were still detectable with reduced intensity (Figure 34A, B) [34].

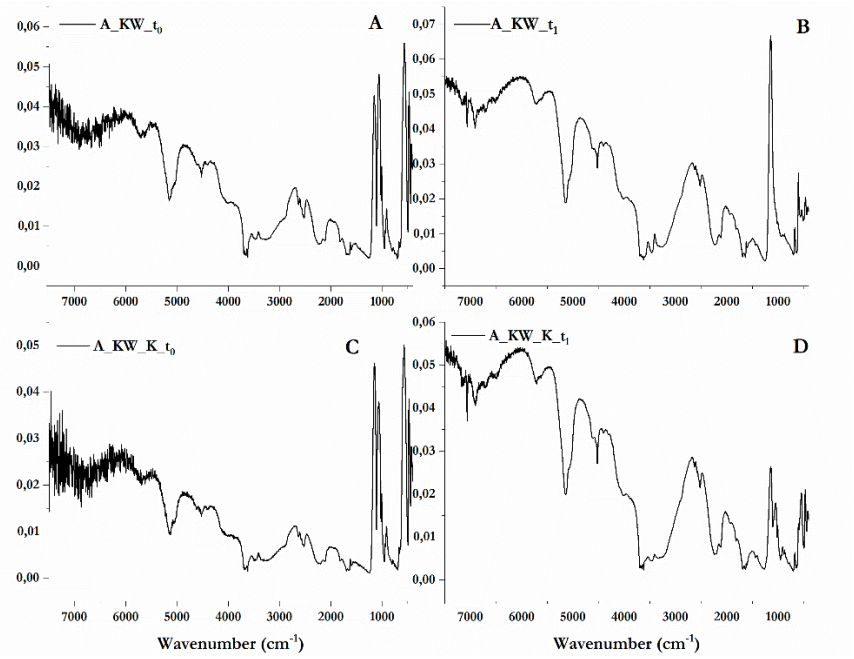

Figure 34. ER-FTIR spectra of sample A_KW before (A), and after light ageing (B). ER-FTIR spectra of sample A_KW_K before (C), and after light ageing (D).

This phenomenon was observed in both types of gypsum-based samples, but was more pronounced in the sample made with alabaster gypsum. These results indicated a partial degradation or loss of the kaolin phase within the matrix during light exposure. In contrast, the gypsum substrate remained chemically stable, as evidenced by the fact that its main vibrational feature remained detectable [31-39]. These observations may not result from the direct photodegradation of the kaolin itself, which is known to be photochemically stable, but rather from physical or chemical alterations in the surrounding organic matrix. These changes, including the formation of carbonyl groups or other reactive compounds resulting from lignin degradation, may affect the detectability or intensity of kaolinite bands in the FTIR spectra [52]. Overall, these observations underline the differential stability of kaolin depending on its application: coatings showed better resistance to light ageing than to cycle ageing, kaolin incorporated into the matrix was less stable.

In summary, light ageing had a limited impact on coatings but caused partial degradation of kaolin when incorporated into the matrix, confirming its lower chemical stability under exposure conditions, particularly when combined with organic components.

4.5.3.2 Optical light profilometry

The surface roughness data collected after light ageing revealed distinct trends between the two gypsum types (Table 21). In contrast to the results observed under cyclic ageing, samples made with alabaster gypsum more frequently exhibited an increase in surface roughness. These results suggested that alabaster formulations may be more sensitive to light ageing, particularly in the absence of effective protective treatments. Among the untreated samples, Paris gypsum exhibited a decrease in surface roughness. P_AG exhibited a notable reduction in Sq from 19.41 μm to 13.72 μm and in Sa from 15.38 μm to 10.64 μm, while A_AG showed a more moderate increase in Sq (from 8.53 μm to 10.06 μm) and Sa (from 6.67 μm to 8.10 μm), suggesting a less stable response to light exposure.

Among the protective treatments, PVA was the most effective in reducing surface roughness in both gypsum types. A_AG_PVA showed a decrease in Sq from 25.59 μm to 14.73 μm and in Sa from 21.63 μm to 12.24 μm, while P_AG_PVA decreased from 15.72 μm to 9.65 μm (Sq) and from 12.58 μm to 7.53 μm (Sa). Similar trends were observed in P_M_PVA and A_M_PVA (Figure 35), confirming the consistent performance of PVA under light ageing conditions.

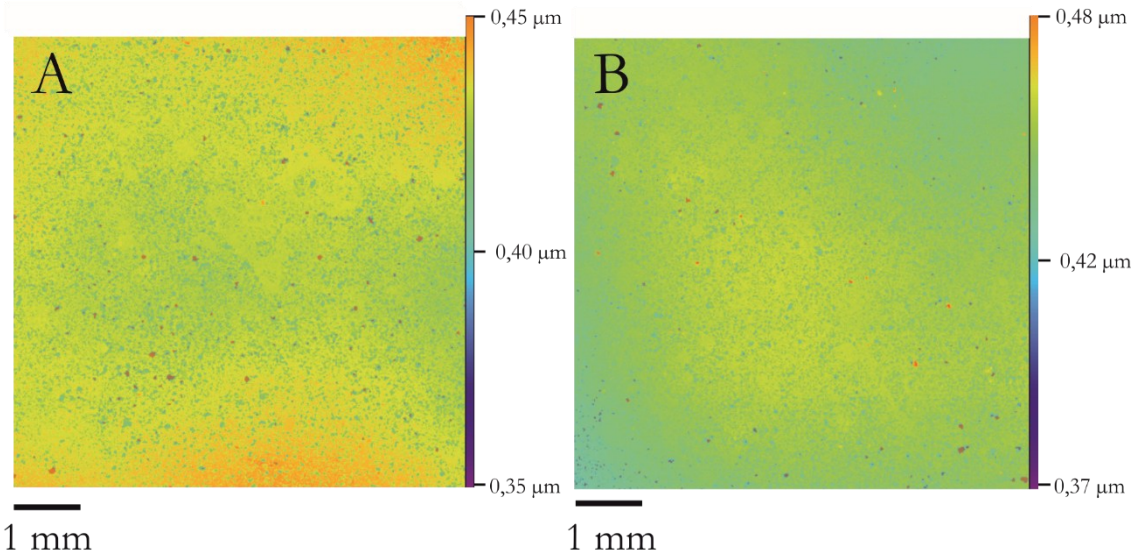

Figure 35. 3D surface comparison of sample A_M_PVA before (A) and after (B) light ageing. Area of analysis = 49 mm².

Acrylic resin samples showed variable behaviour depending on the gypsum type. In the case of Paris gypsum, P_AG_Ac showed a reduction in surface roughness; conversely, A_AG_Ac and A_M_Ac, both based on alabaster gypsum, displayed increases in Sq and Sa values, suggesting that the effectiveness of Acryl-EM 33 may be limited or strongly dependent on the matrix composition. P_M_Ac showed only minor changes in roughness values, suggesting limited impact of the ageing on the treatment. Kaolin-based treatments showed mixed results. A_AG_K and P_AG_K remained relatively stable, with only slight changes in roughness. A_M_K and P_M_K, however, differ significantly despite the use of the same treatment, highlighting the influence of the base formulation on treatment effectiveness.

Samples mixed with kaolin and wood powder showed the most unstable behaviour. P_KW exhibited the largest increase in roughness, with Sq rising from 12.46 µm to 18.76 µm and Sa from 8.82 µm to 14.07 µm. A_KW_PVA also showed substantial increase of these parameters, suggesting that kaolin and wood powder may reduce the effectiveness of the protective treatment.

In summary, PVA was the most reliable treatment for mitigating roughness changes under light ageing. Kaolin and acrylic resin provided less consistent protection, with outcomes strongly influenced by the specific gypsum-additive combinations.

4.5.3.3 Colourimetry

After each ageing cycle, changes in L^*, a^*, and b^* values were observed, though these changes varied across the samples. As L^* increases after ageing, colours became brighter in most samples, showing slight and moderate lightening [53]. Notably, in samples composed of Paris gypsum, such as P_M_Ac and P_M_PVA, there is an increase in the L^* value. Colour components, a^* and b^*, are very similar before and after the treatments. The only case in which we observed a certain degree of change is related to the component yellow-blue (b^*) of samples P_KW and P_M, which is correlated with a significant darkening and a decrease in the L^* values. In this sample we revealed a positive increment toward the yellow component (positive b^* values). Most of the samples showed non-significant colour differences, with ΔE^* values lower than 1 and between 1 and 3, and could not therefore be perceived by the human eye [35-37]. However, it is possible to observe some changes in the samples composed of Paris gypsum, where many values range between 3 and 5, especially in the mixture with Arabic Gum and marble powder (Table 22). In this case, the values are significant but still acceptable. The only exception was in sample P_KW in which ΔE^*_1 value was 5.39, which means that the difference can be observed with the naked eye. From these results, it can be deduced that colour variation is closely related to the composition of the samples. Specifically, Paris gypsum is more prone to colour changes compared to alabaster gypsum, especially when mixed with Arabic Gum and marble powder. Additionally, the application of PVA and Acryl-EM 33 coatings influenced the colour variation, while the kaolin finish proved to be more stable. For samples composed of Paris gypsum mixed with wood and kaolin, the absence of finishing affected the results, as the untreated sample showed the only significant colour variation (ΔE_1^* 5.39), whereas the treated samples were less susceptible to ageing. The ΔE^*_2 values indicate the colour difference after the second ageing cycle. Similar to ΔE^*_1 values, most samples exhibit ΔE^*_2 values lower than 1 or between 1 and 3 units, which are typically not perceivable by the human eye. However, notable exceptions include samples such as P_M_PVA or sample P_M_Ac in which the ΔE^*_2 value of 4.40 confirms the continued significant colour variation, and sample P_KW with a ΔE^*_2 of 6.93. This sample showed a significant colour difference after the second ageing cycle, which is visually perceivable.

After the third ageing cycle, additional variations in colour were recorded, with ΔE^*_3 values further clarifying the impact of material composition and surface treatments on the stability of the samples. While most of the alabaster gypsum samples (e.g., A_KW, A_KW_K, A_KW_Ac, A_KW_PVA) maintained ΔE_3^* values below the perceptibility

threshold of 3, samples composed of Paris gypsum continued to exhibit greater susceptibility to colour changes. Notably, P_KW showed a further increase in colour variation, reaching a ΔE^*_3 of 7.16, confirming its high instability without surface treatments. This result aligns with previous cycles, in which ΔE^*_1 and ΔE^*_2 were already above 5 and 6 units respectively. The application of coatings, such as Acryl-EM 33 and PVA, moderated this effect, with P_KW_Ac and P_KW_PVA showing more acceptable values of 2.92 and 2.55, respectively.

Similarly, other Paris gypsum samples, such as P_M_Ac and P_M_PVA, exhibited ΔE^*_3 values of 4.41 and 3.82 (Table 22), respectively, both exceeding the threshold of perceptibility and confirming the cumulative nature of the colour variation [36]. These changes are associated to the instability of the gypsum-additive matrix and the interactions with the applied coatings.

Among the Arabic gum mixtures, sample P_AG_PVA showed a ΔE^*_3 value of 3.52, indicating a persistent tendency toward colour change, while the untreated sample P_AG remained just above the threshold with 3.60. P_AG_Ac also reached a value of 3.43 (Table 22), highlighting how even coated, Paris gypsum samples may experience notable change when combined with Arabic gum. In contrast, alabaster gypsum samples remained generally stable, without samples exceeding 3. For instance, A_AG_Ac and A_AG_PVA maintained low ΔE^*_3 values of 0.31 and 2.45, respectively. The changes in ΔE^* values for these sample (Figure 36) suggest that the composition of Paris gypsum mixed with kaolin and wood powder is highly susceptible to ageing effects. The analysis underscores the susceptibility of Paris gypsum mixtures to colour variations upon ageing, especially when combined with Arabic gum and marble powder for untreated finishes or coated with acrylic resin.

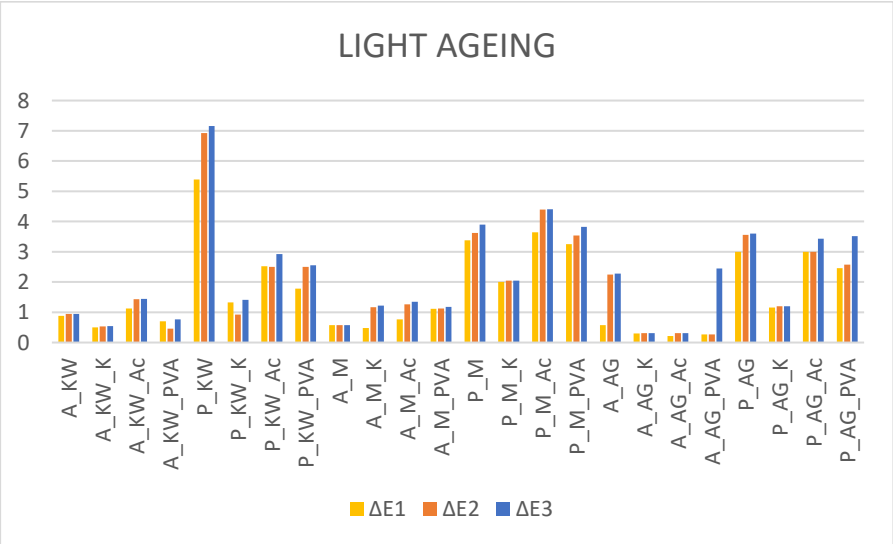

Figure 36. Colour variation (ΔE^*_1, ΔE^*_2 and ΔE^*_3) of samples subjected to accelerated light ageing. The ΔE^* values highlight the protective effectiveness of the coatings and the varying stability of the materials depending on their composition.

4.5.4 Summary of the outcomes

To provide a comprehensive comparison between the two ageing protocols, the main outcomes obtained from each analytical technique are summarised in Table 23. This structure highlighted how hygrothermal and light ageing affected the mock-up samples differently, and how material composition and coatings influenced their response across all analytical methods.

Hygrothermal ageing resulted in the most pronounced chemical and morphological changes, particularly in mixtures containing kaolin and wood powder or in Paris gypsum-based matrix. Light ageing mainly affected chromatic parameters and localised surface features, with limited chemical alteration of coatings. Across both protocols, PVA consistently proved the most effective treatment, while the performance of acrylic resin and kaolin coatings was strongly dependent on gypsum type and formulation. These integrated results form the basis for the final considerations presented in the conclusions.

Table 23. Summary of the main outcomes of hygrothermal and light ageing for each analytical technique.

Technique	Hygrothermal ageing	Light ageing
Macroscopic observation	Under hygrothermal conditions, the most recurrent alterations included edge rounding, micro-fractures and powdering, particularly in the alabaster gypsum formulations and in mixtures containing kaolin and wood powder. Paris gypsum tended to exhibit more superficial powdering but fewer edge losses. Uncoated samples were the most affected, while PVA and acrylic resin generally helped maintain surface cohesion, except in the KW-based mixtures where degradation remained evident.	Under light ageing, the observed changes were generally more limited and confined to the surface. Alabaster gypsum showed moderate increase in surface alteration, while Paris gypsum often exhibited slight smoothing or minimal variation, as observed for P_AG. PVA coatings effectively limited visible changes, although mixtures containing kaolin and wood powder continued to display the most unstable behaviour.
FTIR spectroscopy	Gypsum retained stable vibrational features across all samples. Marble powder also proved chemically stable. In contrast, kaolin bands (OH stretching, Si-O-Si stretching and Al-OH bending) were reduced or disappeared after ageing, particularly in KW formulations. Both PVA and acrylic resin coatings showed notable stability.	Gypsum remained unaffected by light exposure. Kaolin coatings preserved their characteristic spectral bands, while kaolin used as an additive displayed a significant loss of intensity (A_KW, P_KW). PVA and acrylic coatings exhibited excellent stability; the good performance of acrylic resin is likely related to the relatively limited UV-exposure time of the experiment.
Optical profilometry (Sq, Sa)	Paris gypsum formulations generally showed the most pronounced increase in roughness, with samples such as P_M and P_KW_K experiencing rises in Sq and Sa. By contrast, alabaster gypsum tended to remain stable or even exhibit a slight smoothing effect. PVA coatings consistently reduced surface roughness across all mixtures, while the performance of acrylic resin varied according to the substrate. Kaolin coatings proved unstable when applied to Paris gypsum mixtures.	Under light ageing, PVA continued to be the most effective treatment, producing a clear reduction in roughness parameter. Acrylic resin showed variable behaviour depending on the gypsum type. Kaolin coatings remained stable when applied to alabaster gypsum but were less effective on Paris gypsum. Mixtures containing kaolin and wood powder displayed the highest increases in roughness.
Colourimetry	Colour changes remained limited, with ΔE^* values ranging from 0.12 to 2.32, all below the perceptibility threshold. The highest variations occurred in P_AG_K, P_KW and P_AG. The b^* coordinate (yellow-blue axis) was the most affected, especially in Paris gypsum mixtures. Both PVA and acrylic resin reduced colour variations, while the behaviour of kaolin was more variable.	Light exposure induced stronger variations in some Paris gypsum samples, with several exceeding the $\Delta E^* = 3$ threshold (P_KW and P_M). Alabaster gypsum remained consistently stable across cycles. PVA and acrylic coatings generally reduced colour shifts, while the kaolin coating showed better performance under light ageing than under hygrothermal conditions.

4.6 Conclusion

This study investigated the behaviour of historical gypsum-based mixtures subjected to accelerated ageing, with the aim of supporting the development of effective conservation strategies for plaster replicas. By combining historical research, mock-up preparation, and multi-analytical approach, it was possible to identify degradation mechanisms and assess the performance of different protective coatings. The experimental design, based on historical recipes and environmental data collected from museum contexts, enabled the simulation of conditions typically experienced by plaster casts exposed to uncontrolled environments.

The type of gypsum had a significant influence on ageing behaviour. Alabaster gypsum samples exhibited greater chemical, morphological, and chromatic stability, maintaining lower surface roughness and showing minimal colour variations after both hygrothermal and light ageing. In contrast, mixtures based on Paris gypsum proved more vulnerable to environmental stress, with pronounced surface roughening, additive loss, and chromatic shifts, in some cases exceeding the perceptibility threshold. These results highlighted the importance of considering original material properties when developing conservation strategies.

Additives strongly affected the durability of the mixtures. Marble powder was the most stable, contributing to both chemical and mechanical integrity during ageing. Arabic gum, although chemically stable, increased moisture sensitivity, particularly in Paris gypsum formulations, but without severely compromising overall durability. Conversely, mixtures containing kaolin and wood powder were the least stable: their hygroscopic nature promoted moisture retention and swelling, which enhanced susceptibility to surface degradation and colour change. These findings confirm the complexity introduced by historical additives and underline the need for detailed material characterisation prior to conservation interventions.

Protective surface treatments significantly influenced material behaviour under ageing. PVA coatings offered the most effective protection, ensuring chemical stability, limiting surface roughness development, and reducing chromatic changes across all formulations. Acrylic resin (Acryl-EM 33) also performed well, particularly on alabaster substrates, although its effectiveness varied more with the matrix composition. Kaolin-based coatings, while historically compatible, were less effective under thermo-hygrometric cycles, showing loss of cohesion and chemical alteration, but were comparatively stable under light ageing. This suggests that inorganic coatings may not ensure sufficient long-term protection in fluctuating environments.

The comparison of the two ageing protocols revealed that hygrothermal cycles induced more severe chemical and morphological changes than light exposure, promoting material loss. Light ageing mainly affected surface layers, with changes confined to chromatic alterations. These results underline the importance of maintaining stable environmental conditions to preserve gypsum-based artefacts.

Overall, the study confirms that conservation strategies must be tailored to material composition, additive content, surface treatments, and the expected environmental conditions. PVA proved the most effective coating in improving the long-term stability of gypsum substrates, particularly those containing fewer stable additives. The integrated approach of historical research, experimental replication, and multi-analytical monitoring adopted has proven effective for understanding material behaviour over time and for developing scientifically supported strategies for the conservation of historical plaster replicas.

References

[1] E. M. Payne, The Conservation of Plaster Casts in the Nineteenth Century, Stud. Conserv., vol. 65 (2022), pp. 37-58.

[2] E. Salavessa, S. Jalali, L. M. O. Sousa, L. Fernandes, A. M. Duarte, Historical plasterwork techniques inspire new formulations, Constr. Build. Mater., vol. 48 (2013), pp. 858-867.

[3] C. Arcolao, Le ricette del Restauro: Malte, intonaci, stucchi dal XV al XIX secolo, Saggi Marsilio, Venezia, 1998. [In Italian]

[4] Turco, Il gesso lavorazione – trasformazione – impieghi, Ulrico Hoepli, Milano, 1861. [In Italian]

[5] K. Elert, P. Bel-Anzué, M. Burgos,Ruiz, Influence of calcination temperature on hydration behavior, strength, and weathering resistance of traditional gypsum plaster, Constr. Build. Mater, vol. 367 (2023), 130361.

[6] M. Mishmastnehi, A. E. S. Van Driessche, G. J. Smales, A. Moya, T. M. Stawski, Advanced materials engineering in historical gypsum plaster formulations, Proc. Natl. Acad. Sci., vol. 120 (2023), e22088361120.

[7] N. B. Singh, B. Middendorf, Calcium sulphate hemihydrate hydration leading to gypsum crystallization, Prog. Cryst. Growth Charact. Mater., vol 53 (2007), pp. 57-77.

[8] B. Lee, G. Kim, J. Nam, K. Lee, G. Kim, S. Lee, K. Shin, T. Koyama, Influence of α-Calcium Sulfate Hemihydrate on Setting, Compressive Strength, and Shrinkage Strain of Cement Mortar, Mat., vol. 12 (2019), 163.

[9] E.-S. I. Al-Wakeel, Alabaster, and selenite gypsum: I-dehydration-rehydration comparison studies, Mater. Res. Technol., vol. 18 (2002), pp. 365-368.

[10] Z. Wei, Q. Zhang, X. Li, Crystallization Kinetics of α-Hemihydrate Gypsum Prepared by Hydrothermal Method in Atmospheric Salt Solution Medium, Crystals, vol. 11 (2021), 843.

[11] M. S. Başpinar, E. Kahraman, Modifications in the properties of gypsum construction element via addition of expanded microporous silica granules, Constr. Build. Mater., vol. 25 (2011), pp. 3327-3333.

[12] V. Risdonne, C. Hubbard, V. H. López Borges, C. Theodorakopoulos, Materials and Techniques for the Coating of Nineteenth-century Plaster Casts: A Review of Historical Sources, Stud. Conserv., vol. 67 (2022), pp. 186-208.

[13] P. M. da Silveira, M. do Rosário Veiga, J. de Brito, Gypsum coatings in ancient buildings, Constr. Build. Mater., vol. 21 (2007), pp. 126-131.

[14] V. Risdonne, C. Hubbard, J. Puisto, C. Theodorakopoulos, A multi-analytical study of historical coated plaster surfaces: the examination of a nineteenth-century V&A cast of a tombstone, Herit. Sci., vol.9 (2021), pp. 70-89.

[15] K. Elert, C. Benavides-Reyes, C. Cardell, Effect of animal glue on mineralogy, strength and weathering resistance of calcium sulfate composite materials, Cem. Concr. Compos., vol. 96 (2019), pp. 274-283.

[16] M. Murat, A. Attari, Modification of some physical properties of gypsum plaster by addition of clay minerals, Cem. Concr. Res., vol.21 (1991), pp. 378-387.

[17] K. Regulska, A. Repelewicz, Properties of gypsum composites with sawdust, E3S Web. Conf., vol 97 (2019), 02037.

[18] K. Fabbri, Historic Climate in Heritage Building and Standard 15757: Proposal for a Common Nomenclature, Climate, vol. 10 (2022), pp. 4-12.

[19] M. Doni, I. Fierascu, R. C. Fierascu, Recent Developments in Materials Science for the Conservation and Restoration of Historic Artefacts, Appl. Sci., vol. 14 (2024), 11363.

[20] F. Sitzia, C. Lisci, J. Mirão, Accelerate ageing on building stone materials by simulating daily, seasonal thermo-hygrometric conditions and solar radiation of Csa Mediterranean climate, Constr. Build. Mater., vol. 266 (2021), 121009.

[21] UNI EN 15886:2011, Conservazione dei beni culturali – Metodi di prova – Misurazione del colore delle superfici, UNI, Milano, 2011.

[22] M. Mattone, S. Rescic, F. Fratini, R. Mangalli Del Fà, Experimentation of Earth-Gypsum Plasters for the Conservation of Earthen Constructions, Int. J. Archit. Herit., (2017).

[23] L. N. Warr, IMA-CNMNC approved mineral symbols, Mineral. Mag., vol. 85 (2021), pp. 291-320.

[24] D. Gramtorp, K. Botfeldt, J. Glastrup, K. P. Simonsen, Investigation of Anne Marie Carl-Nielsen's wax models, Stud. Conserv., vol. 60 (2015), pp. 97-106.

[25] G. Vasco, A. Serra, D. Manno, G. Buccolieri, L. Calcagnile, L. Miotto, L. Valli, A. Buccolieri, Diagnostic investigation to support the restoration of the polychrome terracotta relief "Madonna and Child" in Piove di Sacco (Padova, Italy), J. Cult. Herit., vol. 53 (2021), pp. 80-87.

[26] G-L. Liu, S. G. Kazarian, Recent advances and applications to cultural heritage using ATR-FTIR spectroscopy and ATR-FTIR spectroscopic imaging, R. Soc. Chem., vol. 147 (2022), pp. 1777-1797.

[27] L. Bishop, M. D. Dyar, S. J. King, A. J. Brown, G. A. Swayze, What Lurks in the Martian Rocks and Soil? Investigation of Sulfates, Phosphates, and Perchlorates. Spectral properties of Ca-sulfates: Gypsum, bassanite and anhydrite, Am. Mineral., vol. 99 (2014), pp. 2105-2115.

[28] C. Ye, E. C. Sklute, T. D. Clotch, Orientation averaged visible/near-infrared and mic-infrared optical constants of hydrous Ca-sulfates: gypsum and bassanite, Earth Space Sci., vol.8 (2021).

[29] F. Izzo, C. Germinario, C. Grifa, A. Langella, M. Mercurio, External reflectance FTIR dataset (4000-400cm-1) for the identification of relevant mineralogical phases forming Cultural Heritage materials, Infrared Phys. Technol., vol. 106 (2020), 103266.

[30] V. Brunello, C. Corti, A. Sansonetti. C. Tedeschi, L. Rampazzi, Non-invasive FTIR study of mortar model samples: comparison among innovative and traditional techniques, Eur. Phys. J. Plus, vol. 134 (2019), 270.

[31] R. Stach, P. Krebs, F. Jones, B. Mizaikoff, Observing non-classical crystallisation processes in gypsum via infrared attenuated total reflectance spectroscopy, Cryst. Eng. Comm., vol. 19 (2017), pp. 14-17.

[32] Y. Liu, Raman, Mid-IR, and NIR spectroscopic study of calcium sulfates and mapping gypsum abundances in Columbus crater, Mars, Planet Space Sci., vol. 163 (2018), pp. 35-41.

[33] Z. I. Glavcheva, D. Y. Yancheva, Y. K. Kancheva, E. A. Velcheva, B. A. Stamboliyska, Development of FTIR spectra database of reference art and archaeological materials, Bulg. Chem. Commun., vol. 46 (2014), pp. 164-169.

[34] M. Castellano, A. Turturro, P. Riani, T. Montanari, E. Finocchio, G. Ramis, G. Busca, Bulk and surface properties of commercial kaolins. Appl. Clay Sci., vol. 48 (2010), pp. 446-454.

[35] C. M. Grossi, P. Brimblecombe, R. M. Esbert, Francisco Javier Alonso, Color changes in architectural limestones from pollution and cleaning, Color Res. Appl., vol. 32 (2007), pp. 320-331.

[36] D. Benavente, F. Martiñez-Verdú, A. Bernabeu, V. Viqueira, R. Fort, M- A. García del Cura, C. Illueca, S. Ordóñez, Influence of surface roughness on colour changes in building stones, Color Res. Appl., vol. 28 (2002), pp. 343-351.

[37] E. Molina, A. Arizzi, D. Benavente, G. Cultrone, Influence of Surface Finishes and Calcium Phosphate-Based Consolidant on the Decay of Sedimentary Building Stones Due to Acid Attack, Front. Mater., vol. 7 (2020), 581979.

[38] A. Kumar, P. Lingfa, Sodium bentonite and kaolin clays: Comparative study on their FT-IR, XRF, and XRD, Mater. Today Proc., vol. 22 (2020), pp. 737-742.

[39] M. T. Freie, A. S. Silva, M. do Rosário Veiga, J. de Brito, Studies in ancient gypsum based plaster towards their repair: Mineralogy and microstructure, Constr. Build. Mater., vol. 196 (2019), pp. 512-529.

[40] E. Franceschi, F. Locardi, Strontium, a new marker of the origin of gypsum in cultural heritage?, J. Cult. Herit., vol. 15 (2014), pp. 522-527.

[41] E. Playà, L. Rosell, The celestine problem in gypsum Sr geochemistry: An evaluation of purifying methods of gypsiferous samples, Chem. Geol, vol. 221 (2005), pp. 102-116.

[42] M. T. Freire, A. Santos Silva, M. do Rosário Veiga, J. de Brito, The history of Portugese interior plaster coatings: a mineralogical survey using XRD, Archaeometry, vol. 57 (2015), pp. 147-165.

[43] I. P. Cardoso, E. Pye, Gessoes in Portugese Baroque gilding grounds, part 1: a study of historical documentary sources, Stud. Conserv., vol. 62 (2017), pp. 185-209.

[44] Q. L. Yu, H. J. H. Brouwers, Microstructure and mechanical properties of β-hemihydrate produced gypsum: An insight from its hydration process, Constr. Build. Mater., vol. 25 (2011), pp. 3149-3157.

[45] S. D. de Souza Rodrigues, J. G. G de Sousa, N. C. Olivier, Evaluation of the degradation of gypsum subjected to natural aging, Mater. Struct., vol.58 (2025), 96.

[46] M. A. Pedreño-Rojas, M. J. Morales-Conde, P. Rubio-de-Hita, F. Pérez-Gálvez, Impact of Wetting-Drying Cycles on the Mechanical Properties and Microstructure of Wood Waste-Gypsum Composites, Materials, vol. 12 (2019), 1829.

[47] R. Haigh, M. Sandanayake, S. Sasi, E. Yaghoubi, P. Joseph, Z. Vrcelj, Microstructural attributes and physiochemical behaviours of concrete incorporating various synthetic textile and cardboard fibres: A comparative review, J. Build. Eng., vol. 86 (2024), 108690.

[48] M. T. Doménech-Carbó, A. Doménech-Carbó, L. Osete-Cortina, M. C. Saurí-Peris, Characterization of organic materials in art conservation and archaeometry, Technologia Artis, vol. 1 (2006), pp. 39-58.

[49] M. Á. Iglesias-Campos, J. L. Pdara Pérez, S. García Fortes, Microblasting cleaning for façade repair and maintenance: Selecting technical parameters for treatment efficiency, Constr. Build. Mater., vol. 94 (2015), pp. 605-612.

[50] S. Bracci, M. J. Melo, Correlating natural ageing and Xenon irradiation of Paraloid® B72 applied on stone, Polym. Degrad. Stabil., vol. 80 (2003), pp. 533-541.

[51] M. J. Melo, S. Bracci, M. Camaiti, O. Chiantore, F. Piacenti, Photodegradation of acrylic resins used in the conservation of stone, Polym. Degrad. Stabil., vol. 66 (1999), pp. 23-30.

[52] D. Rosu, C. A. Teaca, R. Bodirlau, L. Rosu, FTIR and color change of the modifiec wood as a result of artificial light irradiation, J. Photochem. Photobiol. B., vol. 99 (2010), pp. 144-149.

[53] L. Acke, J. Vleugels, M. Kovač, J. Verlinden, Comparative study of colour stability and shape retention: From virtual reconstruction to physical restoration of a porcelain figurine, Digit. Appl. Archaeol., Cult. Herit., vol. 30 (2023), e00280.

5. Part 3: Inside porosity: effects of artificial ageing on the decay of heritage gypsum materials

This manuscript is currently in preparation for publication. FB, EB, CC and CM designed the study and developed the methodology. NP analyses were carried out, and then processed by FB. MIP measurements were collected by EB and processed by FB. SEM-BSE images for digital image analysis were acquired by FB and Jacopo Nava, and then processed by FB and CC. Micro-CT analyses were performed by Joaquim Sanctorum, and the data were processed by FB. Hygrothermal tests were conducted by FB.
All authors discussed the results and agreed on their interpretation. FB wrote the manuscript, with all co-authors contributing to the final revision.

Federica Bubola[1*], Eleonora Balliana[2], Chiara Coletti[1], Claudio Mazzoli[1]

[1] Department of Geosciences, University of Padova, via Giovanni Gradenigo 6, 35131 Padova, Italy

[2] Department of Environmental Sciences, Informatic and Statistics, Ca' Foscari University, Via Torino 155, 30172 Mestre, Italy

---

Abstract

The study of porosity in gypsum-based samples is essential for understanding their response to environmental stressor and their long-term stability. Pore size, shape, and connectivity influence moisture transport, playing a key role in the physical stability of the material. In this work, mock-up samples composed of different gypsum types and additives were analysed before and after cyclic ageing in controlled temperature and humidity conditions. The formulations included alabaster gypsum and Paris gypsum, combined with marble powder, a mixture of kaolin and wood powder, or Arabic gum as additives. A multi-analytical approach was adopted, combining nitrogen physisorption (NP), mercury intrusion porosimetry (MIP), scanning electron microscopy (SEM) with 2D image processing, X-ray micro-computed tomography (micro-CT), and hygroscopic tests. These complementary methods allowed for a detailed characterisation of the pore system at different scales. The results were compared to evaluate how different formulations affect porosity and its evolution over time, providing useful insight into the material's behaviour under ageing and its capacity to interact with moisture.

5.1 Introduction

Gypsum-based materials have long been used over the centuries for architectural finishes, sculptural decoration, and the production of ornamental or functional components, due to their workability and ability to replicate fine surface details. These characteristics have made gypsum particularly suitable for the production of casts, including architectural ornaments, sculptural replicas, and museum reproductions. However, the intrinsic softness and high porosity of gypsum make it particularly vulnerable to mechanical damage and environmental degradation [1]. In indoor environments, particularly those lacking adequate climate control, fluctuations in temperature and relative humidity can lead to structural and mechanical changes, salt migration, increased water retention, and compromise their long-term stability [2-5]. These factors promote the formation of cracks, surface powdering, and detachment phenomena, especially in porous and poorly cohesive materials. Although many studies have examined how ambient conditions affect traditional building materials [6,7], investigations specifically focused on gypsum-based replicas and heritage casts remain relatively limited. Gypsum casts and replicas have porous microstructure made of intergrown crystals of calcium sulphate dihydrate ($CaSO_4 \cdot 2H_2O$), which makes them particularly sensitive to changes in temperature and humidity. When the relative humidity is high, water can be absorbed into the pores as vapour or through capillary condensation. If the conditions change, this water is released, causing the material to expand and contract repeatedly [8]. Long-term exposure to high temperatures and low humidity can partially dehydrate gypsum, transforming it into bassanite ($CaSO_4 \cdot ½\ H_2O$), leading to a loss of mechanical strength and internal cohesion [9,10]. Although this transformation can be reversed, prolonged dehydration may lead to permanent damage. High relative humidity (<90 %) can also favour biological growth and pollutant accumulation, while condensation on the surface may cause detachments and pulverisation. For this reason, controlling temperature and humidity in museum environments is crucial for preserving the structural and visual integrity of gypsum materials [8].

In the context of conservation science, porosity is essential for assessing the durability of gypsum-based materials and predicting their behaviour under environmental stress. Pore size, shape, and connectivity influence both the hygroscopic response of the material and its susceptibility to physical degradation mechanisms and the effectiveness of conservation treatments. The rapid setting of gypsum further contributes to the formation of a heterogeneous pore network which is influenced by its formulation and processing conditions [11].

Porosity in gypsum systems originates from the hydration of calcium sulphate hemihydrate ($CaSO_4 \cdot ½H_2O$) into dihydrate ($CaSO_4 \cdot 2H_2O$), resulting in a three-dimensional network of elongated crystals. The resulting microstructure is influenced by several variables, such as the type of gypsum (e.g., alabaster gypsum or Paris gypsum), particle size distribution, water-to-powder ratio, and the addition of organic or inorganic additives [12-15]. In this study, the water-gypsum ratio was optimised individually for each formulation through preliminary casting trials. Starting from values reported in historical recipes and technical datasheets, the amount of water was progressively adjusted to achieve suitable workability and proper setting for each mixture. Once identified, the optimal ratio was kept constant throughout the preparation of the mock-ups (see Section 4.2).

This study aims to investigate the relationship between formulation, porosity, and environmental durability in gypsum-based materials through a multi-analytical approach involving:

1. The characterisation of porosity in mock-up formulations combining different gypsum types and additives, to investigate the role of composition in microstructural development;
2. The evaluation of microstructural changes by comparing the internal pore structure before and after artificial ageing, focusing on the evolution of porosity and morphology under simulated indoor environmental conditions;
3. The assessment of hygroscopic behaviour of each formulation under controlled humidity cycles, to investigate the processes linking pore structures with atmospheric moisture interaction [2].

Porosity was studied both before and after artificial ageing to assess how different formulations may react to hygrothermal stress and how their internal structure changes over time. A multi-analytical approach was adopted to characterise the complex pore system of gypsum-based materials, which includes voids of different sizes, shapes, and degrees of connectivity. Each technique was selected to provide insight into specific pore size range, allowing for a comprehensive description of the material's microstructure and its evolution over time.

To compare the pore size distributions obtained from the different techniques, pores were categorised into three dimensional classes: micropores (<10 μm), mesopores (10-400 μm), and macropores (>400 μm). This classification, adapted from De Quervain [16], was adjusted to better match the characteristics of the analysed gypsum samples and the

resolution limits of the methods. Fixed threshold systems often fail to describe materials with heterogeneous or multimodal porosity [17,18]. Mercury intrusion porosimetry (MIP) was employed to evaluate pore size distribution and cumulative pore volume, with a focus on mesopores and macropores. Although widely adopted, MIP has known limitations, including the ink-bottle effect and the potential for sample alteration caused by high intrusion pressure [19,20]. To complement this technique and provide a more complete description of the pore network, nitrogen physisorption (BET and BJH models) analyses were performed. These allowed for the assessment of microporosity and specific surface area, offering valuable information on the material's fine porosity and overall textural characteristics [21,22].

To overcome the limitations of individual techniques and achieve a more comprehensive understanding of the pore system, micro-CT was also employed. Micro-CT enabled the visualisation and quantification of internal structures, such as air voids, cracks, and connected pore networks, with sub-micron resolution depending on the instrument used [23]. The combined use of MIP and micro-CT has proven effective in enhancing the characterisation of pore morphology and connectivity in both mock-up and historical materials. MIP provides information about pore size distribution and cumulative pore volume, especially for meso- and macropores. Micro-CT complements this identifying both open and closed pores, as well as assessing overall pore connectivity and three-dimensional morphology. In addition, microstructural observations were carried out using Scanning Electron Microscopy (SEM), to investigate the spatial distribution, morphology, and connectivity of the pore system. SEM enabled high-resolution 2D imaging of surface features, highlighting differences in crystal shape, and pore structure across samples. This integrated approach allows a more comprehensive analysis of the pore network [17,18]. In this study, the adoption of this approach is particularly useful to evaluate how different additives normally used in historical plasters, such as marble powder, kaolin or organic binders like Arabic gum, affect the resulting microstructure [17,18,24] and the degradation processes [25].

The results provide new insights into the behaviour of historical gypsum-based plasters by correlating porosity with hygrothermal response and microstructural changes, with particular attention to the influence of original formulations and ageing effects.

5.2 Materials

To study the porosity of gypsum-based materials, a series of six mock-up samples was prepared using mixtures derived from historical formulations, as already described in Part 2 [26,27]. These recipes were selected for their relevance to traditional practices and were adapted as necessary to ensure consistency and reproducibility. In this part, only uncoated samples were considered, as the presence of surface treatments could affect the internal pore structure and compromise the reliability of the measurements.

The samples were produced using two types of gypsum, alabaster gypsum (A) and Paris gypsum (P), combined with additives commonly found in historical or conservation contexts: marble powder (M), Arabic Gum (AG), and a mixture of kaolin and wood powder (KW). Animal glue, used as a binder, was incorporated as a pre-diluted aqueous solution to improve workability and delay setting times. Each formulation was previously tested and refined to optimise the water-to-gypsum ratio, taking into account the different absorption properties of the additives. The composition of the samples selected for porosity analysis is summarised in Table 24.

Table 24. Composition of gypsum-based mixtures analysed for porosity.

Acronyms	Gypsum type	Additives	Water content (g)
A_M	Alabaster	Marble powder	125
P_M	Paris	Marble powder	170
A_AG	Alabaster	Arabic gum	700
P_AG	Paris	Arabic gum	730
A_KW	Alabaster	Kaolin + wood powder	360
P_KW	Paris	Kaolin + wood powder	385

A: Alabaster gypsum
P: Paris gypsum

M: Marble powder
AG: Arabic gum
KW: Kaolin and wood powder

All samples were produced as 5x5x5 cm cubes. Subsamples were later taken from the mock-ups to fit the specific needs of each porosity test. To support the visual assessment of internal features, representative samples were sectioned to expose their inner structure. These cross-sections, shown in Figure 37, highlight visible differences in pore-size distribution across the different formulations.

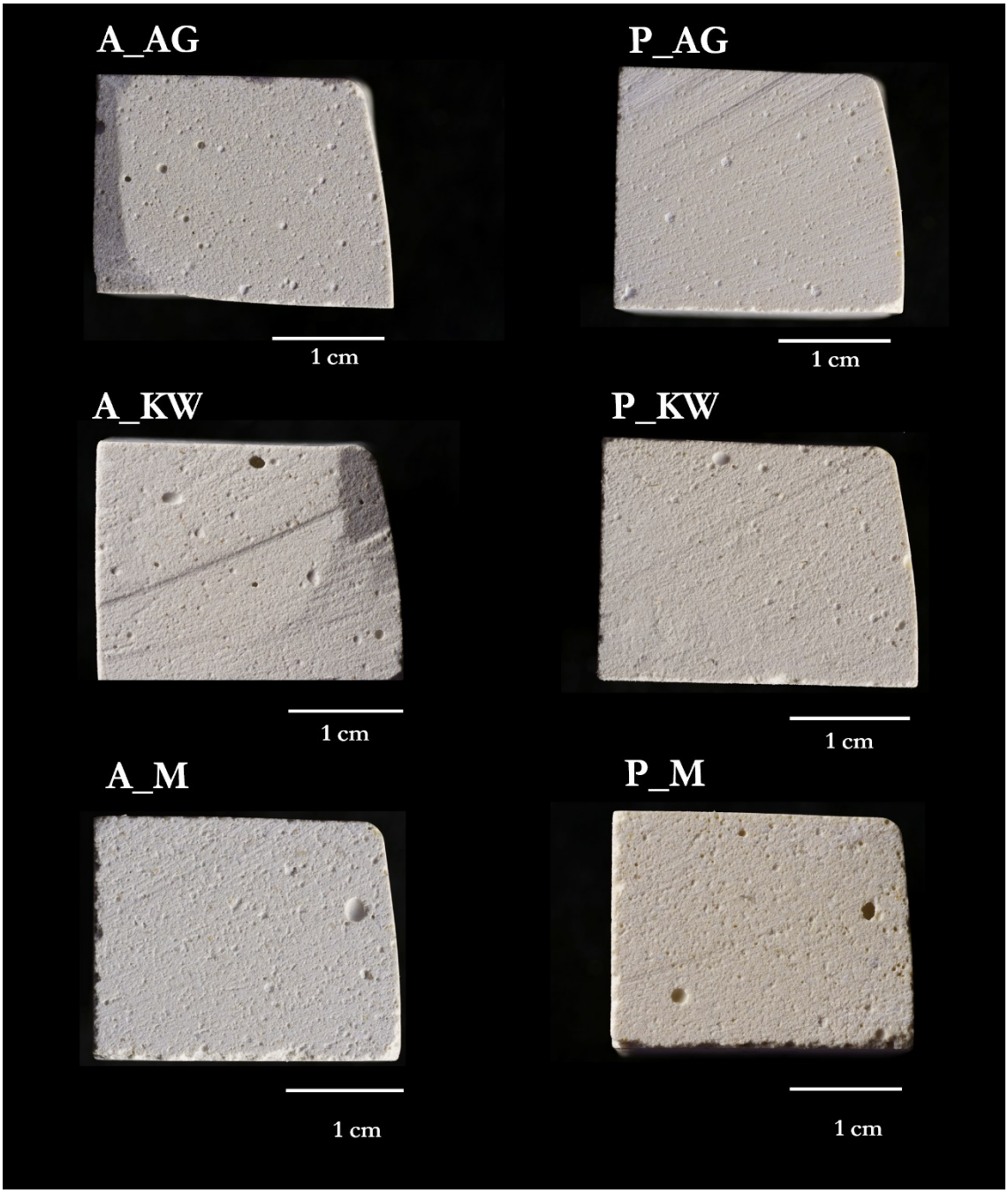

Figure 37. Cross-sections of gypsum-based samples, showing the internal features of the six formulations. The images highlight visible differences in pore size and distribution. Scale bar = 1 cm.

5.3 Methods

5.3.1 Analytical procedure

The experimental procedure (Figure 38) was designed to investigate how different gypsum-based formulations respond to environmental stress, with a focus on the evolution of porosity and its role in moisture interaction. A multi-analytical approach was adopted to evaluate changes before and after artificial ageing. In particular, porosity was studied both before (t_0) and after (t_1) ageing, to assess how thermal and humidity fluctuations affect the internal microstructure. To complement porosity analysis, sorption tests were performed to evaluate the capacity of each formulation to adsorb and desorb moisture under controlled hygrothermal conditions.

The interaction with moisture is a major degradation factor in gypsum materials, often leading to cracking, surface detachment, and other physical damage [2]. For this reason, understanding how pore characteristics influence hygroscopic behaviour is crucial. The presence of large, open pores may promote capillary condensation, while very small and poorly connected pores may limit desorption and favour water retention. For this reason, particular attention was given to the dimensional range and morphology of the pore systems.

Porosity was characterised using four complementary techniques: Nitrogen physisorption to assess microporosity, surface area and fine pore distribution; MIP to quantify meso- and macropores, as well as total pore volume and dominant pore sizes; 2D digital image analysis of SEM-BSE images, to evaluate apparent porosity, pore morphology and visual heterogeneity; micro-CT to provide a three dimensional reconstruction of pore structure, enabling quantification of total porosity, sphericity, and size distribution.

The results obtained from these methods were compared to evaluate the effects of formulation and ageing on the pore network. In addition, hygroscopic sorption tests were performed to understand the interaction between porosity and moisture, to identify which formulations are more prone to water uptake or retention.

The following sections provide a detailed description of the analytical techniques used for porosity characterisation, as well as the procedures adopted for artificial ageing and hygroscopic sorption tests.

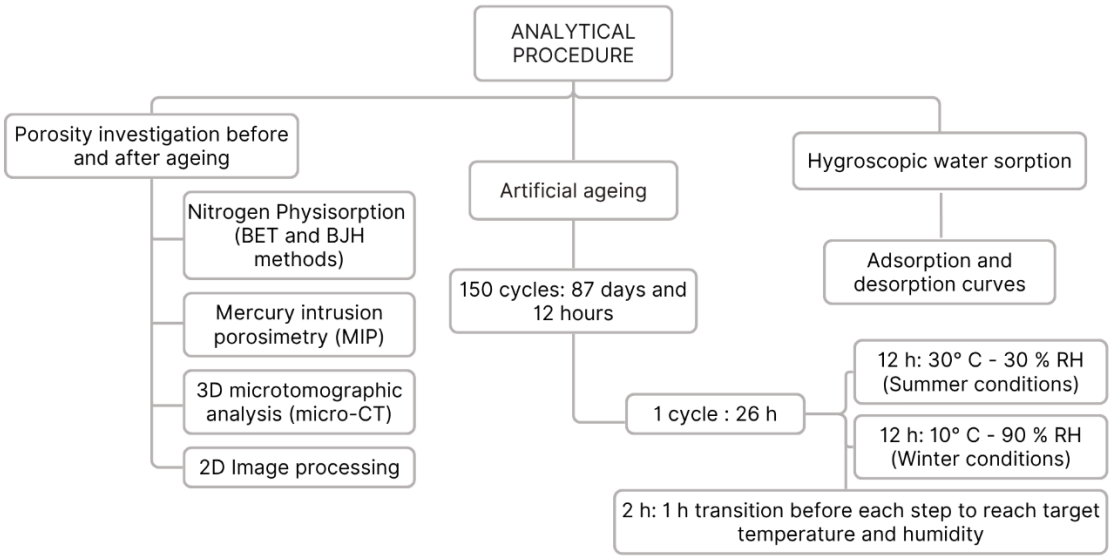

Figure 38. Analytical procedure employed in this study.

5.3.1.1 Porosity

Porosity was evaluated through a combination of nitrogen physisorption analysis, MIP, 2D image analysis of back-scatter electron (BSE) images acquired by SEM, and micro-CT. Each technique contributed to the characterisation of different portions of the pore size spectrum, from the nano- to the macroscopic scale. The following sections describe the analytical procedures and data processing methods used for each porosity analysis.

Nitrogen physisorption (NP) analysis was used to investigate the porosity of the gypsum-based samples in the pore diameter range of approximately 20 to 1000 Å, corresponding to micro- and mesopores. Measurements were carried out at the condensation temperature of nitrogen (-196 °C, 77 K) using a Micrometrics Tristar II Plus instrument. Before each analysis, the samples were degassed at 200 °C under vacuum (10^{-3} Torr) for 2 hours to remove physisorbed moisture and volatile compounds, in accordance with instrument operating protocols. Such conditions may induce partial dehydration of gypsum, potentially leading to the formation of bassanite. This limitation is considered in the interpretation of the results. The specific surface area (expressed in m^2/g) was calculated using the Brunauer-Emmett-Teller (BET) method, applied in the relative pressure range appropriate for multilayer adsorption [28]. The total pore volume was determined from the volume of nitrogen adsorbed at a relative pressure $p/p_0 \approx 0.9$ (expressed in cm^3/g), corresponding to capillary condensation in mesopores. The pore size distribution was calculated using the Barrett-Joyner-Halenda (BJH) model, applied to the desorption branch of the isotherm, which is widely used for mesoporous materials due to its relative stability and resolution [29]. The interpretation of nitrogen physisorption data relies on several theoretical assumptions. The

BJH method, in particular, assumes that the pores are cylindrical and rigid, and that capillary condensation and evaporation occur according to established thermodynamic principles [30,31]. Because of these assumptions, the BJH method may underestimate pore size when the actual pore shapes deviate from the ideal cylindrical model. Nitrogen physisorption at 77 K allows the construction of adsorption-desorption isotherms by recording the amount of nitrogen adsorbed at relative pressure (p/p_0). Initially, adsorption occurs in micropores due to their high surface energy, followed by monolayer and multilayer adsorption in mesopores, and finally by capillary condensation as the relative pressure approaches saturation. The desorption branch, recorded during gradual pressure reduction, provides additional insight into pore connectivity and geometry. The shape of the isotherms and the presence of hysteresis loops offer qualitative information on pore structure and were classified according to the IUPAC system, with specific hysteresis patterns (H1–H4) commonly associated with mesopores [31]. To complement the pore size distribution obtained from the BJH analysis, additional parameters such as total pore volume and average pore radius were calculated using simplified expressions derived from gas sorption theory. The condensed volume of nitrogen (V_{liq}) was estimated as:

$$V_{liq} = \frac{P_a V_{ads} V_m}{RT}$$

where V_{liq} is the volume of adsorbed nitrogen, P_a is the ambient pressure, V_{ads} is the volume of adsorbed vapour, V_m is the volume of nitrogen which is adsorbed as a monolayer, R is the universal gas constant, and T is the absolute temperature (K). The average pore radius (r_p) was then calculated under the assumption of cylindrical pore geometry as:

$$r_p = \frac{2V_{liq}}{S}$$

where S is the specific surface area obtained via BET analysis. These equations were also adopted in similar studies to estimate average pore radii from nitrogen physisorption data [17].

Mercury intrusion porosimetry (MIP) was selected to study the meso- and macro-porous structure of gypsum-based samples. Subsamples were collected using a scalpel, then dried at room temperature before the analysis. Measurements were performed using a Pascal 140 and Pascal 240 (Thermo Nicolet) porosimeters, equipped with an automatic

pressurisation system based on continuous speed-up adjustment logic. This setup enables the characterisation of pores ideally down to a minimum diameter of 3.7 nm.

The method is based on the Washburn equation [32], which relates the radius of a cylindrical pore r to the absolute applied pressure P, the mercury surface tension γ, and the contact angle θ between mercury and the solid surface [20]:

$$r = -\frac{2\gamma cos\theta}{P}$$

where γ is assumed as 484 mN/m and θ as 130 ° [33]. Despite MIP being the most used technique for porosity investigation, several limitations are associated with this method. One of the most significant is the ink-bottle effect: when large pores are connected to the outside by much smaller openings (called throats), the instrument detects only the narrower access, and not the actual size of the internal pore. As a result, the pore size distribution may underestimate larger internal pores [19,34,35]. Additionally, the high pressures applied during analysis can sometimes cause cracks or structural damage in materials such as gypsum, which may not be visible but could impact the results. Finally, it is a destructive analysis: once the measurement is completed, the sample is saturated with mercury, making it unsuitable for any further testing [20].

High-resolution scanning electron microscopy backscattered electron (SEM-BSE) images were acquired using a Tescan Solaris field emission microscope. The imaging was performed at a low voltage (5 keV) and current (300 pA), with a working distance of 4 mm, in order to enhance material contrast and highlight pore geometry. Each image was collected at a magnification of 248x with a resolution of 2048x2048 pixels, corresponding to a pixel size of 0.73 μm, which defines the resolution limit for pore detection. For each sample, approximately 40 to 60 images were collected and then merged to improve representativeness and capture the heterogeneity of the pore structure. This stitching process allowed for the analysis of a larger surface area. Digital image analysis (DIA) was carried out using the open-source software ImageJ®. Greyscale BSE images were binarized to distinguish voids (black pixels) from the solid matrix (white pixels), and total porosity was calculated as the ratio of pore pixels to the total pixel count in the area of interest. Pore size distribution was evaluated by analysing the geometry and area of the segmented voids. All images were processed using uniform contrast and brightness settings, to ensure consistent results.

Micro-CT was employed for investigating the internal structure and porosity of the samples in three dimensions. The analysed specimens were cylindrical micro-cores, approximately 8 mm in diameter and with a variable height ranging from 4 mm to 7 mm. Scans were performed using a UniTom XL system (Tescan XRE), equipped with an X-ray

source (XWT-240-CT by XRAY-WorX) and a flat-panel detector (XRD 4343CT by Varex), as part of the FleXCT system configuration described by De Samber et al. [36]. Acquisitions were conducted at 120 kV, with a voxel size of 5 μm isotropic in all three spatial directions. The projection images were reconstructed into cross-sectional slices using the manufacturer's software, applying beam hardening corrections, ring artefact reduction, and alignment compensation. Image segmentation and quantitative porosity analysis were performed using CTAn (Bruker®). Total porosity was calculated as the ratio of pore voxel to the total number of voxels within the selected Volume of Interest (VOI). Pore size distribution was assessed using the trabecular thickness (Tb.Th) parameter, calculated through the maximal inscribed sphere-fitting method as proposed by Hildebrand and Rüegsegger (1997) [37]. This voxel-based approach allows the estimation of local pore dimensions without requiring the segmentation of individual pores. In parallel, additional morphological descriptors such as sphericity and Sauter diameter were extracted through object-based analysis, applied to each segmented pore to evaluate its overall geometry. For each descriptor, the mean, minimum and maximum values were calculated, providing more comprehensive characterisation of pore morphology. Sphericity is a dimensionless shape factor that describes how closely the shape of an object approximates a perfect sphere. It was calculated using the following formula:

$$Sph = \frac{\sqrt[3]{\pi}\,(6V)^{2/3}}{S}$$

where V is the object volume and S is its surface area [38]. A sphericity value of 1 represents the ideal case of a perfectly spherical object [38]. The Sauter diameter, on the other hand, expresses the diameter of a sphere with the same volume-to-surface ratio as the object, and is an indicator of mean pore size.

For further 3D visualisation and to compute pore sphericity, datasets were also processed using Dragonfly software (Object Research System) under a non-commercial academic licence. In addition, CTVox (Bruker®) was used to generate volumetric renderings from segmented CTAn data, allowing rapid qualitative inspection of the pore network. Together, these tools enabled detailed visual analysis of internal structures and additional morphological measurements, complementing the CTAn dataset.

5.3.1.2 Accelerated ageing

To investigate the response to environmental factors, the gypsum-based formulation samples were subjected to accelerated ageing replicating hygrothermal fluctuations corresponding to the seasonal excursions recorded in Room LI of the Museum of Roman Civilisation in Rome (see Part 1). The procedure followed the same methodology described in detail in Part 2, and was selected to simulate the critical temperature and humidity variations typically found in environments without active climate control.

The ageing process was carried out in a Serie C environmental chamber manufactured by FDM Environmental Makers, capable of regulating temperature and relative humidity across a wide range. A total of 150 cycles were applied, each composed of 6 hours at 30 °C and 30 % RH (to simulate summer conditions), followed by 6 hours at 10 °C and 90 % RH (to simulate winter conditions). An additional 1 hour was allocated for gradual transition between each phase, resulting in a complete cycle duration of 14 hours and a total ageing period of approximately 87 days and 12 hours. Samples were monitored before and after ageing.

5.3.1.3 Hygroscopic water adsorption

Hygroscopic water adsorption and desorption were assessed on six cubic mock-up samples, each corresponding to a different formulation of gypsum and additives, in accordance with the EN ISO 12571 (2000) standard [39]. The specimens were first oven-dried to constant mass and then placed in an FDM Series C environmental chamber and maintained at a constant temperature of 23 °C. Relative humidity (RH) was progressively increased through the following steps: 30 %, 50 %, 70 %, 75 %, 80%, 85 %, 90 % and 95 %. After completing the adsorption phase, the RH was decreased in the same sequence to evaluate desorption. At each RH level, the mass of the samples was measured and recorded after reaching equilibrium, defined as the point at which the sample mass remained constant over time. The collected data were used to construct the corresponding adsorption and desorption curve. The moisture content u was calculated for each specimen at every RH level using the following equation:

$$u = \frac{m - m_0}{m_0}$$

where m is the mass of the specimen at a given RH and m_0 is its dry mass.

5.4 Results

5.4.1 Nitrogen physisorption (NP)

Nitrogen physisorption analysis provided insight into the evolution of pores smaller than 0.1 μm of gypsum-based samples before and after artificial ageing. All specimens exhibited type IV isotherms according to the IUPAC classification [40,41]. These isotherms describe multilayer adsorption followed by capillary condensation and are typically associated with the presence of mesopores [40]. A common feature of type IV isotherms is the presence of a hysteresis loop, related to the differences in condensation and evaporation mechanisms occurring in mesoporous structures [40]. The shape and width of the hysteresis loop are strongly related to pore morphology, and according to IUPAC, they are classified into four main types. In this study, the hysteresis loop corresponds to type H3, commonly associated with mesoporous materials with slit-shaped pores or aggregates of plate-like particles.

Before ageing all samples showed type IV isotherms with H3 hysteresis loops in the relative pressure range $p/p_0 \approx 0.4\text{-}0.9$. After ageing, all samples maintained the same isotherm type, as highlighted in the figure presented in Section 5.5.1.

The BET surface area ranged from 16.85 to 24.60 m^2/g before ageing and from 11.05 to 16.96 m^2/g after ageing. Total pore volume ranged from 0.03 to 0.04 cm^3/g across all formulations (Table 25).

Pore size distributions, shown in Section 5.5.1 and derived from the desorption branch using the BJH method, showed broad curves with a main peak between 20 and 30 Å across all formulations. After ageing, most BJH curves became flatter and less defined. In many cases, the distribution also shifted towards larger pore widths, with desorption curves extending up to or beyond 900-1000 Å, as also shown in the corresponding figure discussed in Section 5.5.1. In contrast, sample P_M exhibited a BJH desorption curve confined within the mesoporous range (<500 Å) after ageing.

Table 25. BET specific surface area (m^2/g) and total pore volume (cm^3/g) of gypsum-based samples before and after artificial ageing. Data are reported as mean ± standard deviation. Measurements were performed at -196 °C using nitrogen physisorption, with pore volume calculated at $p/p_0 \approx 0.9$ cm^3/g.

Before ageing		
Sample	**B.E.T (m^2/g)**	**Pore volume (cm^3/g)**
A_KW	20.57 ± 0.43	0.04
A_AG	16.85 ± 0.42	0.04
A_M	20.62 ± 0.44	0.03
P_KW	24.60 ± 0.31	0.04
P_AG	17.84 ± 0.36	0.04
P_M	21.75 ± 0.38	0.03
After ageing		
Sample	**B.E.T (m^2/g)**	**Pore volume (cm^3/g)**
A_KW	15.67 ± 0.22	0.03
A_AG	11.05 ± 0.23	0.03
A_M	11.61 ± 0.21	0.03
P_KW	15.18 ± 0.24	0.03
P_AG	16.96 ± 0.22	0.04
P_M	14.40 ± 0.22	0.03

5.4.2 MIP

MIP allowed the investigation of the pore structure in the pore range between 0.005 to 100 μm of the mock-up samples before (t_0) and after (t_1) artificial ageing. The technique provided both differential intrusion volume ($dv/dlogR$) and cumulative porosity curves. The dV/dlogR curves, plotted against the pore radius on a logarithmic scale, highlight the most accessible pore sizes and reflect changes in peak shape and intensity as shown in the figures discussed in Section 5.5.2. This type of plot is especially useful for identifying the presence of a broad or narrow pore size distribution [42]. Broader or flatted peaks suggest a wider range of pore size and increased heterogeneity, while sharper peaks indicate a more homogeneous pore network. The cumulative curves described the progressive mercury uptake, helping visualise the development of porosity across the full pore network.

For each sample, the critical pore radius (CPR) was identified as the peak of the dV/dlogR curve, corresponding to the dominant pore size, while the threshold pore radius (TPR), corresponds to the inflection point in the cumulative porosity curve, as the narrowest entry through which mercury can access the internal pore network.

Table 26 summarises the porosity (%), critical pore radius (CPR, μm), and threshold pore radius (TPR, μm) values obtained for all samples before and after artificial ageing.

Table 26. Total porosity (%), critical pore radius (μm), and threshold pore radius (μm) for all gypsum-based samples before and after ageing, measured by MIP. CPR was identified as the peak of the dV/dlogR curve, and TPR as the inflection point in the cumulative porosity curve.

Before Ageing			
Samples	**Porosity (%)**	**Critical pore radius (μm)**	**Threshold pore radius (μm)**
A_KW	55.77	3.88	5.49
A_AG	45.59	3.90	5.26
A_M	42.78	2.93	4.29
P_KW	54.46	5.33	8.60
P_AG	47.42	4.78	6.26
P_M	43.17	3.07	3.97
After Ageing			
Samples	**Porosity (%)**	**Critical pore radius (μm)**	**Threshold pore radius (μm)**
A_KW	53.79	6.32	7.85
A_AG	43.53	3.77	4.52
A_M	27.78	3.04	4.26
P_KW	49.82	6.32	8.96
P_AG	47.57	4.66	6.84
P_M	41.34	3.18	4.66

Before ageing, CPR values ranged from 3.07 μm (P_M) to 5.33 μm (P_KW), while TPR values ranged from 3.97 μm (P_M) to 8.60 μm (P_KW). After ageing, CPR and TPR values were recorded for each formulation. In A_KW, CPR was 3.88 μm before ageing, and 6.32 μm after ageing; in P_KW, values were 5.33 μm at t_0 and 6.32 μm at t_1. In A_AG, CPR was 3.90 μm at t_0 and 3.77 μm at t_1, while TPR was 5.26 μm and 4.52 μm, respectively. In P_AG, CPR was 4.78 μm at t_0 and 4.66 μm at t_1, with TPR measured at 6.26 μm before ageing and 6.84 μm after ageing (Table 26).

In samples containing marble powder, CPR remained nearly unchanged after ageing. TPR showed minimal variation in A_M, while a slight increase was observed in P_M. Total porosity values before ageing ranged from 42.78 % (A_M) to 55.77 % (A_KW), and after ageing from 27.78 % (A_M) to 53.79 % (A_KW).

5.2.3 2D Image Processing

To characterise the pore structure, high-resolution SEM backscattered images were acquired and merged for each specimen. This approach was supported by previous studies, which have shown that a single BSE image is often insufficient to provide a representative overview of the pore morphology in heterogeneous materials [17,18]. In this study, the threshold limit (minimum pore size detectable) is equal to 0.73 μm. The values of total porosity, pore size distribution, minimum Feret diameter and circularity are summarised in Table 27, while Feret diameter distributions are reported in Section 5.5.3.

Table 27. Results of 2D digital image analysis of SEM-BSE for all gypsum-based samples before and after ageing. Parameters included total porosity (%), pore size class distribution (micropores <10 μm, mesopores 10-400 μm, macropores >400 μm, expressed as % of the total porosity), minimum Feret diameter (μm), and average circularity of segmented pores.

Before ageing						
Samples	**Porosity (%)**	**Micropores (<10 μm) %**	**Mesopores (10-400 μm) %**	**Macropores (>400 μm) %**	**Min Feret (μm)**	**Circularity**
A_KW	64.07	41.51	58.48	0.00	3.48	0.87
A_AG	46.24	6.55	42.22	51.21	4.58	0.84
A_M	61.40	53.14	46.86	0.00	2.71	0.87
P_KW	61.68	40.56	59.44	0.00	3.73	0.90
P_AG	64.50	45.12	54.88	0.00	3.18	0.89
P_M	60.69	43.76	52.33	3.91	4.06	0.88
After ageing						
Samples	**Porosity (%)**	**Micropores (<10 μm) %**	**Mesopores (10-400 μm) %**	**Macropores (>400 μm) %**	**Min Feret (μm)**	**Circularity**
A_KW	60.66	41.56	58.44	0.00	2.34	0.91
A_AG	44.96	3.98	57.84	38.18	11.83	0.80
A_M	54.86	10.31	83.49	6.20	7.84	0.82
P_KW	38.71	5.05	66.67	28.28	5.83	0.81
P_AG	59.54	23.78	76.22	0.00	7.33	0.87
P_M	47.30	4.25	27.30	68.45	4.80	0.81

Before ageing, micropores (<10 μm) and mesopores (10-400 μm) were dominant across all samples. A_M recorded the highest fraction of pores <10 μm (53.14 %), followed by P_AG (45.12 %) and P_M (43.76 %). A_KW and P_KW had the higher mesopore content (58.48 % and 59.44 %, respectively), with lower micropore fractions (41.51 % and 40.56 %). A_AG showed 6.55 % of micropores (<10 μm) and 51.21 % of macropores (>400 μm), expressed as fractions of total porosity. Circularity values ranged from 0.84 in A_AG to 0.90 in P_KW, and in general, all samples showed relatively high values (Table 27).

The SEM-BSE image of sample P_AG before ageing (Figure 39A) reflects the high total porosity of the sample (64.50 %), of which 45.12 % correspond to micropores (<10 μm) and 54.88 % to mesopores (10-400 μm). Macropores were not detected. The segmented image (Figure 39 B) showed a pore network composed mainly of small to medium-sized rounded pores. In this binarized image, black areas correspond to pores and white areas to the solid matrix [17]. The minimum Feret diameter measured was 3.18 μm, and the average circularity reached 0.89.

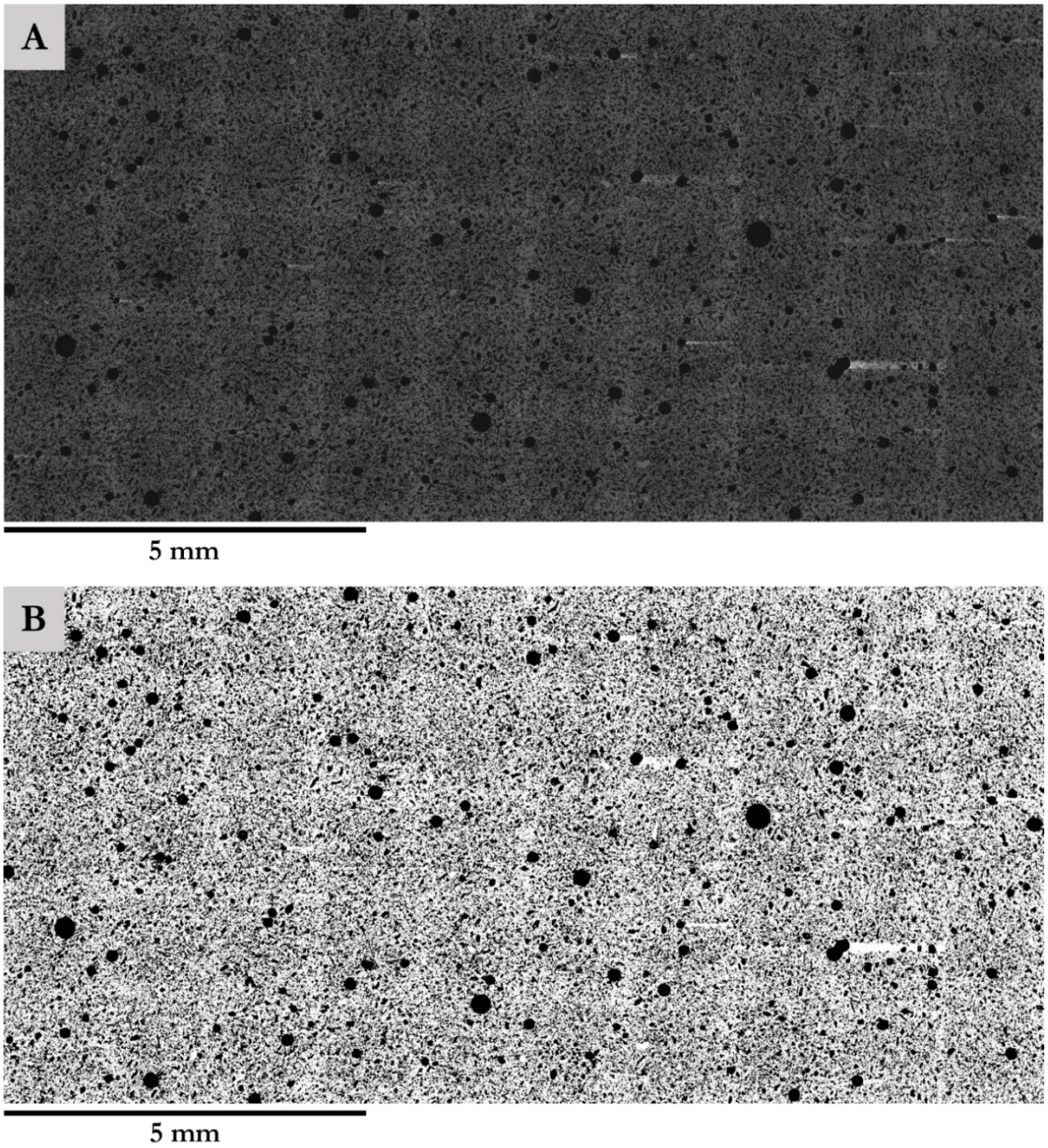

Figure 39. Stitched SEM-BSE images of sample P_AG before ageing. (A) Merged (BSE) image showing the internal pore structure. The image was created by stitching together 50 high-resolution SEM images, providing a representative overview of the pore network. Scale bar: 5 mm. (B) Corresponding binarized image after segmentation: black areas correspond to pores, and white areas to the solid matrix.

After ageing the total porosity was 38.71 % in P_KW, 47.30 % in P_M, 59.54 % in P_AG, 60.66 % in A_KW, 54.86 % in A_M and 44.96 in A_AG (Table 27).

In P_KW, micropores (<10 μm) represented 5.05 %, mesopores (10-400 μm) 66.67 %, and macropores (>400 μm) 28.28 % of the total porosity. P_M showed 4.25 % of micropores, 27.30 % of mesopores and 68.45 % of macropores. The sample A_AG showed 3.98 % micropores, 57.84 % mesopores, and 38.18 % macropores. Its minimum Feret diameter was 11.83 μm, with circularity of 0.80. In A_KW, micropores accounted for 41.56 % and mesopores for 58.44 % of the total porosity, without macropores detected. The minimum Feret diameter was 2.34 μm and the circularity was 0.91. In A_M, micropores were

10.31 %, mesopores 83.49 %, and macropores 6.20 % of the total porosity. The minimum Feret diameter was 7.84 μm and the circularity 0.82. Finally, P_AG showed 23.78 % micropores and 76.22 % mesopores, without macropores detected. The minimum Feret diameter was 7.33 μm and the circularity 0.87. The Feret diameter distribution curves, illustrated in the figure presented in Section 5.5.3, showed broader profiles in samples A_AG and P_M, with the presence of two main peaks. In A_KW and A_M, the distributions were narrower and the majority of pores remained below 30 μm.

5.2.3 3D Micro-CT

The 3D micro-CT analysis provided detailed insight into the internal pore morphology of all gypsum-based samples, both before and after ageing.

Before ageing, total porosity values ranged from 9.262 % (P_M) to 19.984 % (P_KW). After ageing, values decreased in all samples, with porosity ranging from 3.747 % (P_M) to 15.623 % (P_KW) (Table 28). Thus, P_M consistently showed the lowest porosity at both stages, while P_KW was the most porous formulation before and after ageing. Conversely, within the alabaster-based samples, A_M showed the lowest porosity at t_0 (11.440 %), but after ageing its porosity increased to 8.158 %, becoming the most porous alabaster formulation at t_1. A_KW showed intermediate values at both stages (12.425 % at t_0 and 6.795 % at t_1). Sample A_AG showed 13.280 % of porosity before ageing, and 6.004 % after ageing, while P_AG varied from 18.792 % to 8.191 %.

Mean sphericity values ranged between 0.432 (P_M) and 0.554 (P_KW) before ageing, and between 0.437 (P_M) and 0.527 (P_KW) after ageing. For all formulations, the maximum sphericity remained constant at 0.947 except for P_M and P_AG, where slightly lower values were recorded. In particular, P_AG was the only sample showing a decrease in maximum sphericity after ageing, from 0.947 to 0.915. Minimum sphericity values were low across all samples, ranging from 0.004 to 0.073 before ageing, and from 0.003 to 0.064 after ageing.

The mean Sauter diameter ranged from 9.089 μm (P_M) to 13.765 μm (A_M) μm before ageing, and from 8.325 μm (P_M) to 13.320 μm (A_M) after ageing. Overall, variations between t_0 and t_1 were limited, with consistent trends across samples. Minimum Sauter diameters ranged from 2.309 μm to 2.886 μm both before and after ageing, without differences across samples. In contrast, maximum Sauter diameters showed a wider range, varying from 25.168 μm (A_KW) to 194.289 μm (PM) before ageing. After ageing, maximum values ranged from 28.740 μm (P_KW) to 151.277 μm (A_M) (Table 28).

For all samples, pores with the lowest sphericity values corresponded to large Sauter diameters, typically between 17.924 μm and 39.106 μm before ageing, and between 11.680 μm and 29.923 μm after ageing. Conversely, pores with the highest sphericity consistently showed smaller Sauter diameters, between 7.700 μm and 10.482 μm for all samples and both ageing conditions. The sphericity associated with the minimum Sauter diameter was stable across all formulations at 0.845, both before and after ageing. Conversely, the sphericity associated with the maximum Sauter diameter varied more widely, ranging from 0.135 to 0.742 μm before ageing, and from 0.205 μm to 0.409 μm after ageing (Table 28).

To analyse pore morphology at different dimensional scales, the pore network was subdivided into two classes: <10 μm and 10-400 μm (Table 29 and Table 30). For each interval, porosity, mean Sauter diameter, and mean sphericity were calculated.

Before ageing, in all samples, pores in the 10-400 μm class accounted for the vast majority of the total pore volume, contributing between 94.22 % (P_M) and 99.56 % (A_KW). The contribution of pores <10 μm was generally low, ranging from 0.44 % (A_KW) to 5.78 % (P_M). Mean sphericity was consistently higher in the <10 μm class, with values between 0.47 (P_M) and 0.68 (A_KW), while in the 10-400 μm range was lower, between 0.29 (P_M) and 0.52(A_M). Mean Sauter diameters were also larger in the 10-400 μm range than in the <10 μm class (Table 29).

After artificial ageing (Table 30), porosity in the <10 μm range increased for all samples except A_M, where it decreased slightly from 0.57 % to 0.49 %. The most substantial increase within this class occurred in P_M (from 5.78 % to 43.07 %) and P_AG (from 1.37 % to 14.09 %). In the 10-400 μm range, the lowest contribution of large pores was observed in P_M (56.93 %) and P_AG (85.91 %), while samples A_KW, A_AG, A_M and P_KW retained values above 98 %.

Mean sphericity in the <10 μm class ranged from 0.44 (P_M) to 0.60 (A_M), while in the 10-400 μm class it ranged from 0.29 (P_KW) to 0.51 (A_M). Mean Sauter diameter values remained broadly consistent with t_0 in both classes (Table 30).

Table 28. Morphometric parameters obtained from micro-computed tomography analysis before and after ageing. For each sample, the total porosity (%), mean sphericity, and mean Sauter diameter (µm) are reported, along with the minimum and maximum values of sphericity and Sauter diameter. Additionally, the Sauter diameter values corresponding to the minimum and maximum sphericity are shown, as well as the sphericity values corresponding to the smallest and largest diameters. These data allow a detailed interpretation of pore morphology and its evolution following ageing.

Before ageing											
Sample	**Porosity (%)**	**Mean Sphericity**	**Mean Sauter Diameter (µm)**	**Min Sphericity**	**Max Sphericity**	**Sauter Diameter at the Min Sphericity (µm)**	**Sauter Diameter at the Max Sphericity (µm)**	**Min Sauter Diameter (µm)**	**Max Sauter Diameter (µm)**	**Sphericity at the Min Diameter**	**Sphericity at the Max Diameter**
A_KW	12.425	0.523	12.055	0.007	0.947	17.924	10.482	2.886	25.168	0.845	0.582
A_AG	13.280	0.529	12.572	0.017	0.947	28.547	10.482	2.886	140.222	0.845	0.310
A_M	11.440	0.528	13.765	0.073	0.947	39.106	10.482	2.886	159.920	0.845	0.350
P_KW	19.984	0.554	9.180	0.005	0.947	20.281	10.482	2.309	29.535	0.845	0.380
P_AG	18.792	0.544	9.933	0.004	0.947	20.279	8.386	2.309	87.565	0.845	0.742
P_M	9.262	0.432	9.089	0.059	0.915	26.958	7.700	2.309	194.289	0.845	0.135
After ageing											
Sample	**Porosity (%)**	**Mean Sphericity**	**Mean Sauter Diameter (µm)**	**Min Sphericity**	**Max Sphericity**	**Sauter Diameter at the Min Sphericity**	**Sauter Diameter at the Max Sphericity**	**Min Sauter Diameter**	**Max Sauter Diameter**	**Sphericity at the Min Diameter**	**Sphericity at the Max Diameter**
A_KW	6.795	0.507	12.250	0.064	0.947	29.923	10.482	2.886	114.286	0.845	0.271
A_AG	6.004	0.513	12.320	0.052	0.947	24.745	10.482	2.886	99.235	0.845	0.216
A_M	8.158	0.526	13.324	0.028	0.947	21.177	10.482	2.886	151.277	0.845	0.242
P_KW	15.623	0.527	9.305	0.003	0.947	15.691	10.482	2.309	28.740	0.845	0.318
P_AG	8.191	0.462	9.326	0.024	0.915	19.178	7.700	2.309	29.374	0.845	0.205
P_M	3.747	0.437	8.325	0.014	0.915	11.680	7.700	2.309	61.301	0.845	0.409

Table 29. Mean Sauter diameter and mean sphericity values calculated separately for two dimensional intervals: pores with diameters <10 µm, and pores between 10 and 400 µm. The data highlight morphological differences between smaller and larger pores within each allow comparison of shape stability across dimensional ranges before ageing.

Before ageing						
Sample	**Range < 10 µm**			**Range 10 - 400 µm**		
	Porosity (%)	**Mean Sauter Diameter (µm)**	**Mean sphericity**	**Porosity (%)**	**Mean Sauter Diameter (µm)**	**Mean sphericity**
A_KW	0.44	6.67	0.68	99.56	13.04	0.49
A_AG	0.77	7.32	0.64	99.23	13.40	0.50
A_M	0.57	8.24	0.57	99.43	14.30	0.52
P_KW	0.78	7.48	0.58	99.22	11.63	0.50
P_AG	1.37	8.13	0.56	98.63	11.75	0.52
P_M	5.78	7.75	0.47	94.22	13.14	0.29

Table 30. Mean Sauter diameter and mean sphericity values calculated separately for two dimensional intervals: pores with diameters <10 µm, and pores between 10 and 400 µm. The data highlight morphological differences between smaller and larger pores within each allow comparison of shape stability across dimensional ranges after ageing.

	After ageing					
Sample	**Range < 10 µm**			**Range 10 - 400 µm**		
	Porosity (%)	**Mean Sauter Diameter (µm)**	**Mean sphericity**	**Porosity (%)**	**Mean Sauter Diameter (µm)**	**Mean sphericity**
A_KW	1.46	8.05	0.58	98.54	13.00	0.49
A_AG	1.46	8.12	0.57	98.54	12.94	0.50
A_M	0.49	7.84	0.60	99.51	13.83	0.51
P_KW	1.63	7.79	0.56	98.37	11.44	0.29
P_AG	14.09	8.45	0.49	85.91	11.05	0.40
P_M	43.07	8.02	0.44	56.93	11.42	0.39

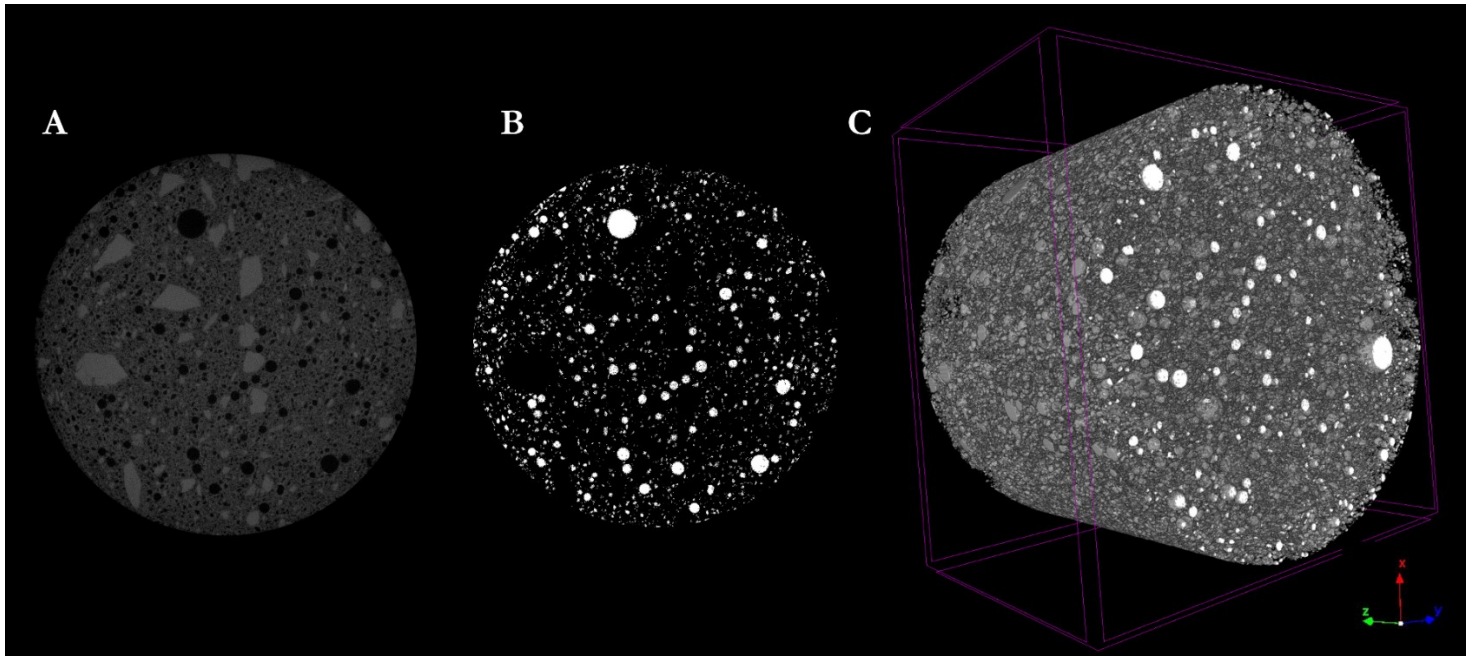

Figure 40. Microtomographic visualisation of sample P_M before ageing. (A) Representative cross-sectional slice from reconstructed greyscale volume. (B) Corresponding binarized slice showing pore segmentation (black = solid matrix; white = pores). (C) 3D rendering of the segmented pore network within the scanned volume, obtained through CTAn and visualised in CTVox.

An example of the internal structure before ageing is shown in Figure 40, where sample P_M is visualised. Figure 40A shows a representative greyscale slice of the reconstructed volume; Figure 40B, the corresponding binarized image (white = pores), and Figure 40 C illustrates the full 3D reconstruction of the segmented pore network. The segmented volume illustrates the distribution of micropores and mesopores within the samples prior to artificial ageing.

Pore size distribution curves based on trabecular thickness (Tb.Th) are shown in Section 5.5.4. Most samples displayed a peak between 10 and 40 μm before ageing, while after ageing several samples exhibited differences in peak height and distribution width.

5.4.5 Hygroscopic sorption behaviour

The hygroscopic behaviour of the gypsum-based formulations was assessed through sorption tests conducted under controlled temperature (23 °C) and relative humidity (RH) conditions, according to the BS EN ISO 12571 (2000) [39]. The sorption curves for each formulation are presented in Figure 41. During the adsorption phase, all samples showed comparable behaviour up to 75 % RH, with mass increases remaining below 0.02 %. Among all formulations, P_AG recorded the highest mass uptake, reaching approximately 0.072 % at the beginning of the desorption phase, around 90 % RH. A similar trend, but less pronounced, was observed in A_AG, which reached values around 0.055 %. The other formulations displayed more gradual increases, with P_M and A_M exhibiting the lowest overall moisture adsorption across the full RH range. Samples containing kaolin and wood powder showed intermediate values, particularly in the 75-95 % RH interval. During the desorption phase Arabic gum-containing samples retained the highest moisture content, remaining above the other formulations throughout the RH decrease. All other samples displayed a smoother and more gradual mass loss during desorption.

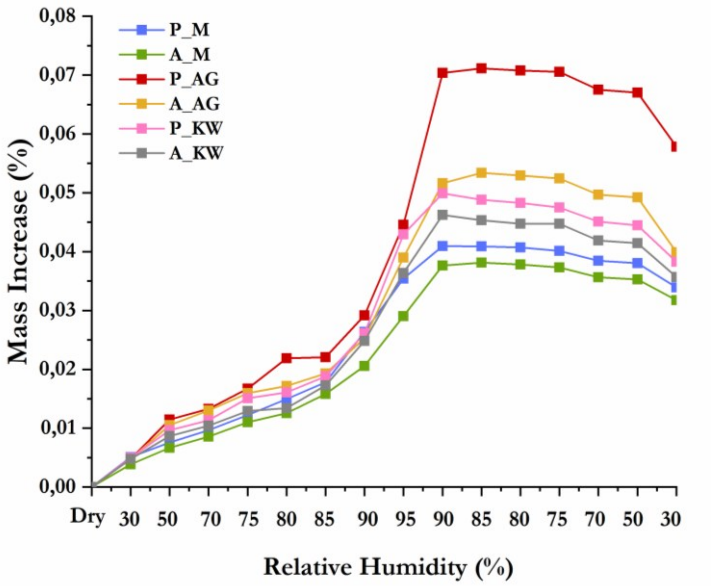

Figure 41. Hygroscopic adsorption and desorption curves of gypsum-based samples with different formulations. the graph shows the percentage increase in mass at equilibrium for each relative humidity step (30-95% adsorption; 95-30% desorption).

5.5 Discussion

5.5.1 Nitrogen physisorption (NP)

Although all samples are characterised by a mesoporous structure, with most of the pores comprised between 10 Å and 500 Å, differences between gypsum types were evident. Before ageing, formulations based on Paris gypsum exhibited higher BET surface areas than those with alabaster gypsum. After ageing, they still showed relatively high surface areas and sharper, more defined BJH pore size distributions (Figure 42). This suggests that Paris gypsum may offer better structural stability under ageing conditions. The BET surface area decreased in all samples after ageing, while the pore volume decreased in samples A_KW, A_AG, and P_KW (Table 25). The decrease in the BET surface area was more pronounced in formulations containing kaolin and in sample A_AG. Samples such as A_M and P_M showed a significant reduction in surface area while maintaining unchanged pore volumes. According to the principles outlined by Sing (1982) [43] and further discussed by Do et al. (2010) [44], such behaviour may reflect a reduction in nitrogen accessibility rather than a loss of porosity. This can occur when pore entrances become narrowed or partially blocked due to structural rearrangement, limiting the penetration of adsorbate molecules into the internal surface area without significantly affecting the total pore volume. In sample P_AG, the nitrogen physisorption isotherm after ageing closely overlapped with the pre-ageing curve in the high relative pressure range ($p/p_0 > 0.8$), suggesting that the mesoporous network remained almost intact and accessible. Unlike most other samples, which exhibited a post-ageing flattening and a shift of the main BJH peak, indicative of pore coalescence or collapse,

P_AG maintained a sharp and well-defined pore size distribution, with a desorption curve extending beyond 1000 Å (Figure 42E). This behaviour indicates a greater resistance to structural rearrangement and supports the interpretation that this formulation preserved its mesoporous structure under hygrothermal stress. This interpretation is coherent with results described in Bochen et al. (2005) [45], which reported that different plaster formulations exhibit distinct structural responses to ageing, with some retaining a more stable pore structure and showing greater resistance to porosity alterations under environmental stress. In contrast, sample P_M (Figure 42F) showed a different behaviour: the BJH desorption curve after ageing was entirely confined within the range <500 Å, without any contribution from larger pores. Among all the analysed samples, P_M was the only one to exhibit a complete disappearance of the macroporous fraction, with the BJH desorption curve after ageing entirely confined within pores smaller than 500 Å. This effect may be attributed to the narrowing or partial occlusion of the pores following structural reorganisation. These observations suggest that the type of gypsum and the presence of specific additives, have a direct impact on the pore structure when subjected to hygrothermal stress.

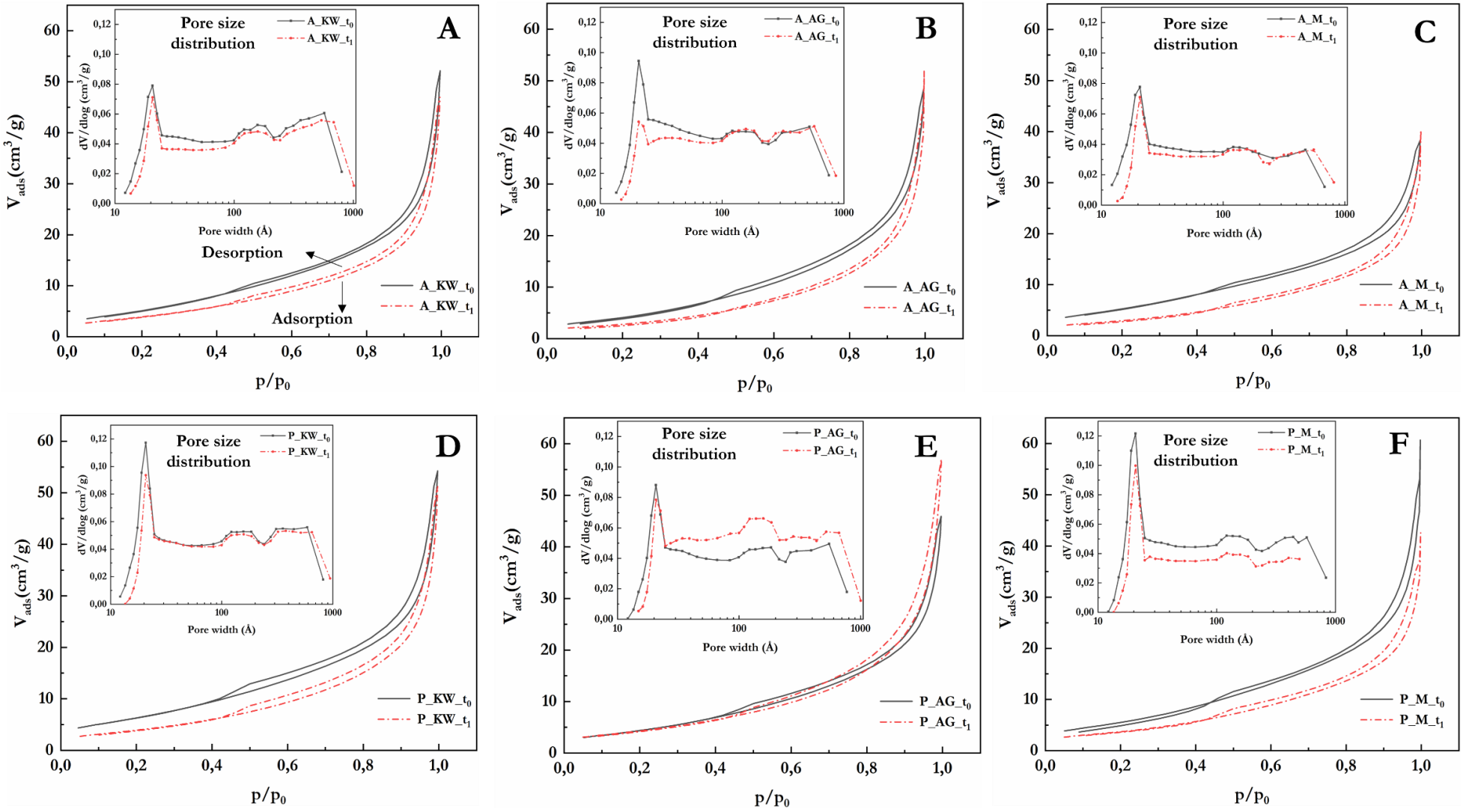

Figure 42. Nitrogen isotherms: volume adsorbed V_{ads} (cm^3/g) vs. relative pressure (p/p_0); and pore size distribution curves: log differential intruded volume (cm^3/g) vs. pore width (Å), for gypsum-based samples before (t_0, black) and after (t_1, red) artificial ageing. Pore size distribution curves are plotted with a logarithmic scale on the x-axis (10-1000 Å). Images A-C show samples with alabaster gypsum (A_KW, A_AG, A_M), and images D-F show samples with Paris gypsum (P_KW, P_AG, P_M).

5.5.2 MIP

The observed variations in CPR, TPR (Table 26), and the shape of the intrusion curves (Figure 43) support the hypothesis that the environmental stressor leads to a reorganisation of the pore structure, which depends on both the additive and the type of gypsum matrix. In particular, samples containing kaolin and wood powder (A_KW, P_KW) showed a significant increase in CPR (e.g., from 3.88 to 6.32 μm in A_KW) and TPR (from 5.49 to 7.85 μm in P_KW) after ageing, along with a broader and less defined dV/dlogR peaks. This suggests the development of a more heterogeneous and interconnected pore network, resulting from the coalescence of pores within the <10 μm range. Similar trends have been documented in heritage materials, where changes in intrusion curves morphology are correlate with merging of pores [19].

In contrast, Arabic gum-based samples were more stable, especially P_AG, which maintained nearly constant porosity and a minimal reduction in pore size parameters. A_AG, although prepared with the same additive, showed a small decrease in CPR, TPR and overall porosity, which may reflect a partial closure of the pore network, possibly influenced by the interaction between the organic component and the alabaster gypsum matrix [46].

Samples containing marble powder (A_M Figure 43, and P_M Figure 44) showed different levels of stability. P_M exhibited minimal variations in porosity and pore size parameters, confirming a stable pore network. In contrast, A_M showed a substantial decrease in total porosity, despite CPR and TPR remaining nearly unchanged (Table 26).

Among all formulations, those based on Paris gypsum generally showed a better response to artificial ageing compared to mixtures made with alabaster gypsum. This is supported by CPR and TPR trends, which indicate smaller structural changes in Paris gypsum samples, while alabaster-based mixtures appeared more susceptible to pore rearrangement.

These results underline the importance of both the binder and the additive in determining the long-term durability of gypsum-based materials. Understanding how the binder and additive influence the pore structure under environmental stress is essential for selecting appropriate formulations in conservation.

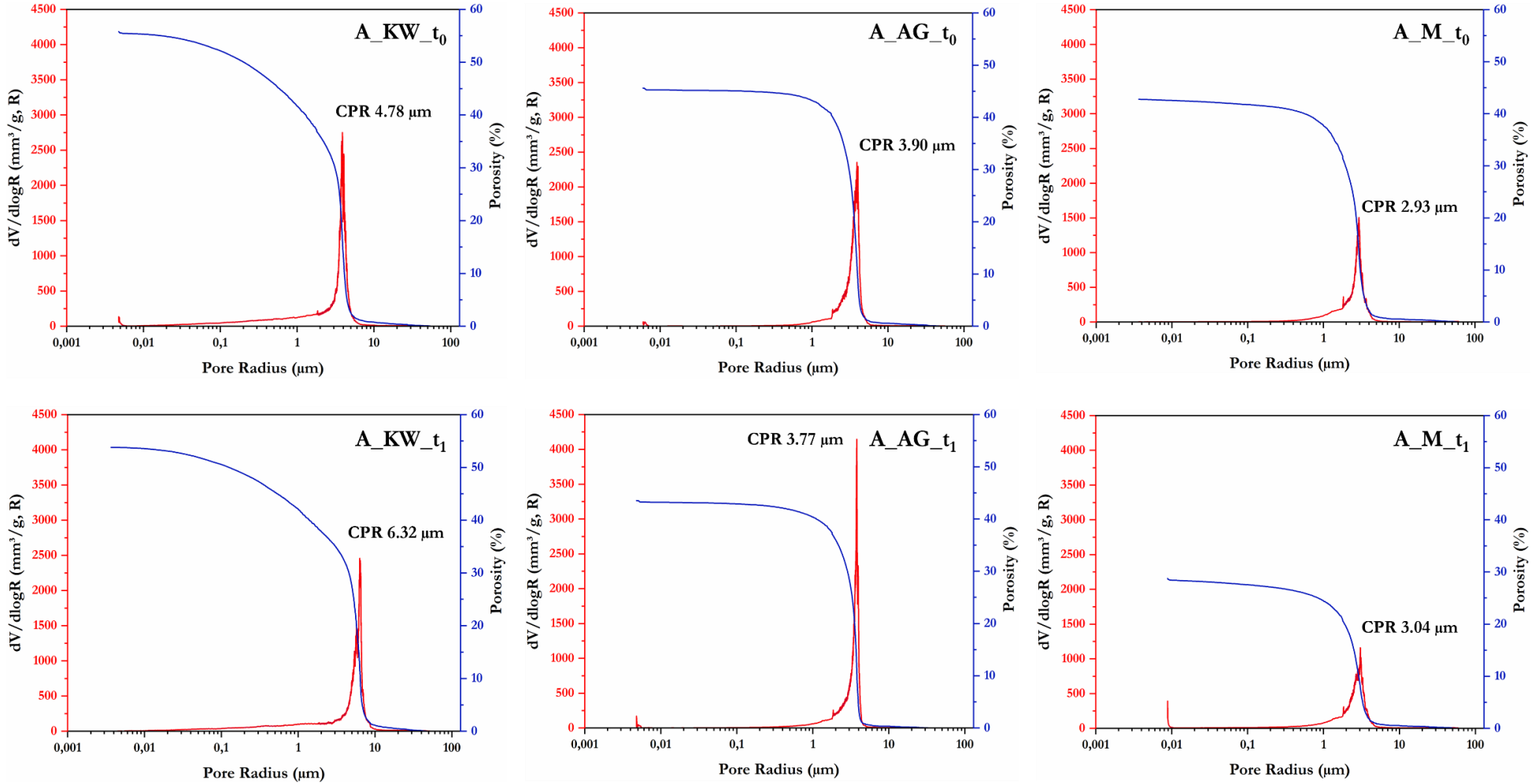

Figure 43. Differential intrusion volume (dV/dlogR, red curves) and cumulative porosity (blue curves) obtained by mercury intrusion porosimetry for alabaster gypsum samples before (t_0) and after (t_1) ageing. The critical pore radius (CPR), labelled on each curve, reflects the dominant pore size in each formulation.

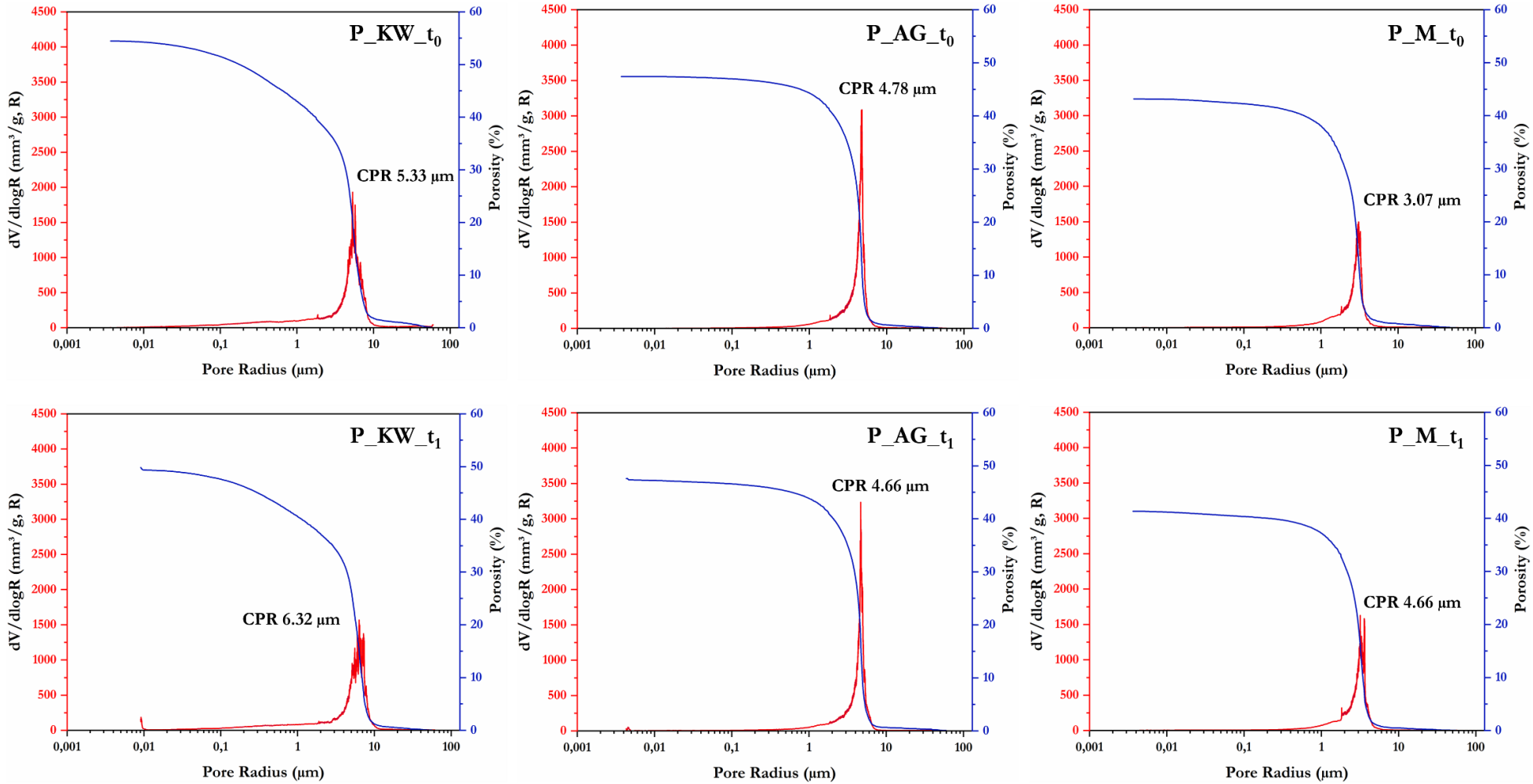

Figure 44. Differential intrusion volume (dV/dlogR, red curves) and cumulative porosity (blue curves) obtained by mercury intrusion porosimetry for Paris gypsum samples before (t_0) and after (t_1) ageing. The critical pore radius (CPR), labelled on each curve reflects the dominant pore size in each formulation.

5.5.3 2D Image processing

The results obtained through 2D digital image (Figure 45A-L) analysis demonstrate the different evolution of pore networks in the six gypsum-based formulations following artificial ageing. An important observation is that ageing generally leads to a reduction in total apparent porosity, accompanied by a shift from microporosity towards larger pore classes [19].

In particular, P_KW and P_M (Figure 45C-D and K-L) exhibited a marked transition from micropores (<10 μm) to macropores (>400 μm), which reached 28.28 % and 68.45 %, respectively. This transformation was reflected in broader Feret diameter distributions, suggesting that large pores may have formed through the coalescence of smaller ones. Such behaviour is consistent with previous studies, which have shown that cyclic exposure to humidity and temperature fluctuations can promote the merging of fine pores due to microstructural rearrangements and local recrystallisation within the gypsum matrix [47]. As smaller pores collapse or become less accessible, the pore system reorganises into fewer but larger voids, reducing total porosity while increasing average pore size.

A_AG and P_AG (Figure 45E-H) exhibited a more moderate degree of pore structure changes. While P_AG maintained a relatively stable porosity (from 64.50 % to 59.54 %) and a mesoporous-dominated distribution within the range 10-400 μm (with pores <10 μm decreasing from 45.12 % to 23.78 %), its Feret diameter increased (from 3.18 μm to 7.33 μm) without significant alteration in circularity (from 0.89 to 0.87), suggesting a controlled reorganisation of the internal structure. The pore network remained evenly distributed and predominantly regular in shape, as also confirmed by the segmented SEM-BSE images before ageing, which did not show pores in the range >400 μm and a uniform population of small to medium-sized voids. These observations point to a more gradual transformation of the microstructure, likely limited to pore enlargement without disruption of overall geometry.

In contrast, A_AG exhibited more pronounced changes: although total porosity remained nearly unchanged (46.24 % to 44.96 %), the lowest measured Feret diameter increased significantly from 4.58 to 11.83 μm, and circularity decreased from 0.84 to 0.80. These modifications point to the development of more irregular and potentially interconnected pores, likely influenced by the interaction between Arabic gum and the alabaster gypsum matrix, which may have favoured microstructural instability.

The most stable behaviour was observed in A_KW and A_M. A_KW that maintained a high porosity (from 64.07 % to 60.66 %) and consistent pore class distribution, with circularity increasing from 0.87 to 0.91, indicating possibly a more regular pore geometry

after ageing. Similarly, A_M showed moderate porosity reduction (from 61.40 % to 54.86 %), accompanied by a limited increase in Feret diameter (to 7.84 μm) and a slight decrease in circularity (from 0.87 to 0.82). In both cases, the pore size distribution remained narrow, with most pores being below 30 μm, indicating a stable and compact microstructure. The Feret diameter curves (Figure 45) confirm these observations: aged samples such as A_AG and P_M displayed broader and more complex curves, consistent with pore growth or merging, whereas A_KW and A_M retained narrow and defined distributions.

These findings showed how much the composition of each formulation can influence the stability of the internal structure when exposed to environmental stress.

However, it is worth nothing that 2D image analysis has its limitations. Since it only provides a cross-sectional view, it may not fully represent the three-dimensional shape of pores. For example, a pore detected as small in the 2D plane may correspond to a larger void in three dimensions. For this reason, DIA results should be combined with 3D techniques such as micro-CT for a more complete understanding. It should also be considered that artefacts such as surface charging [48], which are often present in SEM images of non-conductive materials like gypsum, can affect image quality and compromise the identification of pores. These artefacts may cause errors in the thresholding process and result in less accurate measurements of pore shape and size.

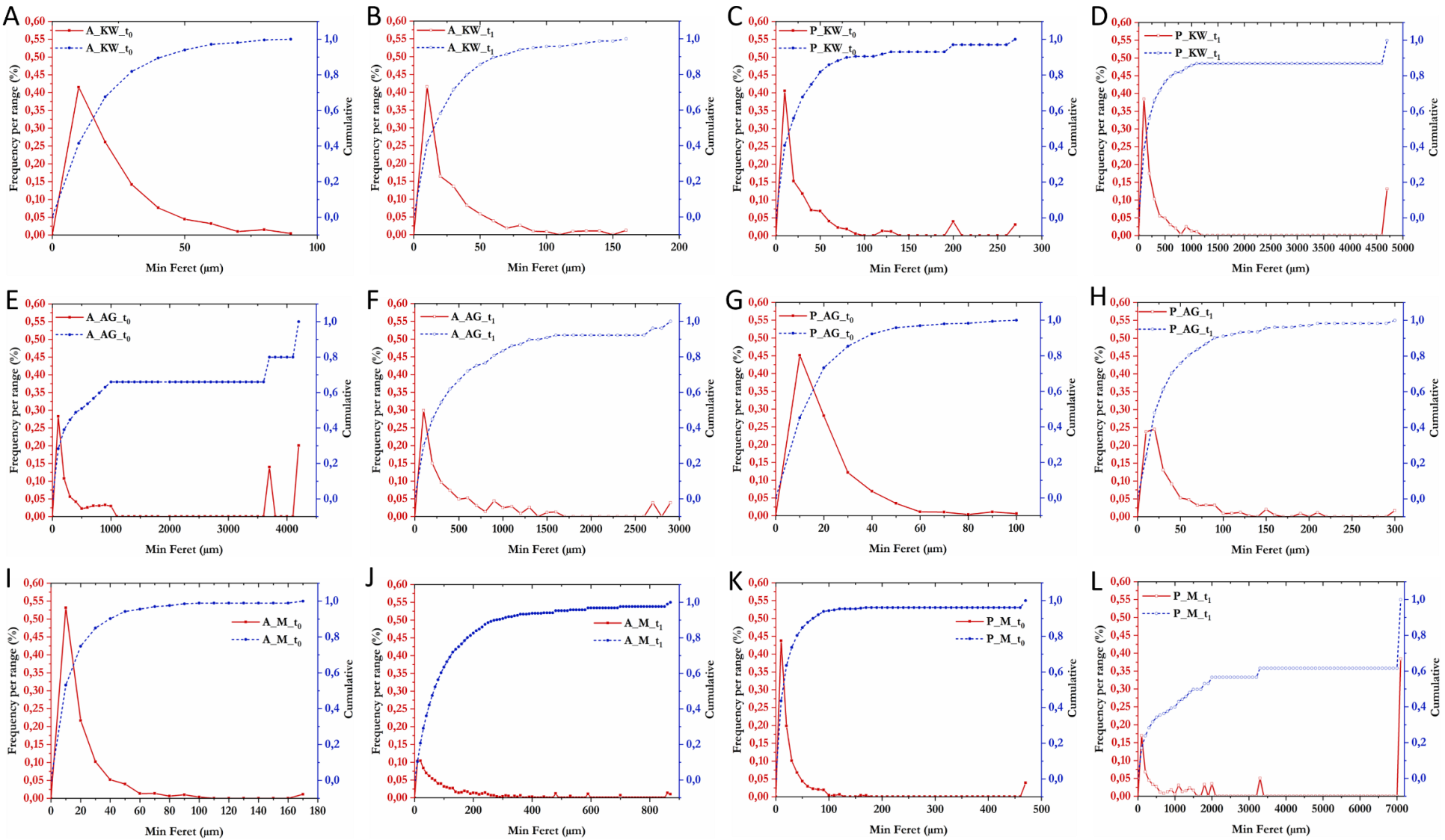

Figure 45. Frequency per range (%) and cumulative distribution of minimum Feret diameters obtained from 2D digital image analysis (DIA) on SEM-BSE images for all mock-up samples before (t_0) and after ageing (t_1). Red curves represent the frequency of pore sizes per range, while the blue curve show the cumulative results. The graphs highlight changes in pore size distribution and pore system evolution due to ageing.

5.5.4 3D Micro-CT

The micro-CT analysis revealed that artificial ageing induced measurable changes in the internal pore structure of all gypsum-based formulations. The most consistent trend across the dataset was the reduction in total porosity, observed in every sample (Table 28). The decrease was particularly pronounced in Paris gypsum mixtures, such as P_AG (from 18.792 % to 8.191 %) and P_M (from 9.262 % to 3.747 %). Among alabaster-based formulations, A_AG showed a comparable reduction (from 13.280 % to 6.004 %), while A_M exhibited a smaller decrease, becoming the alabaster sample with the highest porosity at t_1. The relative ranking of samples in terms of porosity was therefore preserved after ageing, with P_KW remaining the most porous and P_M the least porous formulation in both conditions. These results suggest that hygrothermal ageing promoted a redistribution of pore volume, with a reduction of large connected pores in formulations such as P_AG, P_M, and A_AG. [49,50].

Although less pronounced than the reduction in total porosity, a decrease in mean sphericity values was observed in most formulations, indicating a partial modification of pore geometry after ageing. In several samples, the least spherical pores appeared more affected than the most regular ones, suggesting that structural rearrangement altered the larger and more irregular voids. These observations are consistent with the decrease in maximum Sauter diameters recorded in P_AG and P_M (Table 28), indicating a reduction in large connected pores and an increase in pores <10 (Table 30).

To further investigate this relationship, pores were divided into two dimensional groups: <10 μm and 10–400 μm. Pores below 10 μm generally showed higher sphericity values (up to 0.68) and more stable geometry, even after ageing. In contrast, pores in the 10-400 μm range showed lower sphericity (down to 0.29) and more variability, indicating that even a slight increase in pore size can lead to shape instability, possibly due to the loss of cohesion in the surrounding matrix. These findings align with previous research highlighting the influence of pore size ranges on pore stability under fluctuating relative humidity and temperature conditions [50].

The 3D visualisation of sample A_M before ageing (Figure 46) provides a direct confirmation of these results. Small pores (represented in red to yellow) are more numerous and homogeneously distributed, while larger voids (green to blue) are more isolated and morphologically irregular. When observed within the matrix, these larger pores are embedded deeper in the structure, confirming their lower sphericity.

This relationship between size and shape is particularly relevant when considering the connectivity and moisture transport capacity of these materials. Pore size and morphology

directly influence how water vapour and liquid moisture move through the material. Larger, well-connected pores can facilitate capillary transport and rapid moisture migration, whereas smaller pores (<10 μm), despite their higher sphericity (typically between 0.44 and 0.68), may limit the transport due to reduced pore throat diameter and lower interconnectivity, leading to localised water retention [51,52]. This is particularly critical in gypsum-based materials, where prolonged exposure to moisture can accelerate degradation process such as dissolution, recrystallisation, and mechanical changes [2-5].

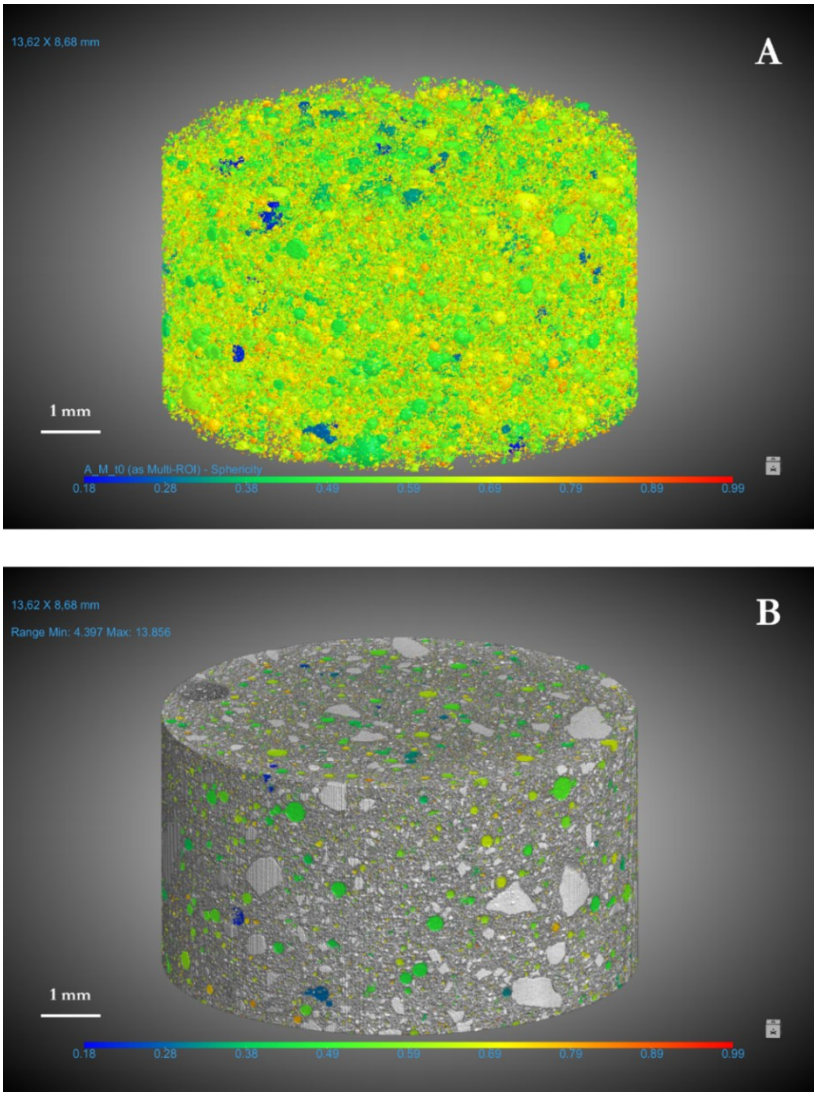

Figure 46. Three-dimensional renderings of sample A_M_t_0 visualised by pore sphericity, generated using Dragonfly software. A: isolated pore network colour-coded by sphericity, from blue (low) to red (high). B: The same sample rendered with solid matrix (grey) and pores mapped by sphericity. The distribution highlights the presence of numerous small, highly spherical pores (yellow-red) and fewer large, irregular ones (blue-green), confirming the inverse relationship between pore size and sphericity.

Across the dataset, differences in behaviour were also linked to the type of gypsum and the presence of additives. Among the alabaster-based samples, A_M showed the smallest changes in porosity and pore morphology, while A_KW and A_AG underwent a substantial

reduction in porosity (from 12.425 % to 6.795 %, and from 13.280 % to 6.004 %, respectively) (Table 28). In contrast, the strongest decreases in the contribution of large pores were observed in the Paris gypsum formulations P_AG and P_M (in the range 10-400 from 98.63 % to 85.91 %, and from 94.22 % to 56.93 %, respectively), while P_KW showed more limited modifications (from 99.22 % to 98.37 %) (Table 29 and Table 30). These results indicate that the impact of ageing differed across mixtures and reflected the combined influence of the gypsum binder and the incorporated additives.

The pore size distribution curves derived from the trabecular thickness (Tb.Th) (Figure 47) showed that ageing primarily resulted in a narrowing of the distributions in several formulations. This behaviour was especially evident in A_KW, P_KW and P_M, which exhibited sharper and more concentrated peaks after ageing. In other samples, such as A_AG and A_M, the differences between t_0 and t_1 were minimal, while P_AG retained a similar peak position with a moderately narrower curve. These trends indicate that the effect of ageing depended from the formulation.

Although the specific mechanisms cannot be fully resolved from the present dataset, the combined reduction in maximum Sauter diameters, the increase in the <10 μm range, and the narrowing of the Tb.Th distributions suggest that the largest and least spherical pores were the most affected by ageing. In mixtures such as P_KW and P_M, the reduction of large pores is consistent with the decreased contribution of the 10-400 μm class and the corresponding rise in the proportion of smaller pores (Table 29 and Table 30). In alabaster-based samples, the changes were more limited and mainly involved.

These modifications may reduce the continuity of the largest pore pathways while increasing the proportion of smaller, more irregular voids. Although connectivity was not directly measured, such redistribution may influence vapour diffusion and moisture retention, with smaller pores offering higher capillary resistance and potentially slower moisture release.

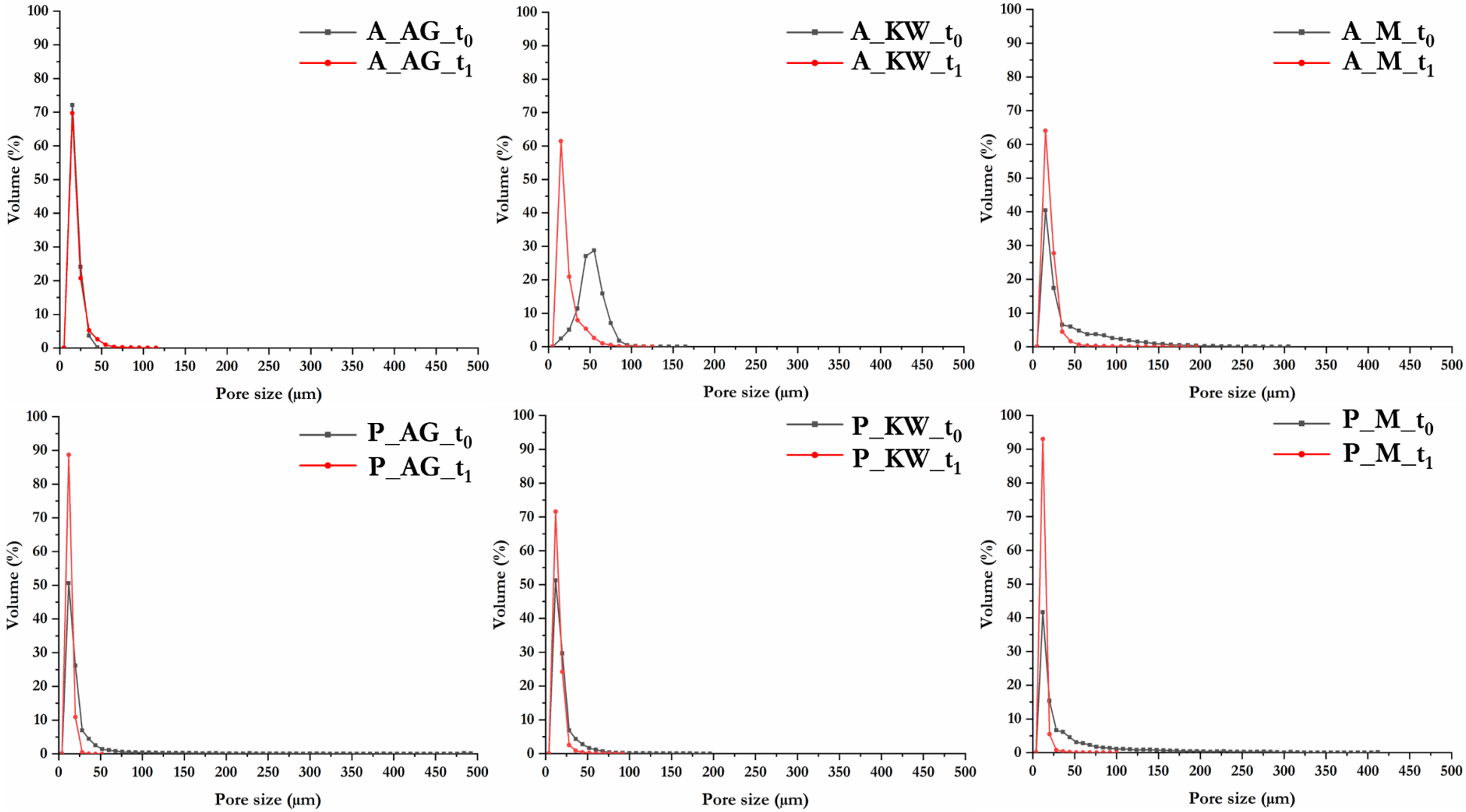

Figure 47. Pore size distribution curves for all samples before (t_0) and after (t_1) artificial ageing, calculated using the trabecular thickness (Tb.Th) parameter. Each curve expressed the percentage of total pore volume associated with specific diameter intervals. All samples exhibited a peak between 10 and 40 µm. After ageing, the curves shifted and became narrower.

5.5.5 Correlation between porosity and hygroscopic sorption behaviour

The hygroscopic behaviour of the six formulations confirmed that not all porosity contributes equally to moisture uptake and retention. An important factor is the morphology and dimensional distribution of the pores, rather than their absolute volume.

Among all samples, those containing Arabic gum, particularly P_AG, showed the highest hygroscopic response. During the adsorption phase, P_AG reached its maximum mass increase of approximately 0.072 % at the beginning of desorption, around 90 % RH, and maintained this moisture value until RH reached 50 %, releasing it rapidly only between 50 and 30 % RH. A_AG exhibited a similar trend, although less pronounced. This behaviour is consistent with the presence of fine, interconnected pores, as suggested by BET and MIP results: P_AG showed a moderate surface area, a stable mesoporous network, and minimal changes in CPR-TPR after ageing. In micro-CT, it retained relatively small pores with moderate sphericity, suggesting a pore network capable of retaining water by capillary condensation.

Samples containing marble powder (A_M, P_M) displayed the lowest hygroscopic response across the entire RH range. The low mass increase and nearly linear sorption curves reflect their compact and poorly accessible pore structure, confirmed by low total porosity, low BET surface area, and stable but narrow pore size distributions in both MIP and 2D image analysis. After ageing, P_M showed a reduction in micropores and a high percentage of large, irregular macropores in 2D analysis, but overall low connectivity and limited moisture retention. In micro-CT, this group had the lowest porosity values and the lowest sphericity, suggesting minimal effective pore pathways.

Formulations with kaolin and wood powder (A_KW, P_KW) exhibited intermediate behaviour. Despite high total porosity, their moisture uptake remained moderate. MIP data indicated a shift towards larger CPR and TPR values after ageing, and broader pore size distributions. However, the micro-CT results revealed low sphericity values and a high proportion of irregular pores, suggesting a less connected and more heterogeneous pore network, potentially containing isolated pores or narrow throats. This morphology may limit capillary condensation and hinder moisture diffusion, which explains the reduced hygroscopic response relative to the total porosity.

Overall, these findings confirm that moisture uptake is not only determined but the amount of porosity, but also by pore size, morphology, connectivity, and accessibility. Notably, the samples with the highest hygroscopic response (P_AG and A_AG) exhibited a significant proportion of pores in the 0.1-10 μm range, according to MIP and BJH data, a

class particularly prone to capillary condensation and delayed water release. From a conservation perspective, this helps explain why Arabic gum-based formulations are more prone to humidity-related degradation: their pore networks combine moderate surface areas with accessible pores in a critical size range for moisture interaction. Conversely, marble powder-based samples showed lower porosity and limited accessibility, thus offering greater stability under RH fluctuations. The ability to predict hygroscopic behaviour based on multiscale porosity analysis is therefore essential when selecting materials for heritage conservation in uncontrolled environments.

5.6 Conclusion

This study investigated how the internal pore structure of gypsum-based materials evolves under hygrothermal ageing, using a multi-analytical approach to assess porosity across different scales. The results demonstrated that both the type of gypsum and the choice of additives significantly influence the long-term behaviour of the formulations.

Artificial ageing generally led to a reduction in total porosity, especially in mixtures with higher initial pore volumes, such as those containing kaolin and wood powder. This reduction can be attributed to microstructural compaction and partial closure of voids under repeated environmental stress. A less marked decrease in mean sphericity was also observed, suggesting a progressive loss of geometric regularity within the pore system. These effects were particularly evident in the 3D μCT dataset, which revealed a shift towards smaller and more irregular pores.

Nitrogen physisorption and mercury intrusion porosimetry confirmed that ageing affects not only the total pore volume but also pore accessibility. In samples such as A_KW and A_M, a pronounced reduction in surface area occurred without a corresponding change in total volume, which may reflect narrowing or partial closure of pore access.

2D SEM image analysis provided further insight into morphological changes, with clear evidence of pore merging in mixtures like P_KW and P_M. Conversely, P_AG retained a homogeneous and finely distributed pore network, without macroporosity and only moderate dimensional variation. Among the alabaster-based formulations, A_KW and A_M remained relatively stable after ageing, whereas A_AG exhibited significant changes in pore shape and size. These observations indicate that both the type of gypsum and the additive influence the stability of the pore structure.

Moisture sorption tests further clarified the relationship between porosity and hygroscopic behaviour. Formulations with Arabic gum (P_AG and A_AG), retained more

moisture due to the presence of smaller, accessible pores in the 0.1-10 μm range and a relatively uniform internal structure as shown by MIP and micro-CT. In contrast, marble powder formulations had fewer accessible pores and lower connectivity, resulting in minimal water uptake. These results indicate that moisture sensitivity is influenced not only by the amount of porosity, but also by pore shape and connectivity.

Although all analytical techniques consistently indicated a reduction in pore volume and a progressive densification of the microstructure, the ageing cycles did not reveal any clear evidence of bulk shrinkage. Dimensional measurements were collected during the experiment, but the variations were extremely limited and did not show a systematic trend. This suggests that the observed densification mainly reflects internal microstructural rearrangements, such as pore narrowing, partial closure of voids, and local compaction, rather than measurable changes in the external dimensions of the specimens.

Overall, the results indicate that the composition of gypsum-based materials has a significant influence on their response to hygrothermal stress. The long-term behaviour is not only determined by total porosity, but depends on pore shape, size distribution, and connectivity. Formulations containing Arabic gum, characterised by finer and more interconnected micropores, were more prone to moisture retention and morphological change. In contrast, mixtures with marble powder developed compact and less accessible pore networks, resulting in greater structural stability. The type of gypsum influenced the results only partially, as the response to ageing depended primarily on the specific combination of binder and additive, rather than on the gypsum phase alone. The combined use of microstructural and sorption-based techniques allowed for a detailed assessment of porosity evolution, supporting the evaluation of material stability in indoor heritage environments.

References

[1] E. M. Payne, The Conservation of Plaster Casts in the Nineteenth Century, Stud. Conserv., vol. 65 (2022), pp. 37-58.

[2] A. Sopagnulo, C. Vetromile, A. Masiello, M. F. Alrberghina, S. Schiavone, C. Lubritto, Climate and Cultural Heritage: The Case Study of "Real Sito of Carditello", Herit., vol. 2 (2019), pp. 2053-2066.

[3] X. Li, M. Ran, Gypsum-Based Humidity-Control Material: Preparation, Performance and Its Impact on Building Energy Consumption, Mater., vol. 16 (2023), 5211.

[4] M. T. Freie, M., M. do Rosário Veiga, A. Santos Silva, J. de Brito, Restoration of ancient gypsum-based plasters: Design of compatible materials, Cem. Concr. Compos., vol. 120 (2021), 104014-104027.

[5] K. Elert, P. Bel-Anzué, M. Burgos,Ruiz, Influence of calcination temperature on hydration behavior, strength, and weathering resistance of traditional gypsum plaster, Constr. Build. Mater, vol. 367 (2023), 130361-130371.

[6] S. Ramírez, M. Zarzo, A. Perles, F. J. García-Diego, A methodology for discriminant time series analysis applied to microclimate monitoring of fresco paintings, Sensors, vol. 21 (2019), pp. 1-29.

[7] Z. Pavlík, J. Fořt, R. Černý, An in situ monitoring system for the study of environmental influences on durability and the destructive process of building materials and structures, WIT Trans. Modelling Simul., vol. 55 (2013), pp. 287-296.

[8] M. Torres-Gonzàlez, C. Rubio-Bellido, D. Bienvenido-Huertas, J. M. Alducin-Ochoa, V. Flores-Alés, Long-Term environmental monitoring for preventive conservation of external historical plasterworks, J. Build. Eng., vol. 47 (2022), 103896-103910.

[9] D. Freyer, W. Voigt, Crystallization and phase stability of CaSO4 and CaSO4 – based salts, Monatshefte Fur Chemie, vol. 134 (2003), pp. 693-719.

[10] E. M. Winkler, E. J. Wilhelm, Salt burst by hydration pressures in architectural stone in urban atmosphere, Geol. Soc. Am. Bull., vol. 87 (1970), pp. 567-572.

[11] J. Adrien, S. Meille, S. Tadier, E. Maire, L. Sasaki, *In-situ* X-ray tomographic monitoring of gypsum plaster setting, Cem. Concr. Res., vol. 82 (2016), pp. 107-116.

[12] D. Jeulin, P. Monnaie, F. Péronnet, Gypsum morphological analysis and modeling, Cem. Concr. Compos., vo. 23 (2001), pp. 299-311.

[13] Z. Wei, Q. Zhang, X. Li, Crystallization Kinetics of α-Hemihydrate Gypsum Prepared by Hydrothermal Method in Atmospheric Salt Solution Medium, Crystals, vol. 11 (2021), 843-852.

[14] A. J. Lewry, J. Williamson, The setting of gypsum plaster – Part I The hydration of calcium sulphate hemihydrate, J. Mater. Sci., vol. 29 (1994), pp. 5279-5284.

[15] B. Middendorf, Physico-mechanical and microstructural characteristics of historic and restoration mortars based on gypsum: current knowledge and perspective, Geol. Soc. Lond., Spec. Publ., vol. 205 (2002), pp. 165-176.

[16] F. De Quervain, Technisce Gesteinskunde. Lehrbücher und Monographien aus dem Gebiete der exakten Wissenschaften, Mineralogisch-geotechnische Reihe, 1.

[17] C. Coletti, G. Cultrone, L. Maritan, C. Mazzoli, Combined multi-analytical approach for study of pore system in bricks: How much porosity is there?, Mater. Charact., vol. 121 (2016), pp. 82-92.

[18] S. Salvini, C. Coletti, L. Maritan, M. Massironi, F. Balsamo, C. Mazzoli, Exploring the pore system of carbonate rocks through a multi-analytical approach, Environ. Earth Sci., vol. 82 (2023), pp. 564-577.

[19] S. P. Rigby, Uses of Gas Sorption and Mercury Porosimetry Methods in Studies of Heritage Materials, Herit., vol. 8 (2025), 132-162.

[20] V. Brunello, C. Canevali, C. Corti, T. De Kock, L. Rampazzi, S. Recchia, A. Sansonetti, C. Tedeschi, V. Cnudde, Understanding the Microstructure for Cultural Heritage Using X-ray CT and MIP, Mat., vol. 14 (2021), 5939-5957.

[21] S. P. Rigby, R.S. Fletcher, S. N. Riley, Characterisation of porous solids using integrated nitrogen sorption and mercury porosimetry, Chem. Eng. Sci., vol. 59 (2004), pp. 41-51.

[22] J. Rathouský, M. Thommes, Adsorption properties and advanced textural characterization of novel micro/mesoporous zeolites, Stud. Surf. Sci. Cat., vol. 170 (2007), pp. 1042-1047.

[23] B. Callow, I. H. Falcon-Suarez, H. Marín-Moreno, J. M. Bull, S. Ahmed, Optimal X-ray micro-CT image based methods for porosity and permeability quantification in heterogeneous sandstones, Geophys, J. Int., vol. 223 (2020), pp. 1210-1229.

[24] G. Bumanis, L. Vitola, X. Zhou, D. Vaičiukynienė, D. Bajare, Towards 3D Pore Structure of Porous Gypsum Cement Pozzolan Ternary Binder by Micro-Computed Tomography, J. Compos. Sci., vol. 8 (2024), 264-274.

[25] A. Grazzini, M. Zerbinatti, S. Fasana, Mechanical characterization of mortars used in the restoration of historical buildings: an operative atlas for maintenance and conservation, IOP Conf. Ser.: Mater. Sci. Eng., vol. 69 (2019), 012024-012030.

[26] C. Arcolao, Le ricette del Restauro: Malte, intonaci, stucchi dal XV al XIX secolo, Saggi Marsilio, Venezia, 1998.

[27] Turco, Il gesso lavorazione – trasformazione – impieghi, Ulrico Hoepli, Milano, 1861. [In Italian]

[28] S. Brunauer, P. H. Emmett, E. Teller, Adsorption of gases in multimolecular layers, J. Am. Chem. Soc., vol. 60 (1938), pp. 309-319.

[29] E. P. Barrett, L. G. Joyner, P. P. Halenda, The determination of Pore Volume and Area Distributions in Porous Substances. I. Computations from Nitrogen Isotherms, J. Am. Chem. Soc., vol. 73 (1951), pp. 373-380.

[30] T. Dang-Vu, J. Hupka, Characterizatio of porous materials by capillary rise method, Physicochem. Probl. Miner. Process., vol. 39 (2005), pp. 47-65.

[31] K. S. W. Sing, D. H. Everett, R. A. W. Haul, L. Moscou, R. A. Pierotti, J. Rouquérol, T. Siemieniewska, Reporting physisorption data for gas/solid systems with Special Reference to the Determination of Surface Area and Porosity, Pure & Appl. Chem., vol. 57 (1985), pp. 603-619.

[32] Beat Münch, L. Holzer, Contradicting Geometrical Concepts in Pore Size Analysis Attained with Electron Microscopy and Mercury Intrusion, J. Am. Ceram. Soc., vol. 9 (2008), pp. 4059-4067.

[33] M. J. Mosquera, B. Silva, B. Prieto, E. Ruiz-Herrera, Addition of cement to lime-based mortars: Effect on pore structure and vapor transport, Cem. Concr. Res., vol. 36 (2006), pp. 1635-1642.

[34] Y. Zhang, B. Yang, Z. Yang, G. Ye, Ink-bottle Effect and Pore Size Distribution of Cementitious Materials Identified by Pressurization-Depressurization Cycling Mercury Intrusion Porosimetry, Mater., vol. 12 (2019), 1454-1468.

[35] F. Moro, H. Böhni, Ink-Bottle Effect in Mercury Intrusion Porosimetry of Cement-Based Materials, J. Colloid Interface Sci., vol. 246 (2002), pp. 135-149.

[36] B. De Samber, J. Renders, T. Elberfeld, Y Maris, J. Sanctorum, N. Six, Z. Liang, J. De Beenhouwer, J. Sijbers, FleXCT: a flexibe X-ray CT scanner with 10 degrees of freedom, Opt. Express, vol. 29 (2021), pp. 3438-3455.

[37] T. Hildebrand, P. Rüegsegger, A new method for the model-independent assessment of thickness in three-dimensional images, J. Microsc., vol. 185 (1997), pp. 67-75.

[38] M. Rajczakowska, D. Stefaniuk, D. Łydżba, Microstructure characterization by means of X-ray micro-CT and nanoindentation measurements, Stud. Geotech. Mech., vol. 37 (2015), pp. 75-84.

[39] BS EN ISO 12571 (2000), Hygrothermal performance of building materials and products – Determination of hygroscopic sorption properties. BSI, London.

[40] K. Sing, The use of nitrogen adsorption for the characterisation of porous materials, Colloids Surf. A: Physicochem. Eng. Asp., vol. 187-188 (2001), pp. 3-9.

[41] S. Storck, H. Bretinger, W. F. Maier, Characterization of micro- and mesoporous solids by physisorption methods and pore-size analysis, Appl. Catal. A: Gen., vol. 174 (1998), pp. 137-146.

[42] Q. Lei, L. Zhang, H. Tang, Y. Zhao, M. Chen, C. Xie, Describing the full pore size distribution of tight sandstone and analyzing the impact of clay type on pore size distribution, Geofluids, vol. 2020 (2020), 1-20.

[43] K. S. W. Reporting Physisorption Data for Gas/Solid Systems with Special Reference to the Determination of Surface Area and Porosity, Pure and Appl. Chem., vol. 54 (1982), pp. 2201-2218.

[44] D. D. Do, L. Herrera, C. Fan, A. Wongkoblap, D. Nicholson, The role of accessibility in the characterization of porous solids and their adsorption properties, Adsorption, vol. 16 (2010), pp. 3-15.

[45] J. Bochen, S. Gil, J. Szwabowski, Influence of ageing process on porosity changes of the external plasters, Cem. Concr. Compos., vol. 27 (2005), pp. 769-775.

[46] V. Brunello, D. Bersani, L. Rampazzi, A. Sansonetti, C. Tedeschi, Gypsum based mixes for conservation purposes: evaluation of microstructural and mechanical features, Mater. Construcc., vol. 70 (2020), 1-14.

[47] A. Ramon, C. Caselle, S. M. R. Bonetto, D. Costanzo, E. E. Alonso, Effect of Microstructure and Relative Humidity on Strength and Creep of Gypsum, Rock Mech. Rock Eng., vol. 54 (2021), pp. 4121-4145.

[48] T. I. Anderson, B. Vega, A. R. Kovscek, Multimodal imaging and machine learning to enhance microscope images of shale, Comput. Geosci., vol. 145 (2020), 104593-104606.

[49] C. L. Reedy, C. L. Reedy, High-resolution micro-CT with 3D image analysis for porosity characterization of historic bricks, Herit. Sci., vol. 10 (2022), pp. 83-104.

[50] T. Buchner, T. Kiefer, L. Zelya-Lainez, W. Gaggi, T. Konegger, A multitechnique, quantitative characterization of the pore space of fired bricks made of five clayey raw materials used in European brick industry, Appl. Clay Sci., vol. 200 (2021), 105884.

[51] M. Doleželová, J. Krejsová, L. Scheinherrová, M. Keppert, A. Vimmorová, Investigation of environmentally friendly gypsum based composites with improved water resistance, J. Clean. Prod., vol. 370 (2022), 133278-133290.

[52] M. Tiennot, L. Cormier, W. Nowik, Insight into deformation and recovery of gypsum plaster under wet and humid environments, Mater. Chem. Phys., vol. 340 (2025), 130754-130761.

[53] P. López-Arce, A. Zornoza-Indart, L. Gomez-Villalba, E. M. Pérez-Monserat, M. Alvarez de Guergo, G. Vivar, R. Fort, Archaeological ceramic amphorae from underwater marine environments: influence of firing temperature of salt crystallization decay, J. Eur. Ceram. Soc., vol. 33 (2013), pp. 2031-2042.

6. Overall conclusions

This research has provided a comprehensive assessment of the conservation issues associated with historical gypsum-based replicas, combining on-site surveys, laboratory investigations, and artificial ageing experiments. The first part of the study focused on the 19th century plaster replicas of Trajan's Column preserved at the Museum of Roman Civilisation in Rome, a particularly significant example of a large-scale gypsum installation, comprising 125 plaster casts. Since 2014, the entire Museum has remained closed to the public, and the casts have been stored in an uncontrolled gallery, without active climate control. This prolonged exposure to fluctuating environmental conditions, combined with a lack of monitoring or maintenance, made it an ideal case study for assessing the long-term deterioration of gypsum materials in indoor museum environments. By combining multi-analytical investigations on both historical replicas and experimentally aged mock-up samples, this thesis has provided new insights into how environmental conditions, material formulation, and microstructural properties affect the degradation behaviour of gypsum-based artefacts.

The first part of the research focused on the diagnostic survey and material characterisation of selected casts from Room LI of the Museum. The investigation revealed that, although housed indoors, these artefacts are still subjected to physical and chemical deterioration, as well as mechanically induced damage caused by environmental stress. Environmental monitoring recorded significant hygrothermal fluctuations, with relative humidity ranging between 35 and 85 %, and dataloggers recording daily fluctuations. These environmental conditions, combined with poor ventilation and the architectural configuration of the space, promoted cyclic moisture absorption and desorption, mechanisms contributing to surface and structural degradation. As shown by FLIR imaging and photographic surveys, surface alteration patterns, such as loss of cohesion, darkening, and micro-cracks, were most evident in areas subjected to greater environmental instability or structural exposure. Microchemical analyses revealed the presence of calcium sulphate dihydrate together with secondary compounds, including calcite, kaolinite, and silica phases, as well as a kaolin-based coating and traces of organic and synthetic materials, suggesting both original formulation and later surface interventions. These findings revealed that the surface composition of the casts is the result of overlapping material phases, degradation products, and conservation residues, highlighting the need for multi-layered analytical investigations.

The second part of the thesis involved the formulation of mock-up gypsum samples simulating historical recipes with specific additives (e.g., Arabic gum, a mixture of kaolin-wood powder, marble powder) and coatings (e.g., PVA, Acryl-EM 33, kaolin). These samples were subjected to controlled cyclic ageing designed to replicate the thermo-hygrometric fluctuations recorded in Room LI. A combination of analytical techniques, including FTIR, optical profilometry, and spectrophotometric measurements, was employed to assess how material composition and protective treatments influenced degradation behaviour over time. The results highlighted significant differences in the performance of the various formulations. Additives such as Arabic gum and marble powder improved initial cohesion but also altered the pore structure. Surface coatings provided limited resistance to ageing stressors, with PVA showing greater stability than acrylic resins and kaolin suspension. Ageing-related changes were observed across all samples, indicating that none of the tested treatments was fully resistant to environmental stress. The findings showed that the effectiveness of protective treatments largely depends on the intrinsic properties of the material. Without addressing internal porosity and phase composition, coatings alone cannot guarantee long-term stability.

The third part of the thesis focused on the relationship between porosity and material degradation. A multi-scale analytical approach was adopted, combining nitrogen physisorption (BET and BJH methods), MIP, 2D image analysis and micro-CT. This integrated methodology enabled the quantification of pore size distribution, connectivity, total porosity, and morphological features, both before and after artificial ageing. The analysis suggested that pore characteristics, such as increased presence of intermediate-sized pores (10-400 μm) and lower sphericity, may contribute to internal microstructural changes and increased susceptibility to environmental stress. Additionally, aged samples generally exhibited a decrease in overall porosity and, in several formulations, a shift toward smaller, more irregular pores, as confirmed by micro-CT analysis. Such microstructural changes tend to increase moisture retention and capillary rise, which can increase the material's susceptibility to internal stress, salt crystallisation, and long-term deterioration. These findings highlighted the need for conservation strategies that are compatible with both the material composition and the internal structure of the artefacts.

Overall, the results offered a deeper understanding of the complex degradation dynamics affecting gypsum-based heritage materials. An important outcome of the research is the integration of analytical and diagnostic methods across multiple scales and conditions, by combining real-case observations with controlled experimental investigations. The

experimental mock-ups allowed for the controlled testing of specific material formulations under defined ageing conditions, facilitating the identification of degradation processes that are often difficult to identify in historical artefacts due to the stratified nature of their conservation history. At the same time, porosity analyses offered insight into internal transformations that can develop gradually and lead to progressive degradation, potentially compromising the long-term stability of the artefact.

While the study has provided valuable insights, several limitations should be acknowledged. The mock-up formulations, although based on historical recipes, simplified the variability and complexity of 19th century manufacturing practices. Similarly, the artificial ageing protocols, although carefully designed to replicate the parameters observed in the Museum, cannot fully reproduce the range of environmental stressors to which the artefacts may have been exposed over time. This limitation highlighted the importance of contextualising experimental data within the conservation history of the object.

Despite these limitations, the study provided clear evidence of the critical role of material microstructure, formulation additives, and environmental context in shaping the long-term stability of gypsum artefacts. It also demonstrated the vulnerability of historical casts to even moderate thermo-hygrometric fluctuations, reinforcing the importance of preventive conservation and environmental control. The findings are particularly relevant for the conservation of gypsum casts displayed or stored in enclosed spaces without climate control, where temperature and humidity may fluctuate over time.

This integrated analytical approach proved to be useful in characterising material changes in gypsum artefacts, particularly in relation to hydration state, surface morphology and microstructural evolution under environmental stress.

6.1 Future developments

The results presented in this thesis open up important perspectives for future research. Among these, a particularly relevant question is the phase stability of gypsum when exposed to dry and warm conditions. This is especially significant for the conservation of artefacts stored in unregulated indoor environments, where fluctuating microclimates may lead to changes in their hydration state.

This aspect will be further explored in a study currently in preparation, in collaboration with the University of Antwerp. In this project, selected mock-up samples were placed in a controlled oven environment on November 2024 and kept at a constant temperature of 40 °C and ambient relative humidity below 25 %. These conditions, identified as critical in the

gypsum phase diagram discussed by Charola et al. (2007) [1], are intended to simulate long-term dry and warm exposure, in order to assess the potential formation of hemihydrate or anhydrite phases through XRPD.

The outcomes will help determine whether prolonged exposure to dry heat induces phase transformations, even under stable conditions. This could contribute to a better understanding of long-term risks for gypsum artefacts exposed to low-humidity and elevated temperature environments, and support the development of artificial ageing protocols. The research may also support the identification of early-stage alterations associated with dehydration phenomena.

Further developments include:

- Exploring the use of digital imaging and machine learning techniques for the detection and classification of surface damage;
- Testing alternative protective coatings with improved permeability and compatibility with gypsum substrates;
- Extending the mock-up approach to include a wider range of historical formulations, including pigmented or polychrome plasters;
- Implementing long-term monitoring campaign in museum settings, to assess real environmental impact and validate laboratory-based observations.

In conclusion, this thesis has contributed to a deeper understanding of the degradation processes affecting gypsum-based heritage materials by integrating on-site diagnostic, laboratory simulations, and analytical techniques. It has provided a coherent methodological framework and a set of practical insights applicable to various conservation contexts. By combining the analysis of surface features with the investigation of internal changes, this work contributed to a more complete understanding of material behaviour and deterioration over time, with insight that can support both diagnostic assessments and the planning of conservation strategies.

The findings also emphasise the importance of combining interdisciplinary perspectives and experimental approaches to advance the study and conservation of gypsum heritage materials.

Reference

[1] A. E. Charola, J. Pühringer, M. Steiger, Gypsum: a review of its role in the deterioration of building materials, Environ. Geol., vol. 52 (2007), pp. 339-352.

Supplementary materials

The following materials are provided as supplementary documentation to this thesis, including peer-reviewed publications and conference abstracts:

- **EGU General Assembly 2023 – European Geosciences Union** (Vienna, Austria, 23-28 April 2023).
  Microclimatic monitoring of the plaster casts of the Trajan's Column in the Museum of Roman Civilisation (Rome)
  Conference abstract.
- **MetroArchaeo 2023 – IMEKO TC-4 International Conference** (Rome, Italy, 19-21 October 2023).
  The diagnostic study of the plaster casts of the Trajan's Column in the Museum of Roman Civilisation (Rome)
  Peer-reviewed conference extended abstract, published in MetroArchaeo Proceedings (IMEKO).
- **Peer-reviewed journal article**
  F. Bubola, C. Coletti, E. Balliana, C. Cecamore, C. Parisi Presicce, C. Mazzoli, *The diagnostic study of the plaster replicas of the Trajan's Column conserved at the Museum of Roman Civilisation (Rome)*, ACTA IMEKO, vol. 13 (2024), pp. 1-8.
- **AIAr 2025 – Associazione Italiana di Archeometria** (Palermo, Italy, 12-14 February 2025).
  Conservation methods for 19th century plaster replicas: understanding gypsum compositions and protective treatments
  Conference abstract.
- **STONE 2025 – 15th International Congress on the Deterioration and Conservation of Stone** (Paris, France, 8-12 September 2025).
  Conservation strategies for 19th century plaster replicas: insight into gypsum mixtures and protective coatings
  Conference extended abstract.

EGU23-12934, updated on 09 Nov 2023
https://doi.org/10.5194/egusphere-egu23-12934
EGU General Assembly 2023

Microclimatic monitoring of the plaster casts of the Trajan's Column in the Museum of Roman Civilisation (Rome)

Federica Bubola[1], Eleonora Balliana[2], Chiara Coletti[1], Claudia Cecamore[3], Claudio Parisi Presicce[3], and Claudio Mazzoli[1]

[1]Università degli Studi di Padova, Geosciences, Padua, Italy (federica.bubola@gmail.com) (chiara.coletti@unipd.it) (claudio.mazzoli@unipd.it)

[2]Università Ca' Foscari, Environmental Sciences, Informatics and Statistics, Venice, Italy (eleonora.balliana@unive.it)

[3]Sovrintendenza Capitolina ai Beni Culturali, Rome, Italy (claudia.cecamore@comune.roma.it) (claudio.parisipresicce@comune.roma.it)

In recent years, the control of the micro-climate in museum environments or in historical buildings has assumed a role of great importance for the protection of the artefacts exhibited and for planning cost-effective and strategic preservation policy. The process of degradation indeed, defined as a result of progressive and cumulative material decay, strongly depends by environmental variables and their changes. Rapid changes and/or strong gradients in temperature and/or relative humidity, are the main causes of internal stress and of material surface detachments. Compared to new museums, historical ones often do not dispose of ideal conservation parameters, and they need specific conservation environments, considering the so-called *historical climate*, i.e. the microclimate to which the Cultural Heritage has adapted over the time. This is the case of the Museum of Roman Civilisation (Rome), which has been closed since 2014 and hosts a huge and valuable collection of plaster casts, such as those of the Trajan's Column made by Napoleon III in 1861-1862 and gifted from Vatican City to Rome City Hall in 1953. In view of the imminent museum reopening and restoration, it is essential to define the actual level of microclimate quality, compared to the expected one, considering also economic and regulatory aspects and the future welfare of the artefacts. The research is focused on the response of the materials to the micro-climate by evaluating the incidence of temperature and relative humidity, presumably the main chemical and physical degradation factors for the plaster casts. A multidisciplinary diagnostic approach (i.e. Hyperspectral Imaging, Raman Spectroscopy, Infrared Spectroscopy) is also planned to characterise the constituent materials, to suppose the manufacturing techniques of the casts and to identify the degradation forms. The analysis of the complex interaction between the dynamics of the climate and the need for the conservation of the artefacts under conditions of maximum stability represents the starting point for proposing a sustainable restoration of the Trajan's Column plaster casts of the Museum of Roman Civilisation and a future exhibition project that will allow their valorisation and exposure.

2023 IMEKO TC-4 International Conference on
Metrology for Archaeology and Cultural Heritage
Rome, Italy, October 19-21, 2023

The diagnostic study of the plaster casts of the Trajan's Column in the Museum of Roman Civilisation (Rome)

Federica Bubola[1], Chiara Coletti[1], Eleonora Balliana[2], Claudia Cecamore[3], Claudio Parisi Presicce[3], Claudio Mazzoli[1]

[1] *Department of Geosciences, University of Padua, Via Gradenigo 6, Padua, Italy, federica.bubola@phd.unipd.it, chiara.coletti@unipd.it, claudio.mazzoli@unipd.it*
[2] *Department of Environmental Sciences, Informatics and Statistics, Ca'Foscari University, Via Torino 155, Mestre, Italy, eleonora.balliana@unive.it*
[3] *Sovrintendenza Capitolina ai Beni Culturali, Piazza Lovatelli 35, Rome, Italy, claudia.cecamore@comune.roma.it, claudio.parisipresicce@comune.roma.it*

Abstract
In recent years, the control of the microclimate in museums has been increasingly recognised as important. This research focuses on state of conservation assessment of 34 plaster casts of Trajan's Column at the Museum of Roman Civilisation and on the microclimate monitoring of the Room LI, where they are conserved. The results continue to demonstrate that the main causes of decay derive from unsuitable climate conditions, which lead to cracks and detachments.

I. INTRODUCTION

The control of the microclimate in museum environments or historical buildings is a fundamental aspect in the protection of artefacts and the planning of an appropriate conservation strategy. Deterioration processes, defined as a result of progressive and cumulative material decay, depends on environmental variables and their changes. In particular, inappropriate temperature and relative humidity levels speed up chemical and physical deterioration and may cause irreversible decay to cultural artefacts.

Variations in hygrothermic conditions can generate physical and structural changes on the surface, influence and catalyse chemical reactions, i.e. hydrolysis and oxidation-reduction [1], and cause biodeterioration. Gypsum-based plaster artefacts may undergo issues such as deformations, loss of adhesion and in general structural and mechanical changes, solubilisation, migration and salt crystallisation.

The plaster casts of the Trajan's Column, made by Napoleon III between 1861 and 1862, are the object of this study.

In view of the imminent reopening of the Museum of Roman Civilisation (MCR) and the restoration of its plaster casts, the assessment of the current microclimate quality is crucial for long-term preservation of them.

II. MATERIALS AND METHODS

A. Experimental strategy

The complete set of plaster casts reproducing the Trajan's Column, has been housed in Room LI at the Museum of Roman Civilisation since around the mid-1900s. Unfortunately, limited information is available regarding their previous state of conservation. The current study of the microclimate enables a comparison between the current state of preservation and the condition of the plaster casts in 2012, year in which the Museum conducted a conservation survey campaign.

In this first research phase of the microclimate monitoring campaign in the Museum, a sensor was placed for a period of approximately seven months. Climate data was collected from November 23, 2022, to June 8, 2023, for a total of 4407 readings.

In this study 34 plaster casts were analysed (the complete set reproducing the Trajan's Column counts 125 plasters). A photographic campaign was carried out to identify and highlight the details and main visible causes of degradation. The images acquired were used to support the decay mapping carried out for each cast. The on-site macroscopic investigation was supported by the use of the Dino-Lite contact optical microscope, both in natural and ultraviolet light. In addition, InfraRed Thermography was applied to investigate detachments and cracks.

Two micro-samples, in the form of small spalling (samples A and B) were collected from the MCR_3045 plaster cast. The samples were analysed using different analytical methodologies: X-Ray Powder Diffraction (XRPD) was used in order to identify the mineral phases; Field Emission Scanning Electron Microscopy (FESEM) to investigate the mineralogy and morphology of the samples; Attenuated Total Reflection Infrared Spectroscopy (ATR-FTIR) performed qualitative analyses for the identification of organic and inorganic compounds;

and μ-Raman spectroscopy was applied to identify the composing materials.

B. Microclimatic monitoring

The microclimatic monitoring was carried out using an OM-EL-USB-2LCD by OMEGA® data logger. Monitoring was performed recording climate data with a frequency of 30 minutes.

C. Analytical Techniques

The photographs were taken with a Canon camera under lighting conditions using 230V 750W halogen lamps. White balance was carried out in situ directly from the camera.

Thermal diffusion was studied using an InfraRed-Thermocamera (FLIR). InfraRed-images were captured in time lapse mode every 30s (41 frame total) after heating the plaster casts with halogen lamps for 20 min at a distance of 1m. The IR-images and the profiles of thermal diffusion were extrapolated using FLIR ResearchIR 4 Max + HSDR software® Images were saved in false colour with palette GF White Hot function, in the thermal range of 11-35°C using the FLIR system DDE (Digital Detail Enhancement) algorithm.

Diffraction data were acquired on a PANalytical X'Pert PRO diffractometer operating in Bragg-Brentano reflection geometry with CoKα radiation, 40kV voltage and 40mA filament current, equipped with an X'Celerator detector. Qualitative analysis of diffraction data was carried out with X'Pert HighScore Plus® software (PANalytical) and the PDF-2 database.

Raman measurements were made using a Thermo Scientific DXR Raman Microscope using a 532nm laser excitation source. Analyses were performed using a 50x long working distance objective with ~2.5cm^{-1} spectral resolution, ~1μm pinhole operating at 3mW of power. To minimize noise, each spectrum was acquired 30 times with an exposure time of 1s. Spectra were recorded in the frequency range from 100 to 3500cm^{-1}. Spectral fitting was carried out using the Thermo Scientific OMNIC Spectra Software (Version 9) and then processed with OriginPRO 2018b.

For the Attenuated Total Reflection Infrared Spectroscopy, a Bruker ALPHA II by Bruker Optics® Fourier transform IR Spectrometer was used. ATR-FTIR analyses were recorded in the spectral range from 4000 to 400cm^{-1}, using a synthetic diamond crystal for sample compression. The background was measured with 48 scans before each acquisition, while the samples were analysed with 48 scans, with a resolution of 4cm^{-1}. The spectra obtained were processed with the Thermo Scientific OMNIC Spectra Software (Version 9), and then further processed with OriginPRO 2018b.

Sample mineralogy and morphology were investigated with a FESEM Tescan Solaris. Microchemical analysis was performed on mineral phases as observed under the FESEM, using an Oxford Instrument Ultim Max 65 Silicon drift detector EDS and operating at 15KeV with a current of 3nA and a working distance of 5mm. Backscattered electron (BSE) images were acquired working at lower tension and current (5KeV, 300 pA and at a working distance of 4mm) to improve image resolution.

III. RESULTS AND DISCUSSION

A. Experimental strategy

The temperature graph in Fig.1A shows a curve devoid of fluctuations and significant peaks with an average value of 14.06°C. The minimum value reached on 10 February 2023 is 8°C, while the maximum value of 26°C was reached on 7 June 2023.

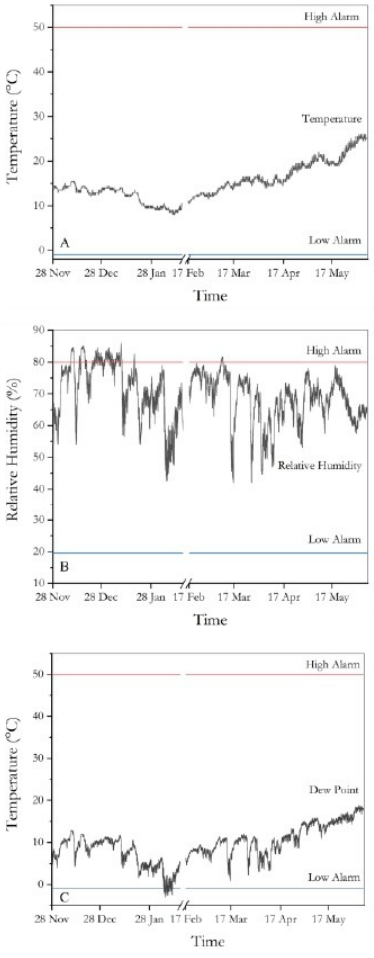

Figure 1. Temperature (A), Relative Humidity (B) and Dew Point (C) data obtained from the microclimatic monitoring of Room LI, over a period of seven moths.

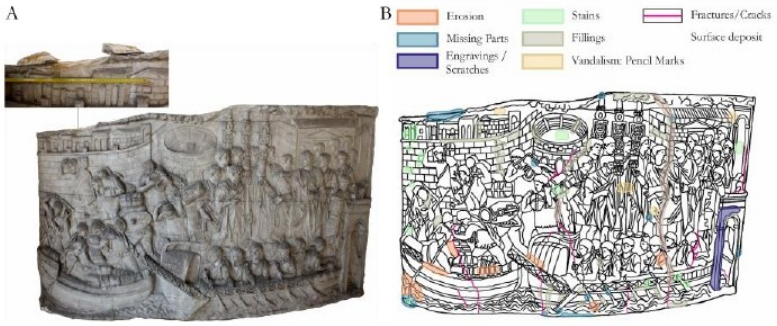

Figure 2. Plaster cast MCR_3045, with a detail of missing part from which sample A was taken (A). Degradation map of the MCR_3045 plaster cast and the legend showing the degradation patterns (B).

The relative humidity data (Fig.1B) shows a non-linear trend, with the presence of numerous peaks and fluctuations. Daily fluctuations in relative humidity are influenced by the day-night cycle, with a strong relationship between relative humidity and temperature: low temperatures correspond to an increase in relative humidity, particularly in the early morning hours. The sensor was set in a range between 19.5% and 80.0%. The RH levels exceeded the maximum set level of 80% numerous times. The minimum value of RH% was recorded on the evening of 28 March 2023 and is 42%, while the maximum value is 86%, recorded on 9 January 2023.

The acquired dew point data (Fig.1C) show that the minimum value was reached on 6 February 2023 at 11 p.m., and was -3°C, while the maximum value was reached on 23 November 2022 at 1 p.m., and was 18.8°C.

B. Plaster casts characterisation

In the 2012 campaign to survey their conservation state, the 125 gypsum-based plaster casts have been divided into three classes, depending on the typology and the severity of the degradation patterns (mediocre, discreet and poor). From each of these classes, ten casts were selected to be studied. Moreover, four other plaster casts which did not fit into one of the classes were selected. The analysed plaster casts were chosen on the basis of the institution's requirements, their state of preservation and their location within the gallery.

The casts consist of sections, held together by a wooden and metal structure placed on the back. This complex structure of heterogeneous materials can react with the surrounding environment under very humid conservative conditions, and in the presence of liquid water can cause specific decay patterns. In fact, the presence of rust stains was observed both on the back and on the surface of the casts. In general, the surface of the casts is covered by coherent deposits, particularly in the most exposed areas, due to the porosity and hygroscopicity of gypsum, which are mainly responsible for the tendency of this material to retain dust. In addition, diffuse yellow and pink tonal variations are present, probably due to historical patinas. Pencil marks are present in some areas, while surface scratches cover most of the surface of the casts. All the plaster casts, especially those belonging to the discreet and poor classes show presence of micro-cracks and deep fractures, some of which extended over almost the entire height. In addition to the rust stains, a large amount of dark-coloured and red/brown stains of different size, and residues of mortar are visible, probably related to the modelling of the casts (Fig.2). Several casts also display areas subjected to erosion, pulverisation and lifting.

The thermograms emphasise detachments and cracks [2]. In Fig.3B, the area underneath, having absorbed less heat, shows a dark colour, while the more exposed surface area is highlighted by a strong yellow colour, since it has absorbed more heat, as it is closer to the source.

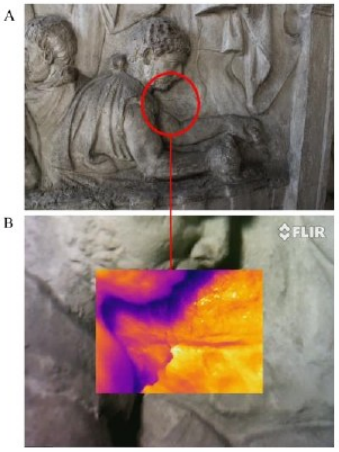

Figure 3. Detail of a fracture in the MCR_3045 plaster cast (A). Thermogram acquisition highlighting the deep fracture with the uplift of the material (B).

The mineralogical characterisation by XRPD analysis (Fig.4A) on the collected samples (Fig.5A) showed that the main constituent material is gypsum ($CaSO_4 \cdot 2H_2O$) indicated by the presence of the characteristic diffraction peaks (*Gp)*, marked with approved mineral symbols [3,4]. The diffractogram of sample A shows the presence of gypsum and calcite ($CaCO_3$). The analysis also showed traces of quartz and kaolinite ($Al_2Si_2O_5(OH)_4$). The diffractogram of sample B, shows only the presence of gypsum and quartz (SiO_2).

FESEM analyses confirmed what was drawn by mineralogical characterisation. The matrix of the sample is characterised by a heightened porosity in the bulk, while a more compact gypsum morphology characterises the surface layer. Analyses confirmed quartz and kaolinite inclusions characterised by the presence of Al, Si and K. The presence of these elements revealed also a surface finishing layer highlighted in green in the map (Fig.4B), mainly composed of kaolinite.

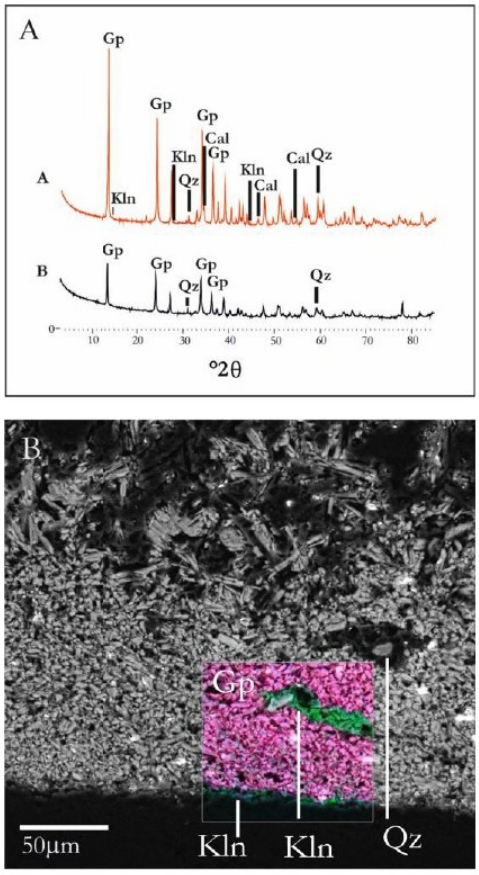

Figure 4. XRPD patterns of sample A and B (A); FESEM image of sample B. The map highlights less porous gypsum-based matrix with inclusions of quartz and kaolinite, and a finishing rich in kaolinite (B).

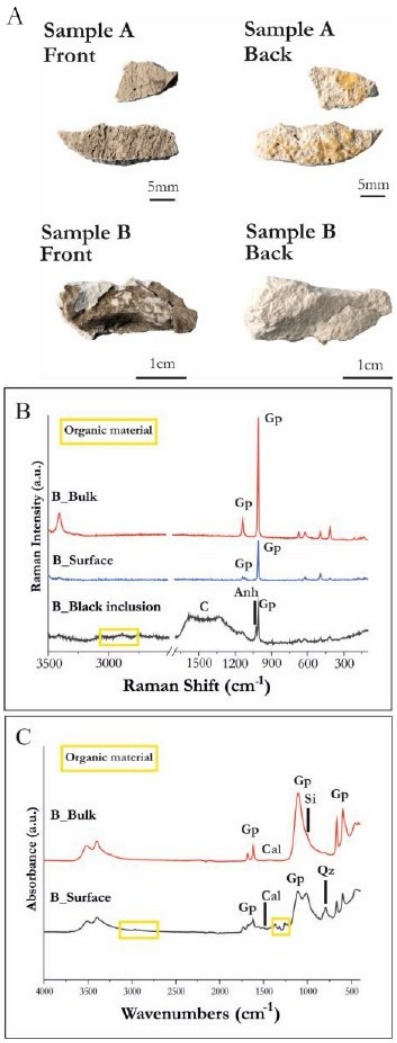

Figure 5. Micro-samples (samples A and B, front and back) collected from the plaster cast MCR_3045 (A). Raman spectra of sample B (B); ATR-FTIR spectra of sample B (C).

The three µRaman spectra show the characteristic bands of gypsum at 1140, 1008, 673, 492 and 414 cm^{-1}, corresponding to the stretch vibrational mode of SO_4 (Fig.5B) [5,6]. The two Raman bands observed around 3405 and 3490 cm^{-1} correspond to the O-H stretching vibration of water molecules in gypsum. The spectra show traces of anhydrite, with the characteristic bands of the sulphate ions at 1170, 1026 and 630 cm^{-1}. The presence of anhydrite can be ascribed to the raw material used in the moulding of the casts [6].

ATR-FTIR spectra of sample B, determined the presence of gypsum ($CaSO_4 \cdot 2H_2O$) by the peaks at 1680, 1620 cm^{-1} (bending OH), and at 1110, 670 and 620 cm^{-1} (Fig.5C). These peaks correspond to the

stretching vibration of SO_4^{2-}, while the stretching vibrations of the water molecules of the gypsum occur at ~3500 and ~3400 cm^{-1} [7].

The peak at 3340 cm^{-1} in the spectrum of the surface corresponds instead at the stretching OH of non-bonding water molecules. The carbonate functional group relates to the presence of calcite can be detected in both the spectra due to the presence of the characteristic peaks at ~1420-1430 and 873 cm^{-1} [8]. The broad low intensity in the range 800-770 cm^{-1} could be ascribed to the presence of quartz, present in the raw material or added during the moulding process [9]. The bands at 2964, 2920, 2850 cm^{-1} can be related to the stretching CH of an organic substance, as well as the peaks at 1736 cm^{-1} (stretching C=O), 1562 and 1511 cm^{-1} (stretching C-C), and the bands at ~1370 and 1230 cm^{-1} (bending CH) [10]. This organic material can be attributed to some compound used in previous intervention or as a finishing.

IV. CONCLUSION

The microclimate data recorded in the period between November 2023 and June 2023 show an average temperature of 15.06°C, with relative humidity levels occasionally exceeding 80%. When compared to the 2012 reports, it becomes evident that environmental conditions, especially fluctuations in relative humidity, have had a significant impact on the state of preservation of the gypsum-based plaster casts. This impact is evident in the development of various forms of degradation, including new fractures, erosion, and material pulverisation. Additionally, the surfaces exhibit scratches, deposits, and stains.

These results will support the restoration efforts for the plasters casts, ensuring their optimal preservation once the Museum reopens.

Some ongoing analyses include on-site Hyperspectral Imaging to map and confirm forms of degradation such as the presence of biological attacks; colorimetric measurements to understand tonal variations on the surfaces of the plaster casts; and Thermogravimetry-Differential Scanning Calorimetry and Pyrolysis Gas-Chromatography to identify organic materials.

Furthermore, a result of a structural analysis of Room LI will be conducted using IR Thermography. Based on the results of this analysis, a comprehensive microclimatic monitoring campaign will be initiated, employing higher-performance sensors, strategically positioned at critical points within the gallery.

REFERENCES

[1] A. Spagnulo, C. Vetromile, A. Masiello, M.F. Alberghina, S. Schiavone, C. Lubritto, “Climate and Cultural Heritage: The Case Study of “Real Sito of Carditello”, Heritage, vol.2, No.3, July 2019, pp. 2053-2066.

[2] F. Mercuri, U. Zammit, N. Orazi, S. Paoloni, M. Marinelli, F. Scudieri, “Active infrared thermography applied to the investigation of art and historic artefacts”, J. Therm. Anal. Calorim., May 2011, vol.104, No.2, pp. 475-485.

[3] J. C. A. Boeyens, V. V. H. Ichharam, “Redetermination of the crystal structure of calcium sulphate dihydrate, $CaSO_4 \cdot 2H_2O$”, Z. Kristallogr., vol.217, January 2002, pp. 9-10.

[4] L. N Warr, “IMA-CNMNC approved mineral symbols”, Mineral Mag., vol.85, No.3, June 2021, pp. 291-320.

[5] V. Antunes, A. Candeias, M. J. Oliveira, S. Longelin, V. Serrão, A. I. Seruya, J. Coroado, L. Dias, J. Mirão, M. L. Carvalho, “Characterization of gypsum and anhydrite ground layers in 15th and 16th centuries Portuguese paintings by Raman Spectroscopy and other techniques”, J. Raman Spectrosc., vol.45, No.11-12, November 2014, pp. 1026-1033.

[6] N. Prieto-Taboada, O. Gómez-Laserna, I. Martínez-Arkarazo, M. A. Olazabal, J. M. Madariaga, “Raman Spectra of the Different Phases in the $CaSO_4$-H_2O System”, Anal. Chem., vol.86, No.20, October 2014, pp. 10131-10137.

[7] D. Gramtorp, K. Botfeldt, J. Glastrup, K. P. Simonsen, “Investigation of Anne Marie Carl-Nielsen’s waz models, Stud. Conserv., vol.60, No.2, March 2015, pp. 97-106.

[8] F. A. Andersen, L. Brečevic, “Infrared Spectra of Amorphous and Crystalline Calcium Carbonate”, Acta Chem. Scand., vol.45, 1991, pp. 1018-1024.

[9] I. Fikri, M. El Amraoui, M. Haddad, A. S. Ettahiri, C. Falguères, L. Bellot-Gurlet, T. Lamhasni, S. A. Lyazidi, L. Bejjit, “Raman and ATR-FTIR analyses of medieval wall paintings from al-Qarawiyyin in Fez (Morocco)”, SAA, June 2022.

[10] F. Pozzi, E. Basso, S. Alderson, J. Levinson, M. Neimar, S. Alcalá, “Aiding the cleaning of four 19th-century Tsimshian house posts: investigation of museum-applied surface coatings and original polychromy”, Herit. Sci., vol.9, No.42, December 2021.

ACTA IMEKO
ISSN: 2221-870X
June 2024, Volume 13, Number 2, 1 - 8

The diagnostic study of the plaster replicas of the Trajan's Column conserved at the Museum of Roman Civilisation (Rome)

Federica Bubola[1], Chiara Coletti[1], Eleonora Balliana[2], Claudia Cecamore[3], Claudio Parisi Presicce[3], Claudio Mazzoli[1]

[1] *Department of Geosciences, University of Padua, Via G. Gradenigo 6, Padua, Italy*
[2] *Department of Environmental Sciences, Informatic and Statistics, Ca' Foscari University, Via Torino 155, Mestre, Italy*
[3] *Sovrintendenza Capitolina ai Beni Culturali, Piazza Lovatelli 35, Rome, Italy*

ABSTRACT
The management of indoor microclimate in museums has recently received growing attention. Museum climatology and the mechanism for the degradation process, defined as a result of progressive and cumulative decay, depends on environmental variables and their changes. In fact, temperature and relative humidity gradients are often the main causes of chemical and physical decay of artefacts. This research focuses on assessing the state of conservation of 34 gypsum-based plaster replicas of Trajan's Column at the Museum of Roman Civilisation and on the microclimate monitoring of Room LI, where they are conserved. The decay assessment of the studied plaster casts was performed using a multidisciplinary analytical approach to characterize the constituent materials and to identify the main degradation patterns by i) on-site investigation with non-destructive methodologies; ii) chemical and petrographical characterization on collected micro samples. Microclimate variables (temperature, relative humidity and dew point) were measured along seven months to define the actual environmental conditions and the response of the materials to the microclimate.

Section: RESEARCH PAPER

Keywords: Gypsum-based plaster replicas; microclimatic monitoring; museum environment; multidisciplinary analytical approach; cultural heritage

Citation: F. Bubola, Ch. Coletti, E. Balliana, C. Cecamore, C. Parisi Presicce, C. Mazzoli, The diagnostic study of the plaster replicas of the Trajan's Column conserved at the Museum of Roman Civilisation (Rome), Acta IMEKO, vol. 13 (2024) no. 2, pp. 1-8. DOI: 10.21014/actaimeko.v13i2.1808

Section Editor: Fabio Leccese, Università Degli Studi Roma Tre, Rome, Italy

Received February 27, 2024; **In final form** May 30, 2024; **Published** June 2024

Corresponding author: Federica Bubola, e-mail: federica.bubola@phd.unipd.it; federica.bubola@gmail.com

1. INTRODUCTION

The regulation of microclimatic conditions within museum environments and historical buildings constitutes a fundamental aspect for preserving artefacts and developing effective conservation strategies. Degradation processes, as the result of progressive and cumulative material decay, are contingent upon environmental variables and their temporal fluctuations. Specifically, suboptimal levels of temperature and relative humidity expedite chemical and physical deterioration, potentially leading to the irreversible decay of Cultural Heritage. Compared to new museums, historic buildings and archaeological sites, often lacking ideal conservation parameters, present a distinct challenge. Variations in hygrothermal conditions can induce physical and structural changes on the surface. Gypsum-based artefacts may undergo deformations, cracks, loss of adhesion and general structural and mechanical changes, as well as solubilisation, migration and salt crystallisation. Moisture presence also influences and catalyses chemical reactions, including oxidation-reduction and hydrolysis [1]. Moreover, a high level of relative humidity and temperature fluctuations can also lead to the development of biodeteriogens. However, previous research has demonstrated that adhering to rigid temperature and relative humidity values is unnecessary. Instead, it is crucial to thoroughly understand the conservation environment and the microclimate to which the Cultural Heritage goods has adapted [2].

Although in recent years the study of plaster replicas has broadened, there are still few individual case studies that manage to fully capture the complexity of these artworks [3], [4]. Valuable information on the characterisation and the manufacture technologies of gypsum-based materials can be found in studies

on decorative stucco and mortars [5]-[9]. Nevertheless, the majority of the previous literatures prioritizes examining the physical and mechanical properties [10], [11], [12], [13], with an insight in the mineralogical composition [14], [15], [16], while research into hygroscopic properties and the interaction between the material and indoor microclimate is still relatively limited.

While gypsum typically serves as the primary material for nineteenth-century plaster replicas [17], the plaster manufacturing process often involved the addition of inorganic materials such as clays and sand, as well as organic materials such as gums and resins, to enhance mechanical properties and modify the setting time [3], [5]. Additionally, wooden and metal support structures may have been integrated during the casting process or later added during restoration interventions. Considering the multi-materiality of the plaster replicas, and that the typical decay patterns observed are often associated with environmental conditions, conducing a full characterisation of the casting materials is essential to obtain information about the deterioration processes and the relation between materials and microclimate.

This study focuses on the gypsum-based plaster replicas of Trajan's Column (113 A.D.) conserved in Room LI of the Museum of Roman Civilisation (MCR), reproducing the Trajan's military campaign to conquer Dacia. This complete set of plaster casts was produced by Pius IX for Napoleon III in 1861-1862 through the electrotyping (or galvanoplasty) process and comprises 125 casts.

Given the imminent reopening of the Museum of Roman Civilisation (the Museum has been closed since 2014) and the concurrent restoration of its plaster casts, the assessment of the current microclimate quality is crucial for the long-term preservation of these artefacts. The starting point involves the analysis of the complex interaction between microclimate dynamics and materials, focusing on evaluating the influence of temperature and relative humidity.

The following section details the materials and methods applied in the microclimatic campaign and outlines the analytical techniques employed. Section 3 presents the most significant results obtained from the analysis of the microclimate and plaster replicas. Subsequently, in the concluding section, the principal outcomes of the research are summarized.

2. MATERIALS AND METHODS

2.1. Experimental strategy

The entire collection of plaster casts reproducing the Trajan's Column has been housed in Room LI at the Museum of Roman Civilisation since around the mid-1900s, with limited information on their previous conservation status. The ongoing microclimate study enables a comparison between the current preservation state and the cast's condition in 2012, when the Museum conducted a conservation survey.

In the initial phase of the Museum's microclimate monitoring campaign, a sensor was deployed for approximately seven months, collecting climate data from November 23, 2022, to June 8, 2023, yielding a total of 4407 readings. This microclimate dataset forms the basis for understanding the environmental conditions affecting the plaster replicas.

The onsite investigation comprises the detailed analysis of 34 plaster casts, a subset of the total 125 casts reproducing the Trajan's Column. A dedicated photographic campaign documented visible degradation patterns, supporting a comprehensive decay mapping for each cast. The macroscopic examinations were complemented using the Dino-Lite contact optical microscope, applied under natural and ultraviolet light. Additionally, InfraRed Thermography served as a valuable tool for investigating cracks and detachments in the plaster.

Two micro-samples (1-2 cm in size), A and B, were collected from the MCR_3045 plaster cast to provide insights into its material composition and degradation mechanisms. These micro-samples were analysed using different analytical methodologies: X-Ray Powder Diffraction (XRPD) for identifying mineral phases; Field Emission Scanning Electron Microscopy (FESEM) to investigate the mineralogy and morphology of the samples; Attenuated Total Reflection Infrared Spectroscopy (ATR-FTIR) for qualitative analyses of organic and inorganic compounds, and μ-Raman spectroscopy for identifying the materials constituting the plaster replicas.

The heterogeneous composition of the plaster casts and the complexity of their structure, characterized by the presence of organic and inorganic materials, underscores the necessity of employing a multi-analytical approach, complemented by a microclimatic monitoring campaign, to assess the state of conservation and the correlation between the decay patterns and the influence of temperature and relative humidity.

2.2. Microclimatic monitoring

Microclimatic monitoring was carried out using an OM-EL-USB-2LCD data logger by OMEGA®. The monitoring protocol included recording climate data at 30-minute intervals in the central area of Room LI over seven months. The sensor was set with an active alarm system based on predetermined maximum and minimum thresholds for temperature (T) and relative humidity (RH %). Specifically, the maximum temperature alarm was set at 50 °C, with a corresponding minimum temperature alarm set at -1 °C. Concerning relative humidity, the maximum alarm was triggered at a threshold of 80 %, while the minimum alarm was activated at 19.5 %.

On 17 February, the sensor was temporarily removed from the Room LI to retrieve the accumulated data. Consequently, data collected on that particular day were excluded from subsequent processing to ensure the integrity of the dataset.

The ongoing monitoring methodology has facilitated valuable data collection, essential for evaluating the microclimatic conditions within the monitored environment. Notably, this initial approach has allowed for the subsequent extension of microclimatic monitoring, involving the deployment of additional sensors strategically positioned along Room LI.

2.3. Analytical techniques

The photographs were captured using a Canon camera under 230 V 750 W halogen lamps lighting conditions. White balance adjustments were conducted in situ directly from the camera.

Thermal diffusion studies employed an InfraRed-Thermocamera (FLIR). InfraRed-images were obtained in time-lapse mode every 30 seconds (41 frames total). They were captured after heating the plaster casts with halogen lamps for 20 min at a distance of 1 m. The IR images and thermal diffusion profiles were extrapolated using FLIR ResearchIR 4 Max + HSDR software®. Images were saved in false colour using the palette GF White Hot function, in the thermal range of 11-35 °C using the FLIR system DDE (Digital Detail Enhancement) algorithm.

Diffraction data were acquired on a PANalytical X'Pert PRO diffractometer operating in Bragg-Brentano reflection geometry with CoKα radiation, 40 kV voltage, and 40 mA filament current,

equipped with an X'Celerator detector. Qualitative diffraction data analysis was carried out with X'Pert HighScore Plus® software (PANalytical) and the PDF-2 database.

Raman measurements were carried out with a Thermo Scientific DXR Raman Microscope using a 532 nm laser excitation source. Analyses were carried out using a 50x long working distance objective with ~2.5 cm spectral resolution, ~1 μm pinhole operating at 3 mW of power. Each spectrum was acquired 30 times to minimize noise with an exposure time of 1 s. Spectra were recorded in the frequency range from 100 to 3500 cm^{-1}. Spectral fitting was carried out using the Thermo Scientific OMNIC Spectra Software (Version 9) and then processed with OriginPRO 2018b.

For the Attenuated Total Reflection Infrared Spectroscopy, a Bruker ALPHA II by Bruker Optics® Fourier transform IR Spectrometer was used. ATR-FTIR analyses covered the spectral range from 4000 to 400 cm^{-1}, using a synthetic diamond crystal for sample compression. The background was measured with 48 scans before each acquisition, while the samples were analysed with 48 scans, with a resolution of 4 cm^{-1}. The spectra obtained were processed with the Thermo Scientific OMNIC Spectra Software (Version 9), and then further processed with OriginPRO 2018b.

Sample mineralogy and morphology were investigated with a FESEM Tescan Solaris. Microchemical analysis was carried out on mineral phases as observed under the FESEM using an Oxford Instrument Ultim Max 65 Silicon drift detector EDS operating at 15 keV with a current of 3 nA and a working distance of 5 mm. Backscattered electrons (BSE) were acquired to improve image resolution by working at lower tension and current (5 keV, 300 pA and at a working distance of 4 mm).

3. RESULTS AND DISCUSSION

3.1. Microclimatic monitoring

The temperature graph in Figure 1A illustrates a consistently smooth curve devoid of notable fluctuations and significant peaks, maintaining an average value of 15.06 °C. Notable temperature extremes include a minimum of 8 °C recorded on February 10, 2023 and a maximum of 26 °C documented on June 7, 2023.

In contrast, the gathered relative humidity data in Figure 1B shows a non-linear trend marked by numerous peaks and fluctuations. Daily variations in relative humidity are influenced by the day-night cycle, with a strong correlation between relative humidity and temperature. Low temperatures coincide with heightened relative humidity, especially in the early morning hours. The sensor was configured within a range from 19.5 % to 80.0 %, and instances where the relative humidity exceeded the predefined maximum level of 80 % were observed frequently. The minimum value of RH % (42 %) was recorded on the evening of March 28, 2023, while the maximum value was 86 %, recorded on January 9, 2023.

Analysing the calculated dew point data in Figure 1C reveals that the minimum dew point of 3 °C occurred on February 6, 2023, at 11 p.m., while the maximum dew point of 18.8 °C was registered on November 23, 2022, at 1 p.m.

The collected microclimatic data, displays temperature fluctuations, which, especially when combined with high humidity levels, can affect the state of conservation of the plaster replicas. Indeed, gypsum plaster, being a partially soluble material, is highly vulnerable to these fluctuations, which can lead to the formation of condensation and subsequent material

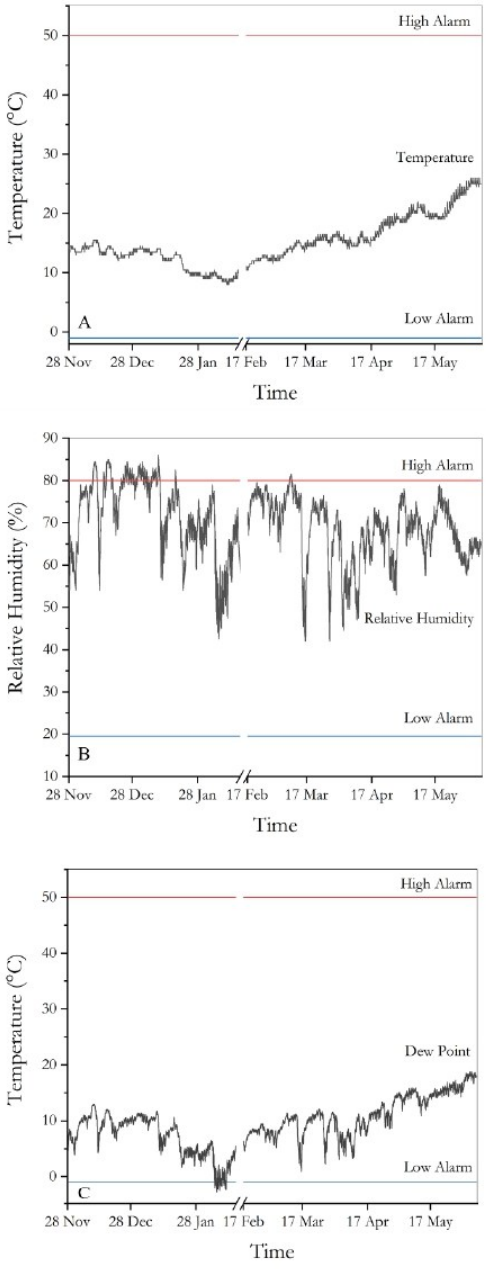

Figure 1. A) Temperature, B) Relative Humidity, and C) Dew Point data obtained from the microclimatic monitoring of Room LI over a period of seven months.

dissolution. Moreover, a high content of relative humidity can catalyse the dissolution and solubilisation of salts, resulting in recrystallisation that may cause deformations, fractures and cracks [5], [18]. This phenomenon can further increase the existing decay or even cause additional damage. The recorded temperature fluctuations from 8 °C to 26 °C suggest that decay cannot be related to freeze-thaw events, that can modify the pores connected to the environment resulting in detachment and loss of material [5], [18], [19].

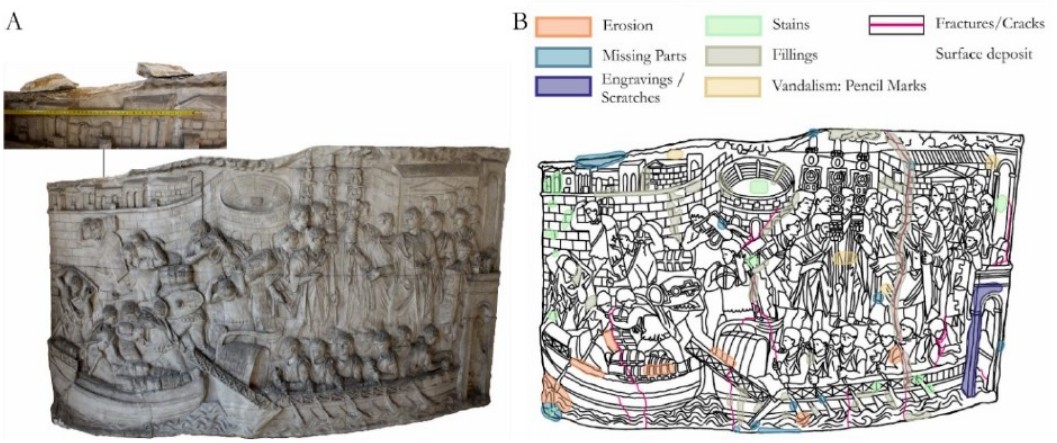

Figure 2. Plaster cast MCR_3045, with a detail of the missing part from which sample A was taken (A). Degradation map of the MCR_3045 plaster cast and the legend showing the degradation patterns (B).

3.2. In situ survey

In the conservation state survey conducted in 2012, 125 gypsum-based plaster casts were categorized into three classes based on the typology and severity of observed degradation patterns. These classes were explicitly labelled as mediocre, discreet, and poor. For this diagnostic investigation, ten plaster replicas from each class were selected for an in-depth study. Additionally, four plaster casts, not fitting any pre-defined class, were included. The selection criteria were based on institutional requirements, their preservation state, and specific Room LI location. This ensured a representative and comprehensive examination of different conservation states and conditions exhibited by the plaster casts, aligning with the objectives of the institutional conservation campaign. Most casts showed the same surface decay pattern, varying in extent and frequency/localisation.

The plaster casts consist of sections held together by a wooden and metal structure placed on the back (Figure 3A). The structure, consists of curved, horizontal ribs covered with an irregular layer of gypsum. This complex structure of heterogeneous materials can react with the surrounding environment under very humid conservative conditions, and the presence of liquid water exacerbates this tendency, giving rise to distinct decay patterns. In presence of metallic elements within the cast, high levels of relative humidity can involve oxidation phenomena, with consequent corrosion and material expansion which can worsen scaling and detachment phenomena, leading to additional material loss also at the decorative surface [5], [18]. Notably, rust stains have been detected both on the casts' back (Figure 3A) and surface (Figure 3B).

Monitoring indoor environment is crucial in museums to safeguard artworks, which are susceptible to dust accumulation in the form of particles or fibres. Since the Museum of Roman Civilisation is closed, the primary source of dust is likely to be attributed to external factors such as road traffic and emissions

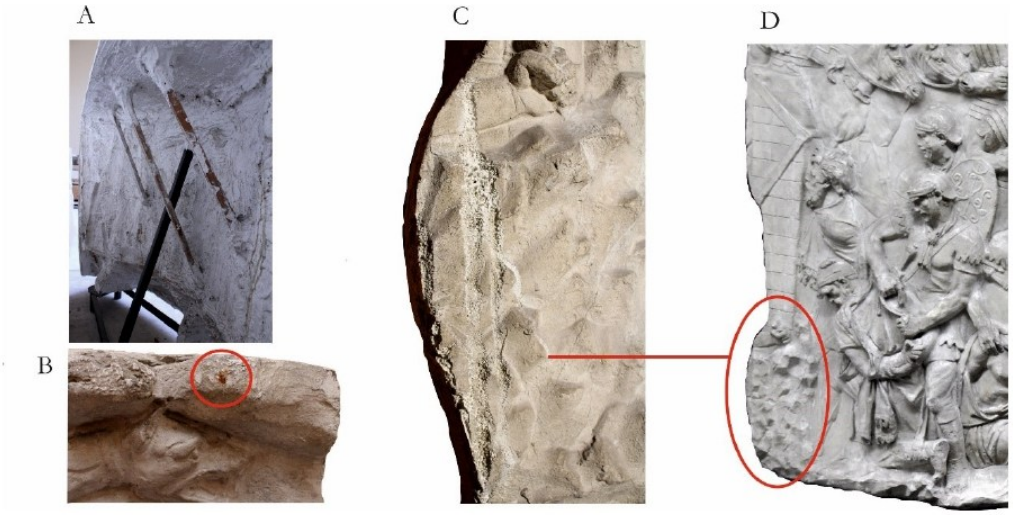

Figure 3. Detail of the wooden and metal structure placed on the back of Plaster cast MCR_3724: rust stains and drippings are visible on the irregular layer of gypsum (A). Detail of a rust stain on the surface of plaster cast MCR_3043 (B). Detail of plaster cast MCR_3052 (photo taken in 2023, during our in situ survey), which displays pulverisation as effect of the microclimate conditions (C). Detail from a photo taken during the 2012 survey of same plaster cast on Figure 2C (MCR_3052) where the material is not affected by decay patterns (D).

from industrial activities [20], [21]. Indoor conditions such as high humidity levels, can promote the adhesion of the dust to the surface [22], [23]. In general, the cast surfaces exhibit coherent deposits, especially in the most exposed areas, due to the porosity and hygroscopicity of gypsum, which primarily accounts for the tendency of this material to retain dust. Furthermore, diffuse tonal variations in yellow and pink areas are evident, likely due to historical patinas. Pencil marks are present in some areas, while scratches cover most of the cast surfaces. Each plaster cast, especially those belonging to the discreet and poor categories, shows the presence of micro-cracks and/or deep fractures, some of which extend nearly the full height of the cast. Beyond rust stains, many dark-coloured and red/brown stains of varied dimensions (up to 1-2 cm), and mortar residues are visible. These features are likely remnants from the casting process itself. Several casts exhibit regions subjected to erosion, pulverisation and lifting. Temperature and relative humidity variations can enhance weathering processes also in short time span. Photographic materials from the previous survey dated 2012 was a meaningful documentation to observe areas of erosion and pulverisation at the surface of the casts, occurred in the last decade (Figure 2C and Figure 2D). A closer examination reveals that some missing components, with surface details lost after the casts were made, subsequently required restoration efforts. Notably, these interventions are conspicuous, particularly near fractures, many coated with stucco. The fillings, discerned upon examination, exhibit varying thicknesses.

Active Infra-Red Thermography was employed to investigate the surface and subsurface features. When exposed to unsuitable environmental conditions, the artefacts can generate thermal, hygrometric and mechanical stresses, leading to alterations in the integrity of the artworks. In this regard, applying thermographic methods can provide a distinct advantage in examining surface phenomena [24]. The thermograms emphasise detachments and cracks. In Figure 4B, the area underneath, which has absorbed less heat, shows a dark colour, while the intense yellow colour highlights the more exposed surface area, since it has absorbed more heat, as it is closer to the source.

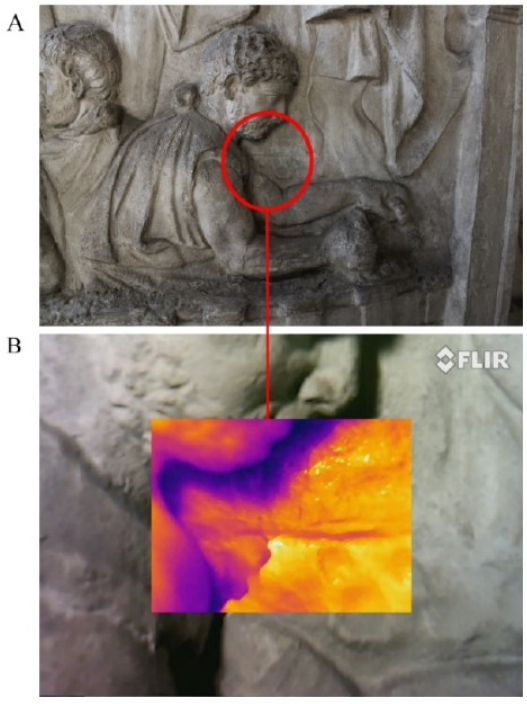

Figure 4. Detail of a fracture in the MCR_3045 plaster cast (A). Thermogram acquisition highlights the deep fracture with the uplift of the material (B).

3.3. Microchemical and mineralogical characterisation

The mineralogical characterisation by XRPD analysis (Figure 5A) on the collected samples (Figure 6A) showed that the primary constituent material is gypsum (*Gp*) indicated by the presence of the characteristic diffraction pattern, with the most intense peak related to the (020) crystal plane [25], [26]. The diffractogram of sample A, collected from the bulk, shows the presence of gypsum and calcite (*Cal*) [27]. The analysis also showed traces of quartz (*Qz*) and kaolinite (*Kln*), ascribable to the manufacturing. The diffractogram of sample B, which corresponds to the surface, shows only the presence of gypsum (*Gp*) and quartz (*Qz*).

High resolution FESEM analysis allowed the study of bulk's texture and their surface and chemical analysis. The matrix of the specimen is distinguished by an elevated porosity in its bulk composition with large gypsum tabular crystals, coexisting with needle-like intermediate ones, while the surface of the sample is characterised by minerals of lower crystal size dimensions, more compactly distributed from a layer of circa 100 µm (Figure 5B). FESEM observations confirmed the XRPD data: the matrix is

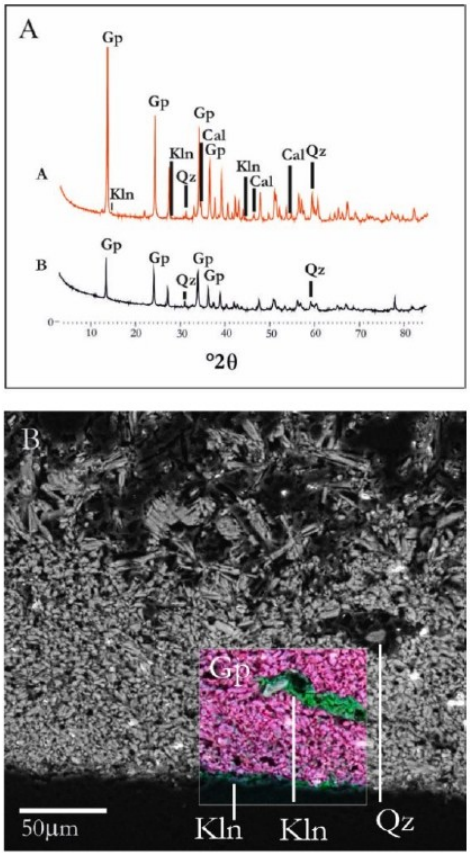

Figure 5. XRPD patterns of sample A and B (A); FESEM image of sample B. The map highlights a less porous gypsum-based matrix with inclusions of quartz and kaolinite, and a finishing rich in kaolinite (B).

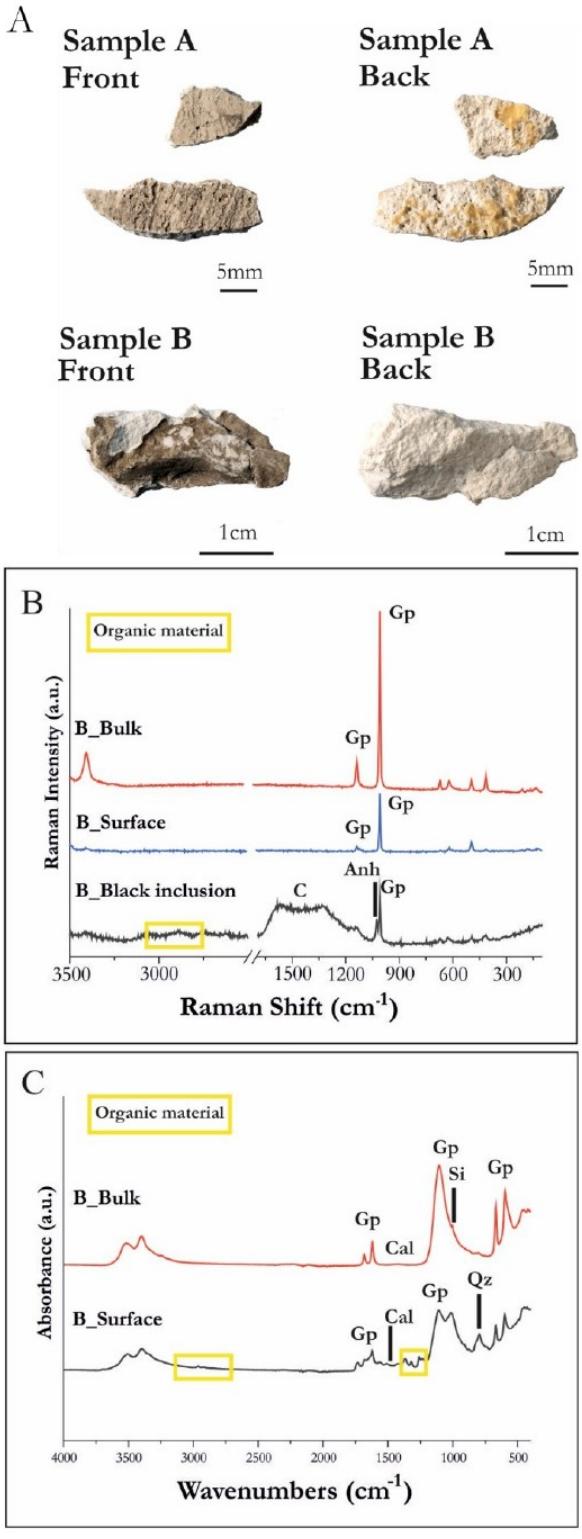

Figure 6. A) Micro-samples (Sample A and sample B, front and back) were collected from the plaster cast MCR_3045; B) Raman spectra of sample B; C) ATR-FTIR spectra of sample B.

mainly formed by gypsum crystals, with the presence of few quartz grains. EDS chemical maps on the surface area of the sample show the presence of a clayey-base coating (Figure 5B), characterised by the presence of aluminium (Al), silicon (Si) and potassium (K). Such finishing may have been applied after the moulding process. A clay finishing is indeed attested in historical recipes [28], used to change the gypsum's colour appearance and level and fill the base surfaces.

The three μRaman spectra show the characteristic bands of gypsum at 1140, 1008, 673, 492 and 414 cm^{-1}, corresponding to the stretch vibrational mode of SO_4 (Figure 6B) [29], [30], [31], [32], [33], [34], [35], [36]. The two Raman bands observed around 3405 and 3490 cm^{-1} correspond to the O-H stretching vibration of water molecules in gypsum [32], [34]. The spectra show traces of anhydrite, with the characteristic bands of the sulphate ions at 1170, 1026 and 630 cm^{-1} [32], [34], [36]. The presence of anhydrite can be ascribed to the raw material used in the moulding of the casts [30]. μRaman measurements did not detect the presence of calcite, given the absence of the characteristic peak at 1087 cm^{-1} [36], [37], [38]. On the other hand, amorphous carbon was detected by the narrower width and higher intensities of the characteristic bands between 1600 and 1300 cm^{-1} [33], [38].

The ATR-FTIR spectra of sample B revealed the presence of gypsum ($CaSO_4{\cdot}2H_2O$), as evidenced by the characteristic peaks at 1680, 1620 cm^{-1} (bending OH), and at 1110, 670 and 620 cm^{-1} (Figure 6C), which correspond to the stretching vibration of SO_4^{2-}, while the stretching vibrations of the water molecules within the gypsum occur at approximately 3500 and 3400 cm^{-1} [39], [40], [41], [42].

Notably, the peak at 3340 cm^{-1} in the spectrum of the surface corresponds to the stretching OH of non-bonding water molecules. The identification of the carbonate functional group, indicative of the presence of calcite, can be detected in both spectra, marked by the characteristic peaks at around 1420-1430 and 873 cm^{-1} [6], [41], [43], [44], [45]. Furthermore, the broad, low-intensity signal within the 800-770 cm^{-1} range may be attributed to quartz, either inherent in the raw material or added during the moulding process [46]. Bands at 2964, 2920, and 2850 cm^{-1} can be ascribed to the stretching CH of an organic substance, along with peaks at 1736 cm^{-1} (stretching C=O), 1562 and 1511 cm^{-1} (stretching C-C), and the bands at approximately 1370 and 1230 cm^{-1} (bending CH) [47], [48]. This organic material can be attributed to some compound used in previous interventions or as a part of a finishing application.

4. CONCLUSION

While the study of plaster replicas has expanded in recent years, few individual case studies fully capture the complexity of these materials due to their specificity. Valuable insights into gypsum-based materials' characterisation and manufacturing technologies often arise from studies on decorative stucco and mortars. However, these studies primarily focus on physical and mechanical properties, with limited research on hygroscopic properties and further research is needed to develop a deeper understanding of gypsum-based materials and their interaction within indoor environments.

The control of microclimates in museum environments or historic buildings is a fundamental aspect of protecting artefacts and planning appropriate conservation policies. Simultaneously, characterizing constituent materials and identifying primary degradation patterns through a multidisciplinary analytical

approach is essential for the long-term conservation of plaster replicas.

The microclimate data recorded between November 2023 and June 2023 show an average temperature of 15.06 °C, with relative humidity levels occasionally exceeding 80 %. Compared to the 2012 reports, it becomes evident that environmental conditions, especially fluctuations in relative humidity, have significantly impacted the preservation state of the gypsum-based plaster casts. This impact is evident due to the various forms of degradation, including new fractures, erosion, and material pulverisation. Additionally, the surfaces exhibit scratches, deposits, and stains.

The microchemical and mineralogical analyses conducted on the microsamples, have revealed that calcium sulphate dihydrate is the main component of the plaster replicas. However, traces of calcite, quartz and anhydrite have also been found. The presence of an organic material could probably derive from previous restoration interventions. In order to clarify the nature of this organic compound, the use of additional techniques such as Thermogravimetry-Differential Scanning Calorimetry and Pyrolysis Gas-Chromatography will be considered in the next future.

Ongoing analyses include on-site Hyperspectral Imaging to map and confirm forms of degradation, and colorimetric measurements to understand tonal variations on the surfaces of the plaster casts.

These results will support the restoration efforts for the plaster casts, ensuring their optimal preservation once the Museum reopens.

Furthermore, a result of a structural analysis of Room LI will be conducted using IR Thermography. Based on the results of this analysis, the microclimatic monitoring campaign will be extended, employing higher-performance sensors, strategically positioned at critical points within the gallery. The preservation of the historical gypsum replicas is of fundamental importance as evidence of the flow of time in order to preserve the memory of the evolution of the original monument.

REFERENCES

[1] A. Spagnulo, C. Vetromile, A. Masiello, M. F. Alberghina, S. Schiavone, C. Lubritto, Climate and Cultural Heritage: The Case Study of "Real Sito of Carditello", Heritage, vol. 2 (2019), pp. 2053-2066.
DOI: 10.3390/heritage2030124

[2] K. Fabbri, Historic Climate in Heritage Building and Standard 15757: Proposal for a Common Nomenclature. Climate, vol. 10 (2022), pp. 4-12.
DOI: 10.3390/cli10010004

[3] V. Risdonne, C. Hubbard, J. Puisto, C. Theodorakopoulos, A mullti-analytical study of historical coated plaster surfaces: the examination of a nineteenth-century V&A cast of a tombstone, Herit. Sci., vol. 9 (2021).
DOI: 10.1186/s40494-021-00533-0

[4] V. Risdonne, A. Francescutto Miró, S. Morio, C. Theodorakopoulos, The Victoria and Albert Museum Plaster Casts by the Nineteenth-Century Workshop of the Notre-Dame Cathedral: Scientific Analysis and Conservation, Herit., vol. 5 (2022), pp. 3427-3445.
DOI: 10.3390/heritage5040176

[5] M. Caroselli, G. Cavallo, A. felici, S. Luppichini, G. Nicoli, L. Aliverti, G. Jean, Gypsum in Ticinese stucco artworks of the 16-17th century: Use, characterization, provenance and induced decay phenomena, J. Archaeol. Sci. Rep., vol. 24 (2019), pp. 208-219.
DOI: 10.1016/j.jasrep.2019.01.009

[6] M. Uccelli, M. Caroselli, J. Válek, J. Zapletalová, A. Felici, G. Nicoli, G. Jean, Characterization of the stucco decoration by Baldassarre Fontana in the Gallery of the Angels at Uherče Castle (Cz), J. Archaeol. Sci. Rep., vol. 44 (2022), pp. 103493.
DOI: 10.1016/j.jasrep.2022.103493

[7] L. Rampazzi, B. Rizzo, C. Colombo, C. Conti, M. Realini, U. Bartolucci, M. P. Colombini, A. Spiriti (+ 1 more author), The stucco decorations from St. Lorenzo in Laino (Como, Italy): The materials and the techniques employed by the "Magistri Comacini", Anal. Chem. Acta., vol. 630 (2008), pp. 91-100.
DOI: 10.1016/j.aca.2008.09.052

[8] M. Caroselli, G. Cavallo, A. Felici, L. Aliverti, S. Luppichini, G. Jean, G. Nicoli, Characterisation of the stucco decorations at the "Sacro Monte di Ossuccio" (16th-17th century, Como, Italy, Int. J. Conserv. Sci., vol. 7 (2016), pp. 857-870.

[9] M. Caroselli, S. A. Ruffolo, F. Piqué, Mortars and plasters – how to manage mortars and plasters conservation, Archaeol. Anthropol. Sci., vol. 13 (2021).
DOI: 10.1007/s12520-021-01409-x

[10] M. T. Freie, M. do Rosário Veiga, A. Santos Silva, J. De Brito, Restoration of ancient gypsum-based plasters: Design of compatible materials, Cem. Concr. Compos., vol. 120 (2021), pp. 104014.
DOI: 10.1016/j.cemconcomp.2021.104010

[11] M. T. Freie, M. do Rosário Veiga, A. Santos Silva, J. De Brito, Studies in ancient gypsum based plasters toward their repair: Physical and mechanical properties, Constr. Build. Mater., col. 202 (2019), pp. 319-331.
DOI: 10.1016/j.conbuildmat.2018.12.214

[12] E. Salvessa, S. Jalali, L. M. O. Sousa, L. Fernandes, A. M. Duarte, Historical plasterwork techniques inspire new formulation, Constr. Build. Mater., vol. 48 (2013), pp. 858-867.
DOI: 10.1016/j.conbuildmat.2013.07.064

[13] A. Magalhães, R. Veiga, Physical and mechanical characterisation of historic mortars. Application to the evaluation of the state of conservation, Mater. Constr., vol. 59 (2009), pp. 61-77.
DOI: 10.3989/mc.2009.41907

[14] G. Gariani, P. Lehuéde, L. Leroux, G. Wallez, F. Goubard, Anne Bouquillon, Marc Bormand, First insights on the mineral composition of "Stucco" devotional reliefs from Italian Rennaissance Masters: investigating technological practices and raw material sourcing, J. Cult. Herit., vol. 34 (2018), pp. 23-32.
DOI: 10.1016/j.culher.2018.05.003

[15] K. Elert, P. Bel-Anzué, M. Burgos-Ruiz, Influence of calcination temperature on hydration behaviour, strength, and weathering resistance of traditional gypsum plaster, Constr. Build. Mater., vol. 367 (2023), pp. 130361.
DOI: 10.1016/j.conbuildmat.2023.130361

[16] M. T. Freie, A. Santos Silva, M. do Rosário Veiga, J. De Brito, Studies in ancient gypsum based plasters towards their repair: Mineralogy and microstructure, Constr. Build. Mater., vol. 196 (2019), pp. 512-529.
DOI: 10.1016/j.conbuildmat.2018.11.037

[17] V. Risdonne, C. Hubbard, V. H. López Borges, C. Theodorakopoulos, Nineteenth-century Plaster Casts: a Review of Historical Sources, Stud. Conserv., vol. 67 (2022), pp. 186-208.
DOI: 10.1080/00393630.2020.1864896

[18] E. M. Payne, The conservation of Plaster Casts in the Nineteenth Century, Stud. Conserv., vol. 65 (2020), pp. 37-58.
DOI: 10.1080/00393630.2019.1610845

[19] S. Salvini, C. Coletti, L. Maritan, M. Massironi, A. Pieropan, R. Spiess, C. Mazzoli, Petrographic characterization and durability of carbonate stones used in UNESCO World Heritage Sites in northeastern Italy, Environ. Earth Sci., vol. 82 (2023), pp. 49.
DOI: 10.21203/rs.3.rs-1651027/v1

[20] G. Battista, R. de Lieto Vollaro, Correlation between air pollution and weather data in urban areas: Assessment of the city of Rome (Italy) as spatially and temporally independent regarding pollutants, Atmos. Environ., vol. 165 (2017), pp. 240-277.
DOI: 10.1016/j.atmosenv.2017.06.050

[21] A. Winkler, T. Contardo, V. Lapenta, A. Sgamellotti, S. Loppi, Assessing the impact of vehicular particulate matter on cultural heritage by magnetic biomonitoring at Villa Farnesina in Rome, Italy, Sci. Total Environ., vol. 823 (2022), pp. 153729.
DOI: 10.1016/j.scitotenv.2022.153729

[22] A. Proietti, M. Panella, F. Leccese, E. Svezia, Dust detection and analysis in museum environment based on pattern recognition, Meas., vol. 66 (2015), pp. 62-72.
DOI: 10.1016/j.measurement.2015.01.019

[23] A. Proietti, L. Liparulo, F. Leccese, M. Panella, Shapes classification of dust deposition using fuzzy kernel-based approaches, Meas., vol. 77 (2016), pp. 344-350.
DOI: 10.1016/j.measurement.2015.09.025

[24] F. Mercuri, U. Zammit, N. Orazi, S. Paoloni, M. Marinelli, F. Scudieri, Active infrared thermography applied to the investigation of art and historic artefacts, J. Therm. Anal. Calorim., vol. 104 (2011), pp. 475-485.
DOI: 10.1007/s10973-011-1450-8

[25] C. A. Boevens, V. V. H. Ichharam, Redetermination of the crystal structure of calcium sulphate dihydrate, $CaSO_4 \cdot 2H_2O$, Z. Kristallogr., vol. 217 (2002), pp. 9-10.
DOI: 10.1524/ncrs.202.217.1.9

[26] L. N. Warr, IMA-CNMNC approved mineral symbols, Mineral. Mag., vol. 85 (2021), pp. 291-320.
DOI: 10.1180/mgm.2021.43

[27] S. S. Pawelkowicz, P. Svora, Z. Prosek, M. Keppert, E. Vejmelková, N. Murafa, T. Sawoszczuk, J. Sygula-Cholewińska (+ 1 more author), Laboratory assessment of a photoactive Gypsum-based repair plaster, constr. Build. Mater., vol. 346 (2022), pp. 128426.
DOI: 10.1016/j.conbuildmat.2022.128426

[28] T. Turco, Il gesso lavorazione – trasformazione – impieghi, Ulrico Hoepli, Milano, 1861, BID: SBL0247741, BNI616859. [In Italian]

[29] V. Antunes, A. Candeias, M. J. Oliveira, S. Longelin, V. Serrão, A. I. Seruya, J. Coroado, L. Dias, (+ 2 more authors), Characterizaion of gypsum and snhydrite ground layers in 15th and 16th centuries Portuguese paintings by Raman Spectroscopy and other techniques, J. Raman Spectrosc., vol. 45 (2014), pp. 1026-1033.
DOI: 10.1002/jrs.4488

[30] N. Prieto-Taboada, O. Gómez-Laserna, I. Martínez-Arkarazo, M. A. Olazabal, J. M. Madariaga, Raman Spectra of the Different Phases in the $CaSO_4$-H_2O System, Anal. Chem., vol. 86 (2014), pp. 10131-10137.
DOI: 10.1021/ac501932f

[31] H. G. M. Edwards, M. T. Doménech-Carbó, M. D. Hargreaves, A. Doménech-Carbó, A Raman spectroscopic and combined analytical approach to the restoration of severely damaged frescoes: the Palomino project, J. Raman Spectrosc., vol. 39 (2008), pp. 444-452.
DOI: 10.1002/jrs.1854

[32] T. Schmid, P. Dariz, Chemical imaging of historical mortars by Raman microscopy, Constr Build Mater., vol. 114 (2016), pp. 506-516.
DOI: 10.1016/j.conbuildmat.2016.03.153

[33] I. Martínez-Arkarazo, D. C. Smith, O. Zuloaga, M. A. Olazabal, J. M. Madariaga, Evaluation of three different mobile Raman microscopes employed to study deteriorated civil building stones, J. Raman Spectrosc., vol. 39 (2008), pp. 1018-1029.
DOI: 10.1002/jrs.1941

[34] P. S. R. Prasad, A. Pradhan, T. N. Gowd, *In situ* micro-Raman investigation of dehydration mechanism in natural gypsum, Curr. Sci., vol. 80 (2001), pp. 1203-1207.

[35] H. G. M. Edwards, S. E. J. Villar, J. Parnell, C. S. Cockell, P. Lee, Raman spectroscopic analysis of cyanobacterial gypsum halotrophs and relevance for sulfate deposits on Mars, R. Soc. Chem., vol. 130 (2005), pp. 917-923.
DOI: 10.1039/b503533c

[36] A. Sarmiento, M. maguregui, I. Martinez-Arkazo, M. Angulo, K. Castro, M. A. Olazábal, L. A. Fernández, M. D. Rodríguez-Laso (+ 3 more authors), Raman spectroscopy as a tool to diagnose the impacts of combustion and greenhouse acid gases on properties of Built Heritage, J. Raman Spectrosc. Vol. 39 (2008), pp. 1042-1049.
DOI: 10.1002/jrs.1937

[37] D. Seol, Y. Ma, K. Nam, H. Chung, A study on Raman spectroscopic scheme enabling fast and accurate determination of calcite concentration in gypsum, Microchem. J., vol. 172 (2021), pp. 240-252.
DOI: 10.1016/j.chemgeo.2008.11.008

[38] S. E. Spoto, G. Paladini, F. Caridi, V. Crupi, S. D'Amico, D. Majolino, V. Venuti, Multi-Technique Diagnostic Analysis of Plaster Mortars from the *Church of the Annunciation* (Tortorici, Sicily), Mater., vol. 15 (2022), pp. 958-972.
DOI: 10.3390/ma15030958

[39] D. Gramtorp, K. Botfeldt, J. Glastrup, K. P. Simonsen, Investigation of Anne Marie Carl-Nielsen's wax models, Stud. Conserv., vol. 60 (2015), pp. 97-106.
DOI: 10.1179/2047058413y/.0000000111

[40] G. Vasco, A. Serra, D. Manno, G. Buccolieri, L. Calcagnile, L. Miotto, L. Valli, A. Buccolieri, Diagnostic investigation to support the restoration of the polychrome terracotta relief *"Madonna and Child"* in Piove di Sacco (Padova, Italy), J. Cult. Herit., vol. 53 (2021), pp. 80-87.
DOI: 10.1016/j.culher.2021.11.009

[41] G-L. Liu, S. G. Kazarian, Recent advances and applications to cultural heritage using ATR-FTIR spectroscopy and ATR-FTIR spectroscopic imaging, R. Soc. Chem., vol. 147 (2022), pp. 1777-1797.
DOI: 10.1039/d2an00005a

[42] L. Bishop, M. D. Dyar, S. J. King, A. J. Brown, G. A. Swayze, What Lurks in the Martian Rocks and Soil? Investigation of Sulfates, Phosphates, and Perchlorates. Spectral properties of Ca-sulfates: Gypsum, bassanite and anhydrite, Am. Mineral., vol. 99 (2014), pp. 2105-2115.
DOI: 10.2138/am-2014-4756

[43] F. A. Andersen, L. Brečevic, Infrared Spectra of Amorphous and Crystalline Calcium Carbonate, Acta Chem. Scand., vol. 45 (1991), pp. 1018-1024.
DOI: 10.389/acta.chem.scand.45-1018

[44] T. Lamhasni, H. El-Marjaoui, A. El Bakkali, S. Ait Lyazidi, M. Haddad, A. Be-Ncer, F. Benyaich, A. Bonazza (+ 1 more author), Air pollution impact on architectural heritage of Morocco: Combination of synchronous fluorescence and ATR-FTIR spectroscopies for the analyses of black crusts deposits, Chemosphere, vol. 225 (2019), pp. 517-523.
DOI: 10.1016/j.chemosphere.2019.03.109

[45] M. M. Jordán, J. Jordá, F. Pardo, M. A. Montero, Mineralogical Analysis of Historical Mortars by FTIR, Mater., vol. 12 (2018), pp. 55-59.
DOI: 10.3390/ma12010055

[46] I. Fikri, M. El Amraoui, M. Haddad, A. S. Ettahiri, C. Falguères, L. Bellot-Gurlet, T. Lamhasni, S. A. Lyazidi, (+ 1 more author), Raman and ATR-FTIR analyses of medieval wall paintings from al-Qaeaqiyyin in Fez (Morocco), SAA, vol. 280 (2022), pp. 121557.
DOI: 10.1016/j.saa.2022.121557

[47] F. Pozzi, E. Basso, S. Alderson, J. Levinson, M. Neimar, S. Alcalá, Aiding the cleaning of four 19th-century Tsimshian house posts: investigation of museum-applied surface coatings and original polychromy, Herit. Sci., vol. 9 (2021), pp. 42-59.
DOI: 10.1186/s40494-021-00513-4

[48] V. Guglielmi, C. A. Lombardi, G. Fiocco, V. Comite, A. Bergomi, M. Borelli, M. Azzarone, M. Malagodi (+ 2 more authors), Multi-Analytical Investigation on Rennaissance Polychrome Earthenware Attributed to Giovanni Antonio Amedeo, Appl. Sci., vol. 13 (2023), pp. 3924.
DOI: 10.3390/app13063924

XIII Congresso Nazionale AIAr

Conservation methods for 19th century plaster replicas: understanding gypsum compositions and protective treatments

F. Bubola ([*, a]), E. Balliana ([b]), C. Coletti ([a]), T. De Kock ([c]), C. Mazzoli ([a])

([a]) University of Padua, Geosciences, Padua, Italy

([b]) Ca' Foscari University, Environmental Sciences, Informatics and Statistics, Venice, Italy

([c]) University of Antwerp, Design Science, Antwerp, Belgium

* Presenting author

federica.bubola@phd.unipd.it

In the 19th century, academic institutions and museums assembled extensive collections of gypsum-based replicas, primarily reproducing ancient sculptures for educational, documentary and artistic training purposes. These gypsum-based casts have been essential in preserving the intricate details of classical monuments, many of which have since deteriorated or been lost. However, maintaining the durability of these replicas has proven difficult, as their soft, porous nature makes gypsum highly susceptible to environmental fluctuations. Prolonged exposure to uncontrolled temperature and humidity variations, common in many historical buildings lacking modern climate control, accelerates their deterioration. The environmental instability in these historical spaces, stresses the replicas, causing cracking, surface detachment and other material degradation. Managing microclimate conditions in museums and heritage buildings is, therefore, crucial for preserving such vulnerable collections. Rapid changes in temperature and humidity, can induce internal stress and exacerbate damage. For historic collections, maintaining a "historic climate" – the stable microclimate to which artifacts have adjusted over decades – is essential to their conservation. In response to these conservation challenges, this study investigates the traditional gypsum mixtures and additives typical of 19th century recipes used in plaster casting. 72 gypsum-based mock-ups according to the historical recipes were produced. These mixtures included alabaster and Paris gypsum, with the addition of various additives such as marble powder, Arabic gum, kaolin and wood powder. By studying properties of these materials, the research seeks to determine how various combinations of gypsum and additives influence the physical and chemical stability of the casts. Moreover, in order to explore the effectiveness of both historical and modern protective coatings like a mixture of kaolin and water, polyvinyl alcohol and Acryl-EM 33. Mock-up samples undergo accelerated ageing tests, simulating the effects of environmental factors such as humidity and temperature fluctuations. These tests examine the coatings' capacity to prevent plaster deterioration, ensuring the preservation of its original appearance and texture. By combining material analysis, protective testing and environmental assessment, this research aims to develop sustainable, cost-effective methods for conserving plaster replicas, ensuring their continued role as cultural and educational resources. These strategies provide a foundation for preserving and displaying plaster casts in significant historic buildings where modern climate control may be insufficient or lacking, thereby safeguarding their durability and cultural value.

References

[1] E. M. Payne, The conservation of plaster casts in the Nineteenth Century, Stud. Conserv. (2022), vol. 65, pp. 37-58, DOI: 10.1080/00393630.2019.1610845

[2] E. Salavessa, S. Jalali, L. M. O. Sousa, L. Fernandes, A. M. Duarte, Historical plasterwork techniques inspire new formulations, Constr. Build. Mater. (2013), vol. 48, pp. 858-867, DOI: 10.1016/j.conbuildmat.2013.07.064
[3] C. Arcolao, Le ricette del Restauro: Malte, intonaci, Stucchi dal XV al XIX secolo, Saggi Marsilio, Venezia, 1998
[4] T. Turco, Il gesso lavorazione – trasformazione – impieghi, Ulrico Hoepli, Milano, 1861
[5] A. Zornoza-Indart, P. López-Arce, L. López-Polín, Durability of traditional and new nanoparticle base consolidating products for the treatment of archaeological stone tools: Chert artifacts from Atapuerca sites (Burgos, Spain), J. Cult. Herit. (2017), vol. 24, pp. 9-21, DOI: 10.1016/j.culher.2016.10.019
[6] V. Risdonne, C. Hubbard, V. H. López Borges, C. Theodorakopoulos, Materials and Techniques for the Coating of Nineteenth-century Plaster Casts: A Review of Historical Sources, Stud. Conserv. (2022), vol. 67, pp. 186-208, DOI: 10.1080/00393630.2020.1864896

CONSERVATION STRATEGIES FOR 19TH CENTURY PLASTER REPLICAS: INSIGHT INTO GYPSUM MIXTURES AND PROTECTIVE COATINGS

F. Bubola[1]*, C. Coletti[2], E. Balliana[3], T. De Kock[4] and C. Mazzoli[5]

Extended abstract

Keywords: Gypsum-based replicas, Indoor micro-climate, Protective coatings, Accelerated ageing tests, Cultural Heritage.

During the 19th century, museums and academic institutions acquired extensive collections of gypsum-based plaster replicas of ancient sculptures for educational, documentary, and artistic training purposes. Recently, interest in these replicas has grown due to their historical significance, as they preserve the three-dimensional details of historical monuments. However, gypsum is a soft and porous material, making casts particularly vulnerable to degradation, especially in unsuitable indoor environments. This research studies different 19th century gypsum mixtures and protective coatings, evaluating their durability through accelerated ageing tests to enhance conservation strategies. This study highlights that kaolin-based samples are particularly vulnerable to degradation, with increased surface roughness and greater colour variations observed in Paris gypsum samples, especially those mixed with marble powder, emphasising the need for targeted conservation strategies.

1 Introduction

Throughout the 19th century, gypsum-based plaster replicas became essential for art training and heritage studies. Museums and institutions acquired extensive collections, but their fragility made them vulnerable to climatic damage and vandalism. Stored indoors, they are not always exposed to suitable climatic conditions. Historical buildings often lack ideal conservation environments and require specific environmental controls based on the historic climates. This study investigates the interaction between materials used in 19th-century plaster replicas and their microclimate conditions. Mock-ups with different mixtures were prepared to assess traditional and modern coatings (Turco 1961). Ageing tests were conducted using a solar-box and a climate chamber. Periodic monitoring evaluates chemical variations, colour and roughness surface changes.

2 Materials and methods

A total of 72 samples were prepared using three gypsum mixtures: i. alabaster gypsum (A) or plaster of Paris (P) with animal glue and marble powder (M); ii. Alabaster or plaster of Paris with animal glue, kaolin, and wood powder (KW); and iii. Alabaster or plaster of Paris with animal glue and Arabic gum (AG). Each mixture was tested untreated and with three protective coatings: polyvinyl alcohol (PVA), kaolin-water mixture (K), and Acryl-EM33 (Ac). Ageing was simulated by exposing two sets of 24 samples each to controlled conditions in a climate chamber, simulating 150 years of environmental exposure through 150 cycles alternating between summer (30° C and 30 % RH) and winter (10° C and 90 % RH) A third set of 24 samples was exposed to artificial solar radiation for 1512 hours (three cycles of 504 hours each) in a Solar-box 1500, equipped with a 1500 W xenon-arc lamp (550 W/m², 65°C BST). Changes were monitored via spectrophotometry after each light ageing cycle. FTIR analysis (7500–400 cm^{-1}, 4 cm^{-1} resolution) was performed using a Bruker Alpha spectrometer, while surface topography was assessed with a NANOVEA Jr-25 3D profilometer (ISO 25178), and colourimetry followed the UNI-EN 15886 standard using a Konica-Minolta CM-700d spectrophotometer (360–740 nm, 10 nm resolution). Periodic monitoring was carried out at four different stages: before ageing (t_0); and then after 50, 100, and 150 cycles for the samples aged in the climate chamber, or after 504, 1,008, and 1,512 hours for those aged under light exposure (t_1, t_2, and t_3, respectively).

[1] *F. Bubola, Ph.D. Student, Department of Geosciences, University of Padova, Italy, federica.bubola@phd.unipd.it

[2] C. Coletti, Researcher, Department of Geosciences, University of Padova, Italy, chiara.coletti@unipd.it

[3] E. Balliana, Researcher, Department of Environmental Sciences, Informatics and Statistics, Ca' Foscari University, Italy, eleonora.balliana@unive.it

[4] T. De Kock, Professor, Department of Design Sciences, University of Antwerp, Belgium, tim.dekock@uantwerpen.be

[5] C. Mazzoli, Professor, Department of Geosciences, University of Padova, Italy, claudio.mazzoli@unipd.it

*Corresponding author

3 Results and Discussion

The analysis of surface roughness, FTIR spectra, and colourimetric variations provides a comprehensive understanding of the samples' stability and degradation over time. The analysis of surface roughness revealed that Paris gypsum-samples without coatings and mixed with mineral fillers (KW, M) showed increasing roughness over time, indicating gypsum matrix degradation. Acrylic resin initially smoothed the surface but exhibited polymer film degradation over time, whereas PVA-treated samples remained stable, with only a slight increase in roughness at t_3, suggesting its potential for long-term protective properties. Kaolin, on the other hand, stabilized roughness in some samples but led to increased roughness when combined with kaolin and wood powder, indicating limited protective ability like in samples P_KW_K, with Sq values increasing from 7.336 µm at t_0 to 34.900 µm at t_3 and S_a values from 5.580 µm at t_0 to 28.120 µm at t_3. FTIR spectra revealed the stability of the mock-ups and their interaction with environmental conditions. As expected, gypsum was detected in all spectra based on its main characteristic peaks (ν OH of non-bonding water at 3548 and 3407 cm^{-1}, ν SO_4^{2-} peaks at 1110 and 670 cm^{-1}, δ SO_4^{2-} bands at 605 and 470 cm^{-1}) (Ye *et al.*, 2021). While most mock-ups and coatings, especially PVA (Figure 1A), showed minimal spectral changes, those containing or coated with kaolin were the most affected, likely due to the loss of kaolin components. As shown in Figure 1B, the characteristic peaks of kaolin, corresponding to hydroxyl groups (3690, 3670, 3645 cm^{-1}), Si-O-Si bonds (1065, 1010 cm^{-1}), OH bending vibrations (940, 912 cm^{-1}), vibrational modes of octahedra around Al ions (796, 793 cm^{-1}), and Al^{3+} vibrations (570, 470, 430 cm^{-1}), are no longer visible after the ageing cycles, leaving only the peaks related to gypsum (Castellano *et al.*, 2012).

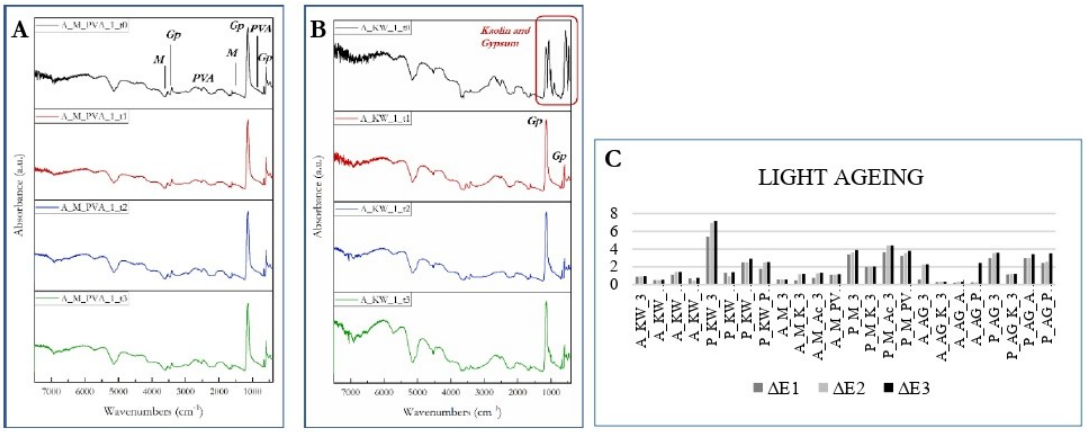

Figure 1. (A) ER-FTIR spectra of A_M_PVA (alabaster gypsum + marble powder + polyvinyl alcohol) at t_0, t_1, t_2, t_3; (B) ER-FTIR spectra of A_KW (alabaster gypsum + kaolin + wood powder - untreated) at t_0, t_1, t_2, t_3; (C) ΔE values obtained from the colourimetric analysis of all samples after 3 cycles of light ageing.

After each light ageing cycle, colourimetric changes in L*, a*, and b* values were observed, (Figure 1C). As L* increases after ageing, colours became brighter in most samples, showing slight and moderate lightening. Paris gypsum mixtures proved to be more susceptible to colour variations compared to alabaster gypsum. In particular, sample P_KW_3 showed progressive and significant colour changes, with ΔE* values increasing from 5.39 (ΔE^*_1) to 6.39 (ΔE^*_2) and reaching 7.16 (ΔE^*_3).

4 Conclusions

In conclusion, FTIR analysis showed that samples with kaolin were the most susceptible to aging. Surface roughness data confirmed that degradation was influenced by the gypsum type, additives, and coatings. PVA was the most effective at maintaining surface stability, while Acryl33 had initial smoothing effects but potential durability issues. Kaolin stabilized roughness in some samples, but when combined with kaolin and wood powder fillers, it increased roughness, indicating limited protective capacity. Colorimetric analysis revealed greater colour variation in Paris gypsum samples, especially in P_KW_3 and those mixed with marble powder, indicating higher sensitivity to degradation.

References

Castellano, M., Turturro, A., Riani, P., Montanari, T., Finocchio, E., Ramis, G., Busca, G., 2010, Bulk and surface properties of commercial kaolins, Applied Clay Science, 48, 446-454.

Turco, T., (1961), "Il gesso lavorazione – trasformazione – impieghi", Ulrico Hoepli, 535pp. [In Italian]

Ye, C., Sklute, E. C., Clotch, T. D., 2021, Orientation averaged visible/near-infrared and mic-infrared optical constants of hydrous Ca-sulfates: gypsum and bassanite, Earth and Space Science, 8, e2021EA001834.

Acknowledgements

I would like to express my gratitude to all the people who made this journey possible.
First and foremost, I wish to thank my supervisor, Prof. Claudio Mazzoli, for giving me this opportunity and for the trust he has placed in me from the very beginning. My sincere thanks also go to Dr. Chiara Coletti and Dr. Eleonora Balliana for their guidance, support and availability.
I extend my gratitude to the Museum of Roman Civilisation, for granting access to this wonderful collection.
A special thank you goes to Prof. Tim de Kock, for allowing me to experience one of the most meaningful periods of my life. In Antwerp I found a family: tank you Sofia, Eda, Teresa, Giorgos and Gaetano for becoming such an important part of my days.
I would also like to thank my wonderful office, Emanuela, Ludovica, Mauro and Eirini, for sharing this adventure with me.
My deepest gratitude goes to my family, without you, I would not be here. I owe you everything.
To Gavino, for being the love of my life.
And Tessi, for always being there Perla Vita.
Thank you, Chiara, for being the first friend I found in Padova when all of this began, and thanks Gio, for your friendship and for all our aperitivi.
Finally, a special thank you to my lifelong friends: Amanda, Ari, Ashia, Marti, Mati, Palli, Sara and Tolo. To many more evenings together.